

Development of Odd-Z-Projectile Reactions for Transactinide Element Synthesis

by

Charles Marvin Folden III

B.S. (Vanderbilt University) 1999

A dissertation submitted in partial satisfaction of the

requirements for the degree of

Doctor of Philosophy

in

Chemistry

in the

GRADUATE DIVISION

of the

UNIVERISTY OF CALIFORNIA, BERKELEY

Committee in charge:

Professor Darleane C. Hoffman, Chair

Professor Luciano G. Moretto

Professor P. Buford Price

Fall 2004

The dissertation of Charles Marvin Folden III is approved:

---

Chair

Date

---

Date

---

Date

University of California, Berkeley

Fall 2004

Development of Odd-Z-Projectile Reactions for Transactinide Element Synthesis

Copyright 2004

by

Charles Marvin Folden III

## Abstract

Development of Odd-Z-Projectile Reactions for Transactinide Element Synthesis

by

Charles Marvin Folden III

Doctor of Philosophy in Chemistry

University of California, Berkeley

Professor Darleane C. Hoffman, Chair

The development of new odd-Z-projectile reactions leading to the production of transactinide elements is described. The cross section of the even-Z-projectile  $^{208}\text{Pb}(^{64}\text{Ni}, \text{n})^{271}\text{Ds}$  reaction was measured at two new energies using the Berkeley Gas-filled Separator at the Lawrence Berkeley National Laboratory 88-Inch Cyclotron. In total, seven decay chains attributable to  $^{271}\text{Ds}$  were observed. These data, combined with previous results, establish an excitation function for the production of  $^{271}\text{Ds}$ . The maximum cross section was  $20^{+15}_{-11}$  pb at a center-of-target energy of 311.5 MeV in the laboratory frame.

The data from the  $^{271}\text{Ds}$  experiments were used to estimate the optimum beam energy for the new odd-Z-projectile  $^{208}\text{Pb}(^{65}\text{Cu}, \text{n})^{272}\text{Ds}$  reaction using the “Fusion by Diffusion” theory proposed by Świątecki, Siwek-Wilczyńska, and Wilczyński. A cross section for this reaction was measured for the first time, at a center-of-target energy of 321.1 MeV in the laboratory frame. The excitation energy for compound nuclei formed at the target center was 13.2 MeV. One decay chain was observed, resulting in a measured cross section of

$1.7^{+3.9}_{-1.4}$  pb. This decay chain is in good agreement with previously published data on the decay of  $^{272}\text{Bh}$ .

The new odd- $Z$ -projectile  $^{208}\text{Pb}(^{55}\text{Mn}, \text{n})^{262}\text{Bh}$  reaction was studied at three different projectile energies, and 33 decay chains of  $^{262}\text{Bh}$  were observed. The existence of a previously reported alpha-decaying isomeric state in this nuclide was confirmed. Production of the ground state was preferred at all three beam energies. The maximum cross section was  $540^{+180}_{-150}$  pb at a projectile center-of-target energy of 264.0 MeV. This cross section is much larger than that previously reported for the even- $Z$ -projectile  $^{209}\text{Bi}(^{54}\text{Cr}, \text{n})^{262}\text{Bh}$  reaction, which may be because the  $^{54}\text{Cr}$  projectile energies in the latter reaction were too high for optimum production of the 1n product. At the highest projectile energy of 268.0 MeV in the target center, two decay chains from  $^{261}\text{Bh}$  were observed as a result of the  $^{208}\text{Pb}(^{55}\text{Mn}, 2\text{n})$  reaction.

In summary, this work shows that odd- $Z$ -projectile reactions can have cross sections comparable to analogous even- $Z$ -projectile reactions, and that the energy of the maximum cross section for 1n reactions can be estimated simply.

## **Dedication**

This dissertation is dedicated to my mother, Betsy Raye Folden. Everything good about me I got from you.

# Table of Contents

Dedication .....	i
Table of Contents .....	ii
List of Figures .....	vii
List of Tables.....	x
Acknowledgements.....	xii
1. Introduction .....	1
1.1. Production and Characterization of Transactinide Elements.....	4
1.2. Excitation Functions .....	10
1.2.1. Magnitudes of Cross Sections .....	10
1.2.1.1. Standard Theoretical Methods.....	10
1.2.1.2. Fusion by Diffusion .....	15
1.2.1.3. Energetics.....	19
1.2.1.4. Cold Versus Hot Fusion.....	21
1.2.2. Location of the Maximum Cross Section for $1n$ Reactions.....	23
1.3. Nuclear Shells and Heavy Element Stability.....	27
1.3.1. “Magic” Numbers .....	27
1.3.2. Liquid-Drop Model.....	29
1.3.3. Strutinsky Shell Corrections .....	32
1.3.4. Illustrative Examples.....	36
1.3.5. Stability of the Transactinide Elements and New Shells .....	38
1.4. Scope.....	41

2. Experimental Apparatus: The Berkeley Gas-filled Separator .....	42
2.1. Targets .....	42
2.1.1. Rotating Wheel Targets .....	43
2.1.2. Target Characteristics.....	44
2.1.3. Stationary Targets.....	45
2.2. Rutherford Detectors and Cross Section Calculations.....	45
2.3. Magnets.....	47
2.3.1. Introduction .....	47
2.3.2. Evaporation Residue Charge States in Helium .....	49
2.4. Focal Plane Detector.....	52
2.4.1. Introduction .....	52
2.4.2. External Calibration Sources.....	56
2.4.2.1. Strip External Energy Calibration .....	56
2.4.2.2. Upstream Energy Calibration .....	65
2.4.2.3. Strip Position Calibration .....	65
2.4.3. Internal Calibration Data: Test Reactions .....	68
2.4.4. High-Energy Calibrations.....	69
2.5. Data Acquisition.....	71
3. Production of $^{271}\text{Ds}$ in the $^{208}\text{Pb}(^{64}\text{Ni}, \text{n})$ Reaction.....	73
3.1. Previous Work .....	73
3.1.1. GSI Experiments.....	73
3.1.2. First LBNL Experiments.....	78
3.1.3. RIKEN Experiments .....	79
3.1.4. Rationale for the New Experiments.....	80

3.2. Experimental Conditions.....	80
3.2.1. $^{271}\text{Ds}$ Production Experiment: $E_{\text{cot}} = 314.3$ MeV.....	81
3.2.2. $^{271}\text{Ds}$ Production Experiment: $E_{\text{cot}} = 311.5$ MeV.....	85
3.3. Observed Decay Chains.....	87
3.3.1. Summary.....	87
3.3.2. $^{271}\text{Ds}$ .....	90
3.3.3. $^{267}\text{Hs}$ .....	91
3.3.4. $^{263}\text{Sg}^m$ .....	92
3.3.5. $^{259}\text{Rf}$ .....	93
3.3.6. $^{255}\text{No}$ .....	94
3.4. Analysis of Expected Random Correlations.....	94
3.4.1. Theory.....	94
3.4.2. Calculations and Interpretation.....	98
3.4.2.1. Expected $^{271}\text{Ds}$ , $^{267}\text{Hs}$ , $^{263}\text{Sg}^m$ , and $^{259}\text{Rf}$ Random Correlations .....	98
3.4.2.2. Expected $^{255}\text{No}$ Random Correlations .....	99
3.5. $^{208}\text{Pb}({}^{64}\text{Ni}, \text{n})^{271}\text{Ds}$ Excitation Function .....	102
4. Production of $^{272}\text{Hs}$ in the $^{208}\text{Pb}({}^{65}\text{Cu}, \text{n})$ Reaction .....	105
4.1. Previous Work .....	105
4.1.1. GSI Experiments.....	105
4.1.2. RIKEN Experiments .....	109
4.1.3. Rationale for the New Experiment .....	112
4.2. Experimental Conditions.....	112
4.3. Observed Decay Chain .....	114

4.4. Exclusion of Other Possible Interpretations.....	121
4.5. Analysis of Expected Random Correlations.....	123
4.6. Comparison with the $^{209}\text{Bi}(^{64}\text{Ni}, \text{n})^{272}\text{111}$ Reaction .....	125
5. Production of $^{262}\text{Bh}$ in the $^{208}\text{Pb}(^{55}\text{Mn}, \text{n})$ Reaction .....	127
5.1. Previous Work .....	127
5.1.1. Dubna Experiments .....	127
5.1.2. Studies of the $^{209}\text{Bi}(^{54}\text{Cr}, \text{n})^{262}\text{Bh}$ Reaction at GSI.....	129
5.1.3. Rationale for the New Experiments to Produce $^{262}\text{Bh}$ .....	132
5.2. Experimental Conditions.....	133
5.3. Observed Decay Chains.....	136
5.3.1. Summary.....	136
5.3.2. Information About Specific Decay Chains.....	140
5.3.3. $^{262}\text{Bh}^g, ^{262}\text{Bh}^m$ .....	142
5.3.4. $^{261}\text{Bh}$ .....	144
5.3.5. $^{258}\text{Db}$ .....	145
5.3.6. $^{258}\text{Rf}$ .....	146
5.3.7. $^{254}\text{Lr}$ .....	147
5.3.8. $^{254}\text{No}$ .....	147
5.3.9. $^{250}\text{Md}$ .....	148
5.3.10. $^{250}\text{Fm}$ .....	148
5.4. Analysis of Expected Random Correlations.....	149
5.4.1. Expected $^{262}\text{Bh}$ , $^{258}\text{Db}$ , and $^{254}\text{Lr}$ Random Correlations .....	149
5.4.2. Expected $^{250}\text{Fm}$ Random Correlations .....	150
5.5. $^{208}\text{Pb}(^{55}\text{Mn}, \text{n})^{262}\text{Bh}$ Excitation Function.....	152

5.6. Comparison of $^{208}\text{Pb}(\text{Mn}, \text{n})$ and $^{209}\text{Bi}(\text{Cr}, \text{n})$ Excitation Functions .....	153
6. Conclusions and Future Work .....	155
6.1. Conclusions .....	155
6.2. Future Work .....	156
7. References .....	159
Corrigendum .....	174
Disclaimer .....	175

## List of Figures

1.1. Periodic table of the elements as of October 2004.....	3
1.2. Average values of $\Gamma_n/\Gamma_{tot} = \Gamma_n/(\Gamma_n + \Gamma_\beta)$ for reactions leading to the production of (a) $^{242}\text{Cf}$ and (b) $^{252}\text{No}$ , as a function of initial excitation energy .....	14
1.3. Predicted excitation functions for the (a) $^{208}\text{Pb}(^{64}\text{Ni}, n)^{271}\text{Ds}$ and (b) $^{208}\text{Pb}(^{55}\text{Mn}, n)^{262}\text{Bh}$ reactions .....	17
1.4. Theoretical predictions for the excitation functions of the $^{209}\text{Bi}(^{64}\text{Ni}, n)$ and $^{208}\text{Pb}(^{65}\text{Cu}, n)$ reactions as functions of (a) the center-of-mass beam energy $E_{cm}$ and (b) $E_{cm}$ less the neutron-emission threshold energy $E_{n, thr}$ .....	18
1.5. Maximum cross section observed versus effective fissility for many compound nucleus heavy element production reactions .....	22
1.6. Physical basis for the “optimum energy rule” .....	24
1.7. Schematic of the optimum compound nucleus excitation energy for heavy element production via cold fusion reactions.....	25
1.8. Shell effects as a function of neutron number for nuclides throughout the chart of the nuclides.....	28
1.9. Comparison of liquid-drop model mass predictions with experimental data .....	30
1.10. Schematic diagram of potential energy surfaces for a deformed heavy nucleus in the liquid-drop model with and without shell corrections applied .....	32

1.11. Schematic diagram of Nilsson level splitting as envisaged by Strutinsky .....	33
1.12. Mass surfaces calculated by Strutinsky using the shell model for various nuclei.....	35
1.13. Shell correction energies for nuclei beyond $^{208}\text{Pb}$ .....	40
2.1. Schematic of the Berkeley Gas-Filled Separator .....	43
2.2. Experimental charge states of EVRs in He .....	51
2.3. The BGS focal plane detector array .....	53
2.4. Raw calibration data .....	57
2.5. Linear energy parameter spectrum .....	58
2.6. Quadratic coefficients of the parabolic fits to raw calibration data.....	61
2.7. Linear and quadratic energy parameters for raw calibration data .....	62
2.8. Final alpha-energy spectrum produced for raw calibration data.....	63
2.9. Observed position parameters for raw calibration data .....	66
2.10. External-to-internal calibration correction .....	68
3.1. Cross sections for the $^{208}\text{Pb}({}^{64}\text{Ni}, \text{n})^{271}\text{Ds}$ reaction obtained at three laboratories .....	74
3.2. Same as Fig. 3.1 except that error bars have been included .....	75
3.3. $^{271}\text{Ds}$ decay chains observed in the irradiation of $^{208}\text{Pb}$ with ${}^{64}\text{Ni}$ at (a) $E_{\text{tot}} = 314.3 \text{ MeV}$ and (b) $E_{\text{tot}} = 311.5 \text{ MeV}$ .....	84
3.4. Heavy-element chart of the nuclides as of October 2004.....	89
3.5. Schematic representation of the random correlation analysis .....	96
4.1. Experimental cross sections and theoretical excitation function prediction for the $^{209}\text{Bi}({}^{64}\text{Ni}, \text{n})^{272}\text{111}$ reaction.....	106

4.2. Decay chain observed in the irradiation of $^{208}\text{Pb}$ targets with $^{65}\text{Cu}$ .....	115
4.3. MWPC signals in coincidence with alpha particles emitted in strip 18 during BGS run 068, as a function of alpha particle energy deposited in the focal plane detector.....	118
4.4. Observed energy versus lifetime for all alpha particles produced in $^{272}\text{111}$ decay chains.....	119
4.5. Theoretical excitation function and experimental data for the $^{208}\text{Pb}(\text{Cu}, \text{n})^{272}\text{111}$ reaction.....	121
5.1. Excitation functions measured for the production of $^{262}\text{Bh}$ in the $^{209}\text{Bi}(\text{Cr}, \text{n})$ and $^{208}\text{Pb}(\text{Mn}, \text{n})$ reactions .....	130
5.2. Bohrium decay chains observed at $E_{\text{tot}} = 264.0$ MeV.....	137
5.3. Bohrium decay chains observed at $E_{\text{tot}} = 260.0$ MeV.....	138
5.4. Decay chains of (a) $^{262}\text{Bh}$ and (b) $^{261}\text{Bh}$ observed at $E_{\text{tot}} = 268.0$ MeV.....	139
5.5. Observed pulse heights for all $Z = 107$ EVRs .....	141

## List of Tables

1.1. International Union of Pure and Applied Chemistry (IUPAC) recommended names and symbols for the transactinide elements known or claimed as of October 2004 .....	2
1.2. Known and reported isotopes and isomers of bohrium ( $Z = 107$ ) .....	6
1.3. Known or reported isotopes and isomers of darmstadtium ( $Z = 110$ ) and element 111 .....	9
1.4. Excitation energies $E^*$ after emission of various particles from the compound nucleus in the reaction of $^{65}\text{Cu}$ with $^{208}\text{Pb}$ as a function of depth in the target.....	19
3.1. Cross sections for the $^{208}\text{Pb}(^{64}\text{Ni}, \text{n})^{271}\text{Ds}$ reaction measured at three different laboratories .....	76
3.2. Analysis of expected random correlations in the $^{271}\text{Ds}$ experiments .....	99
3.3. Analysis of expected random correlations between observed $^{271}\text{Ds}$ decay chains and $^{255}\text{No}$ .....	100
4.1. Cross sections for the $^{209}\text{Bi}(^{64}\text{Ni}, \text{n})$ and $^{208}\text{Pb}(^{65}\text{Cu}, \text{n})$ reactions leading to the production of $^{272}\text{Bh}$ measured at three different laboratories .....	107
4.2. Analysis of expected random correlations in the $^{272}\text{Bh}$ experiments .....	124
5.1. Cross sections for the $^{209}\text{Bi}(^{54}\text{Cr}, \text{n})$ and $^{208}\text{Pb}(^{55}\text{Mn}, \text{n})$ reactions leading to the production of $^{262}\text{Bh}$ at GSI and LBNL, respectively .....	131
5.2. Cross sections for the production of bohrium as a function of $E_{\text{tot}}$ .....	140
5.3. Analysis of expected random correlations in the $^{208}\text{Pb}(^{55}\text{Mn}, \text{n})^{262}\text{Bh}$ experiments .....	150

5.4. Analysis of expected random correlations between observed $^{262}\text{Bh}$ decay chains and $^{250}\text{Fm}$ .....	151
--	-----

## Acknowledgements

There are a large number of people who have helped me finish this dissertation:

My advisor, Darleane Hoffman. She had said that she was not going to take any more graduate students, and I still don't know why she took me as one. Maybe I made a good impression in those early days. I like to think that I turned out OK. She also supported me when the darmstadtium and element 111 experiments were nothing but a crazy idea.

Heino Nitsche, who probably did more than anyone to make the darmstadtium and element 111 experiments a reality. He helped convince everyone who had to be convinced that they were worthwhile experiments, and I owe him a great debt of thanks. He also saved the element 111 experiment when we ran out of  $^{65}\text{Cu}$ .

Ken Gregorich, who answered my innumerable questions about almost every topic conceivable. He has made incredible contributions to the success of every recent student, and never asks for or receives any recognition for it.

Wladek Świątecki, who helped me understand his theories which were so important to my work. When I needed help determining the projectile energy for the element 111 experiment, he gave me the answer I needed and made that experiment a success. He also gave me access to his newest work, even before it was submitted for publication, which has proven invaluable.

Ralf Sudowe, who became a postdoc almost simultaneously with me becoming a graduate student. He and I have seen it all together. He has been a good friend, especially when it was just he and I going to Friday lunch alone for months on end.

Peter Zielinski, Christoph Düllmann, Jon Schwantes, Hassan Mahmud, Greg Pang, and Sarah Nelson, who worked shifts on my experiments. Thank you very much; I couldn't have done it without you!

Dawn Shaughnessy, Josh Patin, Philip Wilk, and Dan Strellis, the “old guard” graduate students who were here when I joined the group. Thanks for making the group so much fun back then!

Sandy Rosenthal, my undergraduate research advisor at Vanderbilt University. She encouraged me to go to Berkeley, and her personal story made me think that a guy from a small town in West Virginia could enter the “big time” in science.

Greg Dodd, my high school chemistry teacher at Capital High School in Charleston, West Virginia. He taught us about nuclear chemistry and first kindled my interest in heavy elements. I know that if it were not for him I would not be where I am today.

My family, who has supported me throughout my graduate career. Although I know they didn’t like it, they rarely complained about me coming to Berkeley, even if I am far, far away. I also want to thank them for helping to keep my spirits up, especially during those early days when I wasn’t enjoying graduate school.

Daniela Leitner and the staff of the 88-Inch Cyclotron. We continually made unreasonable demands for new beams and more beam intensity, sometimes with no preparation time, and they always did a great job.

Lastly, I would like to thank the U.S. Department of Energy, who supported my research through the Office of High Energy and Nuclear Physics, Nuclear Physics Division, under contract number DE-AC03-76SF00098.

# 1. Introduction

This dissertation is concerned with the study of the transactinide elements, which begin with rutherfordium ( $Z = 104$ ). By definition, these are all the elements beyond the actinide (5f) series which ends with completion of the 5f electron shell at lawrencium ( $Z > 103$ ). The currently known transactinides are listed in Table 1.1 and are shown in the periodic table in Fig. 1.1 as 6d transition elements homologous to the 5d transition series beginning with Hf. All the known transactinides are highly unstable and must be created in nuclear reactions at suitable particle accelerators. Typically, they must be studied at or near the accelerator using atom-at-a-time techniques because of their small production cross sections and short half-lives.

Mendelevium is the heaviest (and last) element to have been separated and first identified by chemical techniques [Ghiorso1955]. The heavier elements discovered since then have been positively identified using physical (nuclear) rather than chemical methods and many controversies ensued about identification of new elements. Subsequently, new physical techniques have been developed to positively identify the atomic number and mass of isotopes of new elements using velocity filters and magnetic rigidity separators followed by detailed characterization of the nuclear decay properties of new species on an atom-at-a-time basis. These have permitted studies of nuclei at the extremes of nuclear

TABLE 1.1. International Union of Pure and Applied Chemistry (IUPAC) recommended names and symbols for the transactinide elements known or claimed as of October 2004.

Z	Name	Symbol	Year Discovered <sup>a</sup>
104	rutherfordium	Rf	1969
105	dubnium	Db	1970
106	seaborgium	Sg	1974
107	bohrium	Bh	1981
108	hassium	Hs	1984
109	meitnerium	Mt	1982
110	darmstadtium <sup>b</sup>	Ds <sup>b</sup>	1995
111	roentgenium <sup>c</sup>	Rg <sup>c</sup>	1995
112	[unnamed and unconfirmed]	—	1996
113	[unnamed and unconfirmed]	—	2004 <sup>d</sup>
114	[unnamed and unconfirmed]	—	1999 <sup>e</sup>
115	[unnamed and unconfirmed]	—	2004 <sup>d</sup>
116	[unnamed and unconfirmed]	—	2001 <sup>f</sup>

<sup>a</sup> According to Ref. [Hoffman2000].

<sup>b</sup> Approved by IUPAC in Ref. [Corish2003].

<sup>c</sup> Proposed by the IUPAC Inorganic Chemistry Division Committee but not yet approved.

<sup>d</sup> Reported in Ref. [Oganessian2004a].

<sup>e</sup> Reported in Ref. [Oganessian1999].

<sup>f</sup> Reported in Ref. [Oganessian2001].

stability. Measurements of cross sections and excitation functions furnish valuable information about nuclear production mechanisms. Information about half-lives, decay energies, nuclear structure, and alpha- and SF-branching ratios for these nuclides help describe the nuclear potential energy landscape. The location of the next nuclear shells beyond  $Z = 82$  and  $N = 126$  cannot be predicted with certainty; experiments to investigate extra stability predicted in regions of deformed shells at  $Z \sim 108$ -112 and  $N \sim 162$ -164 are required to help evaluate the validity of various nuclear models and aid in predicting the location of the next spherical shells.

After the decay properties and atomic number of an isotope of a new transactinide element have been conclusively established by physical (nuclear) techniques, then atom-at-a-time chemical studies to explore its chemistry can be conducted. These physical and

1																				18
H 1		2																		He 2
Li 3	Be 4																			Ne 10
Na 11	Mg 12	3	4	5	6	7	8	9	10	11	12									Ar 18
K 19	Ca 20	Sc 21	Ti 22	V 23	Cr 24	Mn 25	Fe 26	Co 27	Ni 28	Cu 29	Zn 30	Ga 31	Ge 32	As 33	Se 34	Br 35	Kr 36			
Rb 37	Sr 38	Y 39	Zr 40	Nb 41	Mo 42	Tc 43	Ru 44	Rh 45	Pd 46	Ag 47	Cd 48	In 49	Sn 50	Sb 51	Te 52	I 53	Xe 54			
Cs 55	Ba 56	La 57	Hf 72	Ta 73	W 74	Re 75	Os 76	Ir 77	Pt 78	Au 79	Hg 80	Tl 81	Pb 82	Bi 83	Po 84	At 85	Rn 86			
Fr 87	Ra 88	Ac 89	Rf 104	Db 105	Sg 106	Bh 107	Hs 108	Mt 109	Ds 110											

Ce 58	Pr 59	Nd 60	Pm 61	Sm 62	Eu 63	Gd 64	Tb 65	Dy 66	Ho 67	Er 68	Tm 69	Yb 70	Lu 71						
Th 90	Pa 91	U 92	Np 93	Pu 94	Am 95	Cm 96	Bk 97	Cf 98	Es 99	Fm 100	Md 101	No 102	Lr 103						

FIG. 1.1. Periodic table of the elements as of October 2004.

chemical experiments are synergistic: once even a rudimentary knowledge of the chemistry of a new element is known, group chemical separations can be used to purify transactinide isotopes with half-lives as short as seconds for studies of their nuclear properties.

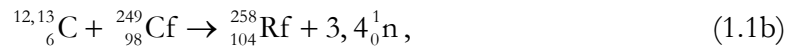
The study of the chemistry of the elements is one of the most fundamental goals in chemistry. Studies of the chemical properties of a new element can be considered valid only if it can be shown unequivocally that the atoms being studied have the correct atomic number. This can be established most accurately using  $\alpha$ - $\alpha$  or possibly  $\alpha$ -SF (spontaneous fission) correlations to known nuclides. The chemical properties of the transactinides are predicted [Pyykkö1979] to be highly influenced by relativistic effects. These are roughly proportional to  $Z^2$  and should be much more important for the transactinide elements than their lighter homologues in groups 4, 5, 6, etc. Recently, much interest has surrounded element 112, which is alternatively expected to have chemistry similar to mercury (a group

12 homologue element) [Pershina2002], or radon, due to its filled shells [Pitzer1975].

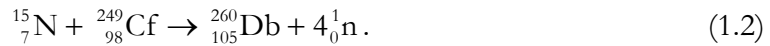
Attempts to characterize the chemistry of element 112 have been reported. These studies and others also allow us to evaluate the validity of trends extrapolated from the properties of lighter homologue elements.

### 1.1. Production and Characterization of Transactinide Elements

The first three transactinides are elements 104, 105, and 106. The claims to the discovery of elements 104 and 105 were extremely controversial and required several years of debate to resolve the conflicting claims between Soviet researchers working at the Joint Institute for Nuclear Research in Dubna, USSR and American researchers at the Lawrence Berkeley Laboratory in Berkeley, USA. Hyde, Hoffman, and Keller [Hyde1987] wrote a comprehensive review of these claims and recommended that the Berkeley group be given credit for the discovery of element 104 [Ghiorso1969] in the following reactions:



Ghiorso *et al.* proposed the name rutherfordium with symbol Rf for element 104. The same review article recommended that the Berkeley group be given credit for the discovery of element 105 [Ghiorso1970] in the reaction



Ghiorso *et al.* proposed the name hahnium with symbol Ha for element 105, but this was later changed by IUPAC to dubnium with symbol Db in recognition of the contributions to nuclear science by the researchers at Dubna.

Element 106 was first produced by Ghiorso *et al.* [Ghiorso1974] in the reaction



This discovery was not contested and the name seaborgium with symbol Sg was accepted, although not until 1997.

The element discovery claims of the Berkeley group were significantly strengthened by the fact that they identified the new isotopes using the genetic correlation technique. If a new, unknown alpha-decaying activity could be shown to produce another activity with decay characteristics consistent with a previously known activity, then the first activity must be the alpha-decay parent of the known nuclide. This technique allowed for precise determination of the atomic and mass numbers of a new isotope and would be a harbinger of things to come, especially with the introduction of position-sensitive detectors.

Unfortunately, the successes of the Berkeley group did not produce the funding required to continue the studies to heavier elements, as priorities within the laboratory changed. It was left to other researchers to continue the work of discovering new elements which the Berkeley scientists had so impressively begun.

The discoveries of Rf, Db, and Sg were achieved using targets of highly radioactive  $^{249}\text{Cf}$  bombarded by light “heavy ions” with masses from 12 to 18. These combinations gave compound nucleus excitation energies of approximately 40 MeV, resulting in the evaporation of 3-4 neutrons. These reactions were labeled “hot fusion” reactions. In 1975, Oganessian *et al.* [Oganessian1975] showed that bombardments of stable Pb and Bi targets with medium-mass ( $>40$ ) projectiles would lead to compound nucleus excitation energies of less than 20 MeV and evaporation of only 1-2 neutrons. These reactions have been labeled “cold fusion” reactions. The advantage of cold fusion reactions is that losses to excited state fission are much less because of the lower excitation energy.

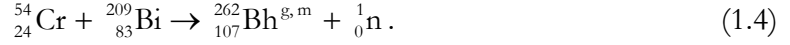
TABLE 1.2. Known and reported isotopes and isomers of bohrium ( $Z = 107$ ).

Nuclide	Half-Life	Decay Mode	Production Method	Ref.
$^{261}\text{Bh}$	$11.8^{+5.3}_{-2.8}$ ms	$\alpha$	$^{209}\text{Bi}(^{54}\text{Cr}, 2n)$	[Münzenberg1989]
$^{262}\text{Bh}^g$	$102 \pm 26$ ms	$\alpha$	$^{209}\text{Bi}(^{54}\text{Cr}, n)$	[Münzenberg1989]
$^{262}\text{Bh}^m$	$8.0 \pm 2.1$ ms	$\alpha$	$^{209}\text{Bi}(^{54}\text{Cr}, n)$	[Münzenberg1989]
$^{264}\text{Bh}$	$0.9^{+0.3}_{-0.2}$ s	$\alpha$ , SF?	$2 \alpha$ daughter of $^{272}\text{Am}$ , $^{243}\text{Am}(^{26}\text{Mg}, 5n)$	[Hofmann2002, Gan2004, Morita2004b]
$^{265}\text{Bh}$	$0.94^{+0.70}_{-0.31}$ s	$\alpha$	$^{243}\text{Am}(^{26}\text{Mg}, 4n)$	[Gan2004]
$^{266}\text{Bh}$	$\sim 1?$ s	$\alpha?$	$^{249}\text{Bk}(^{22}\text{Ne}, 5n)$	[Wilk2000]
$^{267}\text{Bh}$	$17^{+14}_{-6}$ s	$\alpha$	$^{249}\text{Bk}(^{22}\text{Ne}, 4n)$	[Wilk2000]
$^{271}\text{Bh}$	?	$\alpha?$	$4 \alpha$ daughter of $^{287}\text{Am}$	[Oganessian2004a]
$^{272}\text{Bh}$	$9.8^{+11.7}_{-3.5}$ s	$\alpha$	$4 \alpha$ daughter of $^{288}\text{Am}$	[Oganessian2004a]

Also in 1975, the UNILAC (UNIversal Linear ACcelerator), constructed at the Gesellschaft für Schwerionenforschung (GSI) in Darmstadt, Germany, produced its first heavy ion beam. This new accelerator was capable of providing intense beams of the medium-mass projectiles ideal for cold fusion experiments. Additionally, the construction of the Separator for Heavy Ion reaction Products (SHIP) [Ewald1976, Münzenberg1979] was completed in 1976. This separator made it possible to separate products of interest with high efficiency from unwanted activities. Without these interfering activities, the identification of new nuclides was simplified and made more convincing by the virtual elimination of random correlations which might be mistaken for a new element. Given the

very small production cross sections in these reactions, the use of such a separator was critical to the future success of the field, a view which has been confirmed by experience.

Münzenberg *et al.* [Münzenberg1981a, Münzenberg1989] used these new facilities to produce element 107 (bohrium, Bh) in the reaction



This was the first use of a cold fusion reaction to produce a new transactinide element. Since element 107 is studied in this work, the known isotopes of bohrium are listed in Table 1.2. Wilk *et al.* [Wilk2000] discovered the isotope  $^{267}\text{Bh}$ , which has a half-life ( $17^{+14}_{-6}$  s) that was sufficiently long to allow for the first chemical study of bohrium [Eichler2000].

Münzenberg *et al.* continued to use the UNILAC and SHIP to discover elements 109 [Münzenberg1982, Münzenberg1984a, Münzenberg1988] and 108 [Münzenberg1984b, Münzenberg1987] (in that order) in these reactions:



The reader should note that this pair of elements can be produced using the same even- $Z$  beam by changing from  $^{208}\text{Pb}$  to  $^{209}\text{Bi}$  targets. This pattern would be repeated multiple times in future transactinide cold fusion experiments. Examining alternatives to this pattern is a major theme of this work.

Element 110 (darmstadtium, Ds) was discovered by the SHIP group, now headed by S. Hofmann, as the isotope  $^{269}\text{Ds}$  (Eq. 1.7a) [Hofmann1995a], although for this discussion the more important reaction is the discovery of  $^{271}\text{Ds}$  (Eq. 1.7b) [Hofmann1998, Hofmann2003]:



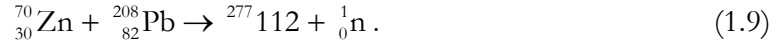


The importance of the second reaction is that during the same experiment the target was changed to  $^{209}\text{Bi}$  to allow for the discovery of element 111 [Hofmann1995b, Hofmann2002]:

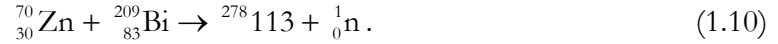


(The name roentgenium with symbol Rg has been proposed for element 111 by the IUPAC Inorganic Chemistry Division Committee but has not yet been approved by the full IUPAC body, and therefore is simply referred to as “element 111”). These  $^{64}\text{Ni}$ -based reactions again illustrate how heavier elements can be produced by adding a proton to the target. Since both elements 110 and 111 are studied in this work, Table 1.3 lists the known isotopes of these elements for reference.

The final element reported using cold fusion reactions is element 112 [Hofmann1996, Hofmann2002]:



Two decay chains attributed to  $^{277}112$  were reported. A group headed by Morita at the RIKEN laboratory in Wako, Saitama, Japan has recently reported the synthesis of two atoms of  $^{277}112$  [Morimoto2004] in the same reaction using the GARIS separator at the RILAC (RIKEN Linear ACcelerator). The latter group has also reported the production of one atom of element 113 [Morita2004a] using the reaction



The reported cross section for the production of  $^{278}113$  was  $55^{+150}_{-45}$  fb. Hofmann’s group [Hofmann2000] has also searched for element 113 in the same reaction but reported no events observed at a sensitivity of  $\sim 600$  fb, averaged over two beam energies.

TABLE 1.3. Known or reported isotopes and isomers of darmstadtium ( $Z = 110$ ) and element 111.

$Z$	Nuclide	Half-Life	Decay Mode	Production Method	Ref.
110	$^{267}\text{Ds}$	$\sim 3 \mu\text{s}$	$\alpha$	$^{209}\text{Bi}(^{59}\text{Co}, \text{n})$	[Ghiorso1995a, Ghiorso1995b]
	$^{269}\text{Ds}$	$270^{+1300}_{-120} \mu\text{s}$	$\alpha$	$^{208}\text{Pb}(^{62}\text{Ni}, \text{n})$	[Hofmann1995a]
	$^{270}\text{Ds}^g$	$100^{+140}_{-40} \mu\text{s}$	$\alpha$	$^{207}\text{Pb}(^{64}\text{Ni}, \text{n})$	[Hofmann2001]
	$^{270}\text{Ds}^m$	$6.0^{+8.2}_{-2.2} \text{ ms}$	$\alpha, \gamma?$ , IC?	$^{207}\text{Pb}(^{64}\text{Ni}, \text{n})$	[Hofmann2001]
	$^{271}\text{Ds}^g$	$1.63^{+0.44}_{-0.28} \text{ ms}$	$\alpha$	$^{208}\text{Pb}(^{64}\text{Ni}, \text{n})$	[Hofmann2003, Morita2004d]
	$^{271}\text{Ds}^m$	$69^{+56}_{-21} \text{ ms}$	$\alpha$	$^{208}\text{Pb}(^{64}\text{Ni}, \text{n})$	[Hofmann2003, Morita2004d]
	$^{273}\text{Ds}$	$0.3^{+1.3}_{-0.2} \text{ ms}$	$\alpha$	$^{277}\text{112} \alpha \text{ decay, } ^{244}\text{Pu}(^{34}\text{S}, 5\text{n})$	[Hofmann2002, Lazarev1996]
	$^{279}\text{Ds}$	$0.29^{+0.35}_{-0.10} \text{ s}$	SF	$^{287}\text{114} \alpha \text{ decay granddaughter}$	[Oganessian2004b]
	$^{281}\text{Ds}$	$9.6^{+5.0}_{-2.5} \text{ s}$	$\alpha$	$^{289}\text{114} \alpha \text{ decay granddaughter}$	[Oganessian2004b]
111	$^{272}\text{111}$	1.6, 3.8 ms	$\alpha$	$^{209}\text{Bi}(^{64}\text{Ni}, \text{n})$	[Hofmann2002, Morita2004]
	$^{279}\text{111}$	$170^{+810}_{-80} \text{ ms}$	$\alpha$	$^{287}\text{115} \alpha \text{ decay granddaughter}$	[Oganessian2004a]
	$^{280}\text{111}$	$3.6^{+4.3}_{-1.3} \text{ s}$	$\alpha$	$^{288}\text{115} \alpha \text{ decay granddaughter}$	[Oganessian2004a]

In each pair of reactions (108 and 109, 110 and 111, and 112 and 113), when there was a choice between using an odd- $Z$  target and an odd- $Z$  projectile, the odd- $Z$  target was used because the cross section was expected to be higher. The current work aims to assess this effect by measuring production cross sections in the  $^{208}\text{Pb}(^{65}\text{Cu}, \text{n})^{272}\text{111}$  and  $^{208}\text{Pb}(^{55}\text{Mn}, \text{n})^{262}\text{Bh}$  odd- $Z$ -projectile reactions for the first time.

Although they are not cold fusion reactions, for completeness we note the recent reports of production of superheavy elements (SHEs) at the Joint Institute for Nuclear Research in Dubna, Russia by two groups, both headed by Oganessian. These experiments used  $^{48}\text{Ca}$  projectiles with actinide targets to produce neutron-rich compound nuclei of elements 112, 114, 115, and 116; element 113 was also formed as the alpha-decay daughter of element 115. These reactions involve the emission of 2-4 neutrons from the compound nucleus. The evaporation residues (EVRs) are reported to decay by the sequential emission of alpha particles with half-lives on the order of seconds, terminated by the spontaneous fission of a long-lived daughter nuclide (see, for example, [Oganessian2002, Oganessian2004a, Oganessian2004b]). These experiments are very controversial and none has yet been confirmed in other laboratories.

## 1.2. Excitation Functions

This work deals primarily with the study of new reactions leading to the production of transactinide elements. It is heavily influenced by the recent theoretical work of Świątecki, Siwek-Wilczyńska, and Wilczyński [Świątecki2003, Świątecki2004a, Świątecki2004b]. This section describes fundamental aspects of the relevant theory and its relationship to the current work.

### 1.2.1. Magnitudes of Cross Sections

#### 1.2.1.1. Standard Theoretical Methods

The most important reaction for the production of heavy elements is the complete-fusion-neutron-evaporation reaction. The projectile and target nuclei are completely fused to form a compound nucleus (CN) in an excited state. The excited CN can decay by the

emission of gamma rays, neutrons, or charged particles, or fission. The most important of these are neutron emission and fission, so they will be focused on exclusively for now. The excitation function, or reaction cross section versus projectile energy, increases with increasing projectile energy because of the increased probability that the two nuclei will fuse. After some maximum, it begins to decrease with increasing projectile energy because the probability of losing compound nuclei to excited state fission increases. We will examine these concepts in more detail.

A crude semi-empirical model, developed by Sikkeland *et al.* (see, for example, [Sikkeland1968a, Sikkeland1968b]) and based on the work of Jackson [Jackson1956], contains the most important ideas and will be examined briefly. The cross section for the production of the  $\alpha n$  reaction  $\sigma_x$  product is given by

$$\sigma_x = \sigma_{CN} P_x \prod_{i=1}^x \left( \frac{\Gamma_n}{\Gamma_n + \Gamma_f} \right)_i, \quad (1.11)$$

where  $\sigma_{CN}$  is the cross section for CN formation,  $P_x$  is the probability of emitting exactly  $x$  neutrons, and  $\Gamma_n$  and  $\Gamma_f$  are the partial widths for neutron emission and fission of state  $i$ , respectively.  $\Gamma_n$  and  $\Gamma_f$  physically represent the full-width-at-half-maximum of the state undergoing neutron-emission or fission, respectively, and are proportional to the decay probability of the respective mode. The classical expression for  $\sigma_{CN}$  is

$$\sigma_{CN} = \begin{cases} \pi R^2 (1 - V_C/E_1), & E_1 \geq V_C \\ 0, & E_1 < V_C \end{cases}, \quad (1.12)$$

where  $R$  is the interaction distance,  $V_C$  is the Coulomb barrier, and  $E_1$  is the projectile energy. Clearly, sub-barrier fusion is disallowed in Eq. 1.12, although quantum-mechanical tunneling through the barrier does allow sub-barrier fusion to occur [Loveland2000].

Equation 1.12 also does not include any variation in the fusion cross section based on different orientations of deformed colliding nuclei. Calculation of the Coulomb barrier is complex, although a simple formula has been proposed [Świątecki2004a] based on a fit to data from several reactions. For reactions with atomic numbers  $Z_1$  and  $Z_2$  and mass numbers  $A_1$  and  $A_2$ ,

$$V_C = 0.85247 \tilde{z}_C + 0.001361 \tilde{z}_C^2 - 0.00000223 \tilde{z}_C^3, \quad (1.13a)$$

$$\tilde{z}_C = \frac{Z_1 Z_2}{A_1^{1/3} + A_2^{1/3}}. \quad (1.13b)$$

$P_x$ , the probability that the excited compound nucleus will emit the desired number of neutrons  $x$ , is a function of the excitation energy and may be zero if  $x$  is sufficiently large. The ratio  $\Gamma_n/(\Gamma_n + \Gamma_f)$  in Eq. 1.11 gives the probability that the compound nucleus decays by neutron-emission instead of fission. (As stated above, other decay modes are possible but are ignored). This probability is included in the cross section  $x$  times, so there may be multiple chances for the compound nucleus to fission, destroying the CN. Typically,  $\Gamma_n/(\Gamma_n + \Gamma_f)$  is much less than 1, so many more CNs fission than emit neutrons.

$\Gamma_n/(\Gamma_n + \Gamma_f)$  is usually given in terms of  $\Gamma_n/\Gamma_f$  and the two are related by

$$\frac{\Gamma_n}{\Gamma_n + \Gamma_f} = \frac{(\Gamma_n/\Gamma_f)}{(\Gamma_n/\Gamma_f) + 1}. \quad (1.14)$$

Unfortunately, Sikkeland *et al.* computed the average value  $\langle \Gamma_n/\Gamma_f \rangle_{avg}$  from the  $x$ th-root of the product of all  $x$  measured  $\Gamma_n/\Gamma_f$  values in each of their reactions of interest, and use this in Eq. 1.11. This ignores the dependence of  $\Gamma_n/\Gamma_f$  on both excitation energy and angular momentum.

Among others, Vandenbosch and Huizenga [Vandenbosch1973] have attempted to estimate  $\Gamma_n/\Gamma_f$  more realistically. Consider a nucleus with neutron-binding energy  $B_n$ , fission barrier  $B_f$ , and excitation energy  $E$ . Suppose also that the kinetic energy and mass of an emitted neutron are  $\varepsilon$  and  $m_n$ , respectively, and that upon fission the kinetic energy in the fission degree of freedom is  $K$ . When a nucleus decays, any level up to the original excitation energy minus the emitted energy can be occupied. Thus, the more of these levels there are, the more likely is that mode of decay. Therefore, the decay probability must be integrated over the “level density”  $\rho$  in the residual nucleus. The level density represents the number of states per unit energy and is inversely proportional to the level spacing. The ratio of neutron-to-fission decay probabilities  $\Gamma_n/\Gamma_f$  is

$$\frac{\Gamma_n}{\Gamma_f} = \left( \frac{2m_n r_0^2 g A^{2/3}}{\hbar^2} \right) \frac{\int_0^{E-B_n} \varepsilon \rho(E - B_n - \varepsilon) d\varepsilon}{\int_0^{E-B_f} \rho(E - B_f - K) dK}, \quad (1.15)$$

where  $g$  is the intrinsic spin degeneracy of the neutron,  $r_0$  is the radius parameter, and  $A$  is the CN mass number. At constant nuclear temperature  $T$ , the level density is given by

$$\rho(E) \propto \exp(E/T) \Rightarrow \rho(E) = a \exp(E/T), \quad (1.16)$$

where  $a$  is the “level density parameter.” Performing the appropriate integrals with this level density yields

$$\frac{\Gamma_n}{\Gamma_f} \approx \frac{2TA^{2/3}}{K_0} \exp\left[-(B_n - B_f)/T\right], \quad (1.17)$$

where  $K_0 = \hbar^2 / 2m_n r_0^2 \approx 10$  MeV. A more realistic level density dependent on excitation energy is

$$\rho(E) \propto \exp[2(aE)^{1/2}]. \quad (1.18)$$

If Eq. 1.18 is used to evaluate Eq. 1.15, then the result is

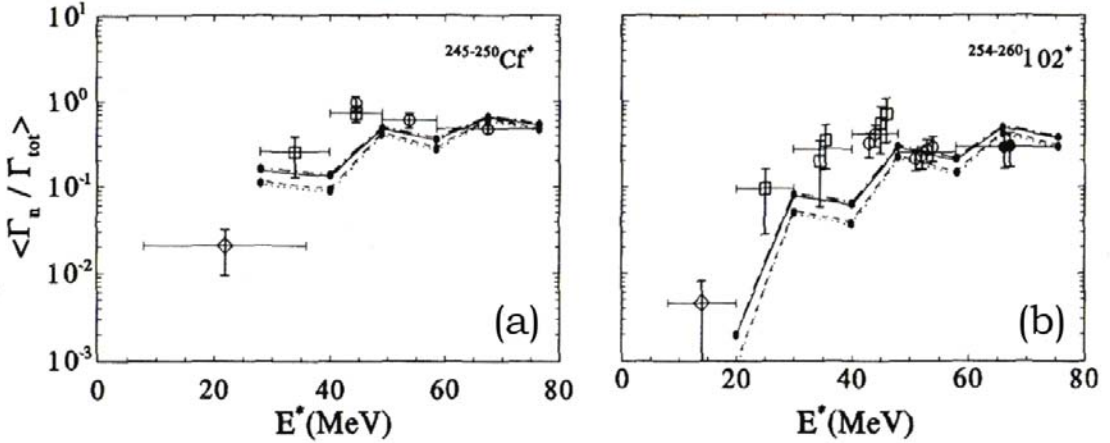


FIG. 1.2. Average values of  $\Gamma_n/\Gamma_{tot} = \Gamma_n/(\Gamma_n + \Gamma_f)$  for reactions leading to the production of (a)  $^{242}\text{Cf}$  and (b)  $^{252}\text{No}$ , as a function of initial excitation energy. The compound nuclei are indicated. Symbols connected by lines are predictions from several models; other symbols are experimental data. For more information see [Andreyev1994]; adapted from that work.

$$\frac{\Gamma_n}{\Gamma_f} = \left[ \frac{4A^{2/3}a_f(E - B_n)}{K_0a_n[2a_f^{1/2}(E - B_f)^{1/2} - 1]} \right] \frac{\exp[-2a_f^{1/2}(E - B_f)]}{\exp[-2a_n^{1/2}(E - B_n)]}, \quad (1.19)$$

where  $a_f$  and  $a_n$  are the level density parameters appropriate for describing the level densities above the fission and neutron saddle points, respectively. A canonical expansion of the exponentials in Eq. 1.19 gives a form similar to Eq. 1.17, so that the neutron-emission-to-fission ratio depends primarily on the difference between the neutron binding energy and the fission barrier height. This competition controls the decrease in cross section above the peak of the excitation function. Fig. 1.2 shows some representative values of  $\Gamma_n/\Gamma_f$  as a function of excitation energy for two heavy element reactions. Note that  $\Gamma_n/\Gamma_f$  can also be much lower than indicated in the figure; Smolańczuk predicts  $\Gamma_n/\Gamma_f$  on the order of  $10^{-3}$ – $10^{-6}$  for stable-beam cold fusion reactions ranging from  $^{48}\text{Ca} + ^{208}\text{Pb}$  to  $^{86}\text{Kr} + ^{208}\text{Pb}$  [Smolańczuk1999].

### 1.2.1.2. Fusion by Diffusion

In addition to calculating  $\Gamma_n/\Gamma_f$  using a method similar to that above, Świątecki, Siwek-Wilczyńska, and Wilczyński introduce a new factor to represent observed hindrance factors in the cold fusion of very heavy systems. They express the measured cross section  $\sigma_{\text{ln}}$  as the product of three terms, a sticking cross section  $\sigma_{\text{stick}}$ , a “diffusion” probability  $P_{\text{diffuse}}$ , and a survival probability  $P_{\text{survive}}$ :

$$\sigma_{\text{ln}} = \sigma_{\text{stick}} P_{\text{diffuse}} P_{\text{survive}}. \quad (1.20)$$

The sticking cross section is principally the probability for overcoming the Coulomb barrier. They use a form of Eq. 1.12, modified to smooth the discontinuity at  $E = V_C$  by including a distribution of barrier heights centered on the Coulomb barrier  $V_C$  with width  $w$  [Świątecki2003]:

$$\sigma_{\text{stick}} = \pi R^2 \frac{w}{E \sqrt{2\pi}} \left[ X \sqrt{\pi} (1 + \text{erf } X) + \exp(-X^2) \right], \quad (1.21a)$$

$$X = (E - V_C) / w \sqrt{2}. \quad (1.21b)$$

The diffusion probability is the new feature of the work. Similar diffusion concepts have recently been applied to the formation of superheavy elements, most notably by Abe [Abe1997, Abe2002]. After touching, the dinuclear complex undergoes a rapid neck growth since a large decrease in surface energy is achieved with only a minimal rearrangement of nucleons. Neck growth occurs rapidly and with high probability, similar to the rapid formation of a neck when two drops of water come into contact. The system finds itself in an “asymmetric fission valley,” having just lost significant surface energy but still facing an additional barrier to compound nucleus formation because it is outside the saddle point. (In the region of the transactinides, the fission saddle point is found at

shorter nuclear elongations with increasing  $Z$  because of the high fissility of the compound nucleus).

“Diffusion” in the new system refers to the analogy of a particle suspended in a solution with temperature  $T$  diffusing over a repulsive potential. Let this potential be represented by the inverted parabola  $V(L) = -b(L - L_{max})^2/2$ , where  $L_{max}$  is the center and  $b$  is some proportionality constant.  $V(L)$  represents the final barrier the dinuclear system faces in the elongation coordinate such that systems reaching  $L < L_{max}$  continue to the compound nucleus while other systems fission. If a delta function distribution of systems is “injected” onto the parabola at some  $L_{inj}$  then, as time tends to infinity, the probability of having diffused across the barrier to the compound nucleus tends to the following equations:

$$P_{\text{diffuse}} = \begin{cases} (1/2)(1 - \text{erf} \sqrt{H/T}), & L_{inj} \geq L_{max} \\ (1/2)(1 + \text{erf} \sqrt{H/T}), & L_{inj} < L_{max} \end{cases}, \quad (1.22)$$

where  $H = |V(L_{inj})|$  is the height of the barrier as seen by the system at  $L_{inj}$  and  $T$  is the nuclear temperature. The barrier height can be calculated from macroscopic models, and the nuclear temperature estimated from the excitation energy at  $L_{inj}$ . The value of  $L_{inj}$  depends on the separation  $s$  between the surfaces of the approaching nuclei at which the neck begins its rapid growth. Its precise value cannot be estimated reliably, so  $s$  is introduced as an adjustable parameter. It is the only adjustable parameter in the model and a value is given below.

The survival probability is calculated by similar means as those described previously.  $\Gamma_n/\Gamma_f$  is calculated by integrating the level density from the height of the appropriate saddle point to the total available energy. An additional factor in the survival probability takes

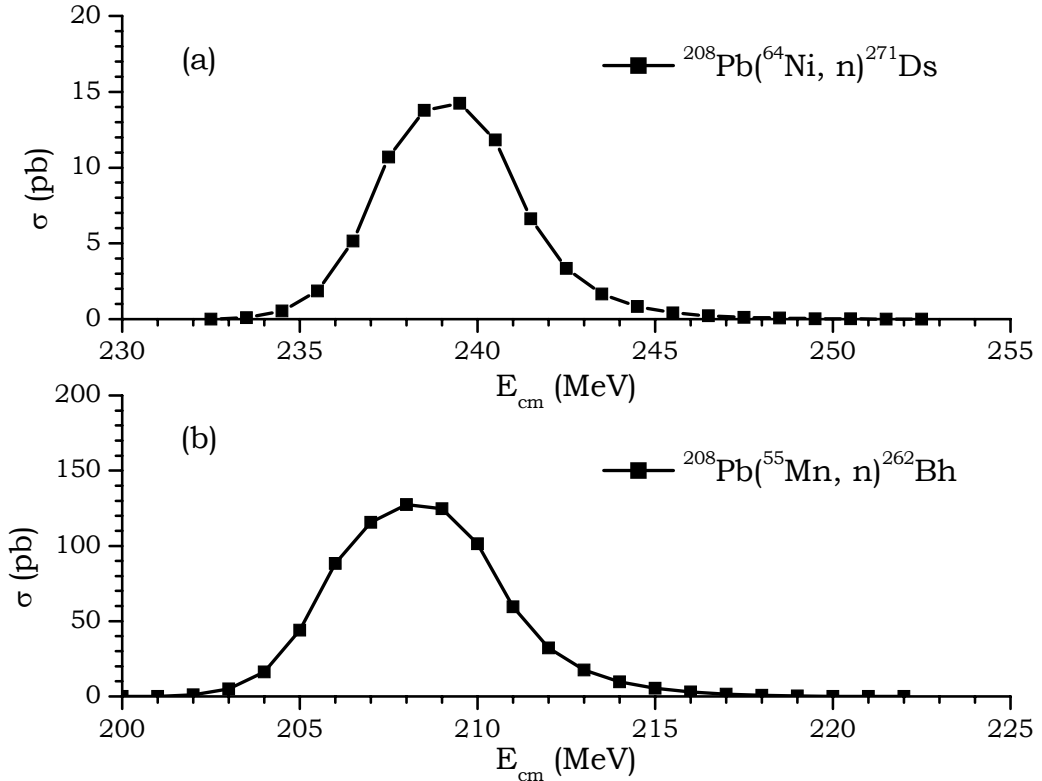


FIG. 1.3. Predicted excitation functions for the (a)  $^{208}\text{Pb}(^{64}\text{Ni}, \text{n})^{271}\text{Ds}$  and (b)  $^{208}\text{Pb}(^{55}\text{Mn}, \text{n})^{262}\text{Bh}$  reactions. The finite target thicknesses of (a) 4 MeV and (b) 5 MeV have been factored into the results. Adapted from [Świątecki2004a].

into account the probability that the emission of a single neutron will lead to a state with excitation energy below the fission barrier of the new  $A - 1$  nucleus.

The model can thus be summarized as follows: the sticking and neutron emission probabilities are conventional, as is  $\Gamma_n/\Gamma_f$ . The new feature is the diffusion probability which represents a hindrance factor for the formation of the compound nucleus. This hindrance factor depends on the parameter  $s$ . Świątecki, Siwek-Wilczyńska, and Wilczyński find good agreement with experimental results when  $s = 1.6 \text{ fm}$  [Świątecki2004a]. This formulation gives excitation functions in which the predicted cross

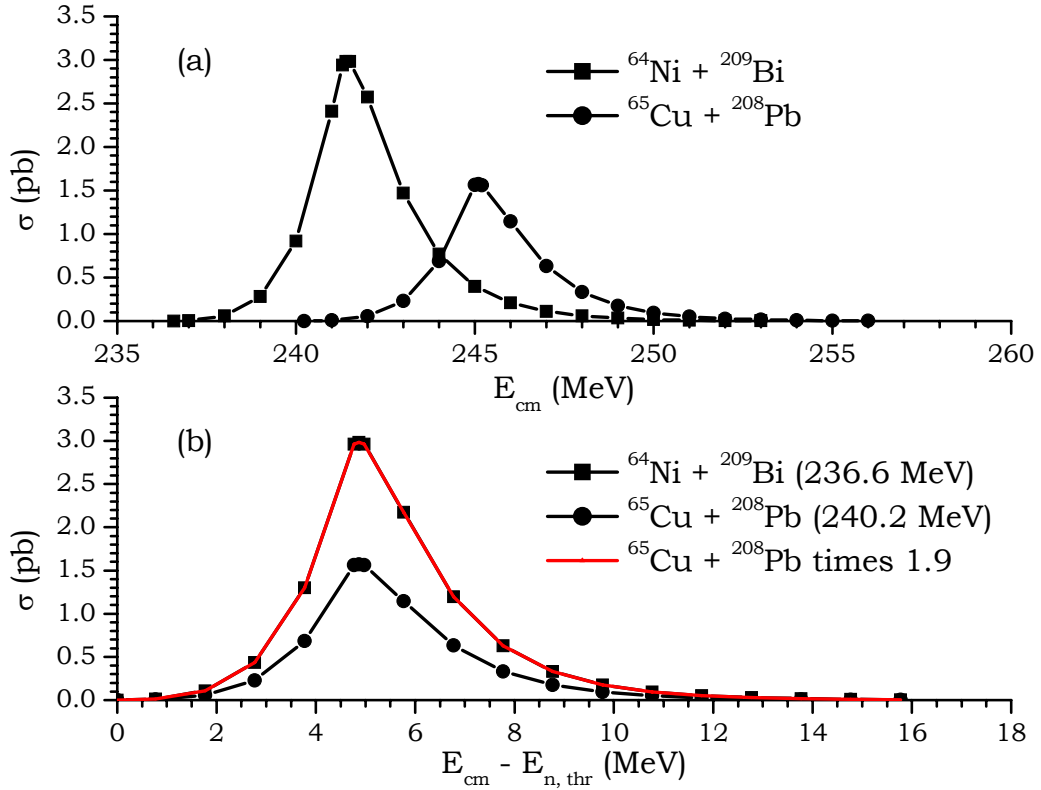


FIG. 1.4. Theoretical predictions for the excitation functions of the  $^{209}\text{Bi}(^{64}\text{Ni}, \text{n})$  and  $^{208}\text{Pb}(^{65}\text{Cu}, \text{n})$  reactions as functions of (a) the center-of-mass beam energy  $E_{cm}$  and (b)  $E_{cm}$  less the neutron-emission threshold energy  $E_{n, thr}$ .  $E_{n, thr}$  is given in parentheses. The red line in (b) represents the  $^{65}\text{Cu} + ^{208}\text{Pb}$  excitation function multiplied by 1.9, showing the agreement between the shapes of the excitation functions. These excitation functions do not factor in the beam energy dispersion in the target. Adapted from [Świątecki2004a].

sections differ from the experimentally measured ones by generally less than a factor of 2. Figure 1.3 shows the predictions of the theory for the  $^{208}\text{Pb}(^{64}\text{Ni}, \text{n})^{271}\text{Ds}$  and  $^{208}\text{Pb}(^{55}\text{Mn}, \text{n})^{262}\text{Bh}$  reactions with finite target thicknesses equivalent to 4 MeV and 5 MeV, respectively, folded in. The prediction for the  $^{208}\text{Pb}(^{65}\text{Cu}, \text{n})^{272}\text{111}$  reaction is shown in Fig. 1.4b without the target thickness folded in.

TABLE 1.4. Excitation energies  $E^*$  after emission of various particles from the compound nucleus in the reaction of  $^{65}\text{Cu}$  with  $^{208}\text{Pb}$  as a function of depth in the target. The center-of-target, lab-frame  $^{65}\text{Cu}$  beam energy was 321.1 MeV and the total energy lost in the target was 5.6 MeV. The particles are assumed to be emitted with zero kinetic energy. The  $\alpha$  and  $\alpha n$  exit channels give increased excitation energies because of the Q-value for alpha decay (see the main text for a discussion). If the excitation energy is negative, then that exit channel is energetically forbidden. Dashes indicate that the appropriate masses were not available in the mass table.

Particles Emitted	Mass Table	$E^*$ Beginning of Target (MeV)	$E^*$ Center of Target (MeV)	$E^*$ End of Target (MeV)
None	[Myers1994]	15.35	13.22	11.08
	[Audi2003]	14.62	12.49	10.35
	[Möller1995]	16.96	14.83	12.69
1n	[Myers1994]	7.06	4.93	2.79
	[Audi2003]	6.61	4.48	2.34
	[Möller1995]	8.75	6.62	4.48
2n	[Myers1994]	-0.18	-2.31	-4.45
	[Audi2003]	—	—	—
	[Möller1995]	1.59	-0.54	-2.68
p	[Myers1994]	15.21	13.08	10.94
	[Audi2003]	14.48	12.35	10.21
	[Möller1995]	16.82	14.69	12.55
$\alpha$	[Myers1994]	26.43	24.30	22.16
	[Audi2003]	25.70	23.57	21.43
	[Möller1995]	28.04	25.91	23.77
$\alpha n$	[Myers1994]	18.16	16.03	13.89
	[Audi2003]	17.43	15.30	13.16
	[Möller1995]	19.77	17.64	15.50

### 1.2.1.3. Energetics

In any heavy element experiment, the very low production rates of the activity of interest require that all alternative explanations for the data observed be rejected either because of implausibility (or impossibility) or because they are not consistent with the data. In the cold fusion reactions studied in this work, the compound nucleus emits a single neutron. In these cases, the excitation of the compound nucleus is low (11-18 MeV using

masses from [Myers1994]), and many exit channels are energetically forbidden. Table 1.4 shows an analysis of the energetics of various exit channels in the reaction of  $^{65}\text{Cu}$  with  $^{208}\text{Pb}$ .

Clearly, the  $2n$  exit channel is forbidden energetically throughout most of the target, since the emission of two neutrons reduces the excitation energy to less than zero. This is especially true once the kinetic energy of the emitted neutrons is included in the calculation (generally 1-2 MeV each, although Ref. [Andreyev1994] reports 2.9 MeV). The radiative capture channel ( $0n$ ) has a very low probability and has never been observed in a heavy system [Morita2004b]. For example, Loveland *et al.* [Loveland2001] report that in the  $^{48}\text{Ca} + ^{208}\text{Pb}$  reaction the  $0n$  channel has an upper limit cross section four orders of magnitude less than the  $1n$  and  $2n$  channels.

Table 1.4 indicates that charged particle emission from the compound nucleus should, in principle, compete effectively with neutron emission, but this is not the case. Although the proton separation energy is low in  $^{272}\text{111}$  due to its neutron deficiency, protons must overcome Coulomb and angular momentum barriers during emission, whereas neutrons face only the latter. Thus, lifetimes for proton emission are long compared to those for neutron emission, and the latter are favored. Regardless, care must be exercised when interpreting data since proton emission from the compound nucleus, followed by alpha decay, leads to the same nuclide as neutron emission followed by alpha decay and electron capture. Alpha particles face an even larger Coulomb barrier (on the order of 30 MeV) and are significantly hindered relative to neutron emission. The information in Table 1.4 is misleading; it suggests that the  $\alpha$  and  $\alpha n$  exit channels produce greater excitation than the initially formed compound nucleus due to the large positive Q-values for alpha emission. In reality, the kinetic energy of the alpha particle would have to be very high (greater than

20 MeV) for alpha particle barrier penetration to compete favorably with neutron emission, and the excitation energy would be reduced considerably. It is possible that the separation factor of the Berkeley Gas-filled Separator (BGS; see Chapter 2) would be increased for alpha-emission products because the recoil from the alpha would direct the remaining nucleus out of the separator's acceptance cone. In practice, this is not observed in these experiments because of the high forward momentum of the medium-mass beams used. The  $\alpha n$  channel is mentioned for completeness, since this channel leads into the same alpha decay chain as the  $1n$  channel. This could lead to misinterpretation of data, but the activities produced in this work decay to known nuclides, so definite atomic and mass number assignments can be made through genetic correlations. In fact, the use of genetic correlations allows us to assign decays to specific nuclides with high confidence so that interfering exit channels will cause us little concern. Regardless, alternative explanations for the data observed will consider exit channels other than  $1n$  when appropriate.

#### 1.2.1.4. Cold Versus Hot Fusion

This section has discussed the theory behind both hot and cold fusion reactions. Compound nucleus theory predicts that there is a maximum in the excitation function for a certain  $xn$  evaporation channel. The increase with energy is caused by the increase in fusion probability, which favors hot fusion reactions. The decrease above the maximum cross section is caused by the increase in fission probability (and the increased likelihood of emitting  $x + 1$  neutrons instead of  $x$ ).

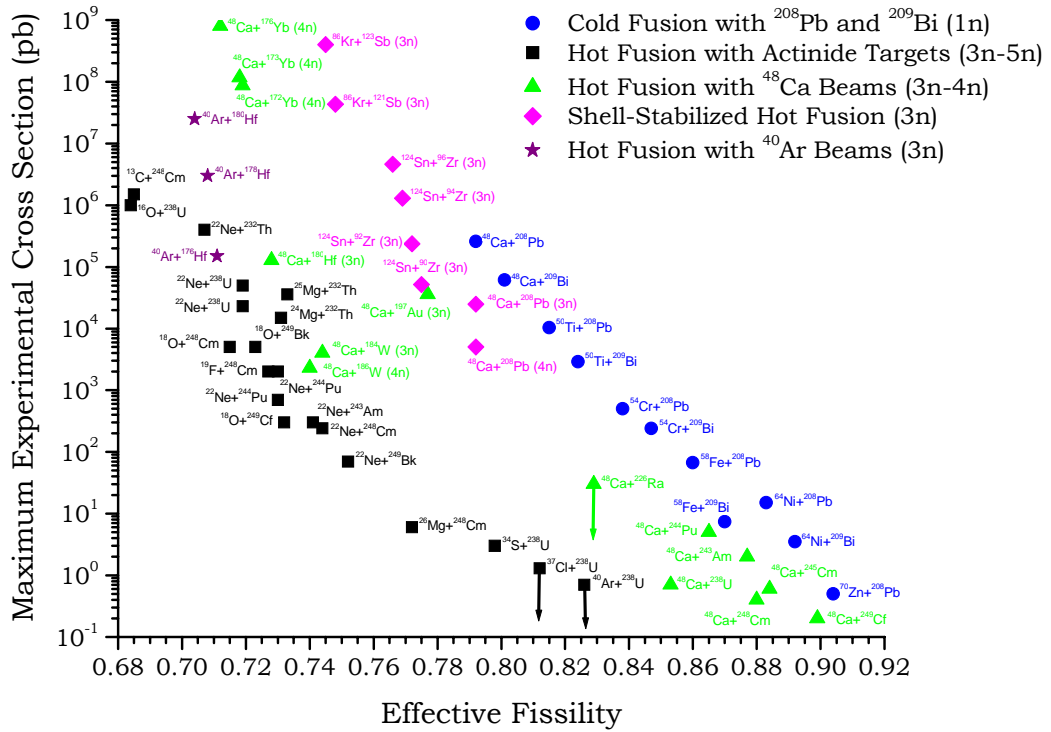


FIG. 1.5. Maximum cross section observed versus effective fissility for many compound nucleus heavy element production reactions. Effective fissility, as defined by Armbruster [Armbruster2003], is a combination of two-thirds compound nucleus fissility and one-third fissility of the binary fusing system, which increases roughly with compound nucleus atomic number. Cold fusion reactions are shown as blue circles. Hot fusion reactions with actinide targets and  $^{48}\text{Ca}$  beams are shown by black squares and green triangles, respectively. See the main text for a discussion. Upper-limit cross sections are indicated by arrows. Data compiled by K. E. Gregorich.

It is interesting to examine which method is favored for the production of heavy elements. Figure 1.5 shows a plot of the maximum cross section of the excitation function versus effective fissility (defined by Armbruster [Armbruster2003] as two-thirds compound nucleus fissility and one-third the fissility of the fusing reactants) for a number of heavy element production reactions. The cross sections for the cold fusion reactions (blue circles) decrease in a roughly linear way, with each unit increase in the compound nucleus  $Z$  resulting in a decrease of the cross section by a factor of  $\sim 3.7$  [Hofmann1998]. This

pattern may or may not continue beyond  $Z = 112$ , depending on whether the compound nuclei are deformed or spherical, respectively [Świątecki2004a]. In the case of hot fusion reactions, it appears that the cross sections for reactions leading to elements with  $Z \geq 108$  are leveling off. However, it should be noted that all the hot fusion results shown in Fig. 1.5 for  $Z \geq 109$  are either upper-limits or unconfirmed results, so it remains to be seen whether this effect is real. Lastly, the choice of a cold or hot fusion reaction may be dictated by the properties required of the evaporation residue, such as half-life. While element discovery experiments can be sensitive to a wide range of half-lives, experiments designed to produce activities for chemical studies usually require nuclides with half-lives greater than a second (see, for example, [Schädel1997, Eichler2000, Düllmann2002]).

### *1.2.2. Location of the Maximum Cross Section for 1n Reactions*

One of the most important questions to be answered in transactinide production experiments is the optimum beam energy to be used. The selection of the beam energy corresponding to the maximum of the cross section is critical in any attempt to synthesize a new element or isotope, or when using a new reaction to synthesize a known isotope. The very small production cross sections, availability of beam time, and expense of doing experiments often require that the maximum production rate be obtained.

The most important reaction in this field is the complete-fusion-neutron-evaporation reaction, whose excitation function is well known to have a maximum. (See Fig. 19 in Hofmann *et al.* [Hofmann1998] for examples of these). The maximum of the excitation function for a given 1n product can be interpreted as the most favorable outcome in the competition between two factors which vary with energy: the fusion cross section, which increases exponentially with higher beam energies, and the loss of compound nuclei due to

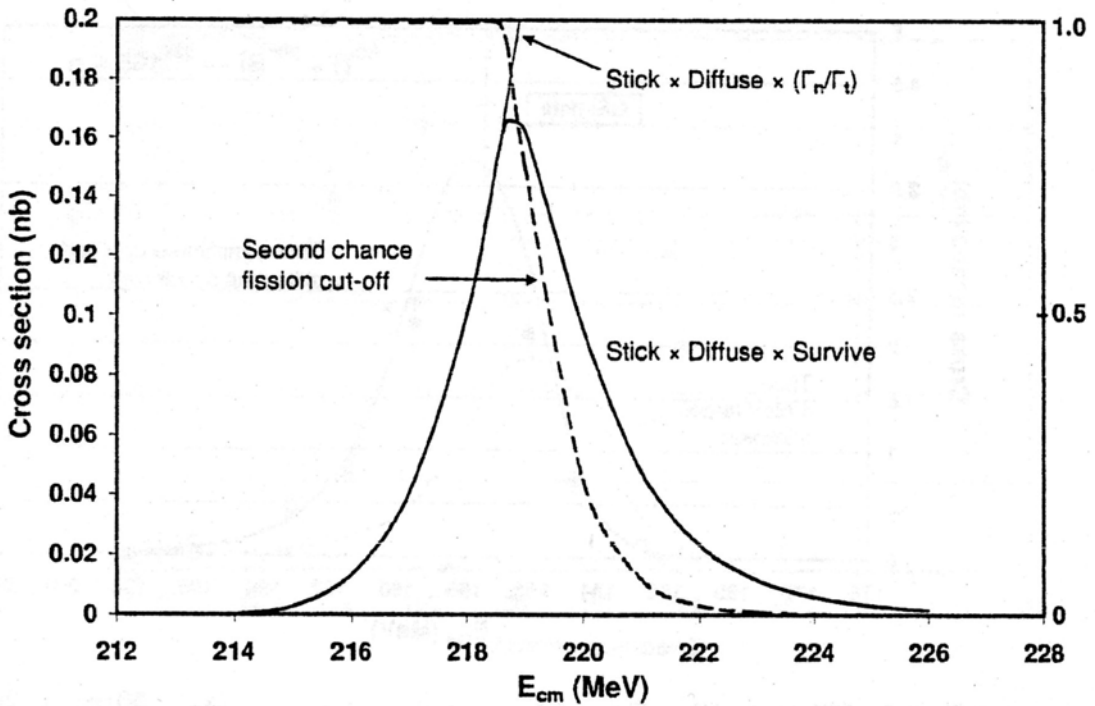


FIG. 1.6. Physical basis for the “optimum energy rule.” The example reaction is  $^{208}\text{Pb}(^{58}\text{Fe}, \text{n})^{265}\text{Hs}$ . The thin solid line is the compound nucleus formation cross section, which increases exponentially with increasing energy. The dashed line is the “second chance fission cut-off,” and shows the influence of fission that occurs after neutron emission. Below a critical “cut-off” value, second chance fission is not possible. The product of these two functions gives the peaked excitation function (heavy solid line). The difference between the cutoff and the maximum of the excitation function gives the 0.3-MeV correction in the “optimum energy rule.” Adapted from [Świątecki2004a].

excited state fission, which also increases with beam energy. The competition between these two factors is shown in Fig. 1.6 and were addressed in more detail in Sec. 1.2.1.

Świątecki, Siwek-Wilczyńska, and Wilczyński have noted the close correlation between the energy of the maximum cross section and the onset of second-chance fission, where fission after emission of the first neutron is possible. They argue that the maximum cold fusion (1n) cross section is obtained when the bombarding energy is as high as possible (to increase the fusion probability), but low enough so that second-chance fission is forbidden after the first neutron emission step because the remaining excitation energy is less than

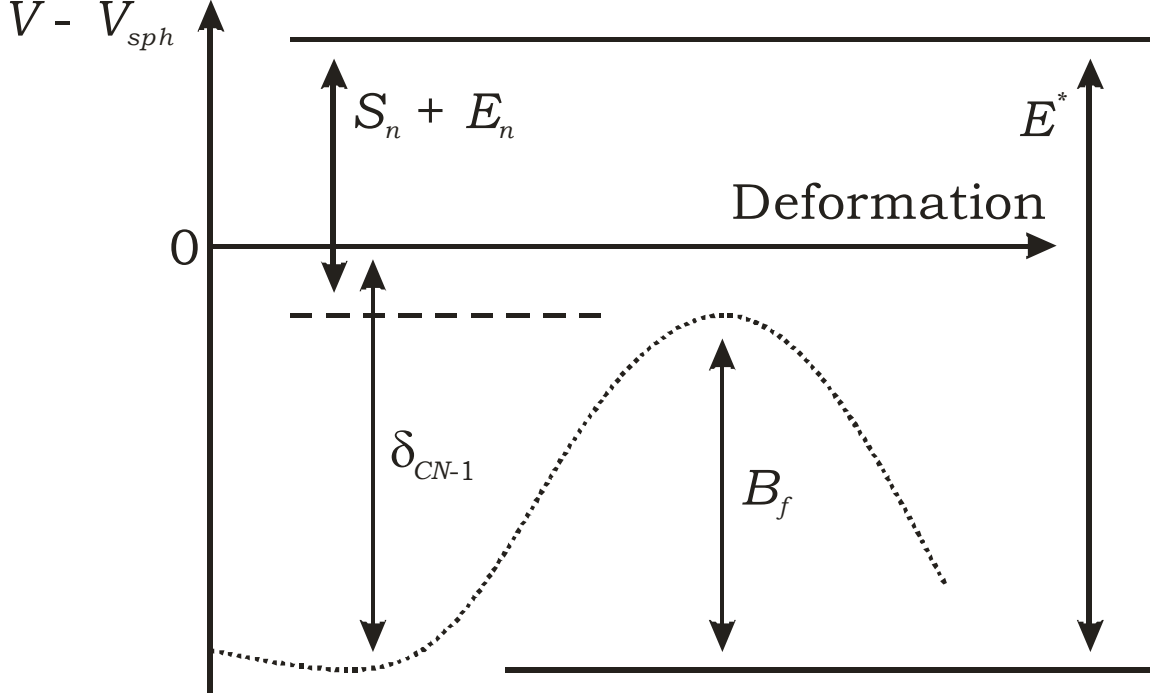


FIG. 1.7. Schematic of the optimum compound nucleus excitation energy for heavy element production via cold fusion reactions. The dotted line is the compound nucleus potential energy surface in its dependence in the deformation (elongation) coordinate.  $V_{sph}$  is the mass of the spherical compound nucleus without shell corrections,  $E^*$  is the initial excitation energy of the compound nucleus,  $S_n$  is the separation energy of the one neutron emitted,  $E_n$  is the kinetic energy of this neutron,  $\delta_{CN-1}$  is the shell correction of the ground state of the residual nucleus, and  $B_f$  is the fission barrier. The dashed line is the desired excitation energy remaining after emission of the neutron ( $\sim 0.3$  MeV above the saddle point); the beam energy yielding this energy should have the highest 1n cross section. See [Świątecki2004a].

the height of the fission barrier. Thus, the optimal beam energy is that which results in a residual nucleus with an excitation energy near its fission barrier after emission of one neutron. These researchers have developed an “optimum energy rule,” which might be expressed mathematically as [Świątecki2004a]

$$\begin{aligned}
 E_{cm, opt} &\approx (M_{sp} + M_n) - (M_1 + M_2) + 0.3 \text{ MeV} \\
 &= (M_{CN-1} + B_f + M_n) - (M_1 + M_2) + 0.3 \text{ MeV}.
 \end{aligned} \tag{1.23}$$

where  $E_{cm, opt}$  is the optimum center-of-mass bombarding energy,  $M_{sp}$  is the mass of the residual nucleus saddle point,  $M_n$  is the mass of the neutron,  $M_1$  is the mass of the

projectile,  $M_2$  is the mass of the target,  $M_{CN-1}$  is the mass of the ground state of the residual nucleus, and  $B_f$  is the fission barrier of the compound nucleus. The first four terms of the first line are simply the Q-value for formation of the saddle-point configuration of the residual nucleus. If we assume that the shell correction to the fission barrier is negligible [Zubov2003, Myers1999], then the saddle point mass can be approximated by the ground state mass plus the ground state shell correction  $\delta_{CN-1}$ :

$$E_{cm, opt} \approx (M_{CN-1} + \delta_{CN-1} + M_n) - (M_1 + M_2) + 0.3 \text{ MeV}, \quad (1.24)$$

The energetics contained in Eq. 1.24 is illustrated in Fig. 1.7. The agreement of these predictions with experiments in this work is described in later Chapters.

It is interesting to note that the theory predicts that 1n reactions leading to the same compound nucleus will have excitation functions whose magnitudes differ only by a scaling factor. For example, the  $^{64}\text{Ni} + ^{209}\text{Bi}$  and  $^{65}\text{Cu} + ^{208}\text{Pb}$  reactions both produce the compound nucleus  $^{273}\text{111}^*$ , which then emits a single neutron. After this emission, the deexcitation proceeds essentially identically in the two reactions and can be described by statistical methods as described in Sec. 1.2.1. Once the Q-value for ground state compound nucleus formation and the neutron separation energy are subtracted from the center-of-mass projectile energy, the same excitation energy results. The sum of these two quantities (the ground state Q-value and neutron separation energy) plus the 0.3-MeV correction is the neutron separation threshold energy  $E_{n, thr}$ . If  $E_{cm}$  is the center-of-mass projectile energy, then  $E_{cm} - E_{n, thr}$  should be the same for both reactions at the maxima of their excitation functions. This is illustrated in Fig. 1.4. Figure 1.4a shows excitation functions for these two reactions as a function of  $E_{cm}$ , computed according to [Świątecki2004a]. Figure 1.4b shows identical calculations, but plotted as a function of  $E_{cm} - E_{n, thr}$ , and the alignment is clearly visible. The red line in Fig. 1.4b shows the

theoretical excitation function for the  $^{65}\text{Cu} + ^{208}\text{Pb}$  reaction multiplied by a factor of 1.9, which causes it to overlap with the  $^{64}\text{Ni} + ^{209}\text{Bi}$  excitation function. Thus, the magnitudes of the cross sections for reactions producing the same compound nucleus depend primarily on the fusion cross section, with the peak being determined by the energy at which second-chance fission takes over. The same mechanisms are at work in both cases, with only a scaling factor differentiating them. The current work tests this theory in the  $^{208}\text{Pb}(^{65}\text{Cu}, n)^{272}\text{Rh}$  and  $^{208}\text{Pb}(^{55}\text{Mn}, n)^{262}\text{Bh}$  reactions.

### 1.3. Nuclear Shells and Heavy Element Stability

None of the transactinide elements described in Sec. 1.1 occur naturally and all must be produced artificially at appropriate particle accelerators. Although chemistry concerns itself primarily with the study of the electronic properties of the elements, their stability (and general availability on Earth) is determined by physics occurring within the nucleus. The transactinide elements should, in principle, have very low nuclear stability due to their high nuclear charge. The reason these elements exist with relatively long half-lives (on the order of milliseconds to minutes) is because of enhanced nuclear stability due to shell effects, where the potential energy (mass) of the ground state nucleus is reduced due to quantum mechanical effects. These shell effects are a microscopic phenomenon; let us first begin by describing the so-called “magic” numbers and the macroscopic properties of the nucleus.

#### 1.3.1. “Magic” Numbers

Protons and neutrons have shells, similar to electron shells in chemistry, that grant enhanced stability to nuclei, just as the closed-shell noble gases are known to be chemically

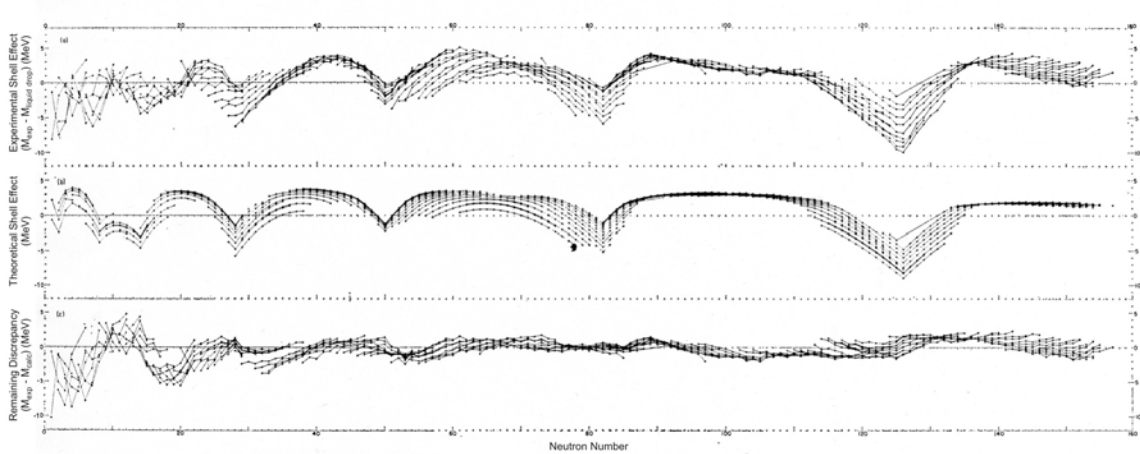


FIG. 1.8. Shell effects as a function of neutron number for nuclides throughout the chart of the nuclides. Solid lines connect isotopes. Upper figure: Experimental shell effect, defined as the difference between experimental and liquid-drop masses. Middle figure: Theoretical shell effects as computed in [Myers1967]. Lower figure: Difference between experimental and theoretical masses. Adapted from [Myers1967].

very stable. While chemical closed-shells occur at electron numbers 2, 10, 18, 36, 54, and 86, the “magic” numbers of 2, 8, 20, 28, 50, 82, and 126 protons and/or neutrons have long been known to be particularly stable. In these cases, all orbitals below some large gap in the level structure are filled; that is, the addition of another particle results in a substantial increase in total energy. The nuclear magic numbers were explained by Mayer [Mayer1950a, Mayer1950b] using spin-orbit coupling between a nucleon’s spin and its motion.

The magic numbers for neutrons can be clearly seen in Fig. 1.8 as local minima in the masses of nuclei. Clearly, there is a close association between improved stability and less mass. The reference point in the figure is the liquid-drop mass, that is, the mass that is calculated for a nucleus by treating it as if it had properties similar to drops of a liquid. The difference between the experimental mass and the liquid-drop mass is the shell correction or shell effect. In the following sections, it is shown that both liquid-drop

masses and shell corrections are necessary to describe nuclear masses, and that shell effects lead to the relative stability of the heaviest elements.

### 1.3.2. Liquid-Drop Model

Before discussing the liquid-drop model (LDM) specifically it is insightful to examine some properties of nuclear matter. Bulk nuclear matter is defined to be an infinite medium of equal numbers of protons and neutrons with no Coulomb force. These nucleons are subject to a short-range attractive force. This medium is described by two quantities: the binding energy per nucleon (approximately  $14\text{-}15 \text{ MeV}/A$ ) and the density (approximately  $0.17 \text{ nucleons/fm}^3$  [Seaborg1990]). A neutron star may be a close approximation of such a system. Unfortunately, ordinary nuclei are significantly different; they are finite in extent (and thus have a surface), have a significant Coulomb force, and the numbers of neutrons and protons may or may not be equal.

The liquid-drop model is a semi-classical attempt to estimate the mass of a nucleus by treating it as if it were a drop of a macroscopic liquid. Liquids also experience internal attractive forces and have a surface. The nucleons on the surface are not saturated by the attractive force, so a surface energy correction is needed. An additional correction is made for unequal numbers of protons and neutrons. Weizäcker [Weizäcker1935] developed a “semi-empirical mass formula” (SEMF) incorporating these concepts that was later simplified by Bethe and Bacher [Bethe1936]:

$$M = NM_n + ZM_p - \alpha A + \beta(N - Z)^2/A + \gamma A^{2/3} + (3/5)(e^2/4\pi\epsilon_0 r_0)Z^2 A^{-1/3}, \quad (1.25)$$

where  $N$ ,  $Z$ , and  $A$  are the neutron, proton, and mass numbers, respectively,  $r_0$  is the radius parameter, and  $\alpha$ ,  $\beta$ , and  $\gamma$  are constants to be determined empirically. The first two terms represent the mass of the protons and neutrons; the third term is a “volume” term resulting from the increase in binding energy from the attractive strong force among all nucleons. The fourth term corrects for the loss of binding energy by nucleons on the

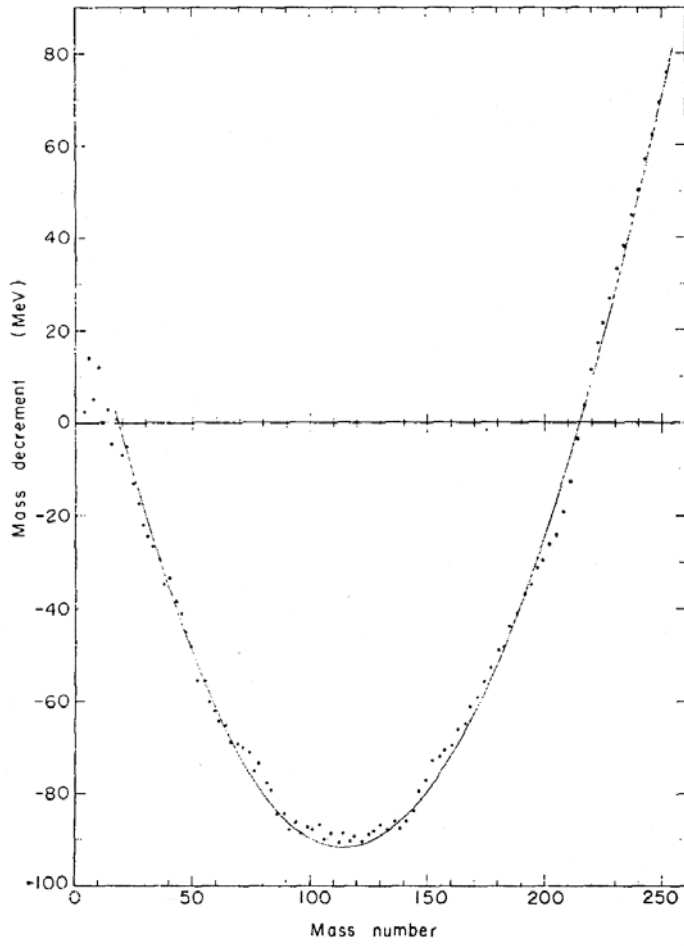


FIG. 1.9. Comparison of liquid-drop model mass predictions with experimental data. The dots are masses of actual nuclei along the long of beta stability and the solid line represents the prediction for beta-stable nuclei. In both cases, the masses are plotted as mass decrement (mass defect). The deviations from the liquid-drop models are due to shell effects. Adapted from [Myers1966].

surface, and the final term is the Coulomb energy of the nucleus, which adds to the mass.

An additional quantum mechanical pairing energy  $\delta$  [Bohr1939, Mayer1948] can also be included to account for the strong binding observed between identical nucleons:

$$\delta = \begin{cases} +0.036 A^{-3/4} \text{ u, } A \text{ even, } Z \text{ odd} \\ 0, \quad A \text{ odd} \\ -0.036 A^{-3/4} \text{ u, } A \text{ even, } Z \text{ even} \end{cases} \quad (1.26)$$

Equations 1.25 and 1.26 treat all nuclei as spherical; appropriate terms for deformed nuclei can be added in a straightforward fashion. The surface energy and Coulomb energy can be corrected using the ratio of deformed energy to spherical energy. The pairing energy  $\delta$  also varies with deformation, but in a more complex way.

The next logical question is, once we have the SEMF, how accurately does it predict atomic masses? This question is answered in Fig. 1.9, which shows the mass decrement (mass defect) of nuclides along the line of beta stability when their masses are computed solely from the LDM, compared to the experimental masses. The general agreement is good, but close inspection reveals that the deviations from the predictions are not random but follow definite trends. This effect is shown more clearly in Fig. 1.8, which shows the difference between experimental and liquid-drop masses. These deviations from the liquid-drop masses result from shell corrections, where the proximity of a nucleus to closed shells of protons and/or neutrons reduces its mass from that expected from the LDM. The result is shown schematically in Fig. 1.10. The figure shows an idealized heavy nucleus with a liquid-drop potential energy surface as a function of deformation. The dotted line indicates the effect of shell corrections on the liquid-drop potential. Note the significant drop in energy at zero deformation and the formation of a second potential well at high deformation. This second well can produce the fission isomers known in the

region from roughly thorium to berkelium. For the deformed, shell-stabilized nuclei studied in this work, the first well occurs at a non-zero deformation and the second well does not appear. Strutinsky showed how the shell correction energy could be calculated, and this is the subject of the next section.

### 1.3.3. Strutinsky Shell Corrections

As stated above, it was well known from the beginning of the study of nuclei that certain numbers of protons and neutrons imparted unusual stability to nuclei (the “magic” numbers 2, 8, 20, 28, 50, 82, 126, etc.). Mayer [Mayer1950a, Mayer1950b] explained these numbers by starting with an almost square well and calculating the energies of the “single-particle levels”. In these single-particle levels, the nucleons, which are fermions, have essentially independent motion because any scattering interactions would require the particle to move to a state with energy higher than the interaction energy. Mayer took these levels and applied spin-orbit coupling between a nucleon’s spin and its motion, which split previously degenerate levels. The magnitude of the splitting increased with increasing angular momentum quantum number  $l$  [Evans1955], resulting in large energy

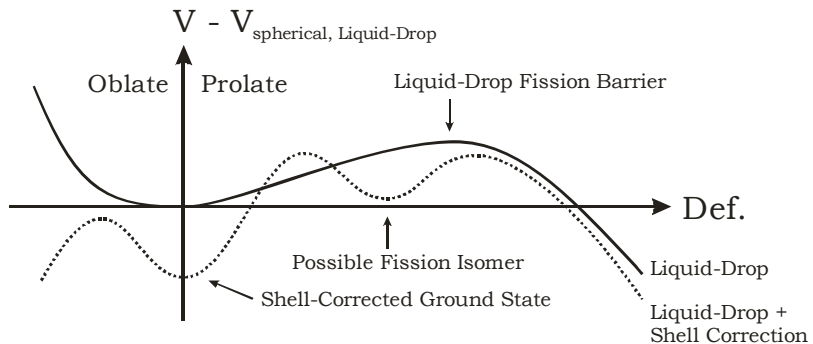


FIG. 1.10. Schematic diagram of potential energy surfaces for a deformed heavy nucleus in the liquid-drop model with and without shell corrections applied. The solid line is the liquid-drop potential; the dotted line is the liquid-drop potential modified by shell corrections. The reference energy is the liquid-drop energy of a spherical nucleus.

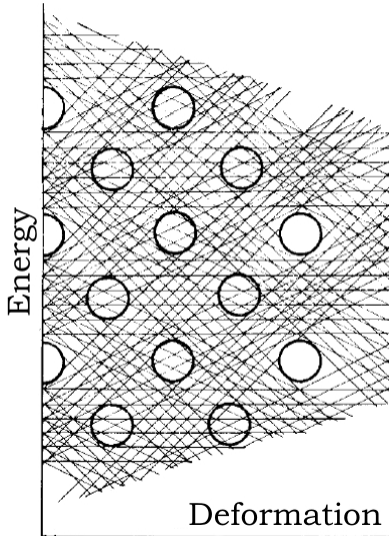


FIG. 1.11. Schematic diagram of Nilsson level splitting as envisaged by Strutinsky. The circles represent areas of low level density (at both zero and non-zero deformations) which should have strong shell effects. Adapted from [Strutinsky1968].

gaps devoid of any particle states. Once all the levels below a major gap were occupied, the nucleus contained a filled shell comparable to the electronic shells known in chemistry, and the addition of another particle would result in a substantial increase in total energy.

Unfortunately, this picture does not completely describe experimental facts. Although a filled shell clearly resulted in increased stability, it was also known that nuclei *near* closed shells exhibited enhanced stability. This is evident in Fig. 1.8, where nuclei on either side of a shell are also stabilized. Thus, shell gaps alone were not a sufficient explanation of the phenomenon.

Strutinsky [Strutinsky1967, Strutinski1966] was the first to show how shell correction energies for all nuclei could be calculated using the density of single-particle states. Strutinsky's insight was that the physical explanation for the shell correction is related to the level density: "Qualitatively, . . . the decrease of the level density at the Fermi energy decreases the single-particle energy (i.e. increases the nuclear binding energy) relative to its

‘uniform’ value. Compression of the levels leads to the opposite effect” [Strutinsky1967].

Strutinsky began with the Nilsson model for deformed nuclei [Nilsson1955] and his schematic representation of a Nilsson diagram is shown in Fig. 1.11. On the diagram, circles represent areas of low level density where few Nilsson states (formed as a result of the breaking of degeneracy in a deformed nucleus) exist. Integrating in energy over the occupied states leads to the total mass of the system.

For a distribution of quantized states with zero width each, the total energy  $\tilde{U}$  is

$$\tilde{U} = \sum_i 2E_i n_i, \quad (1.27)$$

where  $E_i$  is the energy of state  $i$  and  $n_i$  is the occupancy of the state (one if occupied, zero if empty). The factor of two represents the two nucleons allowed per level. For a continuous distribution of states  $n_i$  is replaced by  $g(E)$ , the level density function, and the total energy  $U$  is

$$U = 2 \int_{-\infty}^{\lambda} E g(E) dE, \quad (1.28)$$

where  $\lambda$  is the Fermi energy of the system, the maximum nucleon energy at zero temperature. The lower bound is negative infinity rather than zero because we shall see that  $g(E)$  extends to infinity. The Fermi energy for  $N$  nucleons can be found by solving the equation [Moretto1972]

$$N = 2 \int_{-\infty}^{\lambda} g(E) dE. \quad (1.29)$$

So far  $g(E)$  has not been described. Strutinsky began by taking a set of Nilsson levels  $E_r$ . Since all quantum levels are known to have non-zero widths, a width parameter  $\gamma$  (common to all levels) was introduced and  $g(E)$  was made a sum of Gaussian terms:

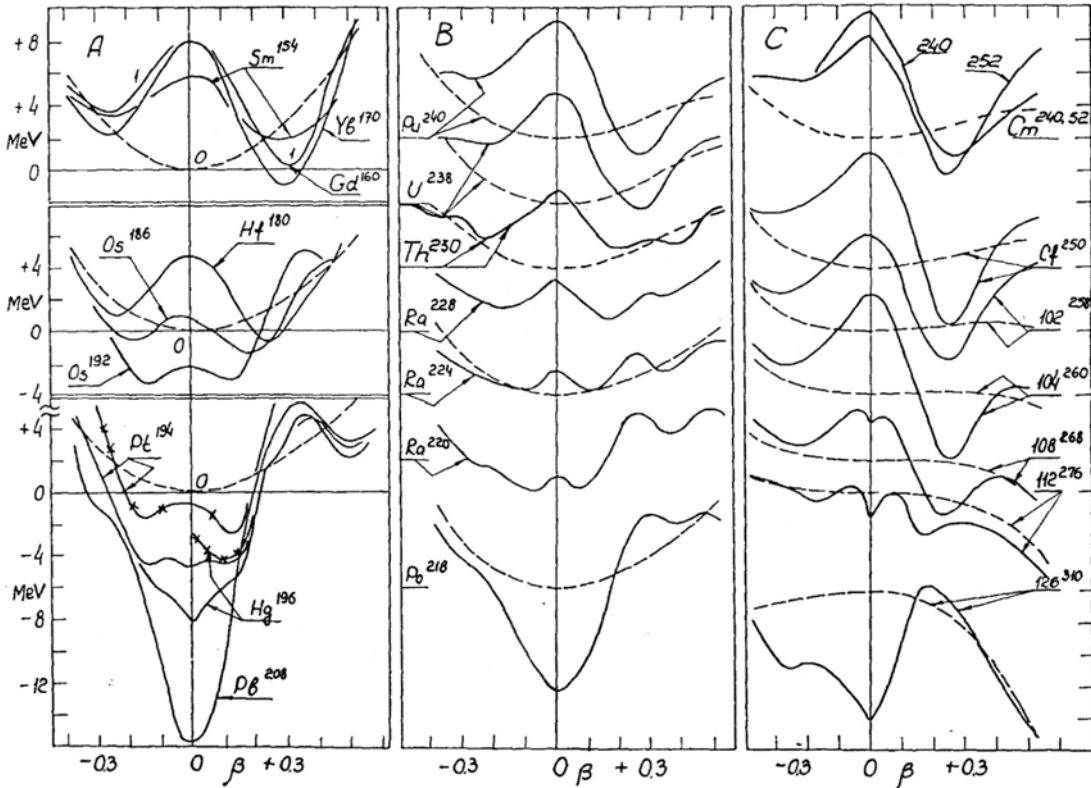


FIG. 1.12. Mass surfaces calculated by Strutinsky using the shell model for various nuclei. The solid lines show the deformation energy and the dashed lines are the liquid-drop energy. Curves with crosses were calculated with no pairing. Note the second potential wells that appear for Po, Ra, and Th nuclei, and the very large shell correction for  $^{208}\text{Pb}$ . Adapted from [Strutinsky1967].

$$g(E) = \frac{1}{\gamma\sqrt{\pi}} \sum_i \exp\left[-(E - E_i)^2 / \gamma^2\right]. \quad (1.30)$$

Each Gaussian represents a level density probability distribution centered on  $E_i$ . Thus, once a deformation was chosen the Nilsson levels and hence total energy could be determined (pairing energy was also included in the calculation). This energy minus the liquid-drop energy gives the shell correction.

Figure 1.12 shows the shell correction energies for several heavy nuclides as a function of deformation, expressed as the deformation parameter  $\beta$ . Note the second minimum in

the shell corrections for  $^{230}\text{Th}$   $^{220, 224, 228}\text{Ra}$  and  $^{218}\text{Po}$ , and that those nuclides heavier than  $^{218}\text{Po}$  tend to have deformed ground states. It should be noted that these energies apply to nuclei in the ground state. The level density tends to increase with excitation energy, leading to a compression of levels, and a reduction of the nuclear binding energy. Thus, shell effects become less negative with increasing excitation energy until they are eventually “washed out” so that there is no longer any shell correction.

An important element of Strutinsky’s work was the Nilsson levels used. Unfortunately, when one attempts to calculate the mass of a nuclide using shell-model states, the results are not satisfactory. The best method is to use the so called “macroscopic-microscopic” approach. The LDM is used to establish “baseline” macroscopic masses, which gives the general trend seen in Fig. 1.9. Then, Strutinsky’s method may be used to calculate the microscopic shell correction. Summing these two quantities gives a much more accurate depiction of nuclear masses.

#### 1.3.4. Illustrative Examples

In the history of the discoveries of the transactinide elements given in Sec. 1.1, there was a transition from initially using hot fusion reactions to cold fusion reactions. What is the origin of these distinctions? Cold fusion reactions are differentiated from hot fusion reactions by the excitation energy created in the compound nucleus as a result of the nuclear reaction. For the complete-fusion reactions studied in this field, the excitation energy  $E^*$  is obtained simply from kinematics:

$$E^* = E_{cm} + Q \quad (1.31)$$

$$Q = M(Z_1, A_1) + M(Z_2, A_2) - M(Z_{CN}, A_{CN}) \quad (1.32)$$

where  $E_{CM}$  is the center-of-mass bombarding energy,  $Q$  is the Q-value for production of the compound nucleus in its ground state,  $M$  represents the mass defect of the appropriate nucleus, and the subscripts 1, 2, and  $CN$  represent the projectile, target, and compound nucleus, respectively. Since both cold and hot fusion reactions are performed with beam energies near the Coulomb barrier, why should cold fusion give excitation energies of 10-16 MeV [Hofmann1998] while hot fusion gives excitation energies of 35-45 MeV (see Table 1.2 in [Patin2002a] for examples)?

Let us begin with two example reactions. The first is the Pb-based cold fusion reaction studied in this work:  $^{64}\text{Ni} + ^{208}\text{Pb} \rightarrow ^{272}\text{Ds}^*$ . The second is a hypothetical hot fusion reaction to produce the same compound nucleus:  $^{24}\text{Si} + ^{248}\text{Cm} \rightarrow ^{272}\text{Ds}^*$  (hypothetical because, currently, a beam of radioactive  $^{24}\text{Si}$  of sufficient intensity is not available for the experiment to be feasible). Assume that the beam energy is equal to the Coulomb barrier  $V_C$ . The mass defect of each nuclide is composed of a macroscopic part  $M^0$  due to the liquid-drop-like properties of nuclei (see Sec. 1.3.2) and a shell correction  $S$  due to quantum mechanical effects in the nucleus (see Sec. 1.3.3). Thus,

$$E^* = V_C + [(M_1^0 + S_1) + (M_2^0 + S_2) - (M_{CN}^0 + S_{CN})]. \quad (1.33)$$

Using the Coulomb barriers calculated from Eq. 1.13 with masses and shell corrections from [Myers1994], the following results were obtained. For the  $^{64}\text{Ni} + ^{208}\text{Pb} \rightarrow ^{272}\text{Ds}^*$  reaction,  $V_C = 242.4$  MeV,  $Q = -222.8$  MeV, and  $E^* = 19.6$  MeV. For the  $^{24}\text{Si} + ^{248}\text{Cm} \rightarrow ^{272}\text{Ds}^*$  reaction,  $V_C = 147.2$  MeV,  $Q = -56.7$  MeV, and  $E^* = 90.5$  MeV! This large difference in excitation energy between the two examples gives rise to the names cold and hot fusion. (In a more realistic example of hot fusion, the  $^{28}\text{Si} + ^{248}\text{Cm} \rightarrow ^{276}\text{Ds}^*$  reaction has  $V_C = 144.6$  MeV,  $Q = -95.7$  MeV, and  $E^* = 48.9$  MeV).

Equation 1.31 shows that the excitation energy of the compound nucleus is determined by the relative sizes of the Coulomb barrier and reaction Q-value. In the examples, the cold fusion reaction has a much larger Coulomb barrier, but the Q-value is sufficiently negative to result in a cold compound nucleus. The hot fusion reaction has a smaller Coulomb barrier but the Q-value is much less negative. When looking at the mass defects and shell corrections used in the calculations, it becomes obvious that the main influence on the Q-values is the macroscopic energy, rather than the shell correction. Macroscopic energies are on the order of tens to hundreds of MeV (positive or negative), while a large shell correction is only -10 MeV. In the  $^{24}\text{Si} + ^{248}\text{Cm}$  reaction, the macroscopic energies of the reaction partners are high:  $^{24}\text{Si}$  has a large surface energy because of its small size and  $^{248}\text{Cm}$  has a large Coulomb energy because of its high  $Z$ . In comparison, the cold fusion reaction uses the heavier projectile  $^{64}\text{Ni}$  and the lower- $Z$  target  $^{208}\text{Pb}$ . The overall reaction Q-value is more negative, meaning that more beam energy will have to be converted to mass to form the compound nucleus, and the excitation energy is lower.

### 1.3.5. Stability of the Transactinide Elements and New Shells

The previous section ended with the conclusion that the macroscopic component of nuclear masses is the most important in determining the excitation energy of a compound nucleus. However, without the influence of shell effects, the transactinides would not exist.

In a classic paper, Myers and Świątecki [Myers1966] noted that the influence of shell effects could increase the fission barriers for heavy nuclei and thus their fission half-lives. They combined a macroscopic liquid drop model with a microscopic shell correction

energy to make plots of the nuclear potential energy as a function of  $Z$ ,  $N$ , and the nuclear shape. Calculations using only a liquid-drop potential indicated that the fission barriers of elements with  $Z \geq 104$  should decrease to zero (see, for example, Fig. 1.12), with a corresponding rapid decrease in spontaneous fission half-lives. The prediction [Myers1966] of larger fission barriers on the order of several MeV led to new hope that SHEs could be produced artificially and might even be found in nature, although this latter expectation was never borne out [Hoffman2003]. (There was also the recognition that the experimental techniques then available were not sufficient to investigate such nuclei [Sikkeland1967]). The hope for artificial production manifested itself in the concept of an “island of stability,” a region of unusually high nuclear stability amongst a sea of unstable nuclei. The location of this island has been the subject of continuous debate among nuclear theorists, with predictions for the next spherical doubly-magic nucleus ranging from  $Z = 114$  and  $N = 184$  [Sobiczewski1966, Meldner1967] to  $Z = 120$  and  $N = 172$  [Rutz1997] to  $Z = 126$  and  $N = 184$  [Meldner1967, Ćwiok1996].

Additional theoretical calculations predicted the existence of deformed shells at  $Z = 108$  and  $N = 152, 162$  [Sobiczewski1987, Patyk1991]. Patyk and Sobiczewski [Patyk1991] also showed theoretically that higher-order deformations influence substantially the stability of nuclei in this region. The existence of these deformed shells was demonstrated by the production of the long-lived seaborgium isotopes  $^{265}_{106}\text{Sg}_{159}$  (half-life  $7.4^{+3.3}_{-2.7}$  s) and  $^{266}_{106}\text{Sg}_{160}$  (half-life  $21^{+20}_{-12}$  s) [Lougheed1994, Lazarev1994, Türler1998]. More recently, Türler *et al.* [Türler2003] reported the possible observation of the doubly magic nucleus  $^{270}_{108}\text{Hs}_{162}$ . With the experimental confirmation of these new deformed shells, the island of stability concept has been modified. It is still likely that a region of spherical, shell-

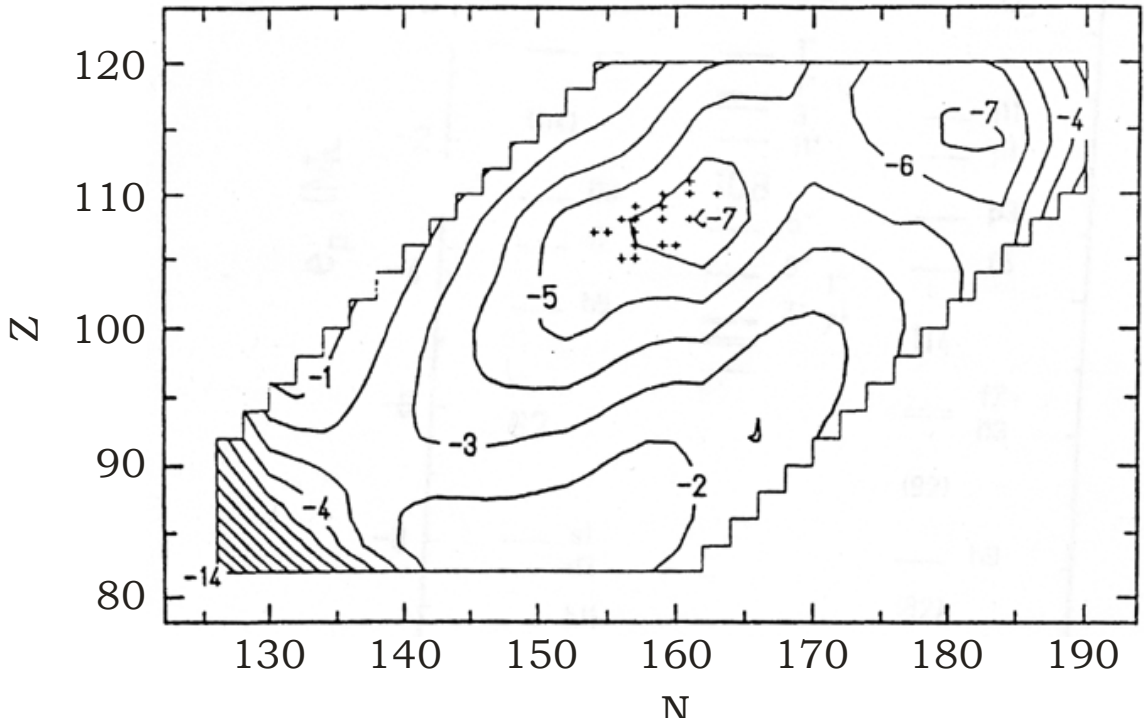


FIG. 1.13. Shell correction energies for nuclei beyond  $^{208}\text{Pb}$ . The units are MeV. Plus signs represent nuclei known in 1998. Note the local minimum at  $Z = 108$  and  $N = 162$  and the larger minimum near  $Z = 114$  and  $N = 184$ . Adapted from [Sobiczewski2001].

stabilized nuclei exists around  $Z \geq 114$  and  $N \geq 184$ , but it is not an isolated region of much greater stability only. Instead, there is a “peninsula” leading from the deformed, shell-stabilized nuclei at  $Z = 108\text{--}110$  to the predicted spherical nuclei around  $Z = 114$ . This peninsula is shown graphically in Fig. 1.13.

It is clear from the preceding paragraphs that the locations of the next spherical shells above  $Z = 82$  and  $N = 126$  are not entirely clear. Theory is unable to definitively provide the location of the next spherical shell as it did with the 2, 8, 20, 28, 50, 82, and 126 shells. Thus, it is left to experimentalists to probe the question. The nuclei studied in the present work ( $^{271}_{110}\text{Ds}_{161}$ ,  $^{272}_{111}\text{I}_{161}$ , and  $^{261,262}_{107}\text{Bh}_{156,155}$ ) are part of the extension of the peninsula of

stability. The impressive accumulation of knowledge from experiments done to study nuclides in this region is leading to a better understanding of the limits to nuclear stability.

## 1.4. Scope

In this dissertation, experimental investigations of the production of neutron-deficient transactinide isotopes using novel cold fusion reactions involving odd- $Z$  projectiles are described. The  $^{208}\text{Pb}(^{64}\text{Ni}, \text{n})^{271}\text{Ds}$  reaction was studied first for the purpose of measuring its excitation function. This reaction has been studied by groups at GSI [Hofmann1998], RIKEN [Morita2002, Morita2003, Morita2004c, Morita2004d], and LBNL [Ginter2003]. Ginter *et al.* had only observed two  $^{271}\text{Ds}$  decay chains at a single energy. The excitation function for this reaction was completed and used to test the BGS magnet settings and data acquisition system. This reaction also allowed us to properly estimate the beam energy for the second reaction,  $^{208}\text{Pb}(^{65}\text{Cu}, \text{n})^{272}\text{111}$ . The second reaction is new and was used to test the theories discussed in Sec. 1.2.1.2 and 1.2.2. This experiment also served as a confirmation of the discovery of element 111 using a different reaction.

The third reaction studied was the production of  $^{262}\text{Bh}$  isomers in the  $^{208}\text{Pb}(^{55}\text{Mn}, \text{n})$  reaction. This reaction has also been studied previously but the experimental techniques were not suitable for an accurate excitation function measurement. The reaction allowed testing of the “optimum energy rule” and cross section calculations using a reaction with a much higher cross section. These results are compared with the analogous  $^{209}\text{Bi}(^{54}\text{Cr}, \text{n})^{262}\text{Bh}$  reaction to produce the same isomers and facilitate investigation of the isomer production ratio as a function of excitation energy.

In addition, new calibration procedures were developed for the multitude of detectors used in the experiments.

## 2. Experimental Apparatus: The Berkeley Gas-filled Separator

The main apparatus used in the experiments described in this work is the Berkeley Gas-filled Separator (BGS). This device uses a series of three magnets to provide physical separation of complete-fusion-evaporation products of nuclear reactions from transfer reaction products and unreacted beam. It is a high-transmission recoil separator that has been used in a variety of heavy-element physics experiments (see, for example, [Patin2002a]) and has been modified for use as a pre-separator for heavy-element chemistry experiments (see, for example, [Kirbach2002, Omtvedt2002, Sudowe2002]). The BGS has been described previously [Gregorich2000, Ninov1998], but important features and improvements will be described in the following sections.

### 2.1. Targets

The BGS is shown schematically in Fig. 2.1. The Lawrence Berkeley National Laboratory (LBNL) 88-Inch Cyclotron delivers a beam of the desired projectile to Cave 1. The beam enters the BGS target chamber (upper left in Fig. 2.1) after passing through a series of focusing magnets and a collimator. The evacuated beam line is separated from the gas-filled separator by a  $^{nat}C$  entrance window which has a typical thickness of  $45 \pm 5$

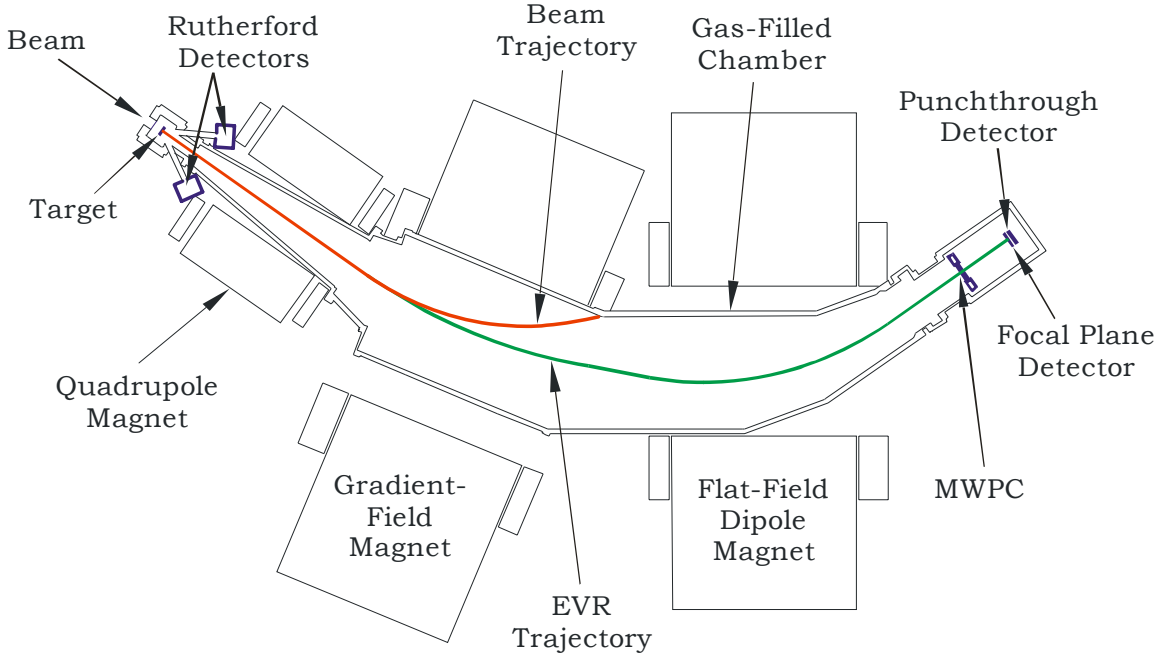


FIG. 2.1. Schematic of the Berkeley Gas-Filled Separator. See the main text for a discussion.

$\mu\text{g}/\text{cm}^2$ . Multiple entrance windows are mounted on a telescoping arm so that windows can be changed quickly when one breaks. Window breaks occur roughly every 24-72 hours during normal high-intensity experiments due to the intense radiation damage windows suffer from the beam. After passing through the entrance window, the beam traverses 0.5 cm of He fill gas at 0.5-0.9 torr which has a negligible effect on the energy of the beam.

### 2.1.1. Rotating Wheel Targets

Nine arc-shaped target segments were mounted around the periphery of a 14-inch diameter circular wheel. This wheel rotated at  $\sim$ 450 rpm during the experiments. The purpose of the rotation was to minimize the time each target spent in front of the beam and to maximize the time spent out of the beam, which maximizes cooling. A stationary

lead target subjected to full beam intensity in a heavy-element experiment would quickly be melted because of the low melting point of lead (327°C).

### *2.1.2. Target Characteristics*

After passing the fill gas the beam strikes the target backing. These backings are used to support the main target material and are attached to frames made of aluminum or stainless steel. The most common targets used in BGS experiments are  $^{207, 208}\text{Pb}$ ,  $^{209}\text{Bi}$ , and  $^{238}\text{UF}_4$ , although  $^{208}\text{Pb}$  is used exclusively in this work. The backings ( $35 \pm 5\text{-}\mu\text{g/cm}^2$   $^{nat}\text{C}$ ) have  $^{208}\text{Pb}$  sputtered on them to a thickness of  $0.47 \pm 0.06\text{ mg/cm}^2$ . The isotopic composition of the Pb was determined by commercial inductively coupled plasma mass spectrometry to be 98.4%  $^{208}\text{Pb}$ , 1.1%  $^{207}\text{Pb}$ , and 0.5%  $^{206}\text{Pb}$ . The Pb layer was covered with a  $5 \pm 2\text{-}\mu\text{g/cm}^2$   $^{nat}\text{C}$  cover foil to prevent loss of target material caused by the beam. These Pb targets were prepared by the target laboratory of the Gesellschaft für Schwerionenforschung (GSI) in Darmstadt, Germany.

Target thicknesses were verified by measuring the energy loss of alpha particles emitted from a three-peak alpha standard source ( $^{239}\text{Pu}$ ,  $^{241}\text{Am}$ , and  $^{244}\text{Cm}$ ) passing through the backing, target, and cover foil. The alpha particles typically lost 130-150 keV of energy while traversing the targets. This information, combined with range calculations from the SRIM-2003 computer code [Ziegler2003], allowed for the determination of the target thicknesses. This same code was used to determine cyclotron beam energy losses in the entrance window, backing, target, and cover foil.

### 2.1.3. Stationary Targets

An additional telescoping arm has five target positions that can each hold a single stationary target. Isotopically enriched medium-mass nuclides are often used as targets for test reactions and calibrations. Among the targets used in this work are  $^{116}\text{Sn}$ ,  $^{120}\text{Sn}$ ,  $^{\text{nat}}\text{BaBr}_2$ ,  $^{\text{nat}}\text{Cs}^{\text{nat}}\text{I}$ , etc. During the primary experiments described in this work, this arm is in its fully retracted position.

## 2.2. Rutherford Detectors and Cross Section Calculations

The experiments described in this work involve the use of the high- $Z$  target material lead ( $Z = 82$ ) being bombarded by medium-mass projectiles, such as  $^{65}\text{Cu}$  ( $Z = 29$ ). Due to the high charge of the target nucleus, there will be a significant Rutherford scattering cross section and many projectiles will be scattered at large angles. This fact can be used to monitor the beam intensity during the experiment and calculate the reaction cross section once the number of observed decay chains has been determined.

Two p-i-n diode detectors are mounted at an azimuthal angle of  $27.2 \pm 0.1$  degrees to the beam axis for the purpose of measuring projectiles scattered by the target. Upstream of these detectors are four wire grid screens to reduce the number particles striking the detectors, preventing excessive radiation damage. The screens' total scaledown factor, or ratio of transmitted particles to incident particles, has been measured previously to be  $(1348 \pm 20)^{-1}$  [Peterson2004]. Particles transmitted through the screens then pass through a circular collimator. The total distance from the target to the Rutherford detectors is  $292 \pm 1$  mm.

Given a cross section  $\sigma$ , beam intensity  $I$ , and areal density of target atoms  $N$ , the production rate  $R$  in the reaction channel of interest is [Krane1988]

$$R = \sigma N I. \quad (2.1)$$

This equation assumes that  $I$  and  $N_\iota$  are constant. While it is safe to assume that  $N_\iota$  is constant over the course of an experiment since very few target nuclei are involved in nuclear reactions, there may be large fluctuations in  $I$  due to changes in the performance and efficiency of the accelerator and ion source. We will see that these fluctuations can be ignored. If Eq. 2.1 is applied to Rutherford scattering, then  $\sigma$  would be the total Rutherford scattering cross section  $\sigma_{Ruth}$ . Since the Rutherford detectors are collimated at a fixed laboratory angle to the beam, we are really interested in the differential Rutherford scattering cross section  $d\sigma_{Ruth} / d\omega$ , given by [Segrè 1977]

$$\frac{d\sigma_{Ruth}}{d\omega} = \left[ \frac{e^2 Z_1 Z_2}{4\pi\epsilon_0 (2E_{lab})} \right]^2 \frac{1}{\sin^4 \theta} \cdot \frac{[(\cos \theta) \pm \sqrt{1 - (m_1/m_2)^2 \sin^2 \theta}]^2}{\sqrt{1 - (m_1/m_2)^2 \sin^2 \theta}}, \quad (2.2)$$

where  $Z_1$  and  $Z_2$  are the respective atomic numbers of the projectile and target,  $E_{lab}$  is the lab-frame projectile energy,  $m_1$  and  $m_2$  are the respective masses of the projectile and target, and  $\theta$  is the lab frame scattering angle. The positive sign must be used before the radical if  $m_1 < m_2$ . If  $m_1 > m_2$  then both the forms must be calculated and added together. (In the experiments described in this work,  $m_1$  is always less than  $m_2$ ). If  $t$  represents the length of the irradiation and  $\epsilon_{Ruth}$  is the detection efficiency, then the number of Rutherford-scattered particles observed  $N_{obs, Ruth}$  is given by

$$N_{obs, Ruth} = \epsilon_{Ruth} R_{Ruth} t = \epsilon_{Ruth} \frac{d\sigma_{Ruth}}{d\omega} N_\iota I t. \quad (2.3)$$

$\epsilon_{Ruth}$  is the product of three factors, the Rutherford detection efficiency  $\epsilon_{det, Ruth} = 1.00 \pm 0.05$ , the screening scaledown factor  $\epsilon_{screen} \approx (1348 \pm 20)^{-1}$ , and the fraction of space at 27.2°

subtended by the collimator  $\Omega = (2.1 \pm 0.2) \times 10^{-4}$ . From Eq. 2.3 we can calculate the product  $N_t It$ :

$$N_t It = \frac{N_{obs, Ruth}}{\epsilon_{det, Ruth} \epsilon_{screen} \Omega (d\sigma_{Ruth} / d\omega)}. \quad (2.4)$$

$N_{obs, Ruth}$  can be measured easily by integrating an appropriate region of the Rutherford spectrum. The reaction cross section  $\sigma_{rxn}$  can now be calculated:

$$N_{obs, rxn} = \epsilon_{det, rxn} R_{rxn} t = \epsilon_{det, rxn} \sigma_{rxn} N_t It \quad (2.5)$$

$$\Rightarrow \sigma_{rxn} = \frac{N_{obs, rxn}}{\epsilon_{det, rxn} N_t It} \quad (2.6)$$

where  $N_{obs, rxn}$  is the number of atoms or decay chains observed and  $\epsilon_{det, rxn}$  is the reaction product detection efficiency. Since  $\sigma_{rxn}$  depends only on the integrated dose  $It$ , any fluctuations in  $I$  are accounted for naturally by the measurement of  $N_{obs, Ruth}$ . Once  $N_t It$  is known, the integrated dose can be determined if  $N_t$  can be established by some independent means, such as the alpha particle energy loss measurements described in Sec. 2.1.2.

## 2.3. Magnets

### 2.3.1. Introduction

Only a small fraction of the interactions between the projectile and target will result in the complete fusion of the two and the large forward momentum of the projectile will be transferred to the compound nucleus. After the rapid emission of neutrons from the compound nucleus, the resulting EVR recoils out of the target and into the first magnet.

The innovative design of the BGS features a quadrupole magnet (Q1) followed by a gradient field dipole magnet (M1) and a flat field dipole magnet (M2); see Fig. 2.1. The quadrupole magnet provides vertical focusing at the expense of horizontal defocusing. The net effect is to increase the size of the BGS EVR acceptance cone to a relatively large 45 msr. Unfortunately, having the only quadrupole magnet so far from the focal plane results in a large focal plane image and requires a large detector to cover that image. The focal plane detector is discussed in Sec. 2.4. The BGS also has a large bending angle (70°) which provides excellent separation of the EVRs from transfer reaction products and unreacted beam. The separation factor is on the order of  $(1-10) \times 10^{14}$ . This large bending angle results in a large dispersion, so that a 1% change in the magnetic rigidity setting of the separator moves the focal plane image horizontally by 2 cm (see below for a discussion of magnetic rigidity). Again, a large focal plane detector is needed to compensate for the large dispersion. Such a detector is in use, so the full capabilities of the BGS can be utilized.

After being focused by the quadrupole magnet, EVRs pass into the first of the two dipole magnets. It is in these dipoles that the actual separation of EVRs from the beam and transfer products occurs. The BGS uses the principle of magnetic rigidity for separation. In the presence of a magnetic field perpendicular to the direction of motion, a charged particle will curve under a Lorentz force vector  $\vec{F} = q(\vec{v} \times \vec{B})$ , where  $q$  is the charge on the particle,  $\vec{v}$  is the velocity vector, and  $\vec{B}$  is the magnetic field vector. In scalar terms, this simplifies to  $F = qvB$ , which must also be equal to the centripetal force on the particle  $F = mv^2/\rho$ , where  $m$  is the mass of the particle,  $v$  is its velocity, and  $\rho$  is the radius of curvature of motion. Solving these two relations for the product of field strength

and radius gives the magnetic rigidity  $B\rho = mv/q$ . The radius of curvature  $\rho$  is constant and fixed by the design of the gas-filled chamber. Thus, selecting the magnetic field strength  $B$  allows for the selection of the magnetic rigidity of those particles that will be transmitted to the focal plane detectors. A corollary of this discussion is that any two particles with the same magnetic rigidity will traverse the BGS to its focal plane, regardless of their identity.

### 2.3.2. *Evaporation Residue Charge States in Helium*

It is necessary to know the magnetic rigidity (equal to  $mv/q$ ) of the EVRs expected before  $B$  can be selected. This is one of the most challenging and important problems in the use of a gas-filled separator. The mass  $m$  can be obtained easily from mass tables or approximated using the EVR's mass number. The velocity  $v$  can be estimated using kinematics. The difficulty lies in the estimation of the charge state  $q$ . The EVR will experience collisions with the atoms in the He fill gas while moving through the BGS and may gain or lose electrons. After a large number of collisions, the EVR should have an electronic state with a charge close to a predictable average charge  $\bar{q}$ . It should be noted that He is not the optimum choice for the fill gas due to its high first ionization potential.  $\text{H}_2$  would be more effective because of its lower first ionization potential but is not used for safety reasons. It has been known for some time that  $\bar{q} \propto vZ^{1/3}$ , where  $Z$  is the atomic number of the EVR (see [Betz1972] and references therein).  $v$  is usually expressed in units of the Bohr velocity  $v_0 = e^2/(2\epsilon_0 b) \approx 2.188 \times 10^6 \text{ m/s}$  (the classical velocity of the 1s electron in a ground-state hydrogen atom) so that

$$\bar{q} \propto (v/v_0)Z^{1/3}. \quad (2.7)$$

Several researchers have suggested formulas for approximating  $\bar{q}$  in dilute He. Ghiorso *et al.* [Ghiorso1988] suggested the following formula based on the work of Betz [Betz1972]:

$$\frac{\bar{q}}{Z} = 1 - C_1 \exp\left[-C_2(v/v_0)Z^{-2/3}\right], \quad (2.8)$$

where  $C_1$  and  $C_2$  were experimentally determined to be 1.04 and 0.91, respectively. The dependence of  $\bar{q}$  on  $(v/v_0)Z^{1/3}$  in Eq. 2.8 can be seen by using the approximation  $C_1 \approx C_2 \approx 1$  and keeping the first two terms of a Taylor series expansion about  $(v/v_0)Z^{2/3} = 0$ . Morita *et al.* [Morita2003] have proposed

$$\bar{q} = 0.62(v/v_0)Z^{1/3} \quad (2.9)$$

when  $(v/v_0)Z^{1/3}$  is in the range 10-20. More recently, Gregorich [Gregorich2004] has suggested the following formula based on an analysis of the data presented in Fig. 3 of Ghiorso *et al.* [Ghiorso1988]:

$$\begin{aligned} \bar{q} &= px + r + s \sin\left\{\frac{2\pi}{32}[Z - (px + r) - t]\right\} \\ &= px + r + q_{\sin} \end{aligned} \quad (2.10)$$

where  $x = (v/v_0)Z^{1/3}$ ,  $p = 0.641$ ,  $r = -0.235$ ,  $s = 0.517$ ,  $t = 74.6$ , and  $q_{\sin}$  is the sinusoidal component. The factor of 32 comes from the length of rows six and seven of the periodic table (see Fig. 1.1) including the lanthanides and actinides, so that the sinusoidal correction to the charge state completes one period per row. Figure 2.2 shows a plot of  $q_{\exp} - q_{\sin}$  versus  $x$  for the charge state data in [Ghiorso1988], illustrating the linear component of Eq. 2.10 ( $q_{\exp}$  is the experimentally observed charge state). This formula has proven very useful for the prediction of charge states for the BGS and was used to aid in the selection of magnet settings for the  $^{208}\text{Pb}(^{55}\text{Mn}, \text{n})^{262}\text{Bh}$  experiment described in Chapter 5.

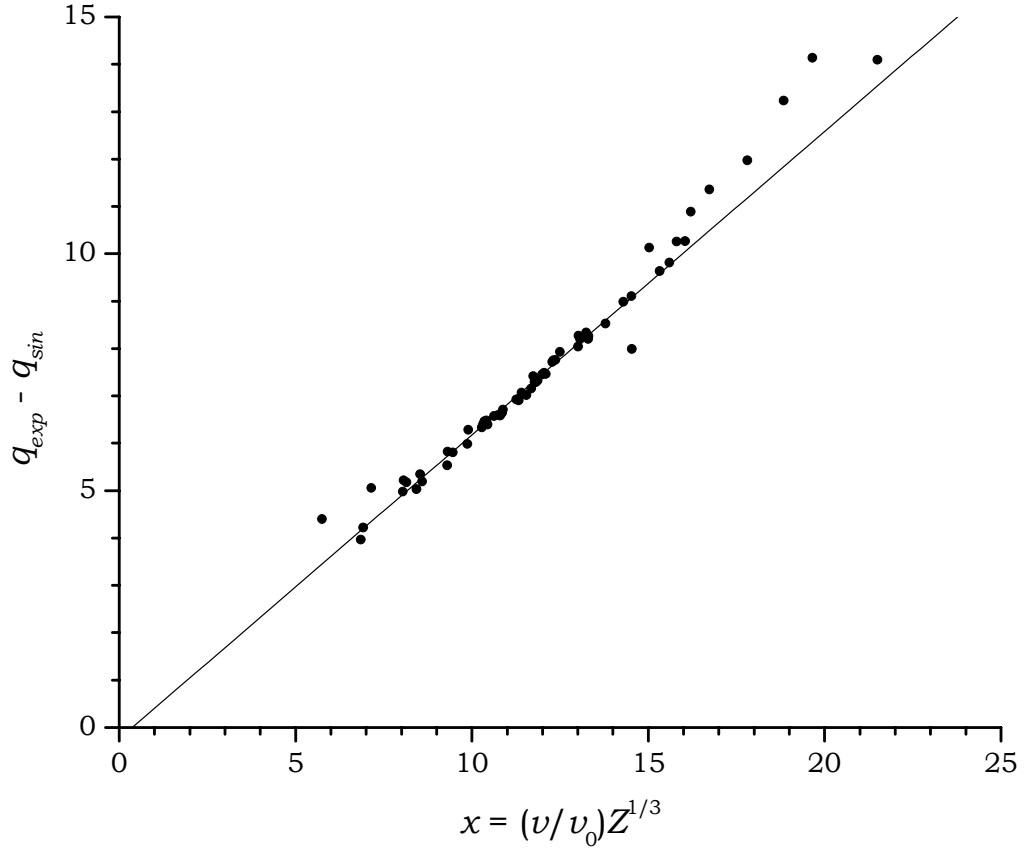


FIG. 2.2. Experimental charge states of EVRs in He. The data are plotted as  $q_{\text{exp}} - q_{\text{sin}}$ , where  $q_{\text{exp}}$  is the experimentally observed charge state [Ghiorso1988] and  $q_{\text{sin}}$  is the sinusoidal component of Eq. 2.10. The line is the linear component of Eq. 2.10. Note the quality of the fit from  $7 \leq (\nu/\nu_0)Z^{1/3} \leq 17$ , which includes the values of  $(\nu/\nu_0)Z^{1/3}$  studied in this work.

Once the expected (mean) charge state  $\bar{q}$  has been calculated, the desired field can be produced in the magnets using the currents given in Eq. 2.11 below. These equations give the currents as a function of the magnetic rigidity and the desired ratio  $R = I(\text{M2})/I(\text{M1})$  [Patin2002b, Gregorich2004]:

$$I(\text{Q1}) = (765 \text{ A T}^{-1} \text{ m}^{-1}) B \rho, \quad (2.11\text{a})$$

$$I(M1) = \frac{B\rho}{0.002467 + 0.002016R} \text{ A T}^{-1} \text{ m}^{-1}, \quad (2.11b)$$

$$I(M2) = \frac{B\rho}{(0.002467/R) + 0.002016} \text{ A T}^{-1} \text{ m}^{-1}. \quad (2.11c)$$

The optimum value for R has been determined experimentally to be 1.69.

The main purpose of the BGS is to separate EVRs from unreacted beam and transfer reaction products. Since  $\bar{q} \propto (v/v_0)Z^{1/3} \propto vZ^{1/3}$ , we have

$B\rho = mv/q \propto mv/(vZ^{1/3}) = mZ^{-1/3}$ .  $Z^{-1/3}$  varies slowly with  $m$  so that heavier complete fusion reaction products have higher magnetic rigidities than the beam and lighter transfer reaction products. (This idealized discussion ignores the variation in electronic properties represented by the sinusoidal correction in Eq. 2.10, which can be significant). Selecting a magnetic field corresponding to a high magnetic rigidity allows complete fusion EVRs to pass freely through the separator to the focal plane detector array. Unreacted beam has a lower magnetic rigidity and thus a lower radius of curvature, and will collide with the tantalum beam stop along the inner edge of the gas-filled chamber as shown in Fig. 2.1.

## 2.4. Focal Plane Detector

### 2.4.1. Introduction

A new detector array was installed at the end of the BGS prior to these experiments. A picture of this detector is shown in Fig. 2.3. This focal plane detector array (hereafter called just the “focal plane”) is made from 14 detector “cards,” each containing a wafer of Si divided into 16 position sensitive strips. These cards are 60 mm  $\times$  60 mm with an active area of 58 mm  $\times$  58 mm. Each strip is 58-mm tall and 3.625-mm wide, including a 0.5-mm gap between adjacent strips. The 300- $\mu\text{m}$  Si wafers are fully depleted, and

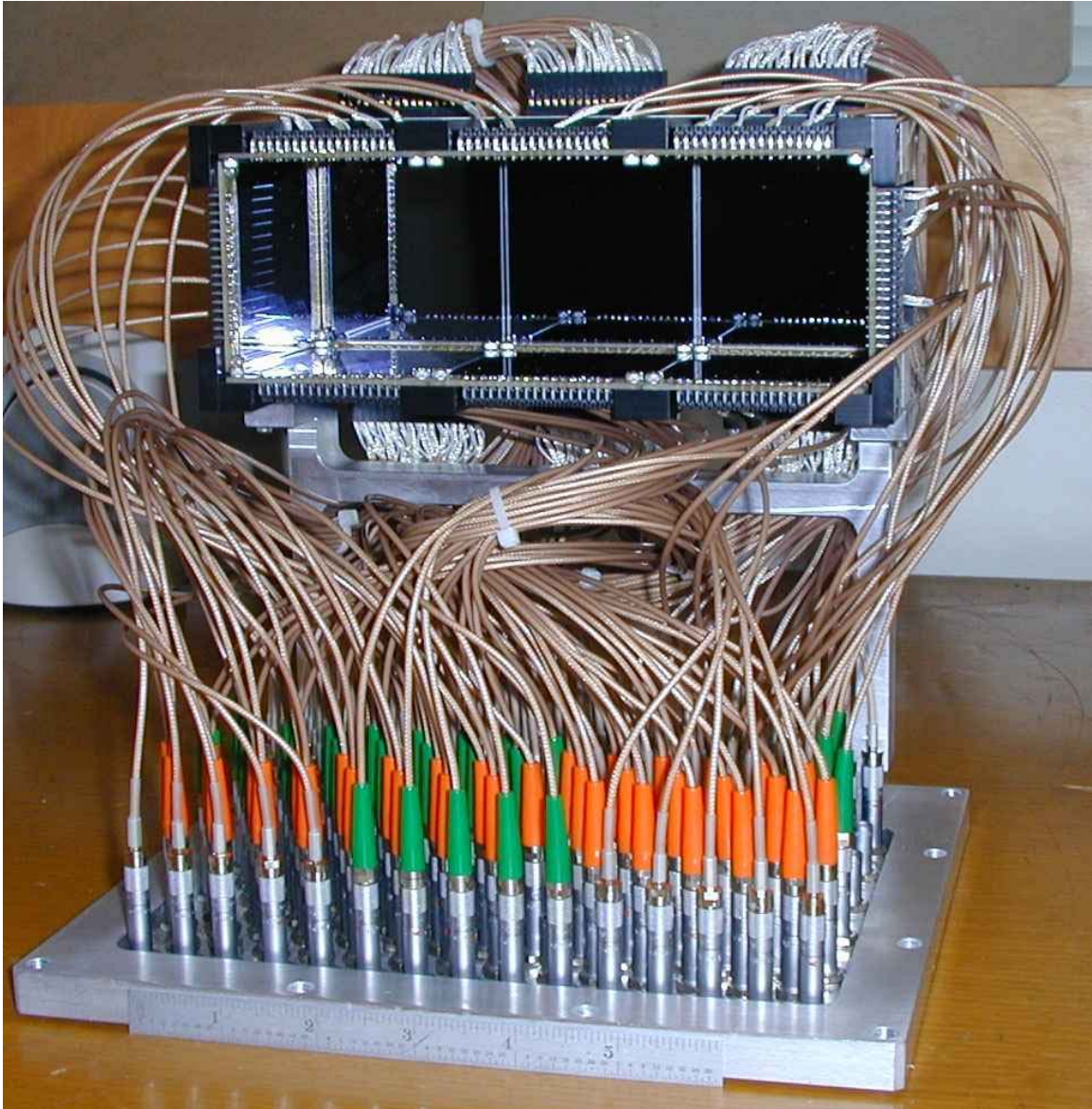


FIG. 2.3. The BGS focal plane detector array. The main strip detectors are in the back facing the reader. Upstream detectors are perpendicular to the strips and protrude roughly from the edges. Punch-through detectors (not visible) are mounted behind and parallel to the strips. The detector is shown sitting upside-down on a desk. In an experiment, the whole focal plane assembly hangs in the detector box by the bottom baseplate. Note that the smooth surface of the strip detectors creates a reflection. The scale on the ruler (lower center) is inches.

mounted on a 1500-Å Al layer. Each card is glued to a circuit board and its strips are connected to signal cables by wire bonds. The strips are biased at +30-40 V.

The most important bank of cards is the one perpendicular to the direction of travel of incoming EVRs. Three cards are mounted side-by-side giving a total of 48 strips. These strips are numbered so that 0 is on the high magnetic rigidity end of the focal plane and 47 is on the low end. Signals are produced from both the top and bottom of the strip when an EVR implantation or radioactive decay occurs, allowing the vertical position of events to be determined. In this dissertation, “position” always refers to vertical position in a strip detector. The position of any event is determined by resistive charge division, so that the position is [Alberi1976]:

$$\text{Position} \approx \frac{Q_T - Q_B}{Q_T + Q_B}, \quad (2.12)$$

where  $Q_T$  is the charge collected at the top of the strip and  $Q_B$  is the charge collected at the bottom of the strip. This definition gives positions from -1 to +1, where -1 is at the bottom of the strip and +1 is at the top of the strip. Multiplying this position by half the strip height gives the absolute position  $P$ . The energy of any event is proportional to  $Q_T + Q_B$ . Determining the position and energy of events is discussed in more detail in the following sections. The EVRs studied in this work are implanted to a shallow depth (<10  $\mu\text{m}$ ), and the geometric probability of any particle emitted fully stopped in these detectors is  $\sim 55\%$ . The circuit boards supporting these cards have a large square hole in the center to allow the transmission of particles through the strip detectors with ranges greater than the sum thickness of the Si and Al. These particles are discussed below.

Eight “upstream” detector cards are mounted perpendicular to the main strip detectors with a gap of  $\sim 5$  mm. Three cards are mounted above and three below and one card is mounted on either side of the main detector cards. This leads to the five-sided box configuration seen in Fig. 2.3. These upstream detectors provide additional detection

efficiency ( $\sim 25\%$ ) for alpha particles and fission fragments emitted from the face of the main detectors. On each upstream card, sets of four adjacent strips are wired to function as one, so that only four effective detectors exist on each card, for a total of thirty-two. Only one signal is collected from the upstream detectors so they are not position-sensitive.

Three “punch-through” cards mounted behind the main strip detectors provide a veto for light, low-ionizing particles which pass through the main strips. These particles are typically protons or alpha particles which can be the result of evaporation reactions in the target material, elastic scattering of the He fill gas, or nuclear reactions in the tantalum beam stop. Like the upstream detectors, sets of four adjacent punch-through strips are connected so they act as one, for a total of twelve punch-through detectors. Again, only one signal is recorded so there is no position sensitivity. Typically, the punch-through detectors are not calibrated; an above-threshold signal in a punch-through detector vetoes any coincident signals in other detectors.

A multi-wire proportional counter (MWPC) is placed 9 inches upstream of the main strip detectors for the purpose of discriminating implantation events from radioactive decays. The MWPC has two thin Mylar windows ( $0.9\text{-}\mu\text{m}$  each) on the upstream and downstream sides which contain isobutane fill gas at a pressure 0.5 bar above the BGS detector box pressure of 0.5-0.9 torr. The MWPC is biased at +400-500 V into the negative high voltage terminal. Any EVR passing through the MWPC initiates a process of charge multiplication, and this charge is collected at electrodes on the top, bottom, left, and right sides. These four signals are recorded by the data acquisition system. Additionally, a signal in the MWPC starts the clock on a time-to-amplitude converter. The stop signal is provided by the main strip detectors, so that a time-of-flight can be measured.

### 2.4.2. External Calibration Sources

A proper calibration is critical to the success of any nuclear science experiment. The calibrations needed for the experiments described in this work are complex: standard one-dimensional linear calibrations can be used for the upstream detectors, but the main strip detectors (hereafter referred to as “focal plane strips” or just “strips”) require the deconvolution of two energy signals, which increases the complexity. Additionally, a position calibration is required for the strips.

A new strip calibration parameterization was developed for this work. This parameterization includes a linear component with a simple gain and offset for an “energy parameter” linearly proportional to energy. Additionally, a position-dependent quadratic component was added which acted as a resolution-sharpening correction. A new algorithm was developed which could perform all the necessary steps automatically, once the appropriate calibration data is acquired.

#### 2.4.2.1. Strip External Energy Calibration

Each calibration starts by acquiring data from a four-peak external alpha-particle source. This source contains samples of four nuclides:  $^{148}\text{Gd}$  (3182.787 keV, 100% branch),  $^{239}\text{Pu}$  (5156.59 keV, 73.3%),  $^{241}\text{Am}$  (5485.60 keV, 85.2%), and  $^{244}\text{Cm}$  (5804.82 keV, 76.4%) [Firestone1996]. It is instructive to begin by examining some raw data produced from these sources. Figure 2.4 shows the external data acquired in strip 3 prior to the  $^{271}\text{Ds}$  experiment described in Chapter 3. The abscissa is the channel number  $B$  from the bottom of the strip and the ordinate is the channel number  $T$  from the top of the strip. This  $(B, T)$  coordinate system will be used throughout this discussion. Each line of data in the figure corresponds to one alpha line from the source. If the  $(B, T)$  coordinate system

is rotated through the angle  $\theta$  shown in Fig. 2.4, then the result is the  $(u, v)$  coordinate system (here  $v$  is unrelated to the velocity discussed in Sec. 2.3.2). Clearly, energy is increasing in the direction of the  $v$  axis; a projection of the  $(B, T)$  data onto the  $v$  axis produces a one-dimensional spectrum which can be calibrated using standard techniques. This lies at the heart of the energy calibration.

Before the projection can be done it is necessary to determine the angle  $\theta$ . An inspection of the data in Fig. 2.4 reveals that the slope of each line of data can be

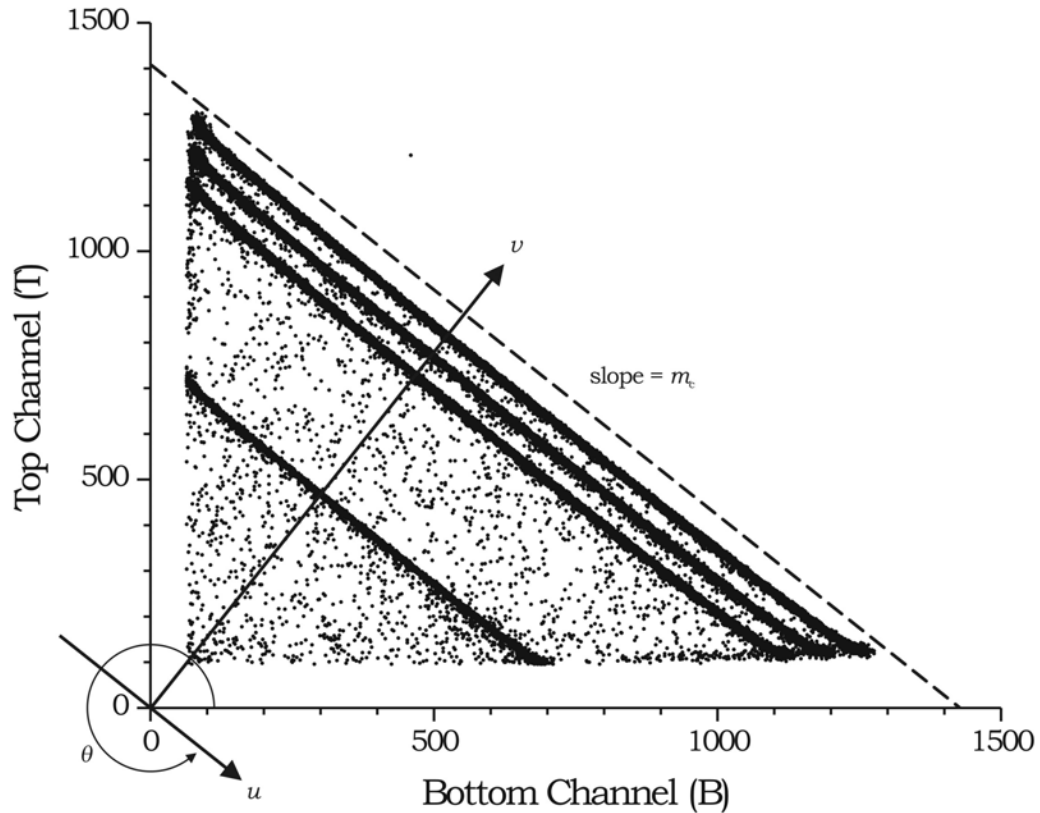


FIG. 2.4. Raw calibration data from focal plane strip 3, taken just before the  $^{271}\text{Ds}$  experiment described in Chapter three. Half of all events were randomly removed for clarity of presentation. The source of events is a four-peak source described in the main text. Rotation of the  $(B, T)$  coordinate system through the angle  $\theta$  gives the  $(u, v)$  coordinate system. A line with slope  $m_c$  is shown. See the main text for a discussion.

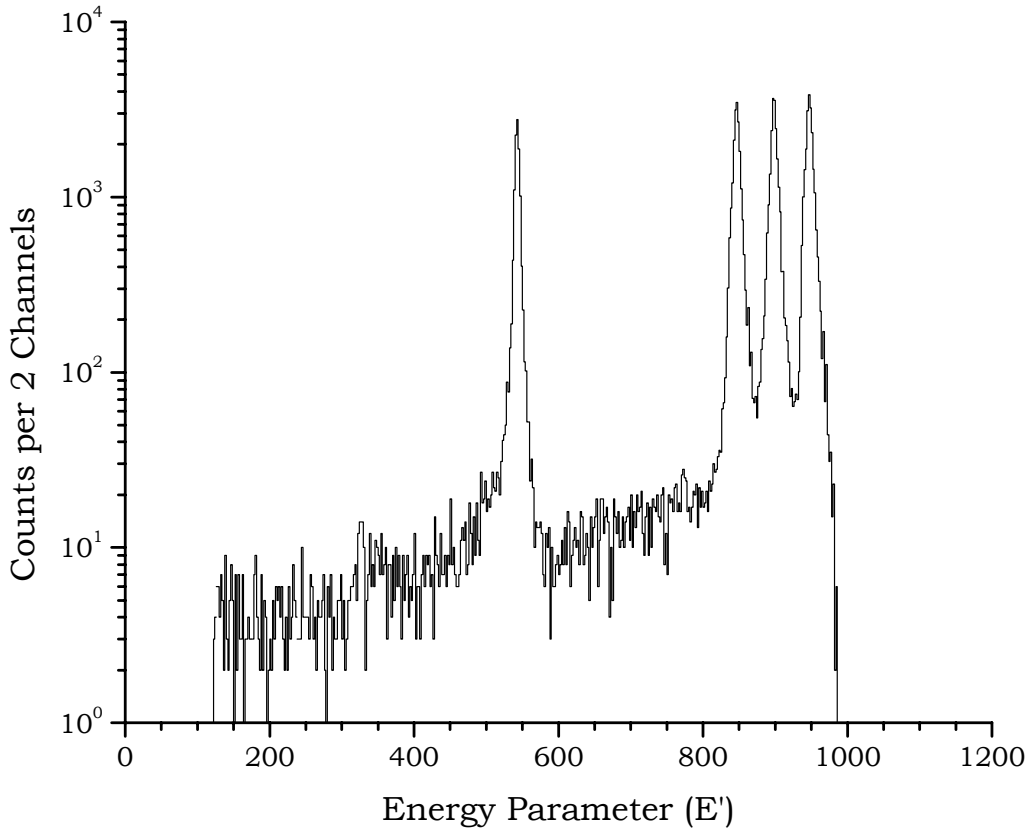


FIG. 2.5. Linear energy parameter spectrum for the data in Fig. 2.4 showing the four-peak source. This data comes from strip number 3 and was taken directly before the  $^{271}\text{Ds}$  experiments described in Chapter three. The optimized value of  $m_c$  used to produce the spectrum was -0.98854.

characterized by a “common slope”  $m_c$  that is a property of the strip. Note that  $|m_c|$  represents the ratio of gains in the top and bottom ADCs and that  $m_c < 0$ . Assume for now that  $m_c$  can be obtained by some means; a procedure to determine  $m_c$  will be described later. Once  $m_c$  is known  $\theta$  can be found by solving

$$\tan \theta = m_c, 3\pi/2 \leq \theta < 2\pi. \quad (2.13)$$

Once  $\theta$  is known, the conversion between the  $(B, T)$  and  $(u, v)$  coordinate systems is:

$$\begin{aligned} u &= T \sin \theta + B \cos \theta, \\ v &= T \cos \theta - B \sin \theta. \end{aligned} \tag{2.14}$$

Since  $\theta$  is known,  $\sin \theta$  and  $\cos \theta$  can be determined as a function of  $m_c$ :

$$\begin{aligned} \sin \theta &= \frac{-|m_c|}{\sqrt{m_c^2 + 1}} = \frac{m_c}{\sqrt{m_c^2 + 1}}, \quad m_c < 0, \\ \cos \theta &= \frac{1}{\sqrt{m_c^2 + 1}}. \end{aligned} \tag{2.15}$$

The explicit form of Eq. 2.14 is thus

$$\begin{aligned} u &= T \frac{m_c}{\sqrt{m_c^2 + 1}} + B \frac{1}{\sqrt{m_c^2 + 1}}, \\ E' = v &= T \frac{1}{\sqrt{m_c^2 + 1}} + B \frac{-m_c}{\sqrt{m_c^2 + 1}} \end{aligned} \tag{2.16}$$

where  $E'$  is the “energy parameter,” a number linearly proportional to energy. Figure 2.5 shows the  $E'$  spectrum for the raw data in Fig. 2.4. The peaks are found in the spectrum by initially setting a horizontal line at a threshold equal to the number of counts in the bin with most counts. This threshold is lowered and the number of peaks it intersects is counted at each step. Once it intersects the correct number of peaks (four), this threshold is recorded. The lowering continues until it no longer intersects four peaks (that is, has dropped into the noise), and this threshold is recorded. Finally, the threshold is raised to some preset level between the two recorded thresholds (usually the lower value plus 70% of their difference). This puts the threshold above any shoulders caused by branches with low intensity. A centroid is calculated for each peak using only those counts above the final threshold. It is then simple to do a linear regression of the true alpha energy versus the centroid locations. If  $m'_E$  and  $b'_E$  are the slope and intercept of this regression, respectively, then the alpha energy  $E$  as a linear function of  $E'$  is

$$E = m'_E E' + b'_E \quad (2.17)$$

The preceding discussion assumes that the common slope  $m_c$  has already been chosen. A simple procedure to determine  $m_c$  is to make an initial guess (usually -1) and produce an  $E'$  spectrum using Eq. 2.16. The peaks are found; each peak defines a separate gate for the data. A linear regression is performed on all data points in the  $(B, T)$  space that fall within the gate and the slopes are averaged. This average slope becomes the guess for  $m_c$  in the next iteration. The process continues until two successive guesses differ by less than some predefined limit. This algorithm tends to find the correct value in less than five to ten iterations as long as the initial guess is within  $\sim 15\%$  of the true value.

A close inspection of the data in Fig. 2.4 reveals that the “lines” formed by the alpha particles are not really lines at all but are slightly curved. This is likely due to the presence of charge-trapping sites caused by radiation damage from previous experiments. This damage is preferentially in the center of the detector and results in less charge collected at each end of the strip, smaller signals digitized by the ADC, and a data point closer to the origin. Let us assume that each “line” can be represented by a parabola of the form  $v = au^2 + bu + c$ . It is simple to show that the vertex of this parabola  $(u_0, v_0)$  is

$$(u_0, v_0) = (-b/[2a], c - b^2/[4a]). \quad (2.18)$$

Since all points on the parabola have the same alpha energy  $E_\alpha$ ,  $v_0$  can be used as the new parabolic energy parameter  $E''$ . Given a point  $(u, v)$  [represented in the data as  $(B, T)$ ], the energy parameter is found from

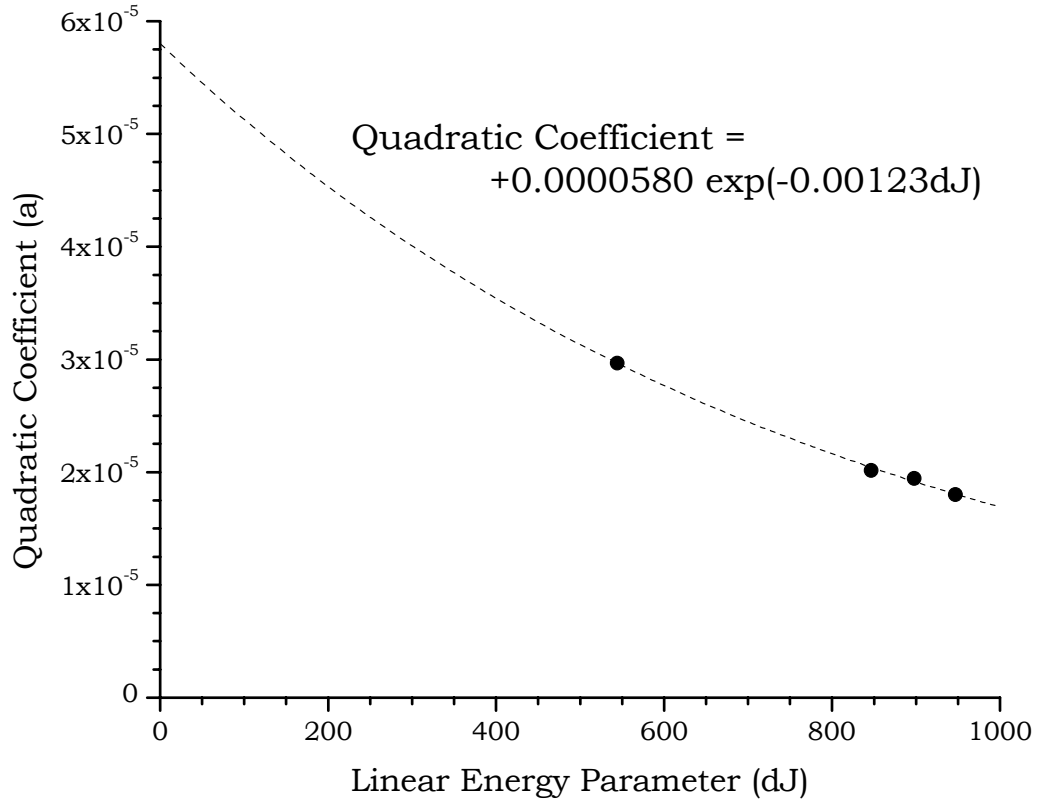


FIG. 2.6. Quadratic coefficients of the parabolic fits to raw calibration data in Fig. 2.4 as a function of the linear energy parameter  $dJ$ . Each point represents the data from a single calibration source. The fits were done in the  $(u, v)$  coordinate system. The dashed line is an exponential fit to the data shown, so that  $A = 0.0000580$  and  $C = -0.00123$ .

$$\begin{aligned}
 E'' = v_0 &= v - a(u - u_0)^2 \\
 &= \frac{T - m_c B}{\sqrt{m_c^2 + 1}} - a \left( \frac{Tm_c + B}{\sqrt{m_c^2 + 1}} - u_0 \right)^2 \\
 &= \frac{T - m_c B}{\sqrt{m_c^2 + 1}} + a \left[ - \left( \frac{Tm_c + B}{\sqrt{m_c^2 + 1}} \right)^2 + \frac{2u_0(Tm_c + B)}{\sqrt{m_c^2 + 1}} - u_0^2 \right]
 \end{aligned} \tag{2.19}$$

after Eq. 2.16 is applied. For convenience, define

$$J = T - m_c B, \tag{2.20a}$$

$$K = Tm_c + B \tag{2.20b}$$

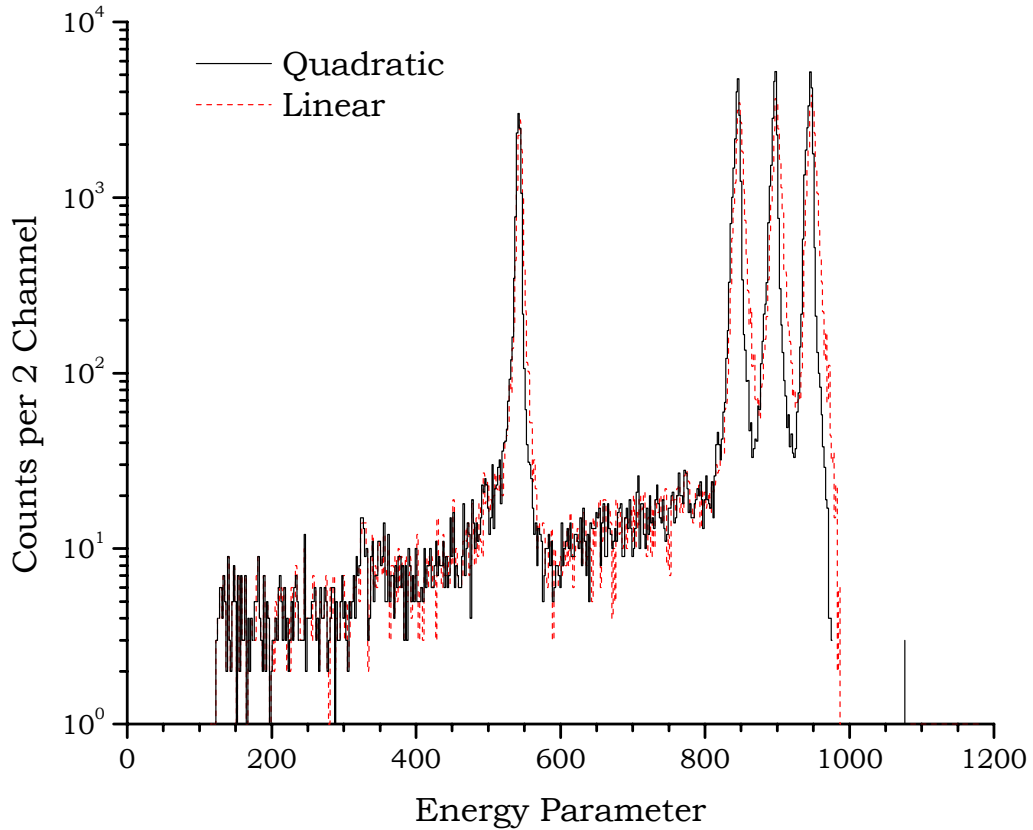


FIG. 2.7. Linear and quadratic energy parameters for raw calibration data in Fig. 2.4. The quadratic energy parameters were calculated using optimum values for  $e'$ ,  $f'$ ,  $g'$ , and  $C$ . Note the improvement in resolution resulting from the use of quadratic energy parameters instead of linear ones.

so that

$$E'' = dJ + a(eK^2 + fK + g), \quad (2.21)$$

where  $d = (m_c^2 + 1)^{-1/2}$ ,  $e = -(m_c^2 + 1)^{-1}$ ,  $f = 2u_0(m_c^2 + 1)^{-1/2}$ , and  $g = -u_0^2$ . Notice that  $dJ$  is the “linear” energy parameter  $E'$  defined in Eq. 2.16. Lastly,  $a$  must be defined. Examining Fig. 2.4 shows that, as alpha energy decreases to zero, the curvature of the corresponding parabola increases because the phase space of channel numbers is becoming smaller. The curvature of a parabola is defined by  $a$  so this was made a variable parameter in the

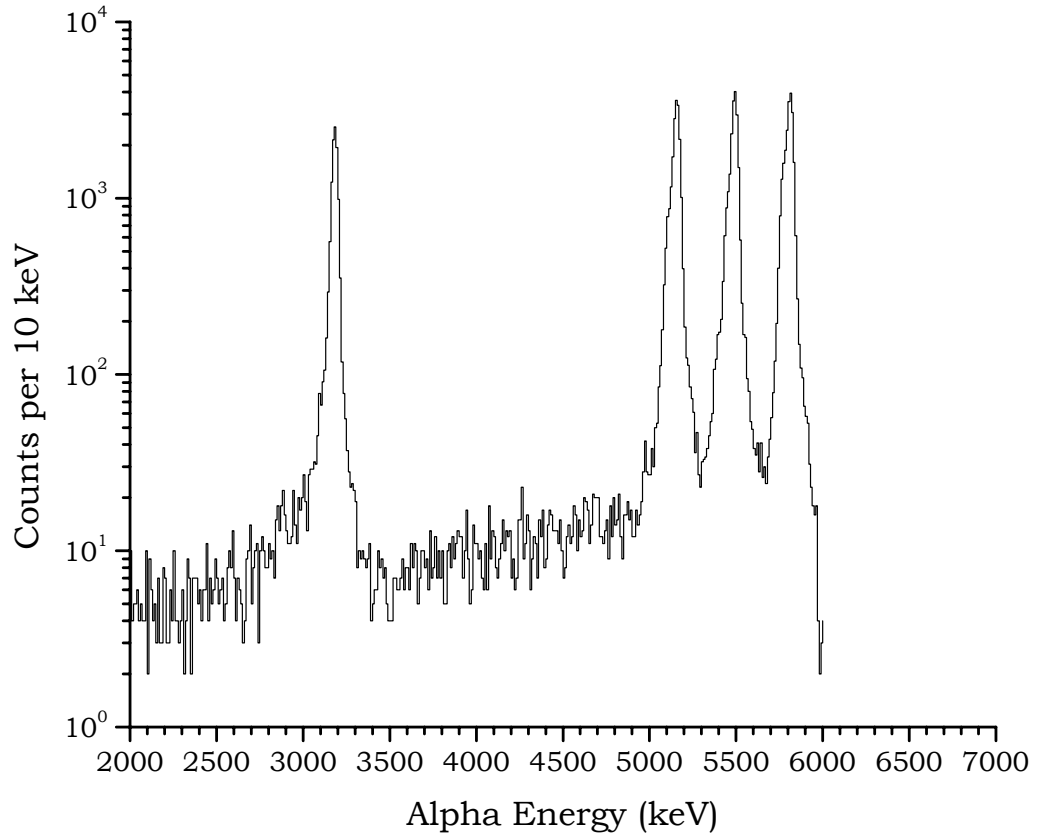


FIG. 2.8. Final alpha-energy spectrum produced for raw calibration data in Fig. 2.4 using optimized values for the constants in Eq. 2.24. From left to right, the alpha peaks are from  $^{148}\text{Gd}$ ,  $^{239}\text{Pu}$ ,  $^{241}\text{Am}$ , and  $^{244}\text{Cm}$ . The FWHM of each peak is  $\sim 40$  keV and the standard deviation is  $\sim 17$  keV.

calibration rather than a constant. Figure 2.6 shows  $\alpha$  as a function of  $dJ$  with an exponential fit to the data. A linear fit could have been used, but if  $dJ$  were sufficiently large then  $\alpha$  would be negative, causing the parabola to curve in the wrong direction. An exponential parameterization prevents this problem. Thus,  $\alpha$  is defined as

$$\alpha = A e^{C dJ}. \quad (2.22)$$

$A$  and  $C$  are obtained through regression. With this definition,  $E''$  can be rewritten (Eq. 2.21) as

$$\begin{aligned} E'' &= dJ + (eK^2 + fK + g)Ae^{CdJ} \\ &= dJ + (e'K^2 + f'K + g')e^{CdJ} \end{aligned} \quad (2.23)$$

where  $e' = eA = -A/(m_c^2 + 1)$ ,  $f' = fA = 2u_0A(m_c^2 + 1)^{-1/2}$ , and  $g' = gA = -Au_0^2$ . Figure 2.7 shows a comparison of the linear energy parameter  $E'$  spectrum and the quadratic energy parameter spectrum  $E''$ . Note the improvement in resolution obtained by adding the parabolic correction for the radiation damage.

As in Eq. 2.17, a standard linear calibration of the  $E''$  spectrum giving slope  $m_E''$  and intercept  $b_E''$  leads to the following parameterization of the energy  $E$ :

$$\begin{aligned} E &= m_E''E'' + b_E'' \\ &= m_E''[dJ + (e'K^2 + f'K + g')e^{+CdJ}] + b_E'' \\ &= (m_E''dJ + b_E'') + (m_E''e'K^2 + m_E''f'K + m_E''g')e^{+CdJ} \\ &= (DJ + I) + (EK^2 + FK + G)e^{-HJ}. \end{aligned} \quad (2.24)$$

The final line is the parameterization of the energy. The external calibration constants are

$$D = m_E''d = \frac{m_E''}{\sqrt{m_c^2 + 1}}, \quad (2.25a)$$

$$I = b_E'', \quad (2.25b)$$

$$E = m_E''e' = \frac{-m_E''A}{m_c^2 + 1}, \quad (2.25c)$$

$$F = m_E''f' = \frac{2m_E''Au_0}{\sqrt{m_c^2 + 1}}, \quad (2.25d)$$

$$G = m_E''g' = -m_E''Au_0^2, \quad (2.25e)$$

$$H = -Cd = \frac{-C}{\sqrt{m_c^2 + 1}}, \quad (2.25f)$$

$$J = T - m_cB, \quad (2.25g)$$

$$K = Tm_c + B. \quad (2.25h)$$

The final alpha-energy spectrum from this parameterization is shown in Fig. 2.8. The FWHM of each peak is  $\sim 40$  keV and the standard deviation is  $\sim 17$  keV. Note the shoulder in the  $^{239}\text{Pu}$  peak which can be assigned to the alpha emission line at 5105.5 keV (11.5% branch). The other major emission line (5144.3 keV, 15.1% branch) is not resolved and appears under the main peak at 5156.59 keV (73.3% branch). Small shoulders can be seen in the  $^{241}\text{Am}$  and  $^{244}\text{Cm}$  peaks which are due to the minor lines with energies 5442.80 keV (13.0% branch) and 5776.27 keV (23.6% branch), respectively. For comparison, note the more symmetric peak produced by monoenergetic  $^{148}\text{Gd}$  alpha particles with energy 3182.787 keV.

#### 2.4.2.2. Upstream Energy Calibration

Each upstream detector produces only one signal, so a plot of counts versus channel resembles Fig. 2.5. The peaks were found in this spectrum and the centroid of each peak calculated. A regression of the known alpha energies versus the centroids produced a simple linear calibration. Since no quadratic resolution sharpening could be done with only one signal, the FWHM of each was typically  $\sim 70$  keV with standard deviation  $\sim 30$  keV. In an actual experiment, alpha particles which escape from the front of the strip detectors can impinge on an upstream detector. The standard deviation in the energy of these “reconstructed” alpha particles was  $\sim 45$  keV.

#### 2.4.2.3. Strip Position Calibration

Positions within the strip detectors are measured using resistive charge division, so a charge-to-position calibration must be obtained. Using Eq. 2.12 as a guide, the observed position parameter  $P'_{obs}$  of a point  $(B, T)$  is defined as

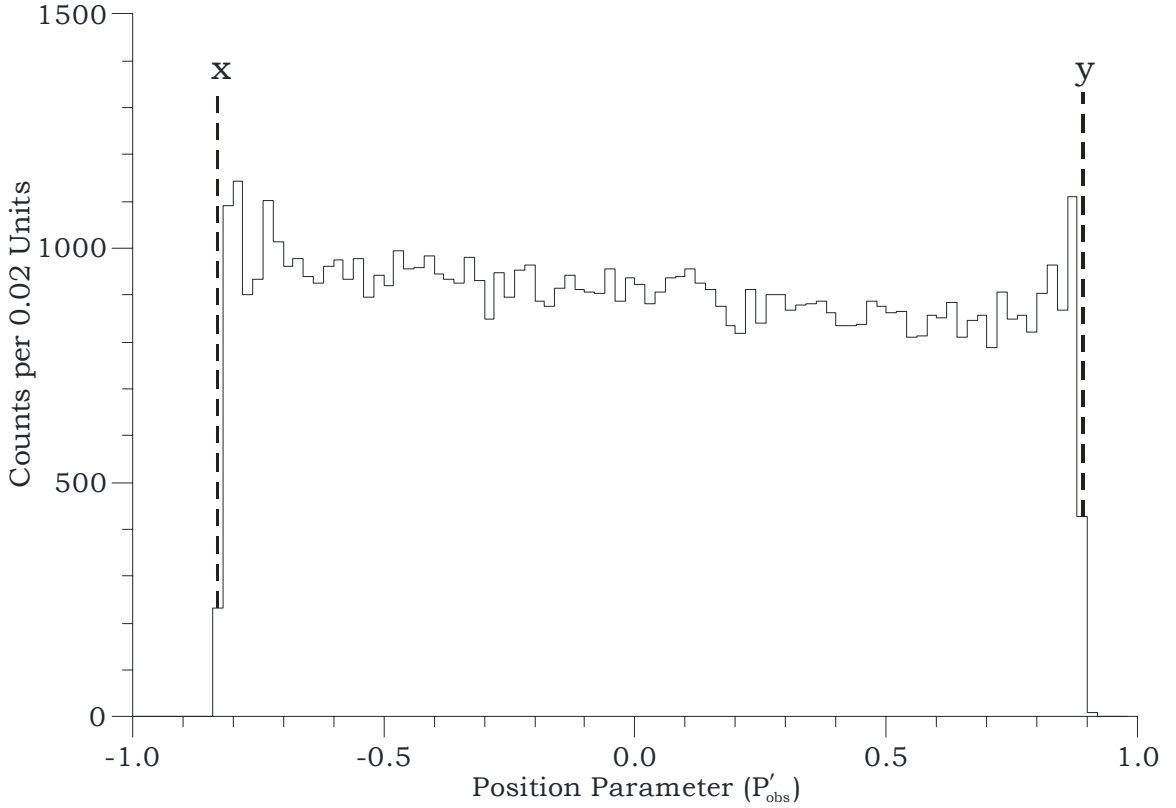


FIG. 2.9. Observed position parameters for raw calibration data in Fig. 2.4. Sample values for  $x$  and  $y$  are shown; see the main text for a discussion.

$$P'_{obs} = \frac{T + m_c B}{T - m_c B}. \quad (2.26)$$

The signs are reversed relative to Eq. 2.12 because  $m_c$  is defined to be negative. As with Eq. 2.12, this definition should give a spectrum that evenly spans the continuum from -1 to +1. In reality, this is not the case, as is shown in Fig. 2.9. This occurs because Eq. 2.12 assumes that an alpha particle emitted from the calibration source implanted at either end of the strip will see an infinite resistance to the other end of the strip. Thus, some data points should be observed with either the top or bottom channel equal to zero. As can be seen in Fig. 2.4, the parabolas do not completely reach either axis. Alpha particles are

emitted isotropically from the calibration source and will be implanted uniformly throughout the strip, so a correction must be applied to  $P'_{obs}$ .

In Fig. 2.9, two points labeled  $x$  and  $y$  are indicated. These are intended to represent the “limits” of the data as defined by some reasonable standard. Typically,  $x$  and  $y$  are chosen so that 0.5% of the distribution lies outside either end of  $[x, y]$  (1.0% total). Once  $x$  and  $y$  are chosen, the goal is to adjust the distribution so that it covers the range from -1 to +1. This is easily accomplished by recentering the distribution on zero (using an offset  $\tilde{x}$ ) and “stretching” it so that it fills the desired range (using a multiplier  $w$ ):

$$\tilde{x} = (x + y)/2, \quad (2.27a)$$

$$w = [1 - (-1)] / (y - x) = 2 / (y - x). \quad (2.27b)$$

The actual position parameter  $P'$  is defined as

$$\begin{aligned} P' &= w(P'_{obs} - \tilde{x}) \\ &= wP'_{obs} - w\tilde{x} \\ &= \frac{2}{y - x} P'_{obs} - \frac{2}{(y - x)} \frac{(x + y)}{2} \\ &= \frac{2}{y - x} P'_{obs} + \frac{x + y}{x - y} \\ &= RP'_{obs} + S, \end{aligned} \quad (2.28)$$

where the position calibration constants are

$$R = 2 / (y - x), \quad (2.29a)$$

$$S = (x + y) / (x - y). \quad (2.29b)$$

Once  $P'$  is known, the actual position  $P$  in mm is found by multiplying by the strip half-height (29 mm):

$$P = 29P' \text{ mm} \quad (2.30)$$

The algorithm described above for calibrating energy and position was implemented as a C language computer code. Combined with a program to read the binary data from disk,

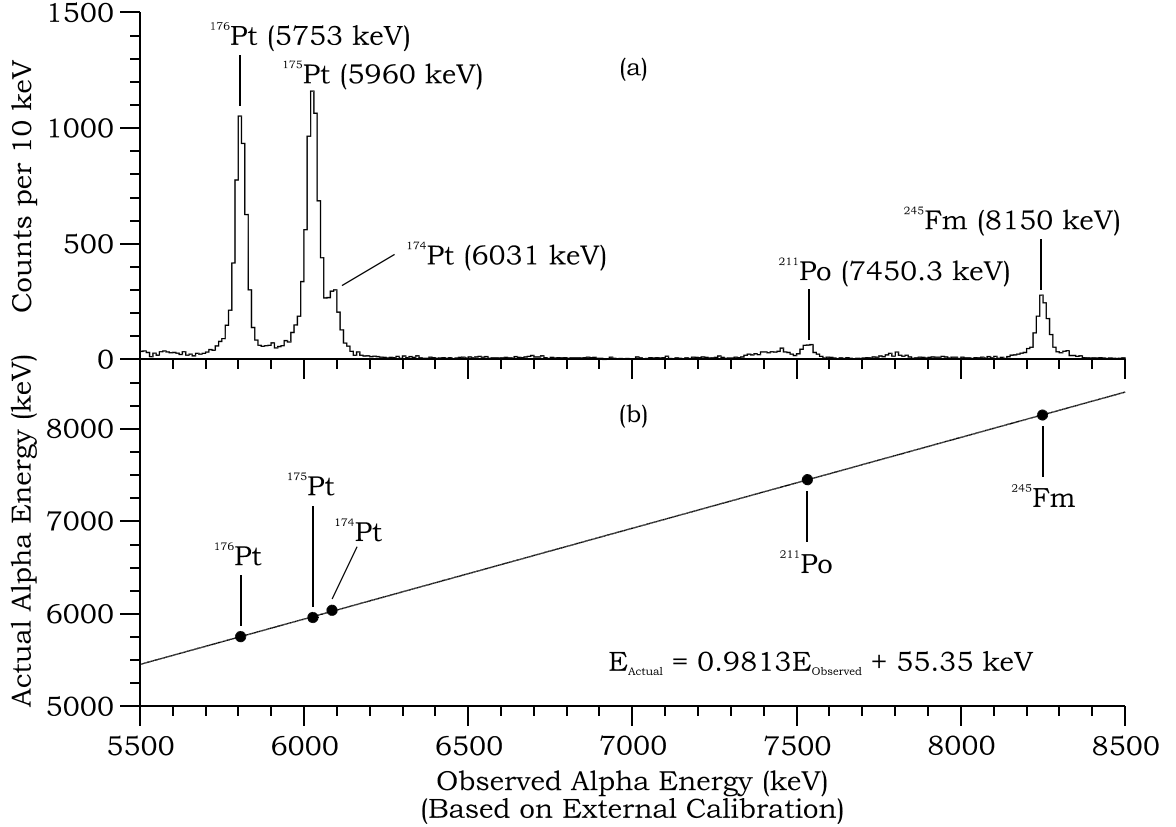


FIG. 2.10. External-to-internal calibration correction. (a) Sum spectrum showing alpha events from the  $^{116}\text{Sn}(^{64}\text{Ni}, xn)^{180-x}\text{Pt}$  ( $x = 4-6$ ) and  $^{208}\text{Pb}(^{40}\text{Ar}, 3n)^{245}\text{Fm}$  reactions with all 48 strip detectors combined. The abscissa represents the energy computed by using the external calibration of Eq. 2.24. Major peaks are labeled with the true alpha decay energy in parentheses (data taken from [Firestone1996]). (b) Plot of true energy versus observed energy for the spectrum in part (a). A linear fit to the data is shown.

this code performs all the steps necessary to calculate the energy calibration constants  $m$ ,  $D$ ,  $I$ ,  $E$ ,  $F$ ,  $G$ , and  $H$ ; and the position calibration constants  $R$  and  $S$ . This code produced separate constants for each strip which were saved in a new file for each experiment.

#### 2.4.3. Internal Calibration Data: Test Reactions

Even though external alpha-particle sources have been used for a preliminary calibration, the calibration is not yet complete. The reason is that the alpha-particle

sources are *external* to the strip detectors, whereas EVRs and their decay products are *implanted* in the detectors. Although we are interested in alpha-particle energies, the preliminary calibration described in the previous section gives the *total* energy deposited, which may include the energy of the recoiling daughter nucleus and any gamma rays or conversion electrons produced at the same time. A final correction is required.

This correction is obtained from test reaction data. At the beginning of each experiment, a small amount of beam time is devoted to ensuring that the MWPC, detectors, and electronics function properly. Using the same beam as in the primary experiment, a lighter target with a higher cross section is used to produce alpha-decaying EVRs which are implanted in the strip detectors. In the  $^{271}\text{Ds}$  experiment the test reaction was  $^{116}\text{Sn}(^{64}\text{Ni}, xn)^{180-\text{x}}\text{Pt}$  ( $x = 4-6$ ), which produces neutron-deficient platinum isotopes. Additionally, the  $^{208}\text{Pb}(^{40}\text{Ar}, 3n)^{245}\text{Fm}$  reaction was used as a test at the end of the experiment.  $^{245}\text{Fm}$  has a high-energy alpha decay (8150 keV [Nurmia1967, Münzenberg1981b]) which “anchors” the calibration at higher energies.  $^{211}\text{Po}$  was also produced as a transfer reaction product. Figure 2.10a shows the alpha sum spectrum from all 48 strips of these experiments with the important peaks labeled. Figure 2.10b shows a linear fit of the true alpha-decay energies to the observed energies computed from the external calibration. As expected, the slope of this line is less than 1, since more energy is deposited than can be attributed to alpha decay alone. This slope and intercept are folded into Eq. 2.24 to give the final low-energy calibration.

#### 2.4.4. High-Energy Calibrations

The BGS data acquisition system uses CAEN N568B amplifiers for signal processing and these provide both high- and low-gain outputs. (The data acquisition system is

described in more detail in Sec. 2.5). Both outputs are digitized and recorded to the data stream to give separate low- and high-energy signals. Any event with energy greater than 20-40 MeV, depending on position, will saturate either or both of the top and bottom low-energy outputs, so the high-energy signals must be used to determine the energy and position of the event.

Once the low-energy calibrations have been established using the algorithms described in Sec. 2.4.2.1-2.4.2.3, the procedure for calibrating the high-energy branches is straightforward. In short, the high-energy calibration program takes a set of experimental data (not calibration source data) and looks for events that have both low- and high-energy signals present, with the additional requirement that neither low-energy signal be saturated. These data may consist of implantation events, fission events, or pile-up alpha events. If  $T_H$  and  $B_H$  are the respective top and bottom channel numbers from the high-energy ADC outputs define

$$J_H = T_H - m_c B_H. \quad (2.31)$$

This definition is the high-energy analog to Eq. 2.20a. The true energy of the event is calculated using the low-energy channels  $T$  and  $B$  and a linear regression of this energy versus  $J_H$  is performed, with an appropriate minimum energy used as a gate to eliminate nonlinearities in the ADC that may be present at low energies. If  $D_H$  and  $I_H$  are the slope and intercept of this regression, then the high energy  $E_H$  is

$$E_H = D_H J_H + I_H. \quad (2.32)$$

Upstream detectors also have a high-energy output. Since only one high-energy signal is recorded, the calibration can be done simply by regression of true energy (determined from the low-energy branch) versus high-energy channel. As with the strip detectors, only

events with above-threshold high-energy signals and non-saturated low-energy signals above a minimum energy are included in the regression.

The position calibration for high-energy strip events is also straightforward. The observed high energy position parameter  $P'_{H,obs}$  is defined similarly to its low-energy counterpart (Eq. 2.26):

$$P'_{H,obs} = \frac{T_H - m_c B_H}{T_H + m_c B_H}. \quad (2.33)$$

Gating on events with energy above a specified threshold, the  $P'_{H,obs}$  spectrum is analyzed to give  $x_H$  and  $y_H$ , the high-energy analogs of  $x$  and  $y$  (see Fig. 2.9). The slope  $R_H$  and intercept  $S_H$  are computed using a derivation analogous to Eq. 2.28-2.30. The event's high-energy position parameter  $P'_H$  and true position  $P_H$  are then

$$P'_H = R_H P'_{H,obs} + S_H, \quad (2.34a)$$

$$P_H = 29 P'_H \text{ mm}. \quad (2.34b)$$

## 2.5. Data Acquisition

The data acquisition system used by the BGS is not complex. The initial signal produced in a detector enters a standard preamplifier and is transmitted to the BGS data acquisition system. The signal enters a CAEN N568B amplifier and a “fast out” signal is sent to an MSU 1806 constant fraction discriminator (CFD). If the signal is above an appropriate threshold, the CFD triggers a data readout by sending a signal to a trigger module developed by the data acquisition group at GSI [Essel1992]. The minimum time allowed between events is 11  $\mu\text{s}$ , although if two signals are separated by less than this time they can be stored as two separate “subevents.”

Shortly after these actions, the N568B amplifier sends its processed “slow out” signals (low- and high-energy) to CAEN V785 ADCs for digitization. Although the gain for high-energy events is variable, the N568B fixes the gain ratio between high-gain and low-gain signals at 10. If the trigger module has received a trigger signal, the ADCs will digitize any signals above threshold.

Readout of the ADCs is controlled by the Multi-Branch System (MBS) program developed at GSI [Essel1996, Essel2000]. The MBS also handles readouts of scalars and bit registers associated with the experiment. The MBS runs on a RIO2 computer located in a VME crate which also contains the ADCs. This computer runs the LynxOS operating system which is designed for real-time performance with virtually no delay. The MBS also handles the writing of data to disk for later analysis, and user input such as instructions to start and stop data acquisition. Each signal is assigned a parameter number, which is written to disk along the channel produced from the ADC.

The MBS can also be programmed to do an online correlation search for possible heavy element decay chains. If a series of events is observed which matches predefined criteria based on the decay properties of the isotopes of interest, the beam can be shutoff quickly ( $\sim 140 \mu\text{s}$ ) so that the remainder of the chain can be observed in an environment with lower background. The shutoff parameters used are described with each experiment in the following Chapters. To reduce the processing time required for the shutoff analysis, only implantation events, alpha particles fully stopped in the strip detectors, and fission events are included in the search.

### 3. Production of $^{271}\text{Ds}$ in the $^{208}\text{Pb}(^{64}\text{Ni}, \text{n})$ Reaction

#### 3.1. Previous Work

##### 3.1.1. GSI Experiments

Element 110 (darmstadtium, Ds) was discovered as the isotope  $^{269}\text{Ds}$  in the reaction  $^{208}\text{Pb}(^{62}\text{Ni}, \text{n})$  at the Gesellschaft für Schwerionenforschung (GSI) in Darmstadt, Hessen, Germany by Hofmann *et al.* [Hofmann1995a, Hofmann1995c, Hofmann2002] using SHIP. This discussion is concerned primarily with  $^{271}\text{Ds}$ , which was discovered in 1998 by Hofmann *et al.* [Hofmann1998] in the  $^{208}\text{Pb}(^{64}\text{Ni}, \text{n})$  reaction. The initial  $^{271}\text{Ds}$  discovery experiment measured an excitation function for the production of this nuclide at five energies; the results are summarized in Fig. 3.1 and 3.2 and Table 3.1. Altogether, nine decay chains of  $^{271}\text{Ds}$  were observed in these initial experiments. Later experiments in 2000 [Hofmann2001, Hofmann2002, Hofmann2003] produced another four decay chains, bringing the total to thirteen.

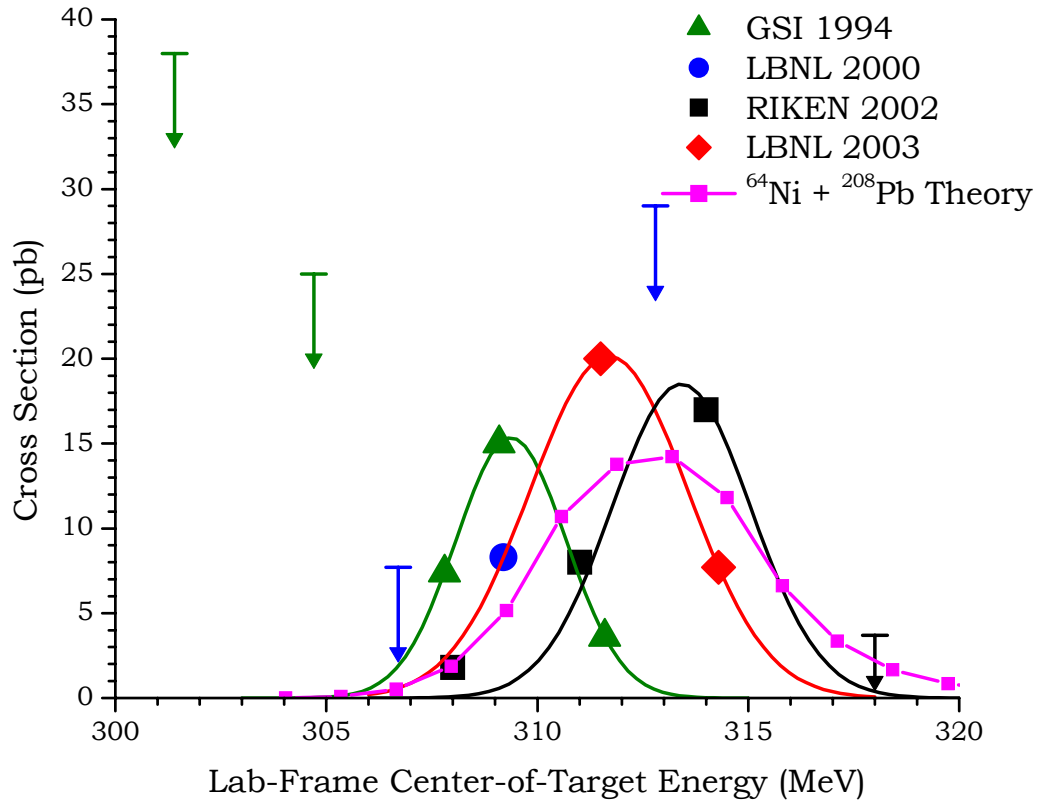


FIG. 3.1. Cross sections for the  $^{208}\text{Pb}(^{64}\text{Ni}, \text{n})^{271}\text{Ds}$  reaction obtained at three laboratories. Error bars have been removed for clarity; see Fig. 3.2. Data comes from [Hofmann1998, Ginter2003, Morita2004d] and this work. Upper limit cross sections are shown by arrows; from left to right, the first two are GSI data, the next two are LBNL data, and the final one is from RIKEN. Gaussian fits to each laboratory's data are shown. The smaller squares connected by lines are theoretical predictions for the reaction [Świątecki2004a] with a 4 MeV target thickness folded in.

In these experiments,  $^{271}\text{Ds}$  was found to decay by emission of  $(10738 \pm 20)-keV alpha particles with a ground state half-life of  $1.1^{+0.6}_{-0.3}$  ms (later refined by Morita *et al.* [Morita2004d] to  $1.63^{+0.44}_{-0.28}$  ms). Also observed was an isomer [Hofmann1998] with a half-life now estimated as  $69^{+56}_{-21}$  ms. This isomeric state decayed by the emission of  $(10709 \pm 20)-keV alpha particles. Morita *et al.* [Morita2004d] have postulated, due to the similar$$

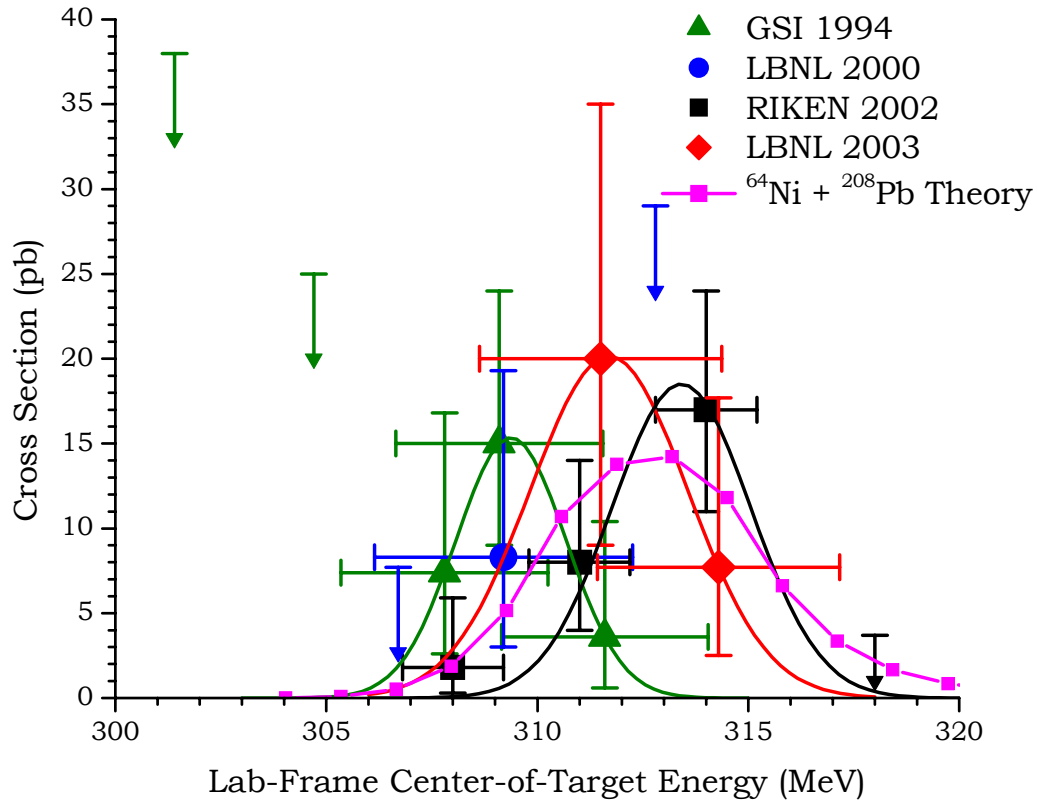


FIG. 3.2. Same as Fig. 3.1 except that error bars have been included. Vertical error bars represent  $1\sigma$  error limits in the cross section of the  $^{208}\text{Pb}({}^{64}\text{Ni}, \text{n})^{271}\text{Ds}$  reaction and horizontal error bars represent the range of energies covered by the beam as it passes through the target.

alpha decay energies of the isomer and ground state, that the isomer actually decays by gamma-ray emission and/or internal conversion to the shorter-lived ground state. It is also possible that the isomer decays by alpha emission to an analog state in the daughter nucleus  $^{267}\text{Hs}$  with a similar excitation energy. So far, no experiments have completely characterized the decay of this  $^{271}\text{Ds}^m$  isomer although it is observed in  $\sim 20\%$  of all  $^{271}\text{Ds}$  decay chains (five isomeric decays of twenty-nine total). Neither the isomer nor the ground state was observed to decay by electron capture.

TABLE 3.1. Cross sections for the  $^{208}\text{Pb}(^{64}\text{Ni}, \text{n})^{271}\text{Ds}$  reaction measured at three different laboratories.  $E_{\text{tot}}$  is the lab-frame beam energy at the center of the target. These data are presented graphically in Fig. 3.1 and 3.2.

Laboratory and Reference	$E_{\text{tot}}$ (MeV)	Target Thickness (mg/cm <sup>2</sup> )	Dose (10 <sup>17</sup> )	Decay Chains Observed	Cross Section (pb)
GSI	301.4	0.45	0.9	0	<38
	304.7	0.45	1.5	0	<25
	307.8	0.45	5.3	2	7.4 <sup>+9.4</sup> <sub>-4.8</sub>
	309.1	0.45	7.8 <sup>a</sup>	6 <sup>a</sup>	15 <sup>+9</sup> <sub>-6</sub>
	311.6	0.45	5.5	1	3.6 <sup>+6.8</sup> <sub>-3.0</sub>
LBNL	306.7	0.50	2.7	0	<7.7
	309.2	0.50	2.7	2	8.3 <sup>+11</sup> <sub>-5.3</sub>
	312.8	0.31	1.1	0	<29
RIKEN	308	0.23	10.0	1	1.8 <sup>+4.1</sup> <sub>-1.5</sub>
	311	0.23	9.5	4	8.0 <sup>+6.0</sup> <sub>-4.0</sub>
	314	0.22	10.7	9	17 <sup>+7</sup> <sub>-6</sub>
	318	0.21	10.1	0	<3.7
LBNL	311.5	0.47	2.3	5 <sup>b</sup>	7.7 <sup>+10</sup> <sub>-5.2</sub>
	[This work.]	314.3	0.47	2	20 <sup>+15</sup> <sub>-11</sub>

<sup>a</sup> Excludes three decay chains observed during preparations for another experiment [Hofmann2002] and one decay chain observed in the irradiation of  $^{64}\text{Ni}$  projectiles onto a  $^{207}\text{Pb}$  target containing 5.5%  $^{208}\text{Pb}$  [Hofmann2001]. In both cases the dose was not specified.

<sup>b</sup> Includes one event (this work, chain 3) which is not included in the cross section (see main text for a discussion).

In the discovery experiments, alpha decay of  $^{271}\text{Ds}$  produced the new daughter nucleus  $^{267}\text{Hs}$ . Hofmann's group observed three alpha groups in the decay of  $^{267}\text{Hs}$ , with a combined half-life of  $59^{+30}_{-15}$  ms (additional data from Morita *et al.* [below] revised this figure to  $52^{+13}_{-8}$  ms [Morita2004d]). These data are consistent with other data obtained in the reported direct production of  $^{267}\text{Hs}$  in the  $^{238}\text{U}(^{34}\text{S}, 5\text{n})$  reaction ( $t_{1/2} = 19^{+29}_{-10}$  ms,  $E_{\alpha} =$

9740-9870 keV) [Lazarev1995], even though it appears possible that the number of random correlations observed in this experiment is significantly larger than their estimates.

The  $^{267}\text{Hs}$  alpha decay daughter  $^{263}\text{Sg}$  was known at the time [Ghiorso1974, Gregorich1994] to decay by the emission of  $9060 \pm 40$  keV alpha particles with a half-life of  $900 \pm 200$  ms. The Hofmann group observed alpha decay of  $^{263}\text{Sg}$  but with an energy of  $9248 \pm 20$  keV and a half-life of  $310_{-80}^{+160}$  ms. These decays are now assigned to an isomeric state ( $^{263}\text{Sg}^m$ ). In the 2000 experiments, one decay of  $^{263}\text{Sg}$  was observed with a lifetime and decay energy consistent with  $^{263}\text{Sg}^g$ . As with  $^{271}\text{Ds}$ , electron capture decay was not observed in the decay of either  $^{267}\text{Hs}$  or  $^{263}\text{Sg}$ . This is not surprising given the high neutron deficiency of the nuclides produced by cold fusion reactions with Pb and Bi targets; large Q-values for electron capture are offset by the even larger Q-values for alpha decay.

The assignment of the evaporation residue (EVR) to  $^{271}\text{Ds}$  was significantly strengthened by the fact that, after three consecutive alpha decays, the known nucleus  $^{259}\text{Rf}$  ( $t_{1/2} = 3.1 \pm 0.7$  s [Bemis1981]) was produced and its decays conclusively identified. This nucleus has small spontaneous fission and electron capture branches ( $0.063 \pm 0.037$  [Bemis1981] and  $\sim 0.003$  [Firestone1996], respectively) and decays primarily by alpha emission to  $^{255}\text{No}$ . Twelve decays were consistent with known  $^{259}\text{Rf}$  alpha decay properties. Hofmann *et al.* inferred the decay of one atom of  $^{259}\text{Rf}$  by electron capture and observed none decaying by spontaneous fission. The alpha decay daughter  $^{255}\text{No}$  ( $t_{1/2} = 3.1 \pm 0.2$  min [Firestone1996]) has a large electron capture branch (38.6%) and a complex alpha decay spectrum with numerous lines. Several  $^{255}\text{No}$  alpha decays were observed and several other electron capture decays inferred.

These data combined to give strong information on the decay of  $^{271}\text{Ds}$ . The maximum production cross section obtained at GSI in the  $^{208}\text{Pb}(^{64}\text{Ni}, \text{n})^{271}\text{Ds}$  reaction was  $15^{+9}_{-6}$  pb, obtained at a lab frame, center-of-target energy  $E_{\text{tot}}$  of 309.1 MeV.

### 3.1.2. First LBNL Experiments

The element 110 discoveries made by Hofmann *et al.* were not confirmed by an independent group for several years. During that time, other isotopes of darmstadtium were discovered, but still none were confirmed independently. The first confirmation of the discovery of an isotope of darmstadtium was performed by Ginter *et al.* in 2000 and published in 2003 [Ginter2003]. These experiments were carried out at the Lawrence Berkeley National Laboratory (LBNL, Berkeley, California, USA) 88-Inch Cyclotron using the Berkeley Gas-filled Separator (BGS), the same facilities and equipment used in the current work. However, it should be noted that the BGS main focal plane detector consisted of only 32 strips compared to 48 now, the upstream detectors were located only above and below the strips compared to all four sides now, and a different approach was used to measure the position of events occurring in the focal plane.

Using the results from GSI as a guide, Ginter and coworkers attempted to measure an excitation function for the  $^{208}\text{Pb}(^{64}\text{Ni}, \text{n})^{271}\text{Ds}$  reaction. Although they succeeded only in measuring upper limit cross sections of  $<7.7$  pb at  $E_{\text{tot}} = 306.7$  MeV and  $<29$  pb at  $E_{\text{tot}} = 312.8$  MeV, they did observe two  $^{271}\text{Ds}$  decay chains at  $E_{\text{tot}} = 309.2$  MeV giving a cross section of  $8.3^{+11}_{-5.3}$  pb. The first chain consisted of an implantation event followed by three high-energy alpha particles recorded with full energy in the focal plane. These three alpha particles matched very well the energies and half-lives of  $^{271}\text{Ds}^g$ ,  $^{267}\text{Hs}$ , and  $^{263}\text{Sg}^m$  measured by the GSI group. A fourth alpha particle escaped from the focal plane with a lifetime

consistent with the half-life of  $^{259}\text{Rf}$ . The second decay chain observed consisted of an implantation event and five alpha particles, three of which escaped from the detector. The other two could be assigned to  $^{267}\text{Hs}$  and  $^{255}\text{No}$ . Neither decay chain gave evidence of the  $^{271}\text{Ds}$  isomer, although this is not surprising since only two decay chains were observed and the isomer production ratio is roughly 20%. The BGS had been set for an estimated magnetic rigidity of 2.10 T m based on [Ghiorso1988], but the two decays chains were observed at an average rigidity of 2.07 T m. These two decay chains confirmed the discovery of element 110.

### *3.1.3. RIKEN Experiments*

In 2002, a group at RIKEN (the Institute of Physical and Chemical Research, Wako, Saitama, Japan) began a new study of the  $^{208}\text{Pb}(^{64}\text{Ni}, \text{n})^{271}\text{Ds}$  reaction using the upgraded Gas-filled Recoil Ion Separator (GARIS) [Morita2004e]. The purpose of these experiments was to prepare for the much more difficult experiments on the production of elements 111, 112, and 113 in cold fusion reactions. Over the course of several irradiations, fourteen decay chains attributed to  $^{271}\text{Ds}$  were observed at four different beam energies [Morita2004d, Morita2004c, Morita2003, Morita2002]. The cross sections measured at the three lower energies constitute a portion of an excitation function, while at the fourth (and highest) energy only an upper limit cross section could be measured.

In general, the data obtained by this group showed good agreement with the data obtained by the GSI and LBNL groups, although larger spreads in energy among the nuclides under study were observed because of lower energy resolution in the detectors. The presence of the  $^{271}\text{Ds}$  isomer was confirmed. Combining the GSI, LBNL, and RIKEN results, the isomer was produced in five of twenty-nine total chains ( $\sim 20\%$ ).

Morita's group also suggested the possibility of an isomer in  $^{267}\text{Hs}$  based on the observation of a single long-lived event. The lifetime of this event was 1158.6 ms, compared to the known  $^{267}\text{Hs}$  half-life of  $52_{-8}^{+13}$  ms. The parent of this long-lived  $^{267}\text{Hs}$  was a  $^{271}\text{Ds}$  isomer event, and the daughter event was an unusually long-lived  $^{263}\text{Sg}$  event (5998.9 ms). The nature of this possible  $^{267}\text{Hs}$  isomer requires further study.

### 3.1.4. Rationale for the New Experiments

With all the data already obtained by the GSI, LBNL, and RIKEN groups, why was it necessary to conduct another experiment to study the  $^{208}\text{Pb}(\text{Ni}, \text{n})^{271}\text{Ds}$  reaction? Most importantly, we wanted to use this reaction as a stepping stone to a more difficult experiment on the production of  $^{272}\text{111}$  in the  $^{208}\text{Pb}(\text{Cu}, \text{n})$  reaction (described in detail in Chapter 4). Although Ginter *et al.* had observed two decay chains of  $^{271}\text{Ds}$  (see Sec. 3.1.2), a complete excitation function was not measured. This was necessary to establish the energy calibration of the LBNL 88-Inch Cyclotron relative to other accelerators and to aid in estimating the optimum beam energy for the  $^{272}\text{111}$  experiment. Given the narrow excitation functions seen in reactions of this type, any mistake in choosing the beam energy could prevent observation of decay chains of interest. Additionally, these new experiments would allow for a more accurate determination of the operating parameters of the BGS using a relatively high cross section reaction (peak cross section 15-20 pb). This information is important for future searches for new isotopes and elements.

## 3.2. Experimental Conditions

Two experiments on the production of  $^{271}\text{Ds}$  in the  $^{208}\text{Pb}(\text{Ni}, \text{n})$  reaction were conducted. These experiments will be identified by the lab-frame beam energy at the

center of the target ( $E_{\text{tot}}$ ). An important question was what beam energy to use, and the answer came mostly by examining Fig. 3.1. Ginter *et al.* [Ginter2003], working at LBNL, observed two events at the center-of-target energy where the GSI group had observed its peak cross section ( $E_{\text{tot}} = 309.2$  MeV). After Ginter and coworkers' experiments but before the current work, the RIKEN group observed its maximum cross section at an energy several MeV higher ( $E_{\text{tot}} = 314.1$  MeV). We decided that our first experiment should be conducted at nearly the same energy as the maximum of the RIKEN excitation function because of the large number of events they had observed (nine) at that energy. It also appeared that the excitation function measured by the GSI group was narrower than one would expect for this reaction; the small cross section measured at their highest energy ( $E_{\text{tot}} = 311.6$  MeV) was likely due to statistical fluctuations.

### 3.2.1. $^{271}\text{Ds}$ Production Experiment: $E_{\text{tot}} = 314.3$ MeV

The LBNL 88-Inch Cyclotron produced a beam of  $^{64}\text{Ni}^{14+}$  with an energy of 319.75 MeV. After energy losses in the entrance window, target backing, and first half of the target (calculated using the SRIM-2003 computer program [Ziegler2003]), the desired energy  $E_{\text{tot}} = 314.3$  MeV was obtained. (See Sec. 2.1 for a discussion of the targets). The average beam current on-target was  $\sim 215$  pnA. The total beam energy loss in the thin  $^{208}\text{Pb}$  targets was estimated to be 5.6 MeV. The excitation energy in compound nuclei formed in the center of the targets  $E_{\text{tot}}^*$  was estimated to be 16.2 MeV using masses from [Myers1994].

Additionally, the magnetic rigidity setting of the separator had to be chosen. Ginter *et al.* had estimated a magnetic rigidity  $B\rho$  or 2.10 T m for this reaction using information in [Ghiorso1988]. The two events observed were in strips 19 and 27 of the old 32-strip

detector, corresponding to an average magnetic rigidity of  $\sim 2.07$  T m. Yet with only two events, the statistical significance of this result is low, so it was decided to use the magnetic rigidity observed by the RIKEN group (2.04 T m [Morita2002]). The magnetic rigidity of the BGS was set to 2.04 T m using magnet currents of  $Q1 = 1552$  A,  $M1 = 347$  A, and  $M2 = 587$  A.

The He gas pressure inside the BGS was 0.9 torr. The energy loss of  $^{271}\text{Ds}$  EVRs traversing this gas should be on the order of 8 MeV. A multi-wire proportional counter (MWPC) was placed upstream of the focal plane to provide discrimination of implantation events from radioactive decays. Due to the two Mylar windows containing the MWPC's isobutane gas, the total energy loss of the EVRs in the MWPC was estimated to be 19 MeV. The implantation energy of the EVRs in the Si strip detectors was expected to be  $\sim 47$  MeV, resulting in an implantation depth of  $\sim 6$   $\mu\text{m}$ . After correcting for an estimated pulse-height defect of  $\sim 45\%$  of implantation energy [Moulton1978], the observed implantation pulse-height should correspond to approximately 26 MeV.

A fast beam shutoff algorithm was also in place within the data acquisition program to search for the beginning of a possible heavy element decay chain and to shut off the beam within  $\sim 140$   $\mu\text{s}$  if one were detected. In order to reduce processing time, only implantation events, fully stopped alpha particles, and fission events were included in the search. The shutoff had two separate searches, one called EVR- $\alpha$  and the other called EVR- $\alpha$ - $\alpha$ . The EVR- $\alpha$  gate searched for correlations between implantation events with energies 15-30 MeV and alpha particle events with energy 8500-12000 keV. (After the first decay chain's implantation event produced an observed pulse height of 28.46 MeV, the EVR energy window was expanded to 15-35 MeV). The maximum correlation time was 3.0 s and the maximum allowable position difference was 3.5 mm. The detection of a

correlation satisfying these criteria initiated the EVR- $\alpha$  beam shutoff for 15 s. While in EVR- $\alpha$  shutoff mode, the EVR- $\alpha$ - $\alpha$  gate looked for additional alpha particles correlated to the original EVR. If another was found in the energy range 8200-12000 keV, the system could extend the shutoff for up to 900 additional seconds. Either gate could shut off the beam; that is, the time windows could overlap. In total, eleven short 15-s shutoffs and two long 900-s shutoffs were initiated. The total time with the beam off was approximately 1967 s (0.9% of the total run time).

This first experiment was BGS run 065. Fourteen eight-hour shifts were available for this experiment. After beam tuning, short test runs using the  $^{64}\text{Ni}$  beam with separate stationary targets of  $^{116}\text{Sn}$  and  $^{120}\text{Sn}$  were conducted for calibration purposes and to check the performance of the data acquisition system. Excluding time lost during window breakages, accelerator problems, and brief breaks to backup data, the total beam-on-target time was  $\sim$ 60 h (2.5 d). During this time, a total dose of  $2.9 \times 10^{17} \text{ }^{64}\text{Ni}$  projectiles was collected. The average count rate of all events in the focal plane detectors was  $7.0 \text{ s}^{-1}$ . After vetoing events coincident with the MWPC or punch-through detectors, the count rate of alpha particles in the strip detectors above 500 keV was  $1.3 \text{ s}^{-1}$ .

In this experiment, two decays chains attributed to  $^{271}\text{Ds}$  were observed (see Fig. 3.3) and are described in Sec. 3.3.

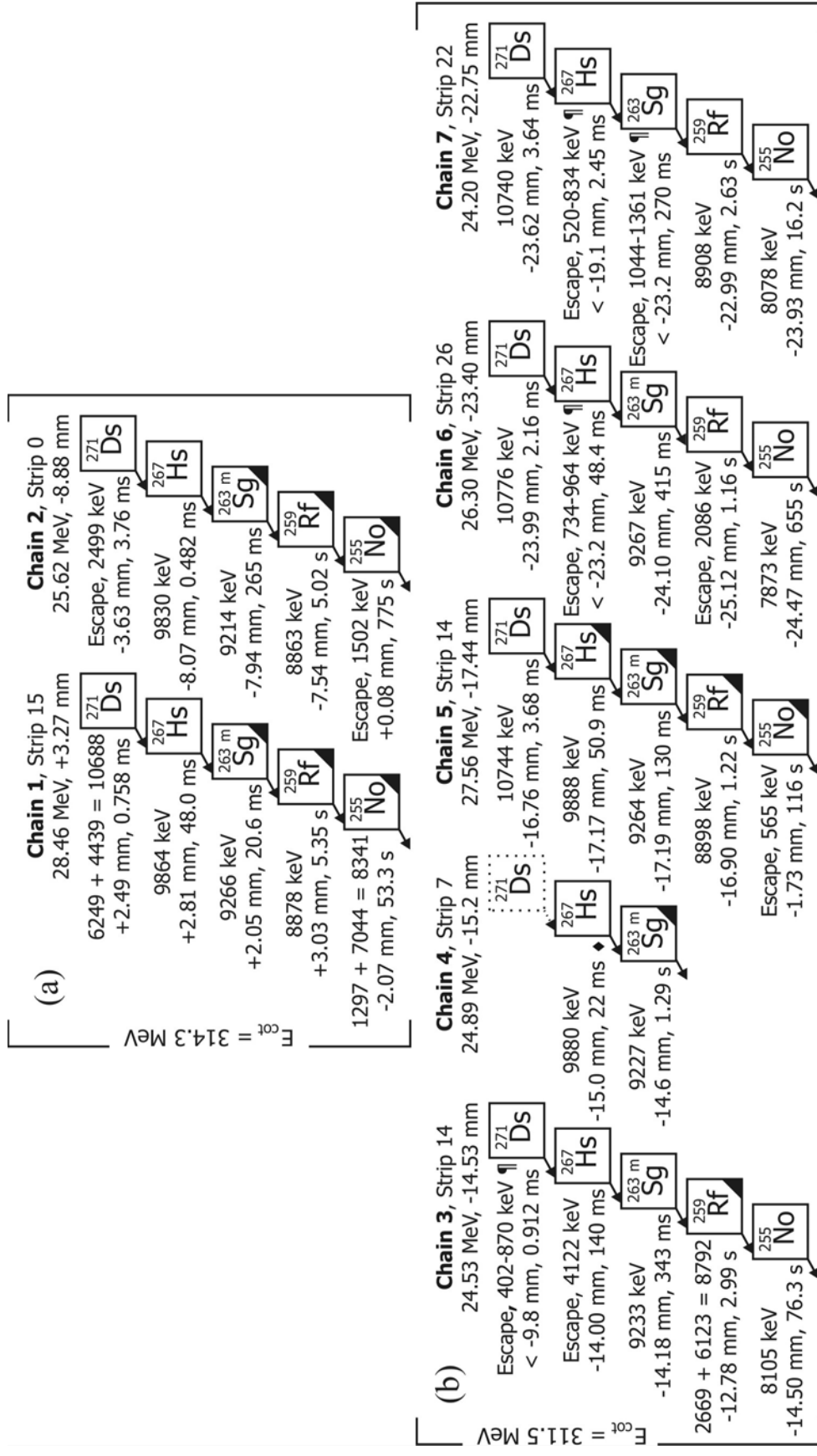


FIG. 3.3.  $^{271}\text{Ds}$  decay chains observed in the irradiation of  $^{208}\text{Pb}$  with  $^{64}\text{Ni}$  at (a)  $E_{\text{col}} = 314.3$  MeV and (b)  $E_{\text{col}} = 311.5$  MeV. For each decay chain, the corresponding implantation event is shown above the chain. The notation  $x + y = \zeta$  indicates that  $x$  keV was observed in the strip detector simultaneously with  $y$  keV in an upstream detector, with sum  $\zeta$  keV. A black triangle in the lower right-hand corner indicates that the beam was off for that event. Events marked with  $\blacktriangleleft$  have their energies estimated from one strip signal (top or bottom) only. The  $^{267}\text{Hs}$  lifetime marked with  $\blacklozenge$  is the sum of the  $^{271}\text{Ds}$  and  $^{267}\text{Hs}$  lifetimes (see main text for a discussion).

### 3.2.2. $^{271}\text{Ds}$ Production Experiment: $E_{\text{tot}} = 311.5 \text{ MeV}$

The second experiment (BGS run 066) was very similar to the  $E_{\text{tot}} = 314.3 \text{ MeV}$  experiment. The two decay chains observed at the previous energy led to a measured cross section of  $7.7_{-5.2}^{+10} \text{ pb}$ . This cross section was approximately the same as the  $8.3_{-5.3}^{+11} \text{ pb}$  cross section measured by Ginter *et al.* at  $E_{\text{tot}} = 309.2 \text{ MeV}$ . There were two possible interpretations of these facts. First, it was possible that the “calibration” of the 88-Inch Cyclotron had changed by  $\sim 5 \text{ MeV}$  over the course of three years. The second possibility was that we had “overshot” the energy and were now on the high-energy side of the maximum of the excitation function, whereas Ginter’s measurement was on the low-energy side. The first possibility was excluded because of the low probability that such a large change would occur (a 5-MeV shift would be well outside the stated uncertainty of 1% in the absolute energy of the 88-Inch Cyclotron). Thus, the second possibility was accepted and a new  $^{64}\text{Ni}$  energy chosen that was roughly centered between  $E_{\text{tot}} = 309.2 \text{ MeV}$  and  $E_{\text{tot}} = 314.3 \text{ MeV}$ . This energy was  $E_{\text{tot}} = 311.5 \text{ MeV}$ , requiring an energy from the cyclotron of 317.0 MeV. The excitation energy of compound nuclei produced at the center of the target was 14.1 MeV using masses estimated from [Myers1994].

The two events in the previous  $E_{\text{tot}} = 314.3 \text{ MeV}$  experiment were observed in strips 15 and 0, indicating that the “true” average magnetic rigidity of  $^{271}\text{Ds}$  EVRs was higher than 2.04 T m. The BGS magnets were changed to  $B\rho = 2.06 \text{ T m}$  using magnet currents of  $Q1 = 1567 \text{ A}$ ,  $M1 = 351 \text{ A}$ , and  $M2 = 593 \text{ A}$  to try to center the distribution on the focal plane.

The targets from the previous experiment received a substantial beam dose during the  $E_{\text{tot}} = 314.3 \text{ MeV}$  irradiation. Thus, a new set of targets was initially used for the new irradiation at the lower energy. These new targets were later found to be too thick for an

accurate cross section measurement and the beam dose applied to them is not included in cross section calculations. Regardless, one  $^{271}\text{Ds}$  decay chain (chain 3, Fig. 3.3) was observed while irradiating these targets and the decay data obtained are used as appropriate. These targets were replaced with the same targets used in the previous  $E_{\text{tot}} = 314.3$  MeV run and performed adequately.

Again, fourteen eight-hour shifts of beam time were available for the experiment. After beam tuning, window breaks, and time lost with the too-thick targets, the total beam-on-target time with the run 065 targets was  $\sim 45$  h (1.9 d). The total dose collected on these targets was  $2.3 \times 10^{17} \text{ }^{64}\text{Ni}^{14+}$  at an average current of  $\sim 225$  pnA. The count rate of all events in the focal plane detectors was  $10.8 \text{ s}^{-1}$ . After vetoing events coincident with the MWPC or punch-through detectors, the count rate of alpha particles in the strip detectors above 500 keV was  $1.1 \text{ s}^{-1}$ .

The beam shutoff parameters in this run were the same as in the  $E_{\text{tot}} = 314.3$  MeV run (see Sec. 3.2.1), except that the EVR- $\alpha$ - $\alpha$  search now looked for a second alpha particle correlated to the first alpha (within 2.0 mm), rather than the EVR. During the run, the beam was shut off for two long (900-s) shutoffs and forty short (15-s) shutoffs. The total time with the beam off was approximately 2364 s (1.4% of total run time). The beam shutoff analysis used preliminary position and energy calibrations, and in two cases (chains 6 and 7, Fig. 3.3) did not shut off the beam when a real decay chain occurred because the observed implantation positions were not within the 3.5-mm position gate of the alpha events that followed.

During the new  $E_{\text{tot}} = 311.5$  MeV run, one decay chain was observed which was not written to disk, but whose presence was indicated by output on the screen of the computer controlling the data acquisition system. This output was produced by the beam shutoff

analysis program, which correctly identified the decay chain and shut off the beam. The data were not written to disk because of a flaw in the data acquisition system. As intended, the system periodically closed the current data file and opened a new one so that a catastrophic error would not corrupt a large amount of data. During a file change, the system attempted to write the data buffers containing the decay chain to disk, but was unable to do so because no file was open. Rather than retrying the write operation at a later time, these buffers were discarded. The creators of the system have supplied us with a patch to correct the problem. See Sec. 3.3.3 for a detailed discussion of this event.

Lastly, at the end of the run, a beam of 193.2-MeV (center-of-target)  $^{40}\text{Ar}^{9+}$  was used to produce  $^{245}\text{Fm}$  ( $E_\alpha = 8150$  keV [Nurmia1967, Münzenberg1981b]) in the  $^{208}\text{Pb}(^{40}\text{Ar}, 3\text{n})$  reaction for calibration purposes. The beam energy from the cyclotron was 196 MeV.

### 3.3. Observed Decay Chains

#### 3.3.1. Summary

Decay chains were identified by searching for correlated implantation and alpha-particle events within appropriate time and energy windows and separated physically by less than 1.5 mm. In total, seven decay chains attributed to  $^{271}\text{Ds}$  were observed and are shown in Fig. 3.3. Chains 1 and 2 were observed at  $E_{\text{tot}} = 314.3$  MeV and chains 3-7 were observed at  $E_{\text{tot}} = 311.5$  MeV. The agreement of the data with that published previously [Hofmann1998, Hofmann2003, Morita2003, Morita2004c, Morita2004d, Ginter2003] is very good.

The two decay chains in the  $E_{\text{tot}} = 314.3$  MeV experiment were observed in strips 15 and 0. Strip 0 is at the very edge of the focal plane so there is some possibility that

additional decay chains were not observed because the recoil distribution was not centered.

In the  $E_{col} = 311.5$  MeV, the distribution of decay chains observed in strips 14, 7, 14, 26, and 22 had a standard deviation of 7.5 strips. Assuming the standard deviation was the same in the previous experiment and the mean strip was  $(15 + 0)/2 = 7.5$ , approximately 84% of the decay chains should have been on the focal plane. Thus, the probability that a decay chain was missed off the edge of the focal plane is not regarded as significant and likely cannot be distinguished from the Poisson probability distribution in the number of decay chains.

The measured cross sections were  $20_{-11}^{+15}$  pb at  $E_{col} = 311.5$  MeV and  $7.7_{-5.2}^{+10}$  pb at  $E_{col} = 314.3$  MeV. The cross sections were calculated based on an estimated BGS transmission of  $0.7 \pm 0.1$ , a chain detection efficiency of  $0.95 \pm 0.05$ , and a Rutherford screening efficiency of  $(1348 \pm 20)^{-1}$ . All errors in this work are reported at the  $1\sigma$  (68%) confidence level. In particular, the cross section errors were calculated using methods detailed in [Schmidt1984], as were all cross section errors reported in this work.

Including all seven events, the average  $^{271}\text{Ds}$  magnetic rigidity in He was  $B\rho = 2.09 \pm 0.03$  T m (statistical uncertainty only), very close to Ginter and co-workers' original estimate of 2.10 T m for this reaction in the BGS. This rigidity (2.09 T m) corresponds to an average EVR charge state of approximately +9.7. The difference between the observed rigidity and that reported for the GARIS separator (2.04 T m) may be an indication of BGS magnet saturation as the currents are increased.

The average pulse height observed for implantation events corresponded to  $25.9 \pm 1.6$  MeV, in good agreement with predictions.

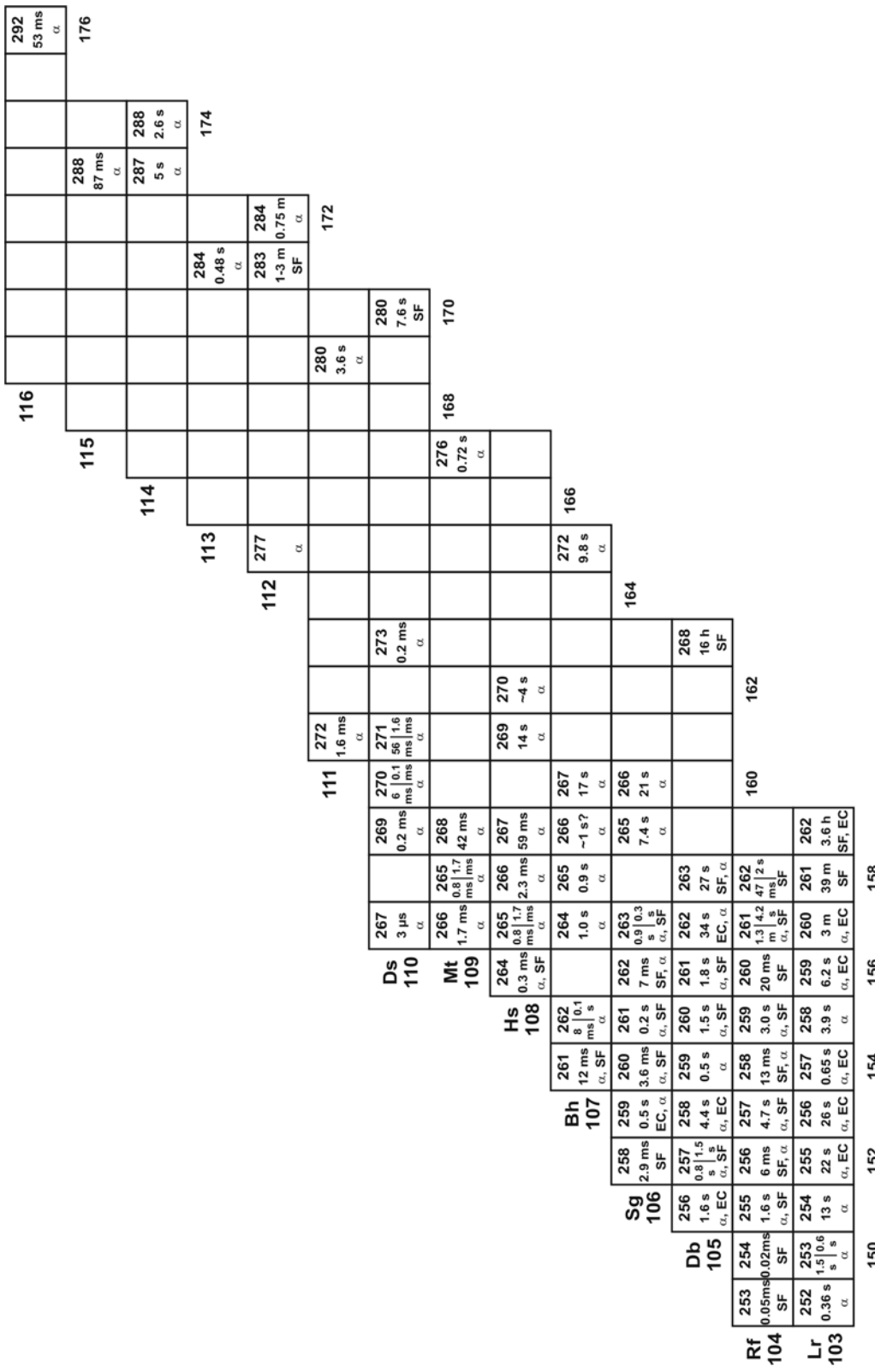


FIG. 3.4. Heavy-element chart of the nuclides as of October 2004. Data are included for which more than one decay chain has been reported and assignments have not been changed. Data compiled by D. C. Hoffman.

The rest of this section attempts to show how the members of the decay chains match with previously published data (see the chart of the nuclides in Fig. 3.4). The data reported in this dissertation have not been corrected for pulse-height defects, although alpha energies have been corrected for the energy of the recoiling daughter nucleus. When assigning individual decays to known alpha branches, the focus will be on comparison with the data obtained by the GSI group (mostly [Hofmann1998]), since the energy resolution of the RIKEN experiments was generally worse than in the GSI experiments. It might also be argued that the previous LBNL experiments are not completely independent of the current work. Keep in mind that the standard deviation in energy is  $\sim 17$  keV for fully stopped alpha particles and  $\sim 45$  keV for reconstructed alphas, that is, those where the total energy is the sum of focal plane and upstream energies.

### 3.3.2. $^{271}\text{Ds}$

The  $^{271}\text{Ds}$  decays in chains 5 (10744 keV) and 7 (10740 keV) are in excellent agreement with the known ground state decay at 10738 keV. Chain 6, with an alpha energy of 10776 keV, can also be assigned to this branch and is in agreement with the alpha energies of chains 12 and 14 reported in [Morita2004d]. The reconstructed alpha in chain 1 with energy 10688 keV likely comes from the 10681 keV branch, but can also be assigned to the 10738 keV branch within the larger error of reconstructed events. The other  $^{271}\text{Ds}$  events in chains 2 and 3 are escape events where only a partial energy signal was observed, and are assigned to the ground state decay of  $^{271}\text{Ds}$  since the observed lifetimes (3.76 ms and 0.912 ms) are not consistent with the half-life of the isomeric state ( $69_{-21}^{+56}$  ms). In fact, no decays consistent with the isomer were observed.

No data are available for the decay of  $^{271}\text{Ds}$  in chain 4; see the discussion in Sec. 3.3.3.

The observed half-life of all six events (chains 1-3, 4-7) was  $1.6^{+0.9}_{-0.5}$  ms, in excellent agreement with the known half-life of  $1.63^{+0.44}_{-0.29}$  ms reported by Morita *et al.* [Morita2004d]. Half-lives are calculated using the MLDS code [Gregorich1991], modified as described in the reference to include the full covariance of all variables.

### 3.3.3. $^{267}\text{Hs}$

The events assigned to  $^{267}\text{Hs}$  in chains 1, 4, and 5 have an average energy of 9877 keV and are in excellent agreement with the known major branch at 9882 keV. The only other  $^{267}\text{Hs}$  decay observed with full energy was in chain 2 (9830 keV) and is in excellent agreement with the known minor branch at 9829 keV. The remaining events in chains 3, 6, and 7 are all escape events.

Chain 4 is the decay chain in which the event data were not written to disk as explained in Sec. 3.2.2. It appears that the  $^{271}\text{Ds}$  event in this chain escaped from the front of the detector and was not recorded by the online analysis program. The  $^{267}\text{Hs}$  event in this decay chain was emitted into the strip detector and was recorded by the online analysis. The correlation between this decay and the implantation event caused the program to initiate a beam shutoff. The program printed this information to the screen, including the time difference. Thus, the only time available (22 ms) is indicative of the sum of the  $^{271}\text{Ds}$  and  $^{267}\text{Hs}$  lifetimes and cannot be used in the half-life measurement of either nuclide, although it is consistent with the known half-lives of both. The lifetime of the following  $^{263}\text{Sg}^m$  event was not affected by this problem. It appears that the (assumed)  $^{259}\text{Rf}$  and  $^{255}\text{No}$  alpha decay particles also were emitted out the front of the strip detector ( $\sim 45\%$  probability each). These data can be accepted as a real decay chain with confidence because of the low background of alpha particles (particularly ones with energies greater

than 9000 keV), the very low probability that two high-energy alpha particles would be correlated to an implantation event on such short time scales, and the agreement with previously published data. Since the online analysis used a preliminary, external calibration, the energies reported had to be corrected using an external-to-internal calibration similar to the one shown in Fig. 2.10 and discussed in Sec. 2.4.3.

The reported half-life of  $^{267}\text{Hs}$  is  $52_{-8}^{+13}$  ms [Morita2004d]. It is difficult to resolve the very short lifetimes observed in chains 2 (0.482 ms) and 7 (2.45 ms) with this half-life. The measured half-life of these two events is  $0.94_{-4.5}^{+12}$  ms, indicating the possibility of an isomer in this nucleus. Unfortunately, this shorter half-life is inconsistent with the long-lived  $^{267}\text{Hs}$  isomer proposed by Morita *et al.*; the one event observed had a lifetime of almost 6 s. Of chains 2 and 7 in this work, only chain 2 was observed with full energy and did not show a new alpha decay energy which might be assigned to an isomeric state. Further study is needed to resolve these issues. The observed half-life is  $55_{-18}^{+32}$  ms for the other four  $^{267}\text{Hs}$  events in this work for which lifetimes were measured (chains 1, 3, 5, and 6), in agreement with the previously reported half-life.

### 3.3.4. $^{263}\text{Sg}^m$

Six events following  $^{267}\text{Hs}$  decays (chains 1-6) were observed with full energy. The statistical average alpha-energy of these events is 9245 keV and they can be convincingly assigned to the decay of  $^{263}\text{Sg}^m$  ( $E_\alpha = 9248 \pm 20$  keV [Hofmann1998]). The statistical standard deviation of these six energies is 23 keV and is consistent with the 17 keV systematic error obtained with much higher statistics at lower alpha-particle energies (for example, from calibration sources). This fact is noteworthy because it gives an idea of the

detector resolution at energies for which direct calibration sources are not available. The half-life of these six events was  $290^{+170}_{-90}$  ms, in excellent agreement with the known  $^{263}\text{Sg}^m$  half-life ( $310^{+160}_{-80}$  ms). The final  $^{263}\text{Sg}$  event in chain 7 is an escape event whose lifetime (270 ms) is consistent with the decay of  $^{263}\text{Sg}^m$ , but which could also be assigned to  $^{263}\text{Sg}^g$  ( $t_{1/2} = 900 \pm 200$  ms [Ghiorso1974]).

Hofmann *et al.* observed only one decay (in chain 12) that could conclusively be assigned to  $^{263}\text{Sg}^g$  following the decay of  $^{267}\text{Hs}$  [Hofmann2003] in thirteen decay chains. Two chains had  $^{263}\text{Sg}$  events recorded as escape alphas. Decays in chains 6 and 7 in [Morita2004d] could potentially be assigned to  $^{263}\text{Sg}^g$  based the decay energies observed, but this is not specifically addressed in the paper. One decay chain could not be followed to  $^{263}\text{Sg}$ , so that thirteen chains did contain  $^{263}\text{Sg}$  events. Although both  $^{263}\text{Sg}$  events in the decay chains reported by Ginter *et al.* [Ginter2003] were attributed to  $^{263}\text{Sg}^m$ , one was an escape event. A liberal interpretation of these facts is that three  $^{263}\text{Sg}^g$  decays were observed after the decay of 25 ( $11 + 13 + 1$ )  $^{267}\text{Hs}$  events, a branching ratio of  $\sim 12\%$ . Given this low probability of observing  $^{263}\text{Sg}^g$  after  $^{267}\text{Hs}$  decay it is not surprising that it was not conclusively observed in the current work.

### 3.3.5. $^{259}\text{Rf}$

The fully stopped alpha events assigned to  $^{259}\text{Rf}$  in chains 5 (8898 keV) and 7 (8908 keV) are assigned to the known transition at 8895 keV. The fully stopped event in chain 2 with energy 8863 keV is assigned to the alpha-group with energy 8861 keV. The other fully stopped alpha assigned to  $^{259}\text{Rf}$  (chain 1, 8878 keV) can be assigned to either of the 8895- and 8861-keV groups based on energy, although the former had a slightly higher intensity in both [Hofmann1998] and [Morita2004d]. The final  $^{259}\text{Rf}$  event observed with

full energy (8792 keV) was in chain 3, and can be assigned to the branch at 8756 keV within approximately one standard deviation for reconstructed events. The observed half-life of all events, including escape events, is  $2.2^{+1.7}_{-0.8}$  s, compared with 2.6 s [Morita2004d],  $2.6^{+1.4}_{-0.7}$  s [Hofmann1998], and  $3.0 \pm 1.3$  s [Bemis1981] reported previously.

### 3.3.6. $^{255}\text{No}$

The decay of  $^{255}\text{No}$  produces a complex alpha spectrum. The following assignments of the present data to the known alpha-groups [Firestone1996] can be made (also indicated are the known branching ratios): chain 1, 8312 keV (1.9%); chain 3, 8121 keV (45.5%); chain 6, 7879 keV (4.2%); and chain 7, 8077 keV (11.9%). The observed half-life of all six  $^{255}\text{No}$  events is  $200^{+140}_{-70}$  s, compared to  $190 \pm 10$  s in [Firestone1996]. See Sec. 3.4.2.2 for a discussion of the probability of  $^{255}\text{No}$  decays being randomly correlated to  $^{271}\text{Ds}$  decay chains.

## 3.4. Analysis of Expected Random Correlations

### 3.4.1. Theory

In any transactinide experiment, the very small number of decay chains observed requires that other possible explanations for the data be examined. Among these is the possibility that a decay chain arises from a random correlation of unrelated events. In this case, a series of events occurs in such a way that they replicate an actual decay chain of interest. This section describes how not just the probability, but the expected number of these random correlations can be calculated. In general, the experiment must be designed

to have a small number of potential random correlations or risk producing data that is not meaningful.

When searching for decay chains, the constituent events are required to have certain properties: they must be correlated in position, energy, and time. That is, they must be located in the same physical position in space, have energies close to those expected for the nuclides of interest, and follow each other in manner consistent with the expected lifetime distribution. Let us examine how these three requirements are addressed.

The BGS focal plane detector is divided into 48 strips and all events in a decay chain are required to be in the same strip, thus ensuring that they have roughly the same horizontal position. The strips are position-sensitive in the vertical direction, and all events must occur within some reasonable vertical position window, which may depend on energy. The size of this window is the pixel size, representing the maximum allowed vertical position difference for which two events can be said to be “in the same place.” The width of the pixel is fixed as the width of a single strip.

The energy requirement is straightforward: the observed implantation and decay energies must match what could reasonably be expected. In the case of these  $^{271}\text{Ds}$  experiments, the decay scheme is already known, so the decay energies should agree with that which has already been published.

Each nuclide in the chain has a known half-life so there is a corresponding distribution of expected lifetimes that might be observed in several decays of that nuclide. A maximum time can be chosen such that any lifetime observed that is greater than the maximum value would not be assigned to a decay of the nuclide of interest. Note that the maximum time for each nuclide should be chosen *a priori*, and not influenced by the

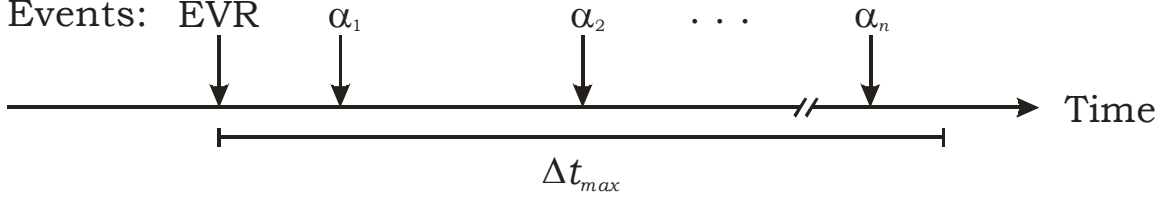


FIG. 3.5. Schematic representation of the random correlation analysis. Each EVR (implantation) event defines the beginning of a time interval  $\Delta t_{max}$  (and a vertical pixel not shown). Alpha events occur within the  $\Delta t_{max}$  window according to a Poisson distribution.

longest lifetime actually observed. Typically, this maximum time is set at five or six times the half-life of the nuclide.

In an actual experiment, the focal plane constantly records the implantation of nuclei and their subsequent decays. Thus, the probability of a random correlation can be estimated from the rates of these events. Each decay chain must start with an implantation event, so let each one define a point in time ( $t_{EVR}$ ) and a pixel in space around it. Suppose that the longest time which one could reasonably expect an individual nucleus to survive is  $\Delta t_{max}$ . This might be, for example, five half-lives of the longest-lived member of the decay chain. Thus, all events must occur in the time interval from  $t_{EVR}$  to  $t_{EVR} + \Delta t_{max}$ . This is illustrated in Fig. 3.5. Now suppose  $R_\alpha$  is the total rate at which alpha events occur within the focal plane, possibly limited to an energy range containing the expected alpha decay energies. Let  $N_{pixel}$  be the number of pixels in the detector, obtained by dividing the total detector area by the desired pixel size (see Sec. 3.4.2.1 for an example). The pixel size is chosen using test reaction data for which correlated decay chains are available, and should be large enough to include the majority of the distribution of position differences from this data. The expected number of alpha events per pixel  $\mu$  (which may be limited to some energy window) from  $t_{EVR}$  to  $t_{EVR} + \Delta t_{max}$  is

$$\mu = (R_\alpha / N_{\text{pixel}}) \cdot \Delta t_{\text{max}}, \quad (3.1)$$

if we assume that the distribution of random alpha-particle events is uniform across the focal plane, which is only approximately true.  $\mu$  is expected to be small and nonnegative and the actual number of alpha events observed  $n_\alpha$  within the pixel and time window is limited to integer values. Thus, Poisson statistics can be used to estimate the probability of observing  $n_\alpha$  events when  $\mu$  are expected:

$$P(n_\alpha | \mu) = \frac{\mu^{n_\alpha}}{n_\alpha!} e^{-\mu}. \quad (3.2)$$

$P(n_\alpha | \mu)$  is the probability that a series of alpha particles resembling a decay chain will follow an implantation event. Thus, the expected number of random decay chains following  $N_{\text{EVR}}$  implantation events is

$$N_{\text{random}} = N_{\text{EVR}} \cdot P(n_\alpha | \mu). \quad (3.3)$$

Note that the rate of any type of decay could be substituted for  $R_\alpha$ , such as the rate of fission or electron-capture, if those could be measured (electron-capture is currently not detectable in the BGS). The value of  $n_\alpha$  is chosen based on both objective and subjective criteria: it is affected by the alpha-particle detection efficiency but also the experimenter's personal definition of what constitutes a "valid decay chain." Lastly, note that this procedure actually gives an upper limit on the number of random decay chains expected. There is no requirement that the lifetimes between subsequent events be consistent with published data or that the energies of the alpha particles match published data. In the case where  $n_\alpha$  is less than the total number of alpha decays in the chain, there is no requirement that additional alpha particle events be present to complete the chain.

Examples of the preceding calculations are given in the following sections.

### 3.4.2. Calculations and Interpretation

#### 3.4.2.1. Expected $^{271}\text{Ds}$ , $^{267}\text{Hs}$ , $^{263}\text{Sg}^m$ , and $^{259}\text{Rf}$ Random Correlations

Table 3.2 shows a summary of the random rate calculation for the  $^{271}\text{Ds}$  experiments. In both experiments the overall rate of alpha-particle events in the focal plane with energies between 8500-12000 keV (encompassing the alpha decays of  $^{271}\text{Ds}^{(m)}$ ,  $^{267}\text{Hs}$ ,  $^{263}\text{Sg}^{(m)}$ , and  $^{259}\text{Rf}$ ) was measured to be  $\sim 10^{-2} \text{ s}^{-1}$ . If the pixel size of generously chosen as 3.0 mm, then the entire focal plane consists of 928 total pixels (48 strips x 58 mm/strip x 1 pixel/3.0 mm). The count rate in the energy range of interest is  $\sim 10^{-5} \text{ s}^{-1} \text{ pixel}^{-1}$ . Within 15 s (approximately five  $^{259}\text{Rf}$  half-lives), the probability of observing two alphas was  $\sim 10^{-8}$ . Thus, even though the number of implantation events was  $\sim 10^5$ , the expected numbers of random EVR- $\alpha$ - $\alpha$  ( $n_\alpha = 2$ ) correlations were  $0.62 \times 10^{-3}$  and  $5.6 \times 10^{-3}$  in the  $E_{\text{tot}} = 314.3$  MeV and 311.5 MeV runs, respectively. As discussed in Sec. 3.4.1, these figures represent upper limits on the number of random decay chains to be expected. Thus, it is reasonable to conclude that all seven  $^{271}\text{Ds}$  decay chains are the result of real correlations beginning with the implantation of a  $^{271}\text{Ds}$  nucleus.

The probability of observing exactly four alphas within 15 was  $10^{-18}$ – $10^{-16}$ . The expected numbers of random EVR- $\alpha$ - $\alpha$ - $\alpha$ - $\alpha$  ( $n_\alpha = 4$ ) correlations were  $0.070 \times 10^{-11}$  and  $3.0 \times 10^{-11}$  in the  $E_{\text{tot}} = 314.3$  MeV and 311.5 MeV runs, respectively. Note that these figures are not completely meaningful since the observed decay chains were only required to have at least two alpha particle events ( $n_\alpha = 2$ ) measured with full energy, either fully stopped or reconstructed. They do illustrate the very low probability that decay chains such as chains 1 and 5 (with four full-energy alpha particles each) could originate from random correlations. Also note that the rates given in Table 3.2 correspond to full

TABLE 3.2. Analysis of expected random correlations in the  $^{271}\text{Ds}$  experiments. In all cases,  $\Delta t_{\max}$  was 15 s (approximately five  $^{259}\text{Rf}$  half-lives) and the pixel size was 3.0 mm (928 total pixels in the focal plane). The alpha particle rates are those measured at full beam intensity and combine alpha particles fully stopped in the focal plane with reconstructed ones.  $^{255}\text{No}$  is treated separately in Table 3.3.

	$E_{\text{tot}} = 314.3 \text{ MeV}$ Experiment (Run 065)	$E_{\text{tot}} = 311.5 \text{ MeV}$ Experiment (Run 066)
Overall Rate of Alphas with Energy 8500-12000 keV (s <sup>-1</sup> )	$0.72 \times 10^{-2}$	$1.6 \times 10^{-2}$
Rate of Alphas Per Pixel with Energy 8500-12000 keV (s <sup>-1</sup> )	$0.78 \times 10^{-5}$	$1.7 \times 10^{-5}$
$\mu$ (Expected Number of Alpha Particles Per Pixel in $\Delta t_{\max}$ )	$1.2 \times 10^{-4}$	$2.5 \times 10^{-4}$
$N_{\text{EVR}}$	$0.92 \times 10^5$	$1.7 \times 10^5$
Probability of Exactly Two Alphas in the Same Pixel in $\Delta t_{\max}$	$0.67 \times 10^{-8}$	$3.2 \times 10^{-8}$
Expected Number of Random Correlations ( $n_{\alpha} = 2$ )	$0.62 \times 10^{-3}$	$5.6 \times 10^{-3}$
Probability of Exactly Four Alphas in the Same Pixel in $\Delta t_{\max}$	$0.076 \times 10^{-16}$	$1.7 \times 10^{-16}$
Expected Number of Random Correlations ( $n_{\alpha} = 4$ )	$0.070 \times 10^{-11}$	$3.0 \times 10^{-11}$

intensity beam. When the beam is shut off the background alpha-particle rate decreases by a factor of approximately 20, so that the probability of random correlations is further reduced by a factor of  $\sim 20^n$ , where  $n$  is the number of alpha particles observed with the beam off.

### 3.4.2.2. Expected $^{255}\text{No}$ Random Correlations

$^{255}\text{No}$  has a much longer half-life ( $3.1 \pm 0.2 \text{ min}$  [Firestone1996]) than the other nuclides in the  $^{271(\text{m})}\text{Ds}$  decay chain, so its random probability analysis will be treated

TABLE 3.3. Analysis of expected random correlations between observed  $^{271}\text{Ds}$  decay chains and  $^{255}\text{No}$ . In all cases,  $\Delta t_{\max}$  was 900 s (approximately five  $^{255}\text{No}$  half-lives) and the pixel size was 3.0 mm (928 total pixels). Full-energy (7500-8600 keV) alpha particle rates combine those fully stopped in the focal plane with reconstructed ones. “Escape” alpha particle rates do not include reconstructed alphas.

Decay Chains Observed	$E_{\text{tot}} = 314.3 \text{ MeV}$		$E_{\text{tot}} = 311.5 \text{ MeV}$	
	Experiment (Run 065)		Experiment (Run 066)	
	Beam On	Beam Off	Beam On	Beam Off
7500-8600 keV ( $^{255}\text{No}$ )	$0.88 \times 10^{-2}$	$0.051 \times 10^{-2}$	$1.7 \times 10^{-2}$	$0.046 \times 10^{-2}$
Total Alpha Rate ( $\text{s}^{-1}$ )				
7500-8600 keV ( $^{255}\text{No}$ )	$0.94 \times 10^{-5}$	$0.055 \times 10^{-5}$	$1.8 \times 10^{-5}$	$0.050 \times 10^{-5}$
Alpha Rate per Pixel ( $\text{s}^{-1}$ )				
Probability of Exactly One Random $^{255}\text{No}$ in $\Delta t_{\max}$	$0.84 \times 10^{-2}$	$0.049 \times 10^{-2}$	$1.6 \times 10^{-2}$	$0.045 \times 10^{-2}$
Expected Number of Random Chain- $^{255}\text{No}$ Correlations	$<0.84 \times 10^{-2}$	$0.099 \times 10^{-2}$	$4.8 \times 10^{-2}$	$0.045 \times 10^{-2}$
Number of Chain- $^{255}\text{No}$ Correlations Observed	0	1	3	0
500-5000 keV (Escape)	$1.2 \times 10^0$	$0.062 \times 10^0$	$1.1 \times 10^0$	$0.074 \times 10^0$
Total Alpha Rate ( $\text{s}^{-1}$ )				
500-5000 keV (Escape)	$1.3 \times 10^{-3}$	$0.066 \times 10^{-3}$	$1.2 \times 10^{-3}$	$0.080 \times 10^{-3}$
Alpha Rate per Pixel ( $\text{s}^{-1}$ )				
Probability of Exactly One Escape Alpha in $\Delta t_{\max}$	$3.6 \times 10^{-1}$	$0.56 \times 10^{-1}$	$3.7 \times 10^{-1}$	$0.67 \times 10^{-1}$
Expected Number of Random Chain-Escape Correlations	$<0.36 \times 10^0$	$0.11 \times 10^0$	$1.1 \times 10^0$	$0.067 \times 10^0$
Number of Chain-Escape Correlations Observed	0	1	0	1

<sup>a</sup> Excludes chain 4, for which no  $^{255}\text{No}$  event was observed.

separately from the other nuclides. In this case, instead of estimating the probability that  $n_{\alpha}$  alpha particles will follow an implantation event, we estimate the probability that a decay chain leading to  $^{259}\text{Rf}$  will be followed by alpha-decay of  $^{255}\text{No}$ . The analysis is similar and is shown in detail in Table 3.3.

All  $^{255}\text{No}$  alpha-particle events were either observed with full energy (fully stopped in the focal plane or reconstructed) or “escaped” from the front of the detector with only a partial energy signal recorded. Table 3.3 shows these separately. In the case of full energy alpha particles which might be assigned to  $^{255}\text{No}$ , the expected number of random correlations between a  $^{271}\text{Ds}$  decay chain and these alpha particles was highest ( $4.8 \times 10^{-2}$ ) when the beam was on during the  $E_{\text{tot}} = 311.5$  MeV experiment. Three  $^{255}\text{No}$  decay chains were correlated to full-energy  $^{255}\text{No}$  decays; the Poisson probability of observing three correlations when  $4.8 \times 10^{-2}$  are expected is  $1.8 \times 10^{-5}$ . Thus, these correlations are interpreted as real correlations, although the small possibility that one of three comes from a random correlation cannot be excluded. One final full-energy correlation was observed with the beam off during the  $E_{\text{tot}} = 314.3$  MeV experiment when  $0.099 \times 10^{-2}$  were expected. The Poisson probability of this being a random correlation is  $9.9 \times 10^{-4}$ , so this correlation is also interpreted as a real correlation. The full-energy  $^{255}\text{No}$  events observed in chains 1, 3, 6, and 7 are likely all real correlations.

The  $^{255}\text{No}$  events in chains 2 and 5 were observed as escape alpha events. Both were observed with the beam off: one each in the  $E_{\text{tot}} = 314.3$  MeV and 311.5 MeV experiments. The expected numbers of random decay-chain-to-escape- $^{255}\text{No}$  correlations were 0.11 and 0.067, respectively. The respective Poisson probabilities of observing one correlation with these numbers expected are 0.099 and 0.063. These probabilities are not insignificant, and it is probable that at least one of the  $^{255}\text{No}$  correlations in chains 2 and 5 is a random correlation. In that case, the  $^{255}\text{No}$  probably decayed by electron capture (38.6% branch) to long-lived  $^{255}\text{Md}$  ( $t_{1/2} = 27 \pm 2$  min) [Firestone1996] and was not detected. One or two  $^{255}\text{No}$  electron-capture decays out of six atoms observed would also bring the observed electron-capture branch into good agreement with the known branch.

### 3.5. $^{208}\text{Pb}(^{64}\text{Ni}, \text{n})^{271}\text{Ds}$ Excitation Function

The current work establishes an excitation function for the  $^{208}\text{Pb}(^{64}\text{Ni}, \text{n})^{271}\text{Ds}$  reaction measured with the BGS at the LBNL 88-Inch Cyclotron. Figures 3.1 and 3.2 and Table 3.1 show the cross sections obtained in the current work combined with previously published results. In terms of the magnitudes of the cross sections, the results agree among the three laboratories, certainly within the large error bars resulting from the few decay chains observed.

Also shown in the Fig. 3.1 and 3.2 are Gaussian fits to each laboratory's data. A cold fusion 1n excitation function is not Gaussian, but the limited number of energies for which data are available does not permit fitting of non-symmetric shapes. The observed center (and FWHM) of each Gaussian is GSI: 309.4 MeV (2.6 MeV); LBNL: 311.7 MeV (3.8 MeV); and RIKEN: 313.4 MeV (3.3 MeV). It should be noted that in a fit of the RIKEN data to a Gaussian, Morita *et al.* [Morita2004d] calculate that it should be centered at 313.8 MeV with FWHM 4.7 MeV. The difference in mean values between that calculation and the current one is likely not significant, but the difference in width is significant. This discrepancy may be attributed to the measurement of only an upper limit cross section on the high-energy side of their excitation function. Regardless, this discussion will assume a FWHM of 3.3 MeV for the RIKEN data.

If a theoretical excitation function for a reaction is computed without the energy loss in the target folded in, then it is not difficult to factor in the target thickness; simply use an average value integral with a variable center-of-target energy. Unfortunately, the reverse process is complex, and mathematically leads to a problem that can be solved for simple cases but cannot be generalized to the more complicated functions required to describe an excitation function. Thus, although it would be interesting to compare the widths of the

fits to pure theoretical predictions (see, for example, Fig. 10 in [Świątecki2003]), this is not possible. Therefore, we shall limit our discussion to the theoretical excitation functions shown in Fig. 3.1 and 3.2, which have a 4-MeV target thickness folded in.

A Gaussian fit to this “Fusion by Diffusion” prediction for the  $^{208}\text{Pb}(^{64}\text{Ni}, \text{n})^{271}\text{Ds}$  excitation function from Świątecki, Siwek-Wilczyńska, and Wilczyński [Świątecki2004a] results in a mean value of 312.8 MeV and a FWHM of 4.9 MeV. The mean value agrees well with both the LBNL and RIKEN results, but differs from the peak of the GSI excitation function by 3.4 MeV (roughly two-thirds of the target thickness in the GSI experiments). The theory predicts maximum-cross-section energies to within 1-2 MeV, so this discrepancy seems significant.

The FWHM of the prediction is larger than any of the experimental results (although in excellent agreement with the FWHM reported by Morita *et al.*). The difference is most pronounced in the GSI data. In all cases, the true shape of the excitation function is not well established by the experiments because insufficient data exist on the cross sections at the “wings,” where they are expected to be smallest. The observation of a single event by the GSI group at  $E_{\text{tot}} = 311.6$  MeV certainly contributes to the apparent narrow excitation function measured at that laboratory and may be the result of statistical fluctuations. It is difficult to make the predicted width of an excitation function agree with experimental data because it depends so sensitively on the fusion probability as a function of energy, as well as on the  $\Gamma_n/\Gamma_f$  ratio. It should also be noted that the FWHM of a measured excitation function depends on the target thickness used, and this was different at each laboratory. The energy of the beam decreases significantly as it passes through the target, so that a measured cross section really integrates over a portion of the “true” excitation function. A larger target thickness results in a “flatter” measured excitation function and

increases the observed FWHM. Regardless, such estimations do give us some idea of the ability of the theory to reproduce experimental data.

The experimental data obtained at all three laboratories have large error bars due to limited statistics but appear to agree with the theoretical prediction of maximum cross section. It appears that the “Fusion by Diffusion” theory outlined in Chapter 1 describes well the experimental data presented here. Yet, the real test of any theory lies in its predictive power, and this will be tested in the next Chapter.

Another question raised by these results is whether a systematic difference exists in the beam energy between the GSI UNILAC, the LBNL 88-Inch Cyclotron, and the RILAC at RIKEN. Morita *et al.* [Morita2004d] address this question, saying, “. . . the difference of our result to that of [Hofmann1998] is not regarded as significant.” This statement seems inconsistent with the necessity that the RIKEN group use a +4-MeV correction between the GSI and RIKEN accelerators to estimate the beam energy for their experiments on the production of  $^{272}\text{111}$  in the  $^{209}\text{Bi}({}^{64}\text{Ni}, \text{n})$  reaction [Morita2004b]. This correction was based on the observed difference in peak cross section energy in the  $^{208}\text{Pb}({}^{64}\text{Ni}, \text{n})^{271}\text{Ds}$  reaction which is clearly visible in Fig. 3.1. Unfortunately, our current results do not shed any light on this problem, as the maximum of our measured excitation function is nearly centered between those obtained at the other two laboratories. The differences of approximately 2.5 MeV are less than the 1% absolute error of the energy from the 88-Inch Cyclotron. Note that in our experiments, the average Cyclotron dee voltage was 68.1 kV and the  ${}^{64}\text{Ni}$  charge state was 14+, so that the total energy gained per gap crossing was  $\sim 0.95$  MeV ( $\sim 1.9$  MeV per revolution). Thus, an error of a single turn (plus or minus) when extracting the beam from the cyclotron would bring our current results into agreement with either the GSI or RIKEN accelerators but not both.

## 4. Production of $^{272}\text{111}$ in the $^{208}\text{Pb}(^{65}\text{Cu}, \text{n})$ Reaction

### 4.1. Previous Work

#### 4.1.1. GSI Experiments

Element 111 was discovered by S. Hofmann *et al.* at GSI using the Separator for Heavy Ion Products [Hofmann1995b]. Preparatory experiments began with the irradiation of  $^{208}\text{Pb}$  targets with  $^{64}\text{Ni}$  projectiles of energy 305.3-315.5 MeV and led to the observation of  $^{271}\text{Ds}$  for the first time [Hofmann1998] as the product of the  $^{208}\text{Pb}(^{64}\text{Ni}, \text{n})$  reaction (see Chapter 3 for a complete discussion of these experiments). In a subsequent experiment designed to produce element 111, Hofmann *et al.* [Hofmann1995b] irradiated  $^{209}\text{Bi}$  targets with 316.1-MeV  $^{64}\text{Ni}$  projectiles at  $E_{\text{tot}} = 312.1$  MeV (lab frame). No decay chains attributable to element 111 were observed. The beam energy was increased to  $E_{\text{tot}} = 314.1$  MeV, and one atom of  $^{272}\text{111}$  was observed. The beam energy was increased again to  $E_{\text{tot}} = 316.0$  MeV and two more  $^{272}\text{111}$  decay chains were observed.

In the year 2000, the  $^{209}\text{Bi}(^{64}\text{Ni}, \text{n})^{272}\text{111}$  and the preparatory  $^{208}\text{Pb}(^{64}\text{Ni}, \text{n})^{271}\text{Ds}$  experiments were repeated [Hofmann2002]. Only the highest energy of  $E_{\text{tot}} = 316.0$  MeV was used in the  $^{209}\text{Bi}$  experiment and three more  $^{272}\text{111}$  decay chains were observed,

bringing the total number of chains observed at GSI to six. In all six cases, the decay chain was followed to the decay of the known nuclides  $^{260}\text{Db}$  and/or  $^{256}\text{Lr}$  (see the chart of the nuclides in Fig. 3.4). The parent nuclide  $^{272}\text{111}$  and its daughters  $^{268}\text{Mt}$  and  $^{264}\text{Bh}$  were characterized for the first time. Results of these experiments and element 111 experiments at other laboratories are summarized in Fig. 4.1 and Table 4.1.

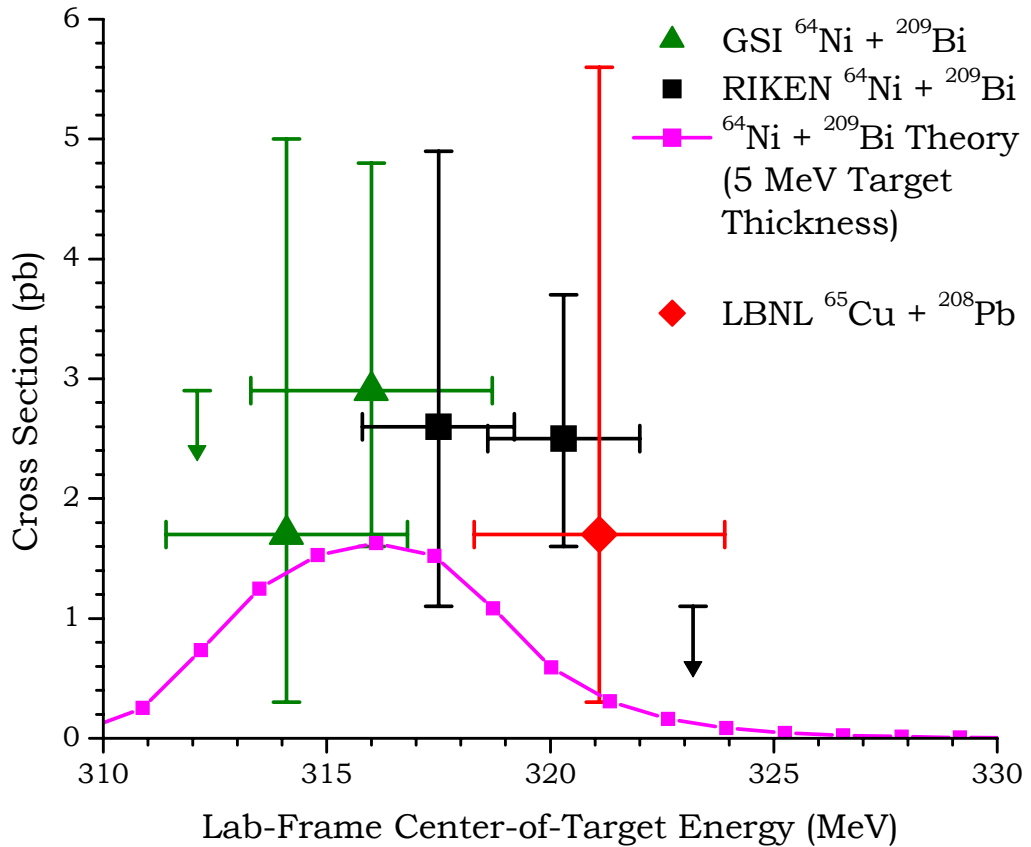


FIG. 4.1. Experimental cross sections and theoretical excitation function prediction for the  $^{209}\text{Bi}(^{64}\text{Ni}, \text{n})^{272}\text{111}$  reaction. The green triangles are GSI data [Hofmann2002] and the black squares are RIKEN data [Morita2004b]. The vertical error bars represent the  $1\sigma$  (68%) error limits for the cross sections, and the horizontal error bars represent the energy loss of the beam as it traverses the target. The magenta squares connected by lines are the theoretical excitation function [Świątecki2004a] and have a 5-MeV target thickness folded in. The red diamond is the cross section for the  $^{208}\text{Pb}(^{65}\text{Cu}, \text{n})^{272}\text{111}$  reaction measured in the current work, and is shown for comparison purposes only.

TABLE 4.1. Cross sections for the  $^{209}\text{Bi}(^{64}\text{Ni}, \text{n})$  and  $^{208}\text{Pb}(^{65}\text{Cu}, \text{n})$  reactions leading to the production of  $^{272}\text{111}$  measured at three different laboratories.  $E_{\text{tot}}$  is the lab-frame beam energy at the center of the target. These data are presented graphically in Fig. 4.1.

Laboratory and Reference	Reaction	$E_{\text{tot}}$ (MeV)	Target Thickness (mg/cm <sup>2</sup> )	Dose (10 <sup>17</sup> )	Decay Chains Observed	Cross Section (pb)
GSI [Hofmann2002]	$^{64}\text{Ni} + ^{209}\text{Bi}$	312.1	0.45	10	0	<2.9
		314.1	0.45	11	1	$1.7^{+3.3}_{-1.4}$
		316.0	0.45	33	5 <sup>a</sup>	$2.9^{+1.9}_{-1.3}$
RIKEN [Morita2004b]	$^{64}\text{Ni} + ^{209}\text{Bi}$	317.5	0.25	20.2	3	$2.6^{+2.3}_{-1.5}$
		320.3	0.29	49.4	8 <sup>b</sup>	$2.5^{+1.2}_{-0.9}$
		323.2	0.30	25.0	0	<1.1
LBNL [This work.]	$^{65}\text{Cu} + ^{208}\text{Pb}$	321.1	0.47	6.6	1	$1.7^{+3.9}_{-1.4}$

<sup>a</sup> Combines two different experiments separated by six years.

<sup>b</sup> Excludes three events observed during the same runs where target deterioration had occurred.

$^{272}\text{111}$  was observed to decay with a half-life of  $1.6^{+1.1}_{-0.5}$  ms. Morita *et al.* [Morita2004b]

report a conflicting half-life of  $3.8^{+1.4}_{-0.8}$  ms for this nuclide (see Sec. 4.1.2 below). It decays by the emission of alpha particles of energy 11027 keV (two events) and 10820 keV (one event). Hofmann and coworkers noted that the difference in these observed alpha energies and the corresponding  $Q_{\alpha}$ -values is close to the energy of a 155-keV gamma ray observed in coincidence with the decay of the first  $^{272}\text{111}$  event in [Hofmann1995b]. They suggested that  $^{272}\text{111}$  may alpha decay to a  $^{268}\text{Mt}$  level at 207 keV, and that the internal-conversion decay of this state leads to the emission of an Mt K electron. Thus, the 155-keV gamma ray may actually be a  $K_{\alpha 1}$  x-ray from Mt. Unfortunately, the coincident alpha particle was not observed with full energy so this hypothesis remains unproven. A half-life of  $42^{+29}_{-12}$  ms was observed by Hofmann *et al.* for  $^{268}\text{Mt}$ , but as with  $^{272}\text{111}$ , Morita *et al.* again

report a different half-life of  $21^{+8}_{-5}$  ms for  $^{268}\text{Mt}$ . Four  $^{268}\text{Mt}$  decays were recorded with full energy and varied from 10097-10294 keV. Using a 93-keV gamma ray coincident with a 10221-keV event as a guide, these decays were tentatively placed into three groups with energies 10097 keV (one event), 10221 keV (one event), and 10276 keV (two events).

The final new nuclide produced in these experiments was  $^{264}\text{Bh}$ . All six decays were observed with full energy and were placed in four groups: 9113 keV (one event), 9365 keV (one event), 9494 keV (two events), and 9619 (two events). The observed half-life was  $1.0^{+0.7}_{-0.3}$  s.

As in the case of element 110, the claims of the GSI group for discovery of a new element were strengthened by the fact that the decay chains could be followed to the decay of known nuclides in all cases. Thus, the mass and atomic numbers of the nuclides could be assigned unequivocally. In this case, the first known nuclide produced by the decay of  $^{272}\text{Fl}$  was  $^{260}\text{Db}$ . This nucleus was discovered by Ghiorso *et al.* [Ghiorso1970] and significantly improved data were later obtained by Bemis *et al.* [Bemis1977], who measured a  $^{260}\text{Db}$  half-life of  $1.52 \pm 0.13$  s. It decays with an alpha branch of  $(90.4 \pm 0.6)\%$ , a fission branch of  $(9.6 \pm 0.6)\%$ , and an upper-limit electron-capture branch of 2.5%. The alpha decay energies (with branches) are  $9040 \pm 14$  keV [ $(48 \pm 5)\%$ ],  $9074 \pm 14$  keV [ $(23 \pm 5)\%$ ], and  $9120 \pm 17$  keV [ $(17 \pm 3)\%$ ]. The GSI data are in reasonable agreement with these data. The other known nuclide in the GSI decays chains was  $^{256}\text{Lr}$ , which had also been observed in the experiments by the Ghiorso and Bemis groups. The half-life of  $^{256}\text{Lr}$  is  $25.9 \pm 1.7$  s. It decays predominantly by alpha-particle emission, producing a complex spectrum. Again, the GSI data were consistent with these previously reported results.

#### 4.1.2. RIKEN Experiments

The production of  $^{272}\text{111}$  in the  $^{209}\text{Bi}(^{64}\text{Ni}, \text{n})$  reaction has also been reported by a group working at RIKEN (the Institute of Physical and Chemical Research, Wako, Saitama, Japan) led by K. Morita [Morita2004b, Morita2004c]. As discussed in Sec. 3.1.3, this group had previously measured the lower portion of an excitation function for the  $^{208}\text{Pb}(^{64}\text{Ni}, \text{n})^{271}\text{Ds}$  reaction in preparation for future experiments on the synthesis of elements 111, 112, and 113. This partial excitation function had its maximum at a center-of-target energy 4 MeV higher in the lab frame than was measured in the GSI experiments (see Sec. 3.1.3, Fig. 3.1 and 3.2, and Table 3.1). Therefore, the RIKEN group began their experiments on the production of  $^{272}\text{111}$  with  $^{64}\text{Ni}$  projectiles of  $E_{\text{tot}} = 320.3$  MeV, approximately 4 MeV higher than the optimum energy measured at GSI. In total, eleven decay chains attributed to  $^{272}\text{111}$  were observed at this energy over the course of several separate irradiations. The combined cross section was  $2.5^{+1.2}_{-0.9}$  pb, although the target thickness was not well defined for three events and these are not included in the cross section calculation. The beam energy was raised to  $E_{\text{tot}} = 323.2$  MeV, but no events were observed and an upper limit on the cross section of 1.1 pb was obtained. The final beam energy studied was  $E_{\text{tot}} = 317.5$  MeV, and three decay chains were observed with a cross section of  $2.6^{+2.3}_{-1.5}$  pb. A total of 14 decay chains was observed.

As in the case of the  $^{208}\text{Pb}(^{64}\text{Ni}, \text{n})^{271}\text{Ds}$  reaction, the data obtained by the RIKEN group were generally consistent with the data obtained by the GSI group, but again showed larger spreads in the measured energies of events. However, this is not surprising, since all the nuclides in the  $^{272}\text{111}$  decay chain are odd-odd and expected to have complex decay schemes. Also, the RIKEN group observed many more decay chains than the GSI

group, so lower-intensity alpha decay branches have a higher probability of being observed.

Morita's group reported the observation of  $^{272}\text{111}$  with full energy in all 14 decay chains. The two energy groups of 11027 keV and 10820 keV reported by Hofmann *et al.* were confirmed. Additionally, new alpha energies of 11373 keV (three events) and 10395 keV (two events) were reported. The half-life of  $3.8^{+1.4}_{-0.8}$  ms measured for  $^{272}\text{111}$  does not agree within the stated errors with that of  $1.6^{+1.1}_{-0.5}$  ms reported by the GSI group. Further experiments are required to resolve this discrepancy.

As in the GSI experiments, only alpha-particle emission from  $^{272}\text{111}$  to produce  $^{268}\text{Mt}$  was observed. The  $^{268}\text{Mt}$  alpha-decay energies observed at RIKEN covered a large energy range from 10280-10780 keV, higher than the range of 10097-10294 keV observed by the GSI group. Morita *et al.* reported a half-life of  $21^{+8}_{-5}$  ms for these decays, compared to the  $42^{+29}_{-12}$  ms reported by Hofmann *et al.* One long-lived  $^{268}\text{Mt}$  event was observed at both laboratories: 122 ms at RIKEN (chain 3 in [Morita2004b]) and 171 ms at GSI (chain 2 in [Hofmann1995b]). The 171-ms event had the lowest measured decay energy (10097 keV) in the GSI experiments, but unfortunately the RIKEN 122-ms event was recorded as an escape event, so its true energy is not known. Morita and coworkers suggest that these two events may be indications of an isomeric state in  $^{268}\text{Mt}$ , and that ignoring these events brings the half-lives measured at the two laboratories into agreement.

The alpha-decay daughter of  $^{268}\text{Mt}$  is  $^{264}\text{Bh}$ , which was also observed in the RIKEN experiments. The most important result was the discovery of a previously unknown SF branch ( $\sim 15\%$ ) in  $^{264}\text{Bh}$ . The majority of  $^{264}\text{Bh}$  events were observed to alpha decay with energies from 9100-9600 keV. One event with an unusually low decay energy of 8870 keV

was assigned to  $^{264}\text{Bh}$  and might actually be due to the decay of  $^{260}\text{Db}$ . The subsequent alpha decay assigned to  $^{260}\text{Db}$  had an energy consistent with  $^{256}\text{Lr}$  decay, so this interpretation seems likely. The observed  $^{264}\text{Bh}$  half-life was  $0.9^{+0.3}_{-0.2}$  s, in good agreement with the GSI data ( $1.0^{+0.7}_{-0.3}$  s).

Twelve events attributed to  $^{260}\text{Db}$  were reported by the RIKEN group. Among these, one was a fission event consistent with the known SF branch of  $(9.6 \pm 0.6)\%$  [Bemis1977], although they suggest that  $^{260}\text{Db}$  might decay by electron-capture to the known nuclide  $^{260}\text{Rf}$  which then underwent SF with a 20-ms half-life [Firestone1996]. Also significant was the observation of three long-lived events which were attributed to an isomer in  $^{260}\text{Db}$ . However, this evidence appears weak as one of these events might actually be due to  $^{256}\text{Lr}$  as described above. Also, the shortest-lived event of these three  $^{260}\text{Db}$  events (10.9 s lifetime) might be due to a statistical fluctuation in the lifetime distribution with known half-life  $1.52 \pm 0.13$  s [Bemis1977]. (The GSI group also observed one  $^{260}\text{Db}$  event with a long lifetime of 14.98 s). Nevertheless, Morita and coworkers attribute these decays to an isomeric state with a half-life of  $19^{+25}_{-7}$  s. Lastly, the RIKEN group observed two decays with higher energies than previously reported (9340 keV and 9400 keV), which is important for the current work (see Sec. 4.3). The measured half-life for the non-isomeric state was  $1.5^{+0.8}_{-0.4}$  s, in agreement with Bemis and coworkers' data.

Finally, the alpha-decay energies and half-life of  $18^{+10}_{-5}$  s measured by Morita *et al.* for  $^{256}\text{Lr}$  are in agreement with literature data [Bemis1977] for the decay of this nuclide. Based on these decay chains, the discovery of element 111 by the GSI group was confirmed at an independent laboratory (RIKEN) using the same reaction as the GSI group.

#### 4.1.3. *Rationale for the New Experiment*

At both GSI and RIKEN, experiments designed to produce  $^{271}\text{Ds}$  in the  $^{208}\text{Pb}(^{64}\text{Ni}, \text{n})$  reaction were conducted in preparation for the experiments on element 111. When these preparatory experiments were completed, both groups faced two options for the next reaction to study. One option would be to add a proton to the target using the  $^{209}\text{Bi}(^{64}\text{Ni}, \text{n})^{272}\text{111}$  reaction; another option would be to add the proton to the projectile using the  $^{208}\text{Pb}(^{65}\text{Cu}, \text{n})^{272}\text{111}$  reaction. Both groups chose the former reaction because of the general perception that the cross section would be larger for the first option. One of the aims of the current research is to quantify this difference by measuring the cross section of the latter reaction for the first time.

In addition to providing additional information on the decay properties of  $^{272}\text{111}$ , this work would provide an even stronger confirmation of the discovery of element 111 using a different reaction than did the GSI group. The observation of decay chains originating from the same nuclide but produced in a cross bombardment reaction would give significant additional credibility to the original work by demonstrating that no systematic problems existed in the original GSI experiments that were then reproduced in the RIKEN experiments.

## 4.2. **Experimental Conditions**

The production of  $^{272}\text{111}$  in the  $^{208}\text{Pb}(^{65}\text{Cu}, \text{n})$  reaction had not been studied before this work, so it was necessary to estimate the beam energy where the largest cross section would be obtained. Using the “optimum energy rule” described in Sec. 1.2.2, it was estimated that the optimum  $^{65}\text{Cu}$  bombarding energy in the  $^{208}\text{Pb}(^{65}\text{Cu}, \text{n})^{272}\text{111}$  reaction should be 9.6 MeV higher in the lab frame than the optimum  $^{64}\text{Ni}$  bombarding energy in

the  $^{208}\text{Pb}(^{64}\text{Ni}, \text{n})^{271}\text{Ds}$  reaction. This calculation included reaction Q-values based on masses and fission barrier heights from [Myers1994] with an additional correction for the pairing energy of the residual nucleus. The optimum  $E_{\text{cat}}$  in the  $^{64}\text{Ni} + ^{208}\text{Pb}$  reaction was 311.5 MeV, so an energy of 311.5 MeV + 9.6 MeV = 321.1 MeV was chosen for the  $^{65}\text{Cu}$  projectiles.

Experimental conditions were similar to those for the experiments on the production of  $^{271}\text{Ds}$  in the  $^{208}\text{Pb}(^{64}\text{Ni}, \text{n})$  reaction (see Sec. 3.2). During two consecutive weeks, two new runs (BGS runs 067 and 068) were conducted with a beam of  $E_{\text{cat}} = 321.1$  MeV  $^{65}\text{Cu}^{15+}$ . The beam energy from the 88-Inch Cyclotron was 326.9 MeV and the average beam current on-target was  $\sim 160$  pnA. The same 0.47-mg/cm<sup>2</sup>  $^{208}\text{Pb}$  targets were used as in the  $^{64}\text{Ni}$  runs, and the excitation energy of compound nuclei formed in the center of the targets was 13.2 MeV. These targets were supported on  $35 \pm 5$ - $\mu\text{g}/\text{cm}^2$  <sup>nat</sup>C backings and covered with additional  $5 \pm 2$ - $\mu\text{g}/\text{cm}^2$  <sup>nat</sup>C foils. During the two runs combined, a total dose of  $6.6 \times 10^{17}$  particles was collected. Based on the magnetic rigidity of 2.09 T m for  $^{271}\text{Ds}$  evaporation residues (EVRs) observed in the  $^{208}\text{Pb}(^{64}\text{Ni}, \text{n})$  reaction, a rigidity of 2.08 T m was estimated for  $^{272}\text{Cu}$  in the  $^{208}\text{Pb}(^{65}\text{Cu}, \text{n})$  reaction. The BGS magnet currents were set to Q1 = 1582 A, M1 = 353 A, and M2 = 600 A. The “window” separating the gas-filled separator from the evacuated beamline was the same as in the  $^{271}\text{Ds}$  experiments. Starting in the middle of the first week (run 067), the BGS He pressure was reduced to 0.5 torr to help minimize the number of broken windows by reducing the pressure difference across the window. The same multi-wire proportional counter (MWPC) was placed upstream of the focal plane detectors to discriminate implantation events from radioactive decays. The test reactions  $^{65}\text{Cu} + ^{116}\text{Sn}$ , <sup>nat</sup>BaBr<sub>2</sub> were used to produce alpha-decaying

neutron-deficient isotopes of Au, Pt, At, and Po to check the performance of the system and for calibration purposes.

The beam shutoff analysis described in Sec. 3.2 was also active during these experiments. The EVR- $\alpha$  gate was activated by an EVR of 15-45 MeV followed within 4.0 s by an alpha particle of 9300-12000 keV. (Halfway through the first run, the EVR window was expanded to 15-60 MeV). The maximum position difference was 3.5 mm, or 7.0 mm if the EVR saturated the signal in the low-energy amplifier. When these conditions were satisfied the beam was shut off for 9.0 s, long enough to observe decays of  $^{264}\text{Bh}$  and possibly  $^{260}\text{Db}$ . An additional alpha particle during the EVR- $\alpha$  shutoff with energy 8800-12000 keV in the same position as the previous alpha would activate the EVR- $\alpha$ - $\alpha$  gate. This latter gate could extend the shutoff for up to an additional 150.0 s. During the two runs, ten short shutoffs were initiated. The EVR- $\alpha$ - $\alpha$  gate conditions were satisfied on one occasion but the beam did not shut off due to a bias supply problem in the beam “chopper.” The decay chain that initiated this “shutoff” is discussed in the next section.

### 4.3. Observed Decay Chain

One decay chain of interest was observed during the two  $^{65}\text{Cu}$  runs and is shown in detail in Fig. 4.2. Alpha decay data have been corrected for the energy of the recoiling daughter. Note that the standard deviation in energy is  $\sim$ 17 keV for fully stopped alpha particles and  $\sim$ 45 keV for reconstructed alphas (those where the total energy is the sum of focal plane and upstream energies). Positions are given so that -29 mm is the bottom of the strip and +29 mm is the top of the strip. No attempt is made to estimate half-lives for

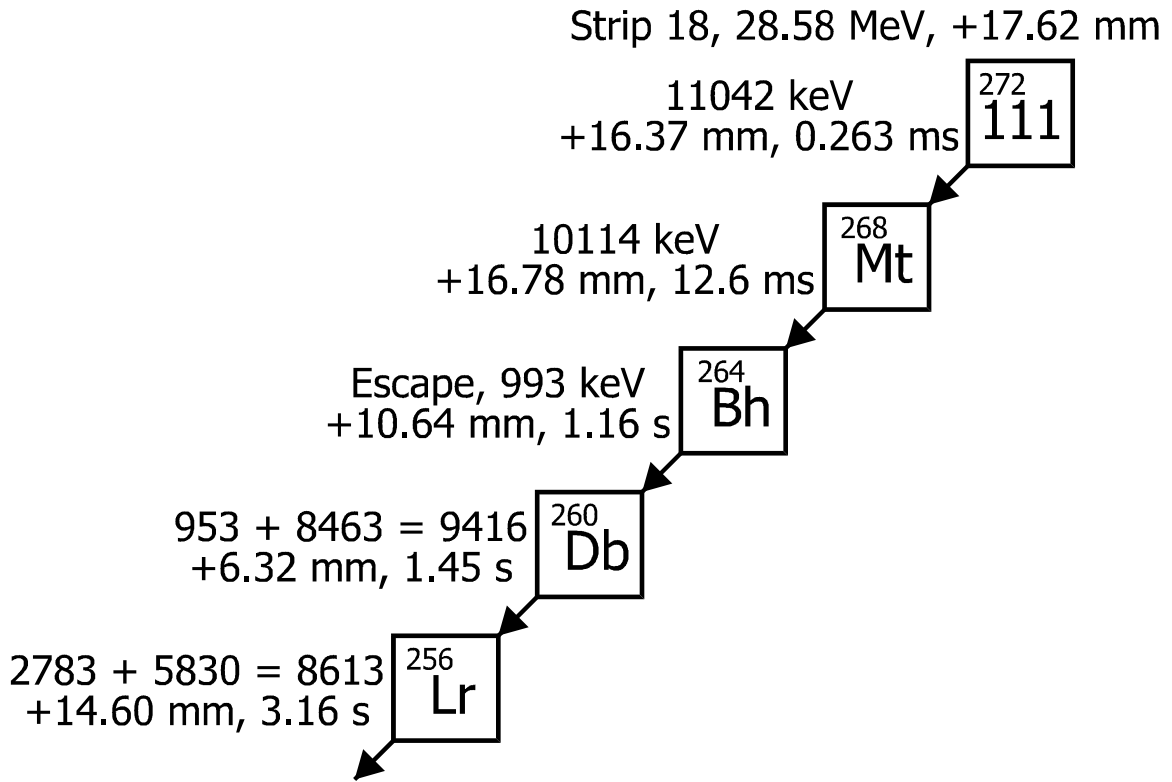


FIG. 4.2. Decay chain observed in the irradiation of  $^{208}\text{Pb}$  targets with  $^{65}\text{Cu}$ . The lab-frame, center-of-target energy was 321.1 MeV. The implantation event is described above the chain. The notation  $x + y = z$  indicates that an event with energy  $x$  keV was observed in the strip detector and an event with  $y$  keV was observed simultaneously in an upstream detector, with sum  $z$  keV. Position are given from -29 mm to +29 mm.

the nuclides produced since only one decay was observed in each case and the half-lives have been measured elsewhere as described earlier.

*Implantation Event.* The event began in strip 18 with an implantation event observed at a position of +17.62 mm whose pulse height corresponded to 28.58 MeV. This pulse height is close to the measured pulse heights of  $25.9 \pm 1.6$  MeV obtained for  $^{271}\text{Ds}$  EVRs described in Chapter 3, as would be expected for a  $^{272}\text{111}$  EVR. The MWPC detector registered four signals (top, bottom, left, and right) as expected for a recoiling high- $Z$  atom. All four signals were above the noise but not saturated, and within the range expected for a  $^{272}\text{111}$  EVR. A time-of-flight signal between the MWPC and the focal plane

was also recorded and is within the range expected. This event appears to be a true implantation event.

$^{272}\text{111}$ . After the implantation event was observed, an alpha particle with energy 11042 keV and position +16.27 mm was observed 0.263 ms later. The decay energy is in excellent agreement with the  $^{272}\text{111}$  alpha group at 11027 keV reported in [Hofmann2002] and [Morita2004b]. This energy is in especially good agreement with the event at 11046 keV reported in chain six of [Hofmann2002] and the 11040-keV and 11060-keV events in chains 2 and 9, respectively, in [Morita2004b]. The lifetime of 0.263 ms is consistent with the measured half-lives of  $3.8^{+1.4}_{-0.8}$  ms [Morita2004b] and  $1.6^{+1.1}_{-0.5}$  ms [Hofmann2002], and is therefore assigned to the decay of  $^{272}\text{111}$ .

$^{268}\text{Mt}$ . Another fully stopped alpha particle of energy 10114 keV was observed 12.6 ms after the  $^{272}\text{111}$  event. The position of this event was +16.78 mm, in close proximity to the previous alpha and implantation events. The observed energy is in good agreement with the alpha-decay energy of 10097 keV observed for the  $^{268}\text{Mt}$  decay in chain 2 of [Hofmann1995b]. Again, the lifetime is consistent with half-lives measured at both RIKEN ( $21^{+8}_{-5}$  ms) and GSI ( $42^{+29}_{-12}$  ms). Based on these considerations, this alpha decay is assigned to  $^{268}\text{Mt}$ .

The presence of these three events (the implantation events and two alpha events), correlated in time, energy, and position, provide strong evidence for the presence of a high- $Z$  element, which is assigned to  $^{272}\text{111}$ . This assignment is strengthened further by the additional decays described below.

$^{264}\text{Bh}$ . An “escape” event with energy 993 keV was observed in the same strip as the previous alpha events, and followed the second one by 1.16 s. This lifetime is consistent

with the reported  $^{264}\text{Bh}$  half-lives of  $0.9_{-0.2}^{+0.3}$  s [Morita2004b] and  $1.0_{-0.3}^{+0.7}$  s [Hofmann2002].

The position of this event was +10.64 mm, which differs from the position of the previous three events. This is because the position resolution of the focal plane is inversely proportional to the energy deposited in the focal plane [Gregorich2004]. This is clearly visible in the reconstructed alpha events that are part of  $^{271}\text{Ds}$  decay chains in Fig. 3.3, some of which differ in position from the full energy events by large amounts (more than 10 mm). A similar degradation of position resolution with decreasing focal plane energy has been reported for the GARIS separator; see Fig. 3 in [Morita2004d]. Thus, the observed position difference is not surprising.

It should also be mentioned that this escape event was observed in coincidence with two signals from the MWPC detector. The MWPC produces four signals, labeled top, bottom, left, and right. The signals recorded in coincidence with the escape event were 489 channels in the “right” signal and 491 channels in the “left” signal. The high- $Z$  EVRs studied in this work produce on-scale signals in all four channels when passing through the MWPC. Thus, this escape event is not actually an implantation event. No punch-through signal was recorded in coincidence with the escape, so it cannot be attributed to a high-energy implanting proton or scattered He from the fill gas. Fig. 4.3 shows the four MWPC signals separately in coincidence with alpha particle events for strip 18 during run 068, when the escape event occurred. First, there is clear evidence that these signals are coming in coincidence with escape alpha particles of energy  $\sim$ 1000 keV, and that they are of the magnitude observed in the present case. It is possible that the escaping alpha particle (now with energy  $\sim$ 8300 keV) passed through the MWPC and deposited some energy, producing the observed signals. The variation of MWPC signal size at constant focal plane energy might be attributed to differences in the position where the alpha particle strikes

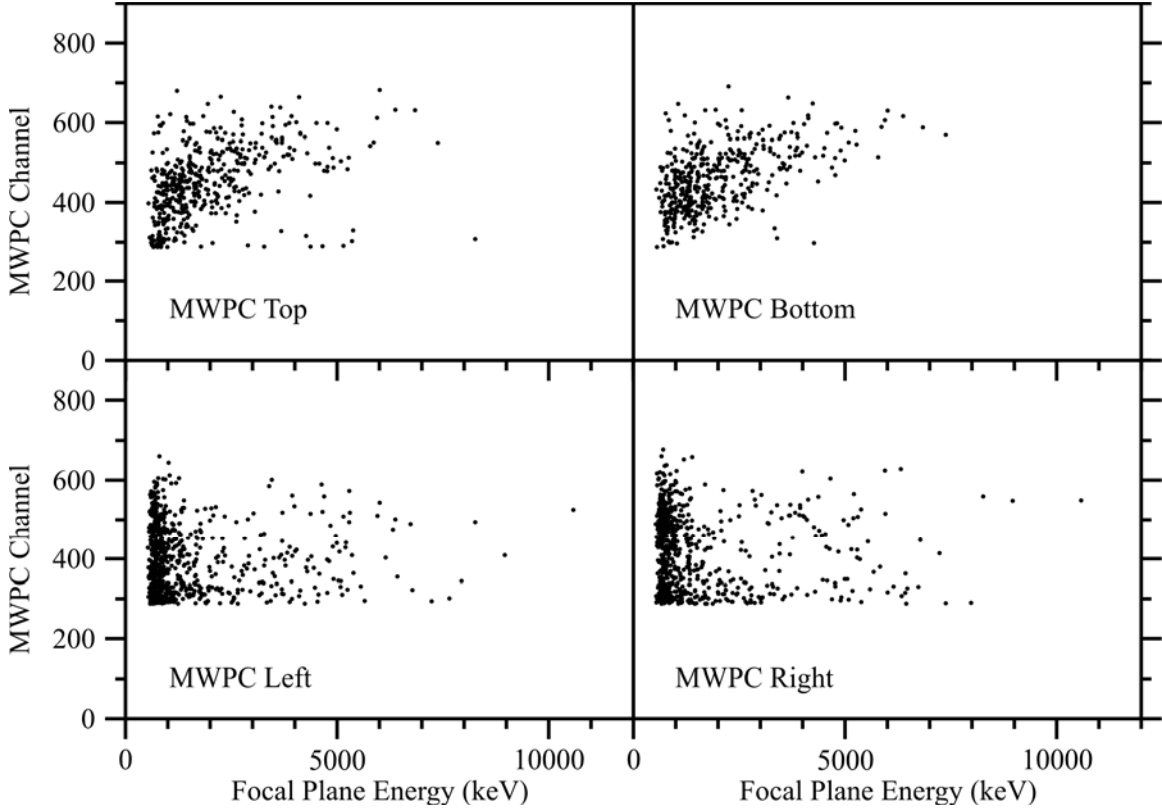


FIG. 4.3. MWPC signals in coincidence with alpha particles emitted in strip 18 during BGS run 068, as a function of alpha particle energy deposited in the focal plane detector. See the main text for a discussion.

the MWPC, although this is seen more clearly in the “top” and “bottom” spectra. Thus, this escape event appears to be a real alpha-particle event. Since this event followed the decay of  $^{268}\text{Mt}$  and has a lifetime consistent with  $^{264}\text{Bh}$ , it is assigned to  $^{264}\text{Bh}$ . The possibility that this event is not part of the chain is considered in Sec. 4.4.

$^{260}\text{Db}$ . The next event was a reconstructed alpha event observed 1.45 s after the escape alpha event. The energy deposited in the focal plane was 953 keV, and the energy deposited in upstream detector 0 was 8463 keV, for a sum of 9416 keV. The lifetime is consistent with the previously reported value of  $1.52 \pm 0.13$  s [Bemis1977], but the decay energy is not consistent with those measured in that work. Yet, it is consistent with the

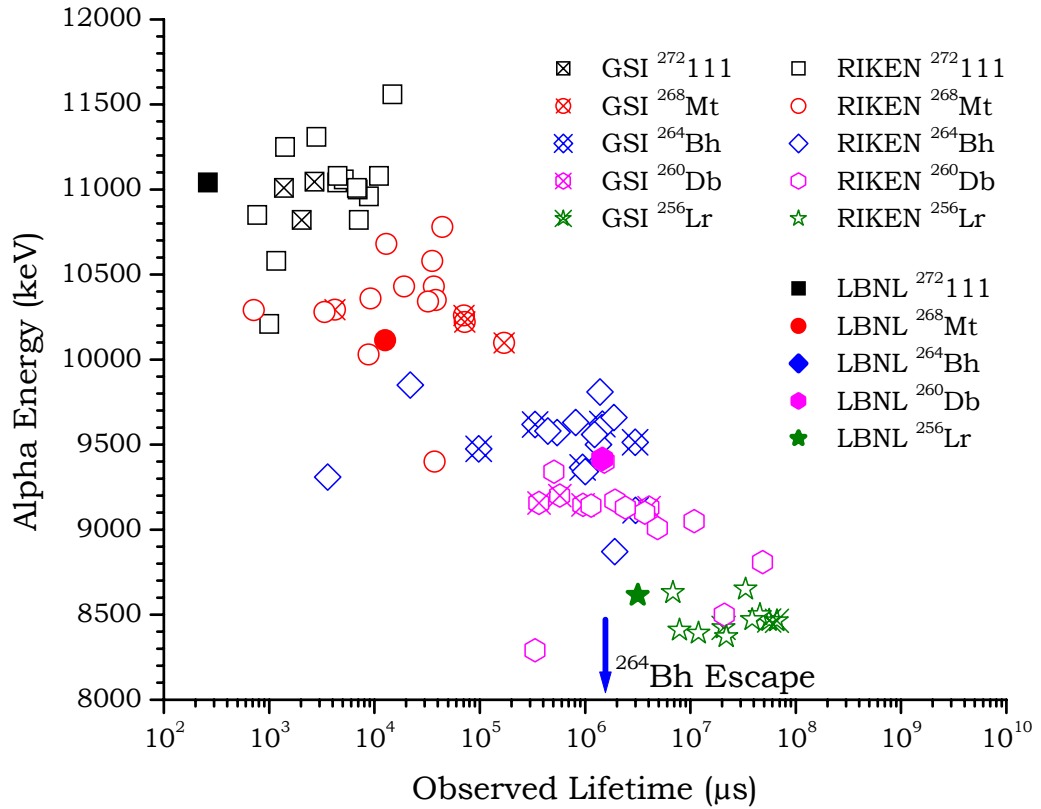


FIG. 4.4. Observed energy versus lifetime for all alpha particles produced in  $^{272}\text{111}$  decay chains. Different nuclides are represented by different shapes and colors: black squares for  $^{272}\text{111}$ , red circles for  $^{268}\text{Mt}$ , blue diamonds for  $^{264}\text{Bh}$ , magenta hexagons for  $^{260}\text{Db}$ , and green stars for  $^{256}\text{Lr}$ . GSI data have an “x” through them, RIKEN data are open symbols, and the current data are filled symbols. The lifetime of the  $^{264}\text{Bh}$  escape event observed in the current work is indicated.

alpha energies measured in chain 4 of [Morita2004b] (9400 keV). The calculated position was +6.32 mm, further illustrating the loss of position resolution with decreasing energy described in this Section. However, due to the agreement of the observed lifetime and decay energy with the previously reported data, this event is assigned to  $^{260}\text{Db}$ .  $^{256}\text{Lr}$ . The final alpha event in the chain is another reconstructed alpha which deposited 2783 keV in strip 18 and 5830 keV in upstream detector 4, with sum 8613 keV.

The position calculated based on the energy deposited in the focal plane is +14.60 mm, illustrating the large improvement in position resolution obtained compared to deposition of only  $\sim$ 1000 keV. The lifetime of this event was 3.16 s and is consistent with the half-life of  $31 \pm 3$  s reported by Eskola, Eskola, Nurmia, and Ghiorso [Eskola1971] obtained in the direct production of  $^{256}\text{Lr}$ . The alpha energy is consistent with one of their measured energies:  $E_\alpha = 8640 \pm 20$  keV [branch  $(3 \pm 2)\%$ ]. With only one event observed in the current work it seems unjustified to debate the likelihood of seeing this small branch. The current alpha-decay energy is also in agreement with chains 3 and 14 in [Morita2002b]. Thus, this event is assigned to  $^{256}\text{Lr}$ . Following this event, no fission or alpha events with energy greater than 1000 keV were observed within 150 s of the implantation event at any location in the strip.

In summary, two experiments were conducted to study the  $^{208}\text{Pb}(^{65}\text{Cu}, n)^{272}\text{111}$  reaction. A total dose of  $6.6 \times 10^{17} \text{ }^{65}\text{Cu}^{15+}$  particles was collected and one decay chain was observed. The comparison of events in the chain with previously reported data for the  $^{209}\text{Bi}(^{64}\text{Ni}, n)^{272}\text{111}$  reaction is shown in Fig. 4.4. Based on this one decay chain, an estimated BGS transmission of  $(70 \pm 10)\%$ , a chain detection efficiency of  $(95 \pm 5)\%$ , and a Rutherford screening efficiency of  $(1348 \pm 20)^{-1}$ , the calculated cross section was  $1.7_{-1.4}^{+3.9}$  pb. This cross section is shown along with a theoretical prediction for the  $^{208}\text{Pb}(^{65}\text{Cu}, n)^{272}\text{111}$  excitation function in Fig. 4.5. Given the magnet settings and observation of this decay chain in strip 18, the estimated magnetic rigidity of the  $^{272}\text{111}$  EVR in He gas was 2.10 T m. The calculated EVR charge state based on this rigidity is approximately +10.

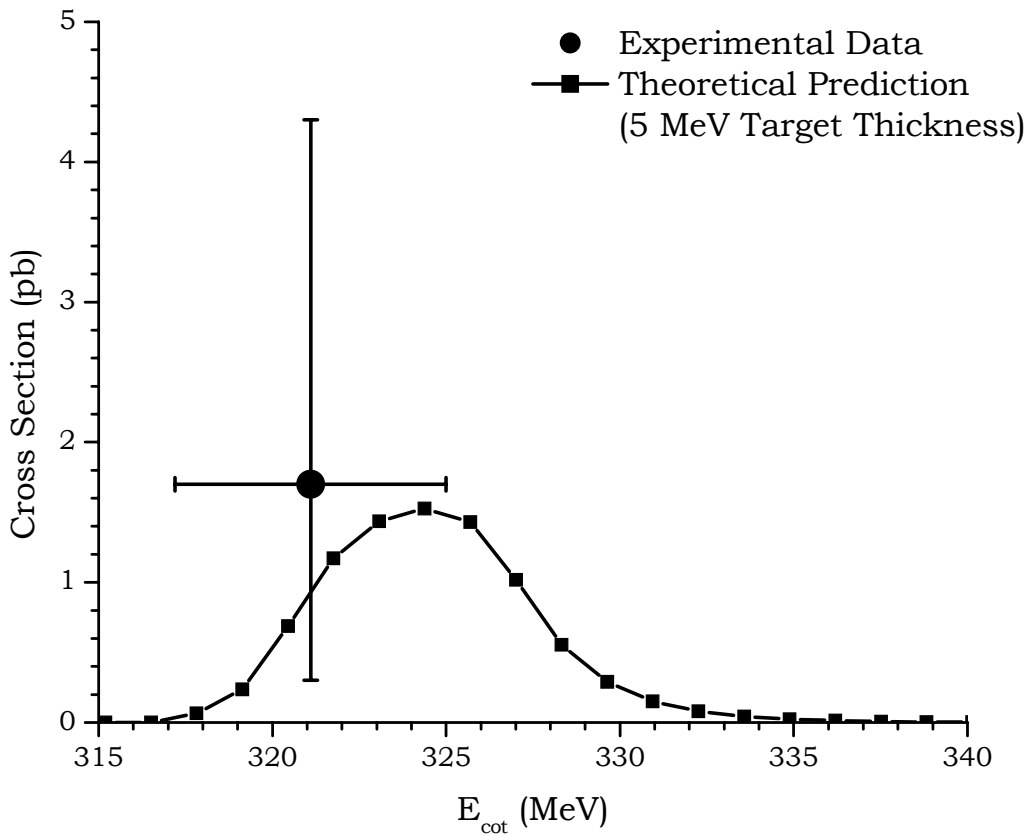


FIG. 4.5. Theoretical excitation function and experimental data for the  $^{208}\text{Pb}(^{65}\text{Cu}, \text{n})^{272}\text{111}$  reaction. The experimental data comes from this work. The theoretical prediction comes from [Świątecki2004a] and has a 5-MeV target thickness folded in. The vertical error bars represent  $1\sigma$  (68%) errors in the cross section and the horizontal error bars represent the range of energies covered by the beam as it passes through the target.

#### 4.4. Exclusion of Other Possible Interpretations

When doing an experiment of this type it is necessary to be able to eliminate other possible interpretations of the results based on careful analysis and evaluation of all relevant data. This leads to confidence in the assignments proposed and assurance that some unexpected factor has not influenced the data. (A similar analysis is conducted in Sec. 3 of [Morita2004b]).

The first sign that the assignments are correct is the agreement between the observed data and that published previously [Morita2004b, Hofmann2002, Hofmann1995b]. This has been discussed extensively in Sec. 4.3 and will not be repeated here.

The first alternative explanation for the data is that the chain begins with a nuclide that is not the product of complete fusion. This possibility can be excluded because lighter elements do not exhibit the very high alpha decay energies (greater than 10 MeV) observed in the current work, except for  $^{212}\text{Po}^m$  [ $E_\alpha = 11650$  (97%), 8520 (2%), 9080 (1%) keV] [Firestone1996]. The only observed alpha-decay energy close to these groups is the  $^{256}\text{Lr}$  decay at 8613 keV, and this differs from 8520 keV by  $\sim 2.7$  standard deviations.

One concern expressed in Sec. 4.3 was that the escape event attributed to  $^{264}\text{Bh}$  might not actually be part of the decay chain. In that case, the two reconstructed alpha events would be “moved up” so that the 9416-keV event is now  $^{264}\text{Bh}$  and the 8613-keV event is now  $^{260}\text{Db}$ . The 9416-keV energy agrees roughly with those reported for  $^{264}\text{Bh}$ , but 8613 keV is more than  $\sim 400$  keV less than the  $^{260}\text{Db}$  energies reported by Morita *et al.* [Morita2004b], Bemis *et al.* [Bemis1977], and Ghiorso *et al.* [Ghiorso1970]. Thus, this possibility is excluded, and the escape event is considered part of the decay chain.

Given the fact that all nuclides in the decay chain are odd-odd and neutron-deficient they are expected to have large Q-values for electron capture. It is possible that one or more electron capture (EC) decays occurred in addition to the alpha decays detected. If only one EC occurred among  $^{272}\text{Rf}$ ,  $^{268}\text{Mt}$ ,  $^{264}\text{Bh}$ , or  $^{260}\text{Db}$ , then the alpha chain would end at 21-ms  $^{260}\text{Rf}$  which decays by SF (100%). Since fission was not observed, this possibility can be excluded. Also, EC in  $^{272}\text{Rf}$  or  $^{268}\text{Mt}$  would lead to  $^{265}\text{Bh}$ , and no decays are consistent with its reported decay properties ( $t_{1/2} = 0.94^{+0.70}_{-0.31}$  s,  $E_\alpha = 9240 \pm 50$  keV) [Gan2004]. Two or more ECs in the decay chain would lead to nuclides with alpha

energies significantly lower than those observed here, so EC can be excluded entirely. No EC decays were reported in [Morita2004b, Hofmann2002, Hofmann1995b].

Additionally, it is possible that the compound nucleus decayed by some mode other than the emission of one neutron. The energetics of some of these deexcitation processes are discussed in Sec. 1.2.1.3. The  $2n$  exit channel is forbidden because the excitation energy in the compound nucleus (13.2 MeV for compound nuclei formed at the center of the target) is insufficient for evaporation of two neutrons. The  $p$  and  $\alpha$  exit channels are significantly hindered relative to neutron emission as discussed in Sec. 1.2.1.3. Also, the  $p$  exit channel decay chain would proceed through the same nuclides as  $1n$  emission followed by ground state EC decay ( $^{272}\text{Ds}$ ,  $^{268}\text{Hs}$ ,  $^{264}\text{Sg}$ , and  $^{260}\text{Rf}$ ), and can be excluded for the same reasons. The alpha exit-channel would produce the unknown nuclide  $^{269}\text{Mt}$ . Its alpha decay leads to  $^{265}\text{Bh}$ , so this exit channel can be excluded as described above. Finally, the radiative capture channel has not been observed in any heavy system [Morita2004b] and is excluded for that reason.

Thus, due to its agreement with published data and the improbability of other explanations, this decay chain is assigned to the nuclide  $^{272}\text{111}$  produced in the  $^{208}\text{Pb}(^{65}\text{Cu}, n)$  reaction.

## 4.5. Analysis of Expected Random Correlations

The same random correlation analysis was performed for the current experiment as in the  $^{271}\text{Ds}$  experiments, except that all five nuclides ( $^{272}\text{111}$ ,  $^{268}\text{Mt}$ ,  $^{264}\text{Bh}$ ,  $^{260}\text{Db}$ , and  $^{256}\text{Lr}$ ) are treated together, rather than the last nuclide being treated separately. The reader is referred to Sec. 3.4.1 for a detailed description of how the calculations are performed. The results are summarized in Table 4.2.

TABLE 4.2. Analysis of expected random correlations in the  $^{272}\text{Rb}$  experiments. In all cases,  $\Delta t_{max}$  was 180 s (approximately six  $^{256}\text{Lr}$  half-lives) and the pixel size was 3.0 mm (928 total pixels). The alpha particle rates are those measured at full beam intensity and combine alpha particles fully stopped in the focal plane with reconstructed ones.

Apparent calculation errors in the “Runs Combined” column are due to rounding errors.

	$E_{cut} = 321.1 \text{ MeV}$		
	Run 067	Run 068	Runs Combined
Overall Rate of Alphas with Energy 8200-12000 keV (s <sup>-1</sup> )	$3.7 \times 10^{-3}$	$5.0 \times 10^{-3}$	$4.4 \times 10^{-3}$
Rate of Alphas Per Pixel with Energy 8200-12000 keV (s <sup>-1</sup> )	$3.9 \times 10^{-6}$	$5.4 \times 10^{-6}$	$4.8 \times 10^{-6}$
$\mu$ (Expected Number of Alpha Particle Events Per Pixel in $\Delta t_{max}$ )	$7.1 \times 10^{-4}$	$9.8 \times 10^{-4}$	$8.6 \times 10^{-4}$
$N_{EVR}$	$2.0 \times 10^{+5}$	$1.8 \times 10^{+5}$	$3.7 \times 10^{+5}$
Probability of Exactly Two Alphas in the Same Pixel in $\Delta t_{max}$	$2.5 \times 10^{-7}$	$4.8 \times 10^{-7}$	$3.7 \times 10^{-7}$
Expected Number of Random Correlations ( $n_\alpha = 2$ )	$5.0 \times 10^{-2}$	$8.4 \times 10^{-2}$	$14 \times 10^{-2}$
Probability of Exactly Four Alphas in the Same Pixel in $\Delta t_{max}$	$1.1 \times 10^{-14}$	$3.8 \times 10^{-14}$	$2.3 \times 10^{-14}$
Expected Number of Random Correlations ( $n_\alpha = 4$ )	$2.1 \times 10^{-9}$	$6.6 \times 10^{-9}$	$8.5 \times 10^{-9}$

The overall rates per pixel of alpha particles with the expected energies (8200-12000 keV) are low in both runs 067 and 068:  $3.9 \times 10^{-6} \text{ s}^{-1}$  and  $5.4 \times 10^{-6} \text{ s}^{-1}$ , respectively. Yet due to lengthy runs, the expected numbers of EVR- $\alpha$ - $\alpha$  correlations ( $n_\alpha = 2$ ) were relatively high:  $5.0 \times 10^{-2}$  and  $8.4 \times 10^{-2}$ . Once this calculation is extended to EVR- $\alpha$ - $\alpha$ - $\alpha$  ( $n_\alpha = 4$ ) correlations, of the type observed in the current decay chain, these numbers drop significantly to  $2.1 \times 10^{-9}$  and  $6.6 \times 10^{-9}$ . In both the  $n_\alpha = 2$  and  $n_\alpha = 4$  cases, these numbers are really upper limits since there are no requirements that  $(5 - n_\alpha)$  escape alpha particles be present to complete the chain, that the lifetimes of the events agree with the

known half-lives, or that the alpha energies vary smoothly from one nuclide to the next along the chain, as is known and predicted by theory below the  $N = 162$  subshell.

## 4.6. Comparison with the $^{209}\text{Bi}(^{64}\text{Ni}, \text{n})^{272}\text{111}$ Reaction

One of the reasons cited for the current study was the desire to quantify the difference in maximum cross section between the  $^{209}\text{Bi}(^{64}\text{Ni}, \text{n})^{272}\text{111}$  and  $^{208}\text{Pb}(^{65}\text{Cu}, \text{n})^{272}\text{111}$  reactions. For the  $^{64}\text{Ni} + ^{209}\text{Bi}$  reaction, the result obtained at RIKEN was  $2.6^{+2.3}_{-1.5}$  pb at  $E_{\text{col}}(^{64}\text{Ni}) = 317.5$  MeV and the result obtained at GSI was  $2.9^{+1.9}_{-1.3}$  pb at  $E_{\text{col}}(^{64}\text{Ni}) = 316.0$  MeV. For the  $^{65}\text{Cu} + ^{208}\text{Pb}$  reaction, measured for the first time in this work, the maximum cross section was  $1.7^{+3.9}_{-1.4}$  pb at  $E_{\text{col}}(^{65}\text{Cu}) = 321.1$  MeV. The cross sections for the two reactions can be said to be comparable within the very large statistical uncertainties on the experimental values. Further work is needed to clarify this point. However, the current results show that using odd- $Z$  projectiles for the synthesis of odd- $Z$  heavy elements is feasible.

One final comment should be made concerning the measured cross section for the  $^{208}\text{Pb}(^{65}\text{Cu}, \text{n})^{272}\text{111}$  reaction. Fig. 4.5 shows the cross section along with a theoretical prediction for the corresponding excitation function from Świątecki, Siwek-Wilczyńska, and Wilczyński [Świątecki2004a]. Their excitation function indicates that it may be advantageous to repeat the experiment at an  $E_{\text{col}}$  3 MeV higher in the laboratory frame. However, their excitation function was not yet published at the time of the experiment, so the “optimum energy rule” was applied to both the  $^{208}\text{Pb}(^{64}\text{Ni}, \text{n})^{271}\text{Ds}$  and  $^{208}\text{Pb}(^{65}\text{Cu}, \text{n})^{272}\text{111}$  reactions and the difference was added to the measured optimum energy for the  $^{64}\text{Ni} + ^{208}\text{Pb}$  reaction. This resulted in the experimental “optimum”  $^{65}\text{Cu} +$

$^{208}\text{Pb}$  energy that we used being less than the rule would predict if used directly. The same discrepancy was observed in the  $^{64}\text{Ni} + ^{208}\text{Pb}$  reaction (see Fig. 3.1).

## 5. Production of $^{262}\text{Bh}$ in the $^{208}\text{Pb}(^{55}\text{Mn}, \text{n})$ Reaction

### 5.1. Previous Work

#### 5.1.1. Dubna Experiments

The  $^{55}\text{Mn} + ^{208}\text{Pb}$  reaction was first studied by Oganessian *et al.* [Oganessian1976, Oganessian1976] at the Joint Institute for Nuclear Research in Dubna, Russia, USSR using their rotating drum technique. (The names “Oganesyan” and “Oganessian” refer to the same person, but differ because the earlier transliteration was different than currently in use. Oganessian will be used hereafter). A thick target of  $^{208}\text{Pb}$  (2-3 mg/cm<sup>2</sup>) was deposited on the surface of a drum which rotated at constant velocity inside an outer housing. The inside surface of the housing was coated with mica track detectors. The  $^{55}\text{Mn}$  beam was incident on the target tangential to the direction of rotation. The target thickness was chosen so that recoiling evaporation residues (EVRs) would be stopped in the target. As the target continued to rotate, any SF events would be recorded as tracks created in the mica detectors by the fission fragments. The half-life of the fissioning nuclide could be estimated later from the known rotation speed of the drum and the distribution of tracks in the mica detectors along the circumference of the housing.

The goal of these experiments was to synthesize element 107 (bohrium, Bh) for the first time using the  $^{208}\text{Pb}(^{55}\text{Mn}, 2\text{n})^{261}\text{Bh}$  reaction. The cross bombardment reaction  $^{209}\text{Bi}(^{54}\text{Cr}, 2\text{n})^{261}\text{Bh}$  was also studied using the same technique. At that time, the systematics of cold fusion reactions producing transactinide elements were not well established and it was believed that the 2n reaction should have a higher cross section than the 1n reaction. With an incident beam energy of 290-MeV  $^{55}\text{Mn}$ , Oganessian and coworkers observed fission tracks with a half-life of 1 to 2 ms. From these data, the branching ratio for SF in  $^{261}\text{Bh}$  was estimated to be  $\sim 20\%$  based on the following reasoning. It was presumed that the  $^{261}\text{Bh}$  alpha-decay daughter  $^{257}\text{Db}$  had been synthesized in the  $^{209}\text{Bi}(^{50}\text{Ti}, 2\text{n})$  reaction and decayed partially by SF. By comparing the yield of fission tracks with a calculated reaction cross section, it was estimated that the SF branch in  $^{257}\text{Db}$  was  $\sim 20\%$ . In the reaction  $^{209}\text{Bi}(^{54}\text{Cr}, 2\text{n})^{261}\text{Bh}$ , the yield of fission fragments was approximately the same as in the  $^{209}\text{Bi}(^{50}\text{Ti}, 2\text{n})^{257}\text{Db}$  reaction, so the same  $\sim 20\%$  SF branch was assigned to  $^{261}\text{Bh}$ . In the cross bombardment reaction  $^{208}\text{Pb} + ^{55}\text{Mn}$ , a 1-to-2-ms SF activity was also observed and again assigned to  $^{261}\text{Bh}$  as the 2n reaction product. The cross section for production of  $^{261}\text{Bh}$  in the  $^{208}\text{Pb}(^{55}\text{Mn}, 2\text{n})$  reaction was later reported to be 20 pb [Flerov1987].

In later Dubna experiments on the production of odd- $Z$  transactinide elements in cold fusion reactions, Oganessian *et al.* [Oganessian1984] continued to use track detectors to record fissions online but added periodic offline chemical separations to look for long-lived daughter activities. The  $^{55}\text{Mn} + ^{208}\text{Pb}$  reaction was studied again but at an initial beam energy of 302.5 MeV, which they assumed would produce  $^{262}\text{Bh}$  via the  $^{208}\text{Pb}(^{55}\text{Mn}, \text{n})$  reaction. The online fission tracks observed with a half-life of  $4.2_{-1.0}^{+1.4}$  s were assigned to  $^{258}\text{Db}$ , assumed to be the alpha-decay daughter of  $^{262}\text{Bh}$ . After chemical

separation, long-lived  $^{246}\text{Cf}$  ( $t_{1/2} = 35.7$  h) was also identified and assumed to be the result of the  $^{262}\text{Bh}$  decay chain. The reported cross section for the  $^{208}\text{Pb}(^{55}\text{Mn}, \text{n})^{262}\text{Bh}$  reaction was 0.1 nb for 310-MeV  $^{55}\text{Mn}$  projectiles incident on the thick target [Oganessian1984].

### 5.1.2. Studies of the $^{209}\text{Bi}(^{54}\text{Cr}, \text{n})^{262}\text{Bh}$ Reaction at GSI

A serious problem in the acceptance of the Dubna work as proof of the first synthesis of bohrium is the nonspecificity inherent in SF detection and the absence of any observations conclusively identifying the nuclide undergoing decay. In the case of bohrium, two different SF activities were identified, but an alpha-decay relationship between them had been assumed, not observed. The chemical separations had revealed the presence of an appropriate long-lived daughter, but this required many assumptions to claim a genetic relationship to bohrium. The rotating drum technique for SF detection was simply not adequate for these new element searches.

The first conclusive proof of the existence of element 107 was reported by Münzenberg *et al.* [Münzenberg1981a, Münzenberg1989] using SHIP [Ewald1976, Münzenberg1979] at GSI. SHIP effectively separates products of interest from background activities and beam, and its focal plane detectors are sensitive to the time, position, and energy of implantation events, alpha decays, and fission fragments. Münzenberg and coworkers studied the production of  $^{262,261}\text{Bh}$  in  $^{209}\text{Bi}(^{54}\text{Cr}; 1,2\text{n})$  reactions. They observed that these bohrium isotopes alpha-decayed through previously unknown nuclides of Db and Lr to known nuclides of  $^{250}\text{Fm}$ ,  $^{250}\text{Md}$ , and  $^{249}\text{Md}$  providing definitive assignments of the mass and atomic numbers. The production cross sections are shown in Fig. 5.1 and Table 5.1, which also summarizes the current experiments.

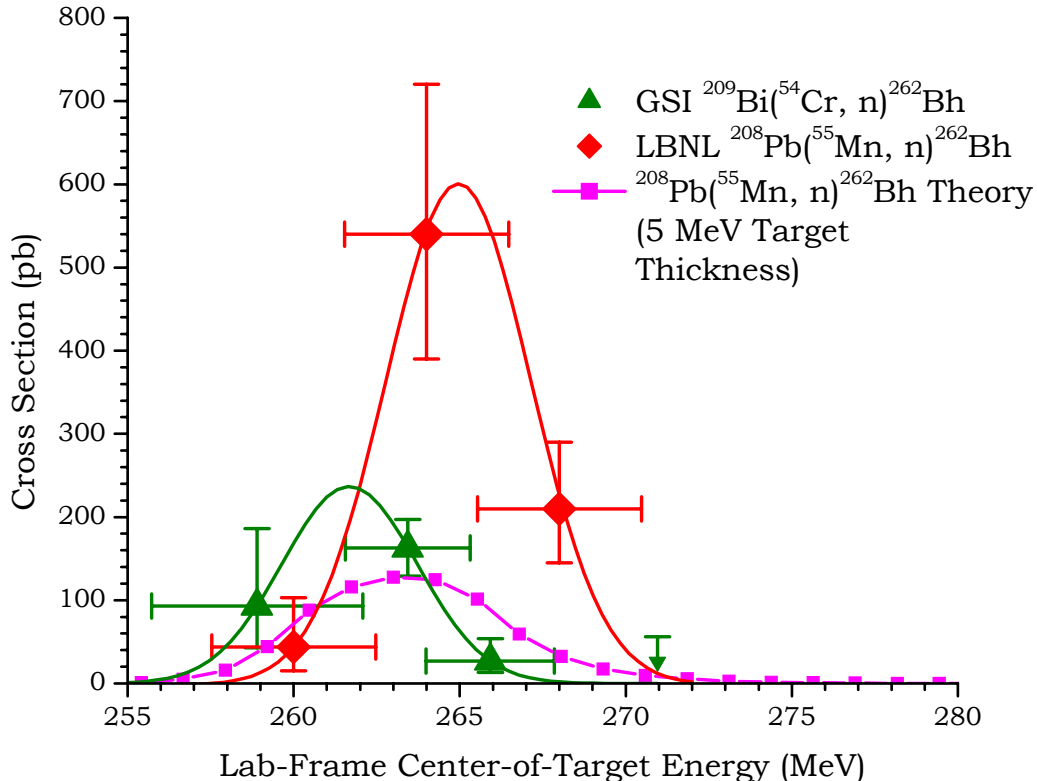


FIG. 5.1. Excitation functions measured for the production of  $^{262}\text{Bh}$  in the  $^{209}\text{Bi}(^{54}\text{Cr}, \text{n})^{262}\text{Bh}$  and  $^{208}\text{Pb}(^{55}\text{Mn}, \text{n})^{262}\text{Bh}$  reactions. Gaussian fits to the experimental data are shown. Also shown is a prediction for the  $^{208}\text{Pb}(^{55}\text{Mn}, \text{n})^{262}\text{Bh}$  reaction from the “Fusion by Diffusion” theory with a 5-MeV target thickness included. In all cases, the cross sections represent the sum of the production cross sections for both  $^{262}\text{Bh}^g$  and  $^{262}\text{Bh}^m$ . The vertical error bars are  $1\sigma$  (68%) limits for the measured cross sections. The horizontal error bars represent the energy loss of the beam as it traverses the target. These data are presented in tabular form in Table 5.1.

In the decays of  $^{262}\text{Bh}$ , two sets of alpha-energy groups with different half-lives were observed. Events in the groups at 9740, 9910, and 10060 keV were fit with a half-life of  $102 \pm 26$  ms. At the higher alpha energies of 10240 and 10370 keV, the measured half-life was  $8.0 \pm 2.1$  ms. The latter decays were assigned to an isomeric state in  $^{262}\text{Bh}$ . The energy of this isomer was estimated to be 500-600 keV above the ground state, although the data for gamma rays in coincidence with these alpha decays were inconclusive. The

TABLE 5.1. Cross sections for the  $^{209}\text{Bi}(^{54}\text{Cr}, \text{n})$  and  $^{208}\text{Pb}(^{55}\text{Mn}, \text{n})$  reactions leading to the production of  $^{262}\text{Bh}$  at GSI and LBNL, respectively. These data are presented graphically in Fig. 5.1.

Laboratory [Reference]	Reaction	$E_{\text{tot}}$ (MeV)	Target Thickness (mg/cm <sup>2</sup> )	Dose (10 <sup>16</sup> )	$^{262}\text{Bh}^g + ^{262}\text{Bh}^m$ Cross Section (pb)
GSI [Münzenberg1989]	$^{54}\text{Cr} + ^{209}\text{Bi}$	258.9 <sup>a</sup>	0.66	7	93 <sup>+93</sup> <sub>-50</sub>
		263.4 <sup>a</sup>	0.39	71	163 <sup>+34</sup> <sub>-34</sub>
		265.9 <sup>a</sup>	0.40	18	27 <sup>+27</sup> <sub>-14</sub>
		271.0 <sup>a</sup>	0.40	14	<56
LBNL [This work.]	$^{55}\text{Mn} + ^{208}\text{Pb}$	260.0	0.47	5.7	44 <sup>+59</sup> <sub>-29</sub>
		264.0	0.47	4.2	540 <sup>+180</sup> <sub>-150</sub>
		268.0	0.47	7.8	210 <sup>+80</sup> <sub>-65</sub>

<sup>a</sup> Calculated from data in Tables 1 and 3 in [Münzenberg1989].

observed alpha-decay energies of  $^{261}\text{Bh}$  were 10030, 10100, and 10400 keV, with a half-life of  $11.8^{+5.3}_{-2.8}$  ms.

The existence of an isomeric state in  $^{262}\text{Bh}$  is not surprising as isomers are known to exist for many transactinide elements. Among the  $Z \geq 106$  nuclides, isomers have also been reported in  $^{263}\text{Sg}$  [Hofmann1998],  $^{270}\text{Ds}$  [Hofmann2001], and  $^{271}\text{Ds}$  [Hofmann1998]. Many even-even nuclei are expected to have high- $K$  excited states with enhanced stability against fission and alpha-emission; these states can be formed as a result of multi-quasiparticle excitations [Xu2004]. The  $^{270}\text{Ds}$  isomer is a high- $K$  isomer [Hofmann2001], and odd-odd nuclei should be even more likely to have such isomers because of the unpaired nucleons. Münzenberg *et al.* reported roughly equal production of  $^{262}\text{Bh}^g$  (15 decay chains) and  $^{262}\text{Bh}^m$  (14 decay chains).  $^{262}\text{Bh}^m$  has also been produced as a result of  $^{266}\text{Mt}$  alpha decay [Hofmann1997, Münzenberg1988].

Spontaneous fission decay was not observed in the decay of  $^{261}\text{Bh}$ ,  $^{262}\text{Bh}^g$ , or  $^{262}\text{Bh}^m$ , in disagreement with the data reported by Oganessian *et al.* It appears that the SF reported in the decay of  $^{258}\text{Db}$  [Oganessian1984] is actually the result of a 33% electron-capture branch in  $^{258}\text{Db}$  which leads to the short-lived SF isotope  $^{258}\text{Rf}$  ( $t_{1/2} = 12$  ms, 100% SF branch). In the case of  $^{261}\text{Bh}$ , the SF reported by Oganessian *et al.* [Oganessian1976] can be attributed to a 17% SF branch in  $^{257}\text{Db}$  [Heßberger1985], formed by alpha-decay of  $^{261}\text{Bh}$ .

### 5.1.3. Rationale for the New Experiments to Produce $^{262}\text{Bh}$

The work by Münzenberg and coworkers focused exclusively on the  $^{209}\text{Bi}(^{54}\text{Cr}, \text{n})^{262}\text{Bh}$  reaction, presumably because the analogous  $^{208}\text{Pb}(^{55}\text{Mn}, \text{n})^{262}\text{Bh}$  reaction was expected to have a lower maximum cross section. Since no SF decay attributable to the decay of bohrium has been observed, the data obtained by Oganessian *et al.* [Oganessian1984, Oganessian1976, Oganessian1976] in the  $^{55}\text{Mn} + ^{208}\text{Pb}$  reaction appear to be erroneous. Thus, a new experiment to study the  $^{208}\text{Pb}(^{55}\text{Mn}, \text{n})^{262}\text{Bh}$  excitation function is necessary in order to quantify the possible difference in cross section that may result from the odd proton being in the projectile rather than the target. A similar comparison was reported in Chapter 4 for element 111 and although the results agreed within the quoted large statistical errors, further investigation is necessary. The  $^{208}\text{Pb}(^{55}\text{Mn}, \text{n})^{262}\text{Bh}$  experiment provides an opportunity to study the excitation function using a reaction with much higher cross sections. In addition, the excitation function obtained by Münzenberg *et al.* for the production of  $^{262}\text{Bh}$  in the  $^{209}\text{Bi}(^{54}\text{Cr}, \text{n})$  reaction shows a maximum at an unusually high excitation energy of  $20 \pm 2$  MeV, so it would be valuable to know if this also occurs in the  $^{208}\text{Pb}(^{55}\text{Mn}, \text{n})^{262}\text{Bh}$  reaction. During these experiments the  $^{262}\text{Bh}$  isomer ratios can also be measured as a function of beam energy.

## 5.2. Experimental Conditions

The experimental conditions were very similar to those described in Sec. 3.2 and 4.2. The beam entered the BGS through the  $45\text{-}\mu\text{g}/\text{cm}^2$   $^{nat}\text{C}$  window separating the gas-filled separator from the evacuated Cyclotron beamline. Details on the  $^{208}\text{Pb}$  target wheel are given in Sec. 2.1. The same MWPC detector was placed upstream of the focal plane detectors as before to discriminate between implantation events and radioactive decays. Prior to the run, targets of  $^{118}\text{Sn}$  and  $^{nat}\text{Cs}^{nat}\text{I}$  were bombarded with 268.7-MeV (Cyclotron energy)  $^{55}\text{Mn}^{13+}$  projectiles to test the data acquisition system and to provide internal calibration standards using the  $^{133}\text{Cs}(\text{Mn}, \text{xn})^{188-x}\text{Hg}$ ,  $x = 3-5$  and  $^{127}\text{I}(\text{Mn}, \text{yn})^{182-y}\text{Pt}$ ,  $y = 3-5$  reactions.  $^{211}\text{Po}$  produced in transfer reactions with the  $^{208}\text{Pb}$  targets was also used as a calibration standard.

The “optimum energy rule” developed by Świątecki, Siwek-Wilczyńska, and Wilczyński [Świątecki2003] was used to estimate the optimum beam energy for the  $^{208}\text{Pb}(\text{Mn}, \text{n})^{262}\text{Bh}$  reaction. Masses were taken from [Myers1994], and an additional beam energy correction of +0.5 MeV (center-of-mass frame) was applied based on the known differences between the theoretical and experimental optimum energies observed in other reactions (see Fig. 18 in [Świątecki2004a]). The optimum energy was estimated to be 264.0 MeV.

In our first experiment, a beam of 268.7-MeV  $^{55}\text{Mn}$  projectiles (lab frame) exited the 88-Inch Cyclotron and lost 1.2 MeV in the entrance window, a negligible energy in the 0.5-torr He gas, and 1.0 MeV in the target backing before entering the  $^{208}\text{Pb}$  targets. The total energy lost in the targets was 4.9 MeV, resulting in the desired  $E_{cat}$  of 264.0 MeV. Comparable energy losses were also calculated for the two other beam energies described below. The excitation energy for compound nuclei produced at the target center was 14.3 MeV. The total dose of  $^{55}\text{Mn}^{13+}$  collected at this energy was  $4.2 \times 10^{16}$  during 18.7 h. The

average beam current at this energy was  $\sim 100$  pnA, lower than those at the other energies described below because of the need to condition the targets by gradually raising the beam current at the beginning of the experiment.

After this initial bombardment, the beam energy from the Cyclotron was reduced to 264.7 MeV, giving  $E_{tot} = 260.0$  MeV. The excitation energy of compound nuclei formed at the center of the target was 11.1 MeV. The total dose collected at this energy was  $5.7 \times 10^{16}$  during 15.8 h. The average beam current at this second energy was  $\sim 170$  pnA.

The final energy studied was 272.7 MeV from the Cyclotron. In this case,  $E_{tot}$  was 268.0 MeV and the excitation energy of compound nuclei formed at the center of the target was 17.4 MeV. Again, the total energy loss in the target was 4.9 MeV. At this energy, a total dose of  $7.8 \times 10^{16}$  was collected during 20.0 h. The average beam current at this final energy was  $\sim 180$  pnA.

For  $^{262}\text{Bh}$ ,  $(\nu/\nu_0)Z^{1/3}$  is expected to be 13.8, and Eq. 2.10 gives good agreement with experimental charge states in the range  $7 \leq (\nu/\nu_0)Z^{1/3} \leq 17$ . Thus, the average charge state of  $^{262}\text{Bh}$  evaporation residues (EVRs) was estimated to be +8.1. Based on this charge state, the magnetic rigidity of the BGS was set at 2.14 T m for all three energies. Magnet currents of  $Q1 = 1719$  A,  $M1 = 363$  A, and  $M2 = 618$  A were used. The He fill gas pressure was 0.5 torr.

At  $E_{tot} = 264.0$  MeV, the initial energy of  $^{262}\text{Bh}$  EVRs was  $\sim 55$  MeV. After approximate energy losses of 3 MeV in the target, 6 MeV in the He fill gas, and 14 MeV in the MWPC, the estimated implantation energy was 32 MeV. Correcting for an estimated pulse-height defect of  $\sim 45\%$  of EVR energy [Moulton1978], the observed implantation pulse heights should correspond to approximately 18 MeV.

The fast beam shutoff analysis described in Sec. 3.2 was active at all three energies. The EVR- $\alpha$  gate searched for EVRs with energies in the range 12-25 MeV correlated within 30.0 s to alpha particles with energies in the range 8300-11000 keV. Midway through the first projectile energy the EVR range was increased to 10-25 MeV. These gate values allowed an EVR correlated to the decay of  $^{262}\text{Bh}^g$ ,  $^{262}\text{Bh}^m$ ,  $^{261}\text{Bh}$ ,  $^{258}\text{Db}$ ,  $^{257}\text{Db}$ ,  $^{254}\text{Lr}$ , or  $^{253}\text{Lr}$  to shut off the beam. The maximum allowed position difference  $|\Delta P_{max}|$  was variable and defined in the following way. For any given event with energy  $E$ , the standard deviation in the measured position of this event was given by [Gregorich2004]

$$\sigma_{pos} = 2800E^{-1} \text{ keV mm.} \quad (5.1)$$

When comparing the positions of two events, the difference  $\Delta P$  should have a distribution with standard deviation  $\sigma_{tot}$ :

$$\sigma_{tot}(\Delta P) = \sqrt{\sigma_{pos,1}^2 + \sigma_{pos,2}^2}. \quad (5.2)$$

$|\Delta P_{max}|$  was made equal to the full-width-at-half-maximum of this distribution:

$$|\Delta P_{max}| = \text{FWHM} \approx 2.35\sigma_{tot} = 2.35\sqrt{\sigma_{pos,1}^2 + \sigma_{pos,2}^2}. \quad (5.3)$$

When the above conditions were met, the beam was shut off for 180.0 s. The EVR- $\alpha$ - $\alpha$  gate was effectively disabled by setting its additional beam-off period to just 0.1 s. This was done because the next likely alpha-decay in the chain,  $^{250}\text{Fm}$  (formed by electron-capture decay of  $^{250}\text{Md}$ ), was long-lived ( $t_{1/2} = 30$  min), and shutting off the beam to search for this nuclide would have significantly reduced the total dose collected.

In the  $E_{tot} = 264.0$  MeV run, the beam shut off 16 times for a total of 2875 s (4.3% of total beam time). In the  $E_{tot} = 260.0$  MeV run, the beam shut off only 4 times, for a total

of 719 s (1.3% of total beam time). In the  $E_{\text{tot}} = 268.0$  MeV run, the beam shut off 13 times for a total of 2337 s (3.2% of total beam time).

## 5.3. Observed Decay Chains

### 5.3.1. Summary

A total of 35 decay chains attributable to  $^{261,262}\text{Bh}$  were observed and are shown in Fig. 5.2-5.4. Eleven chains from  $^{262}\text{Bh}^{\text{m}}$ , twenty-two chains from  $^{262}\text{Bh}^{\text{g}}$ , and two chains from  $^{261}\text{Bh}$  were observed. The chains are shown in the order observed, except that the  $^{261}\text{Bh}$  decay chains are shown separately in Fig. 5.4b for clarity. The number of decay chains observed at each beam energy is shown in Table 5.2. Assignments were made by comparing the observed data to the known decay energies and half-lives. The decay properties of  $^{261}\text{Bh}$  and  $^{262}\text{Bh}^{\text{m}}$  are very similar, as are their daughters  $^{257}\text{Db}$  and  $^{258}\text{Db}$ , so the decays of the bohrium granddaughters  $^{253}\text{Lr}$  and  $^{254}\text{Lr}$  must be used to distinguish decay chains originating from  $^{261}\text{Bh}$  and  $^{262}\text{Bh}^{\text{m}}$ .

Figure 5.5 shows a histogram of the observed implantation pulse heights of EVRs at all three beam energies combined. Although implantation energy varies with beam energy and EVR production location within the target, these variations are not significant (on the order of 1-2 MeV). Thus, the data from all three energies can be combined to improve statistics. This information is useful in planning future experiments.

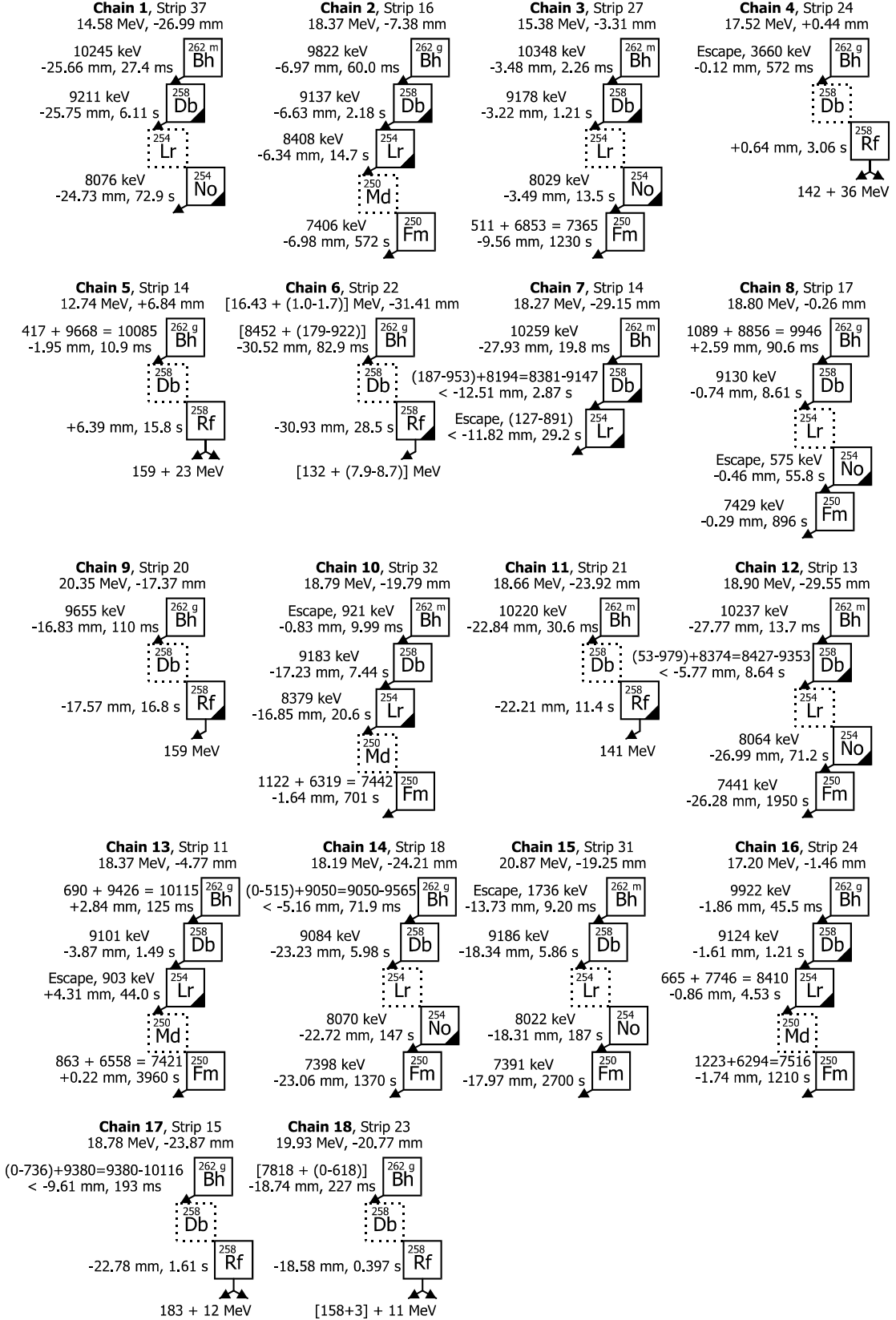


FIG. 5.2. Bohrium decay chains observed at  $E_{\text{col}} = 264.0 \text{ MeV}$ . See Fig. 5.3 for an explanation of symbols.

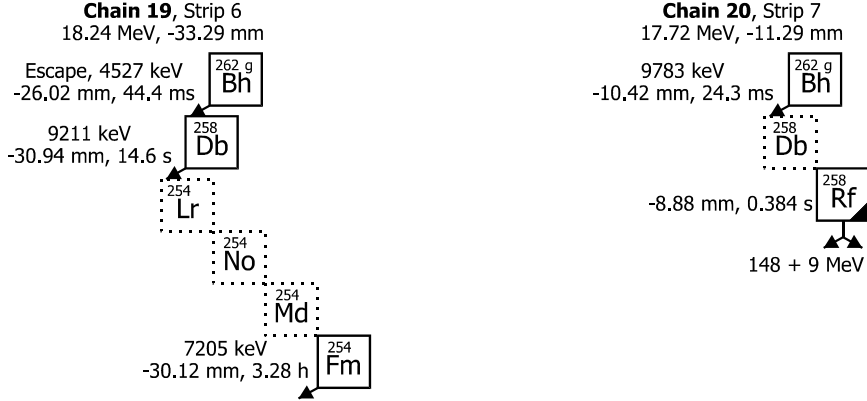


FIG. 5.3. Bohrium decay chains observed at  $E_{col} = 260.0$  MeV. Information about the corresponding implantation event is given above the chain. The notation  $x + y = z$  indicates that  $x$  keV was observed in a strip detector and  $y$  keV was observed in an upstream detector simultaneously, with sum  $z$  keV. A black triangle in the lower-right corner signifies that the beam was off for that event. Fission events are indicated by arrows below the nuclide. Parentheses indicate that only one signal was recorded in a strip so a range of energies is possible. Brackets indicate that some energy was also deposited in an adjacent strip. If units are not listed then they are keV. These symbols also apply to Fig. 5.2 and 5.4.

The observed magnetic rigidity of all  $Z = 107$  EVRs was  $2.16 \pm 0.03$  T m (statistical uncertainty only), corresponding to an average EVR charge-state of approximately +8.0, in good agreement with the prediction of +8.1. Again, observed magnetic rigidity varies with beam energy and EVR production location, but the differences are not significant for the beam energies studied in this work.

The transmission of the BGS was estimated to be  $(65 \pm 5)\%$ . An analysis of the vertical positions of all  $Z = 107$  EVRs showed that the distribution was centered at approximately -13 mm rather than 0 mm as expected. Inspection of the focal plane showed that it was properly aligned to the centerline of the separator. This discrepancy cannot be ascribed to magnetic field inhomogeneities in the magnets [Gregorich2004] and remains unresolved. An additional “vertical efficiency” of  $(93 \pm 3)\%$  was introduced to

account for the tail of the vertical EVR distribution which did not implant on the strip detectors. Horizontally, more than 99% of EVRs were on the focal plane.

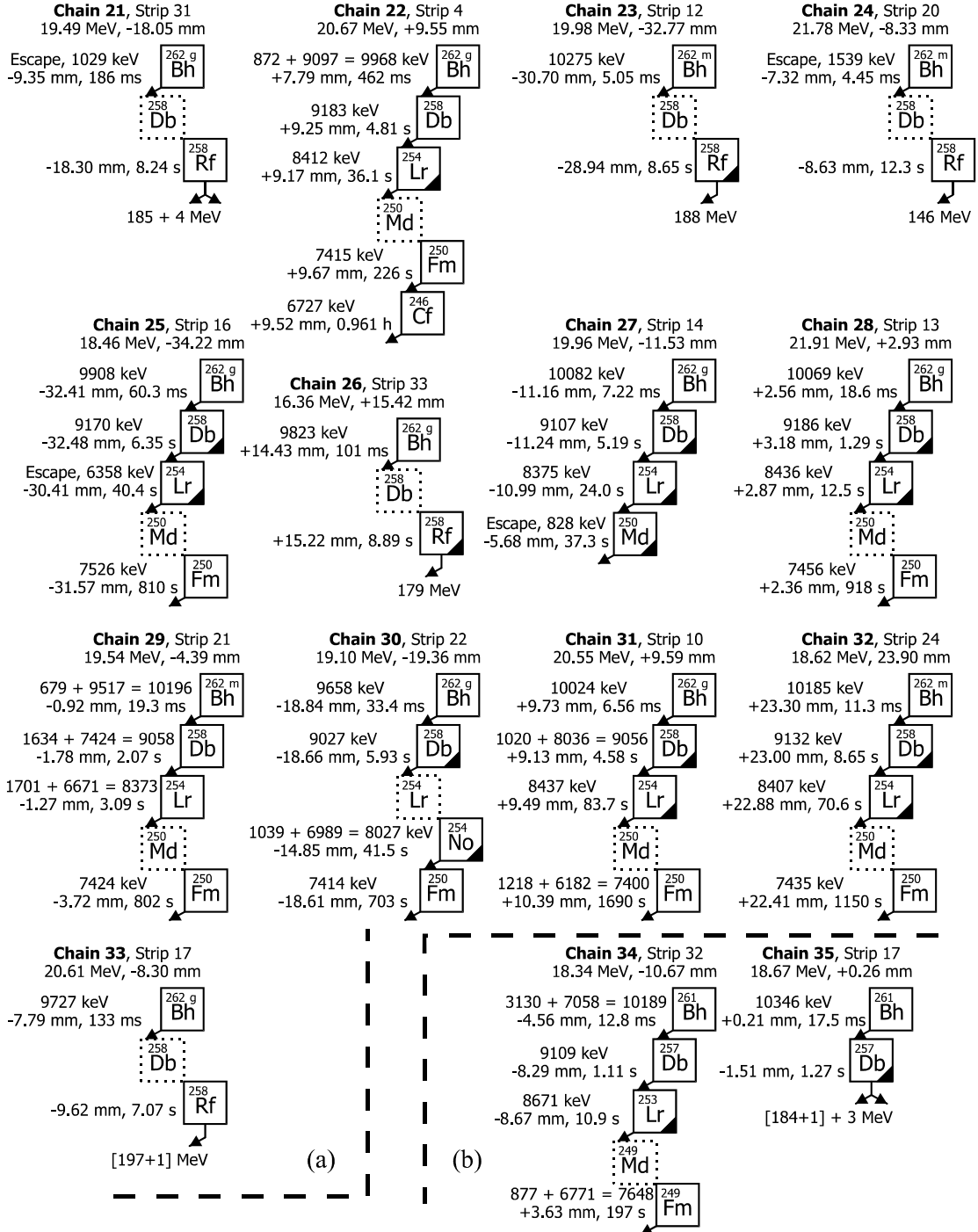


FIG. 5.4. Decay chains of (a)  $^{262}\text{Bh}$  and (b)  $^{261}\text{Bh}$  observed at  $E_{\text{tot}} = 268.0$  MeV. See Fig. 5.3 for a description of symbols.

TABLE 5.2. Cross sections for the production of bohrium as a function of  $E_{\text{tot}}$ . The number in parentheses is the number of decay chains of the given type. Upper limits are “one event” cross sections.

Nuclide	$E_{\text{tot}}$		
	260.0 MeV (pb)	264.0 MeV (pb)	268.0 MeV (pb)
$^{261}\text{Bh}$	<22 (0)	<30 (0)	$32^{+43}_{-21}$ (2)
$^{262}\text{Bh}^g$	$44^{+59}_{-29}$ (2)	$330^{+140}_{-110}$ (11)	$150^{+68}_{-53}$ (9)
$^{262}\text{Bh}^m$	<22 (0)	$210^{+110}_{-85}$ (7)	$65^{+50}_{-34}$ (4)
Total $^{262}\text{Bh}$	$44^{+59}_{-29}$ (2)	$540^{+180}_{-150}$ (18)	$210^{+80}_{-65}$ (13)

### 5.3.2. Information About Specific Decay Chains

Some chains deserve special mention. Chain 3 from the  $E_{\text{tot}} = 264.0$  MeV run could be attributed to  $^{261}\text{Bh}$ , but the fourth alpha-particle event in the chain has an energy too low and lifetime too long to be assigned to  $^{249}\text{Fm}$ . Thus, this chain is assigned to  $^{262}\text{Bh}$ . In chain 6, it appears that the EVR was implanted in strip 22 very close to the boundary with strip 21. All three events in this chain deposited some energy in strip 21 as indicated by the brackets. The long lifetime of 82.9 ms permits its assignment as  $^{262}\text{Bh}^g$  even though the alpha energy is not accurately known. In chain 15, the  $^{254}\text{No}$  energy of 8022 keV is low compared to the known 8093-keV group [Firestone1996] and might be assigned to  $^{253}\text{No}$  ( $E_\alpha = 8010$  keV), but the presence of a correlated  $^{250}\text{Fm}$  decay conclusively identifies this chain as originating from  $^{262}\text{Bh}^m$ . In chain 18, as in chain 6, some energy was also deposited in an adjacent strip. Energy deposited in the strip boundaries is not recorded, which explains the unusually low  $^{262}\text{Bh}^g$  alpha-decay energy. Again, the long lifetime of 227 ms identifies this event as originating from  $^{262}\text{Bh}^g$ .

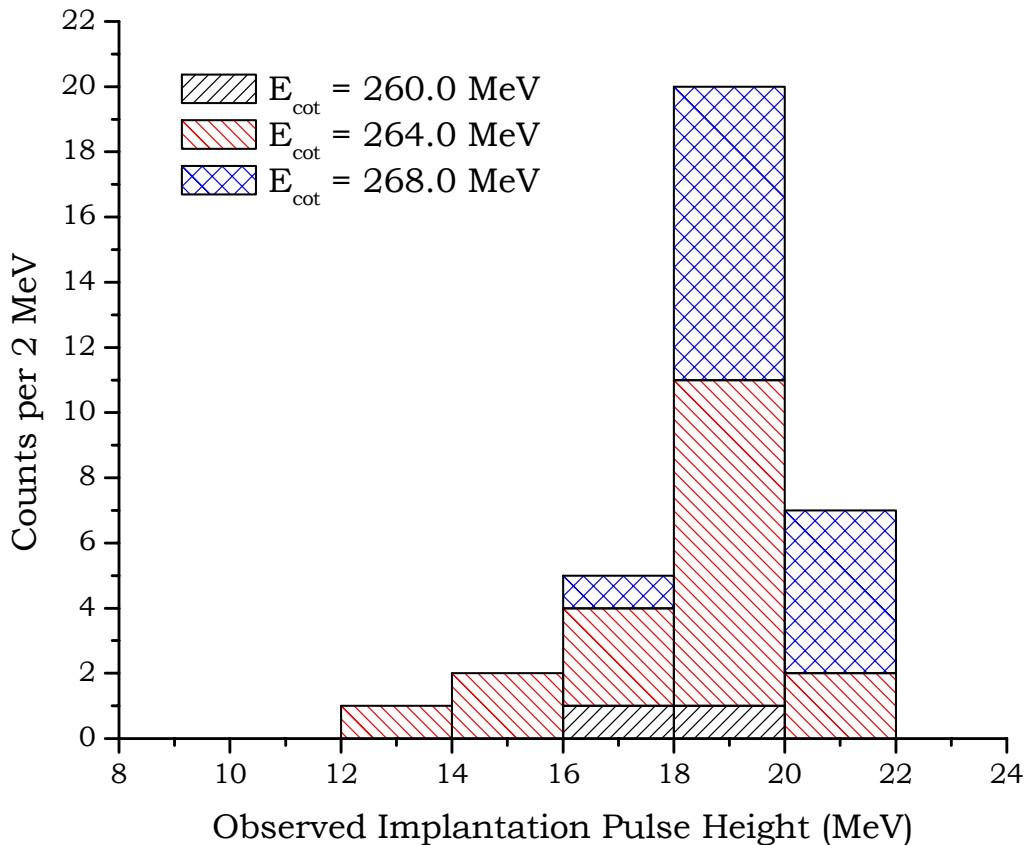


FIG. 5.5. Observed pulse heights for all  $Z = 107$  EVRs.

In the  $E_{\text{tot}} = 268.0 \text{ MeV}$  run, the event assigned to  $^{254}\text{Lr}$  in chain 25 has an unusually large deposition energy for an escape alpha event (6358 keV). This decay chain was observed at the very bottom of the strip, so it is possible that the emitted alpha particle traveled through a large portion of the strip at a shallow angle. It would have then exited the strip with approximately 2000 keV of kinetic energy remaining. This energy may not have been recorded because the alpha particle was implanted in the non-detecting frame which separates the upstream detectors from the strip detectors.

### 5.3.3. $^{262}\text{Bh}^g$ , $^{262}\text{Bh}^m$

The existence of ground and isomeric states in  $^{262}\text{Bh}$  with differing half-lives and alpha-decay energies was clearly observed in the current work. The calculated half-life of all 22 events assigned to  $^{262}\text{Bh}^g$  was  $84^{+21}_{-16}$  ms, a somewhat improved value compared to that of  $102 \pm 26$  ms measured by Münzenberg *et al.* (references throughout this section to Münzenberg *et al.* refer to [Münzenberg1989], and all half-lives were calculated using the MLDS code [Gregorich1991] modified as described previously). The half-life of 11 events assigned to  $^{262}\text{Bh}^m$  was  $9.6^{+3.6}_{-2.4}$  ms, in agreement with the half-life of  $8.0 \pm 2.1$  ms measured by Münzenberg *et al.* Neither  $^{262}\text{Bh}^g$  nor  $^{262}\text{Bh}^m$  was observed to decay by SF.

Production of ground-state  $^{262}\text{Bh}$  was favored at all three beam energies (see Table 5.2). At the lowest energy ( $E_{\text{col}} = 260.0$  MeV), two ground-state decays and no isomeric decays were observed. At the middle energy ( $E_{\text{col}} = 264.0$  MeV), 11 events of  $^{262}\text{Bh}^g$  were observed, compared to only 7 events of  $^{262}\text{Bh}^m$ . At the highest energy ( $E_{\text{col}} = 268.0$  MeV), 9  $^{262}\text{Bh}^g$  decay chains were observed and 4  $^{262}\text{Bh}^m$  decay chains were observed. The total ground-state-to-isomer ratio of  $2.0 \pm 0.8$  (22  $^{262}\text{Bh}^g$  events to 11  $^{262}\text{Bh}^m$  events) is in general agreement with the observation by Münzenberg *et al.* of roughly equal production:  $1.1 \pm 0.5$  (15  $^{262}\text{Bh}^g$  decays and 14  $^{262}\text{Bh}^m$  decays; error estimated by the current author). However, Münzenberg *et al.* conducted their experiments at higher excitation energies than in the current experiments, which may influence the isomer production ratio. The beam energy of the GSI experiments is discussed in more detail in Sec. 5.6. Many more  $^{262}\text{Bh}$  events will be required to firmly establish the isomer production ratio.

There was good agreement between the measured alpha energies and those reported by Münzenberg *et al.*, although the energies of a few decays were not well defined because

some energy was deposited in an adjacent strip with additional energy lost in the resistive gap between strips. A new lower-energy alpha-particle group was observed in the decay of  $^{262}\text{Bh}^g$ . Two decays with energies 9655 keV and 9658 keV were observed in chains 9 and 30, respectively. In both cases, the alpha-particles were fully stopped in the focal plane, resulting in maximum energy resolution. The excellent agreement of energies within the group suggests that they cannot be attributed to incomplete charge collection of decays from the known higher-energy groups. These new decay energies are too low to be assigned to  $^{261}\text{Bh}$ . Also, the long lifetimes observed with the decays are more consistent with the half-life of  $^{262}\text{Bh}^g$  than  $^{262}\text{Bh}^m$ , although the probability is  $\sim 10\%$  that the 33.4-ms lifetime in chain 30 belongs to the  $^{262}\text{Bh}^m$  lifetime distribution with half-life  $9.6_{-2.4}^{+3.6}$  ms. This new alpha-energy is consistent with the fact that all previously known alpha groups in  $^{262}\text{Bh}^g$  have lower energies than those in  $^{262}\text{Bh}^m$ . Thus, this group is assigned to  $^{262}\text{Bh}^g$ . Note that two decays with energies 9822 and 9823 keV observed in chains 2 and 26, respectively, are not consistent with any group given in [Münzenberg1989], but are consistent with the  $^{262}\text{Bh}$  decays in event numbers 2, 10, and 11 in Table 2 of [Hofmann1997].

In summary, the following groups were observed in the decay of  $^{262}\text{Bh}^m$ : 10348 keV (1 event) and 10231 keV (7 events). The following groups were observed in the decay of  $^{262}\text{Bh}^g$ : 10075 keV (5 events), 9936 keV (4 events), 9823 keV (2 events), 9755 keV (2 events), and 9657 keV (2 events). The standard deviation of each group is approximately  $\pm 20$  keV.

### 5.3.4. $^{261}\text{Bh}$

Two decay chains (numbers 34 and 35) were attributed to the decay of  $^{261}\text{Bh}$ . Chain 34 can be assigned with confidence because of the agreement of the  $^{253}\text{Lr}$  alpha energy (8671 keV) with the known group with energy 8722 keV [Heßberger1985]. Chain 35 may originate from  $^{261}\text{Bh}$ . The energy of the alpha-decay assigned to  $^{261}\text{Bh}$  in this chain was 10346 keV, and was followed 1.27 s later by a fission event. Although this decay chain is also consistent with the decay of  $^{262}\text{Bh}^m$  followed by electron-capture of  $^{258}\text{Db}$  and fission of  $^{258}\text{Rf}$ , it is assigned to  $^{261}\text{Bh}$  because the 1.27-s fission lifetime is closer to the reported  $1.4_{-0.3}^{+0.6}$ -s half-life of  $^{257}\text{Db}$  (17% SF branch) [Heßberger1985] than the reported  $4.4_{-0.6}^{+0.9}$ -s half-life of  $^{258}\text{Db}$ . However, the properties are so similar that the assignment to  $^{262}\text{Bh}^m$  cannot be excluded.

The estimated half-life of  $^{261}\text{Bh}$  based on the two decay chains in the current data is  $10_{-5}^{+14}$  ms, in good agreement with  $11.8_{-2.8}^{+5.3}$  ms reported by Münzenberg *et al.* The half-life of  $^{257}\text{Db}$  is estimated to be  $0.8_{-0.4}^{+1.1}$  s, also in agreement with the half-life of  $1.4_{-0.3}^{+0.6}$  s reported by Heßberger *et al.* [Heßberger1985].

These two  $^{261}\text{Bh}$  decay chains were observed at our highest beam energy ( $E_{\text{tot}} = 268.0$  MeV). This nuclide is the 2n evaporation product of the complete fusion reaction. The compound nucleus excitation energies covered by the target at this beam energy range from 15.5 to 19.4 MeV, using masses from [Myers1994]. Once the neutron separation energies and an additional  $\sim 2$  MeV per neutron kinetic energy are subtracted, it can be shown that only the first  $\sim 20\%$  of the target is available for production of the 2n product. Compound nuclei formed in the remainder of the target will have excitation energies too low for the emission of two neutrons. (Similar results are obtained using masses from

[Audi2003]). These data are consistent with the expected 2n excitation function. It would be interesting to continue this study at higher beam energies to observe the onset of 2n product formation and measure the excitation function.

### 5.3.5. $^{258}\text{Db}$

The decay of  $^{258}\text{Db}$  was observed or inferred in all 33 decay chains originating with  $^{262}\text{Bh}$ . Thirteen of these decays were electron-captures inferred from subsequent fission of  $^{258}\text{Rf}$  (100% SF branch), leading to an EC branching ratio of  $(39_{-9}^{+11})\%$ , in good agreement with the known EC branch of  $(33_{-5}^{+9})\%$  [Heßberger1985]. The overall half-life of all 33 events was  $4.8_{-0.8}^{+1.0}$  s, compared to  $4.4_{-0.6}^{+0.9}$  s measured previously.

In a study of the direct production of  $^{258}\text{Db}$  in the  $^{209}\text{Bi}(^{50}\text{Ti}, \text{n})$  reaction, Heßberger *et al.* [Heßberger1985] reported that the measured half-life of  $^{258}\text{Db}$  nuclei undergoing alpha decay ( $4.4_{-0.6}^{+0.9}$  s) was significantly different from the measured half-life of  $^{258}\text{Db}$  nuclei undergoing EC decay ( $6.1_{-0.8}^{+1.0}$  s). This was attributed to a  $(25 \pm 5)\%$  admixture of an EC-decaying isomer in  $^{258}\text{Db}$  with half-life  $20 \pm 10$  s. In the current work, the measured half-life of all EC-decaying  $^{258}\text{Db}$  nuclei was  $6.6_{-1.6}^{+2.4}$  s, in good agreement with that reported by Heßberger *et al.* Unfortunately, there were not enough  $^{258}\text{Db}$  EC events, and the difference in half-lives was too small ( $\sim 4$  s compared to  $\sim 20$  s), for a two-component fit to the  $^{258}\text{Db}$  EC lifetimes in the current work to converge. If only the five EC lifetimes longer than two  $^{258}\text{Db}$  half-lives are considered, then the estimated half-life is approximately 14 s, consistent with the longer-lived isomer proposed by Heßberger *et al.* Approximately one-fourth of all decays should occur with lifetimes longer than two half-lives, and the observed fraction of long-lived decays [ $(38_{-13}^{+19})\%$ ] differs from this figure by

one standard deviation, supporting the existence of an isomer. Regardless, the claim for this EC-decaying isomer in  $^{258}\text{Db}$  is still based on only a few observed events, and further study is required to clarify these data.

In the  $E_{\text{tot}} = 268.0$  MeV run, one decay chain (not shown in Fig. 5.2-5.4) was observed that is consistent with an implantation event followed by alpha-decay of  $^{258}\text{Db}$ , EC-decay of  $^{254}\text{Lr}$ , and alpha decay of  $^{254}\text{No}$  and  $^{250}\text{Fm}$ . A thorough search of the data revealed no event which could be attributed to the decay of  $^{262}\text{Bh}$ . This may be because  $^{258}\text{Db}$  was formed as the *αn* product of the complete fusion reaction, or because the decay of  $^{262}\text{Bh}$  did not trigger a data readout. The *αn* product is not likely to be formed for the reasons discussed in Sec. 1.2.1.3. Even if an alpha-particle emitted by  $^{262}\text{Bh}$  escaped from the front of the detector, it should have triggered a readout, as happened with other  $^{262}\text{Bh}$  escape events. No other event in this work (including the darmstadtium and element 111 experiments described in Chapters 3 and 4, respectively) had this problem, so this chain is not included in the  $^{262}\text{Bh}$  production cross sections.

### 5.3.6. $^{258}\text{Rf}$

$^{258}\text{Rf}$  was formed by the EC decay of  $^{258}\text{Db}$ . Its half-life could not be measured because EC was not observed directly by any detectors in the experiment and its lifetime was observed as the sum of the  $^{258}\text{Db}$  and  $^{258}\text{Rf}$  lifetimes. The known 100% SF branch of this nuclide was used to aid in the identification of  $^{262}\text{Bh}$  decay chains. Fission events are clearly identified by the large energy deposited in the focal plane ( $>140$  MeV) but the experiment was not suitable for measuring the SF total kinetic energy distribution.

### 5.3.7. $^{254}\text{Lr}$

The 9 full-energy alpha-decays assigned to  $^{254}\text{Lr}$  could be divided into two groups with average energies 8437 keV (2 events) and 8394 keV (7 events). These energies agree with those reported by Heßberger *et al.* [Heßberger1985]:  $8460 \pm 20$  keV (64%) and  $8408 \pm 20$  keV (36%).

The measured half-life of all 12  $^{254}\text{Lr}$  alpha-decays, including escape alpha events, was  $22_{-6}^{+9}$  s. This is in rough agreement with the half-life of  $13_{-2}^{+3}$  s reported in [Heßberger1985]. The measured branching ratios of  $^{254}\text{Lr}$  were  $(60_{-15}^{+11})\%$  alpha and  $(40_{-11}^{+15})\%$  EC, consistent with the branches of  $(78 \pm 22)\%$  alpha and  $(22 \pm 6)\%$  EC reported by Heßberger *et al.*

### 5.3.8. $^{254}\text{No}$

$^{254}\text{No}$  has been extensively studied (see the list of references in [Loveland2003]) because of the large cross section of the  $^{208}\text{Pb}(^{48}\text{Ca}, 2\text{n})$  reaction:  $3.4 \pm 0.4 \mu\text{b}$  at 227 MeV (lab-frame) [Nitschke1979]. The alpha-decay energy is known to be 8093 keV. The 6 full-energy  $^{254}\text{No}$  alpha decays observed in this work form a single alpha group with energy  $8048 \pm 30$  keV, in rough agreement with the known group. Recently, an improved half-life of  $48 \pm 3$  s [Leino1999] has been measured for  $^{254}\text{No}$ . However, the half-life of  $^{254}\text{No}$  could not be estimated from the current data because it was always formed as a product of  $^{254}\text{Lr}$  EC. The half-lives of  $^{254}\text{Lr}$  ( $13_{-2}^{+3}$  s [Heßberger1985]) and  $^{254}\text{No}$  are not sufficiently different to allow fitting a parent-daughter decay curve to the observed lifetimes. However, the measured lifetimes are consistent with a 13-s activity feeding a 48-s activity.

### 5.3.9. $^{250}\text{Md}$

Only 1 alpha decay of  $^{250}\text{Md}$  was observed in chain 27 among 11 total events. The lifetime of this event is 37.3 s, consistent with the known half-life of  $55 \pm 6$  s [Eskola1973]. This one alpha decay was an escape event so its true energy is not known. The branching ratios of  $^{250}\text{Md}$  were observed to be EC:  $(91^{+7}_{-19})\%$  and alpha:  $(9^{+19}_{-7})\%$ . These ratios are consistent with the known branching ratios reported by Eskola:  $(94 \pm 3)\%$  EC and  $(7 \pm 3)\%$  alpha.

### 5.3.10. $^{250}\text{Fm}$

$^{250}\text{Fm}$  can be formed in two different pathways in the decay scheme of  $^{262}\text{Bh}$ , either by the alpha-decay of  $^{254}\text{Lr}$  followed by electron-capture in  $^{250}\text{Md}$ , or electron-capture of  $^{254}\text{Lr}$  followed by alpha-decay of  $^{254}\text{No}$ . The measured half-life of  $^{250}\text{Fm}$  fed by alpha decay of  $^{254}\text{No}$  was  $18^{+13}_{-6}$  min, consistent with the known half-life of  $30 \pm 3$  min [Amiel1957]. The 16  $^{250}\text{Fm}$  alpha-decays recorded with full energy form single group with energy  $7430 \pm 50$  keV, in excellent agreement with the known energy of 7430 keV. The decay of  $^{250}\text{Fm}$  was also consistent with the known branch of >90% alpha. The random correlation analysis of  $^{250}\text{Fm}$  is treated separately from the other nuclides in the chain because of its long half-life; see Sec. 5.4.2.

## 5.4. Analysis of Expected Random Correlations

### 5.4.1. Expected $^{262}\text{Bh}$ , $^{258}\text{Db}$ , and $^{254}\text{Lr}$ Random Correlations

An analysis of the expected number of random correlations due to unrelated events was performed. The basis for this analysis has been described previously in this work in Sec. 3.4.1 and the results are given in Table 5.3.

The alpha energy range of interest was 8300-11000 keV, chosen to cover the alpha-decay energies of  $^{262}\text{Bh}$ ,  $^{258}\text{Db}$ , and  $^{254}\text{Lr}$ .  $^{250}\text{Md}$  has been excluded from this discussion because it predominantly decays by EC (94% branch) to  $^{250}\text{Fm}$ , which is treated separately in the next section. At all three beam energies, the rate of alpha-particles per pixel within this energy range was on the order of  $10^{-6} \text{ s}^{-1}$ , and the number of implantation events was approximately  $10^4$ . The probability of an alpha event within the energy range following an implantation event was  $\sim 10^{-4}\text{--}10^{-3} \text{ s}^{-1}$ . Thus, the expected numbers of random EVR- $\alpha$  ( $n_\alpha = 1$ ) correlations were high, more than 5 at each beam energy. Yet, the alpha-particle rate was sufficiently low so that the expected number of EVR- $\alpha$ - $\alpha$ - $\alpha$  ( $n_\alpha = 3$ ) correlations (for example, EVR- $^{262}\text{Bh}$ - $^{258}\text{Db}$ - $^{254}\text{Lr}$ ) was less than  $10^{-6}$  in all cases. Thus, the alpha-decay chains are regarded as real correlations.

In the case of  $^{262}\text{Bh}$  alpha-decay followed by  $^{258}\text{Db}$  EC and  $^{258}\text{Rf}$  fission, the expected number of EVR-fission correlations was estimated to be similar to the number of chain- $^{250}\text{Fm}$  correlations (see Sec. 5.4.2). Once the requirement that an alpha-particle event occur between the implantation and fission events is added, the expected numbers of random EVR- $\alpha$ -fission correlations drops by four to five orders of magnitude and are insignificant. Thus, the decay chains leading to fission of  $^{258}\text{Rf}$  are considered real correlations.

The same analysis performed for the two  $^{261}\text{Bh}$  decay chains leads to similar results.

### 5.4.2. Expected $^{250}\text{Fm}$ Random Correlations

$^{250}\text{Fm}$  has a long half-life ( $30 \pm 3$  min), so the probability that an event with the same energy as  $^{250}\text{Fm}$  will correlate randomly to a real  $^{262}\text{Bh}$  decay chain is high. Also, the

TABLE 5.3. Analysis of expected random correlations in the  $^{208}\text{Pb}(^{55}\text{Mn}, \text{n})^{262}\text{Bh}$  experiments. In all cases,  $\Delta t_{\max}$  was 180 s and the pixel size was 3.0 mm (928 total pixels). The alpha particle rates are those measured at full beam intensity and combine alpha particles fully stopped in the focal plane with reconstructed ones. Note that the experiments are listed in energy order, rather than chronological order.  $^{250}\text{Fm}$  is treated separately in Table 5.4.

	$E_{\text{cut}}$		
	260.0 MeV	264.0 MeV	268.0 MeV
Overall Rate of Alphas with Energy 8300-11000 keV (s <sup>-1</sup> )	$3.5 \times 10^{-3}$	$1.6 \times 10^{-3}$	$3.8 \times 10^{-3}$
Rate of Alphas Per Pixel with Energy 8300-11000 keV (s <sup>-1</sup> )	$3.7 \times 10^{-6}$	$1.8 \times 10^{-6}$	$4.1 \times 10^{-6}$
$\mu$ (Expected Number of Alpha Particle Events Per Pixel in $\Delta t_{\max}$ )	$6.7 \times 10^{-4}$	$3.2 \times 10^{-4}$	$7.4 \times 10^{-4}$
$N_{\text{EVR}}$	$4.1 \times 10^{+4}$	$1.7 \times 10^{+4}$	$2.7 \times 10^{+4}$
Probability of Exactly One Alpha in the Same Pixel in $\Delta t_{\max}$	$6.7 \times 10^{-4}$	$3.2 \times 10^{-4}$	$7.4 \times 10^{-4}$
Expected Number of Random Correlations ( $n_{\alpha} = 1$ )	$2.8 \times 10^{+1}$	$0.55 \times 10^{+1}$	$2.0 \times 10^{+1}$
Probability of Exactly Two Alphas in the Same Pixel in $\Delta t_{\max}$	$2.3 \times 10^{-7}$	$0.51 \times 10^{-7}$	$2.7 \times 10^{-7}$
Expected Number of Random Correlations ( $n_{\alpha} = 2$ )	$9.3 \times 10^{-3}$	$0.88 \times 10^{-3}$	$7.2 \times 10^{-3}$
Probability of Exactly Three Alphas in the Same Pixel in $\Delta t_{\max}$	$5.1 \times 10^{-11}$	$0.54 \times 10^{-11}$	$6.7 \times 10^{-11}$
Expected Number of Random Correlations ( $n_{\alpha} = 3$ )	$21 \times 10^{-7}$	$0.93 \times 10^{-7}$	$18 \times 10^{-7}$

TABLE 5.4. Analysis of expected random correlations between observed  $^{262}\text{Bh}$  decay chains and  $^{250}\text{Fm}$ . In all cases,  $\Delta t_{max}$  was 7200 s (approximately four  $^{250}\text{Fm}$  half-lives) and the pixel size was 3.0 mm (928 total pixels). Full-energy (7200-7600 keV) alpha particle rates combine those fully stopped in the focal plane with reconstructed ones. This discussion ignores the electron-capture branch (<10%) in  $^{250}\text{Fm}$ .

	$E_{tot}$		
	260.0 MeV	264.0 MeV	268.0 MeV
Decay Chains with a Possible $^{250}\text{Fm}$ Decay	0	11	7
7200-7600 keV ( $^{250}\text{Fm}$ ) Total Alpha Rate ( $\text{s}^{-1}$ )	$1.8 \times 10^{-3}$	$1.7 \times 10^{-3}$	$2.3 \times 10^{-3}$
7200-7600 keV ( $^{250}\text{Fm}$ ) Alpha Rate per Pixel ( $\text{s}^{-1}$ )	$2.0 \times 10^{-6}$	$1.8 \times 10^{-6}$	$2.5 \times 10^{-6}$
$\mu$ (Expected Number of Alpha Particle Events Per Pixel in $\Delta t_{max}$ )	$1.4 \times 10^{-2}$	$1.3 \times 10^{-2}$	$1.8 \times 10^{-2}$
Probability of Exactly One Random $^{250}\text{Fm}$ in $\Delta t_{max}$	$1.4 \times 10^{-2}$	$1.3 \times 10^{-2}$	$1.7 \times 10^{-2}$
Expected Number of Random Chain- $^{250}\text{Fm}$ Correlations	$<0.14 \times 10^{-1}$	$1.4 \times 10^{-1}$	$1.2 \times 10^{-1}$
Number of Chain- $^{250}\text{Fm}$ Correlations Observed	0	9	7

transfer reaction product  $^{211}\text{Po}$  ( $E_\alpha = 7450$  keV) is not completely filtered out by the BGS and has a decay energy similar to  $^{250}\text{Fm}$  ( $E_\alpha = 7430$  keV), adding to the probability of random correlations.

The analysis was conducted in the same manner as for  $^{255}\text{No}$  (see Sec. 3.4.2.2) and the results are summarized in Table 5.4. This analysis estimated the number of random correlations between real decay chains and  $^{250}\text{Fm}$ . The total rate of alpha particles per pixel in the range 7200-7600 keV was approximately  $2 \times 10^{-6}$  at all three beam energies. At  $E_{tot} = 260.0$  MeV, no decay chains were observed which led to the production of  $^{250}\text{Fm}$ , and an upper limit of  $<0.014$  is estimated. At  $E_{tot} = 264.0$  MeV and 268.0 MeV, the

estimated number of random chain- $^{250}\text{Fm}$  correlations are 0.14 and 0.12, respectively. These numbers are not insignificant, even considering that 9 and 7 decay chains were observed at each energy, respectively. They suggest that possibly one or even two of the chain- $^{250}\text{Fm}$  correlations at each energy are random. However, the identification of the chains is done using the preceding Bh, Db, and Lr decays, so this result does not affect the integrity of the decay chains. It should be noted that the primary reason for the large number of possible random correlations is the presence of  $^{211}\text{Po}$ , not the long correlation time. This suggests that it is possible to correlate nuclides with half-lives on the order of 30 min as long as full-energy alpha decays are observed and no interfering nuclides are present.

## 5.5. $^{208}\text{Pb}(^{55}\text{Mn}, \text{n})^{262}\text{Bh}$ Excitation Function

The measured  $^{208}\text{Pb}(^{55}\text{Mn}, \text{n})^{262}\text{Bh}$  excitation function is shown in Fig. 5.1 along with a Gaussian fit to the data. The cross sections for the production of  $^{262}\text{Bh}^g$  and  $^{262}\text{Bh}^m$  have been summed. The fit is centered at  $E_{\text{tot}} = 264.9$  MeV. Figure 5.1 also shows the predicted  $^{208}\text{Pb}(^{55}\text{Mn}, \text{n})^{262}\text{Bh}$  excitation function according to the “Fusion by Diffusion” theory. The maximum of the theoretical prediction occurs at 263.3 MeV, in agreement with the mean value of the fit. The FWHM of the fit to the experimental data is 4.3 MeV in the laboratory frame. This width is in good agreement with the widths of previously measured 1n excitation functions (see Fig. 19 in [Hofmann1998]), but less than the FWHM of the prediction.

The height of the fit to the experimental data is  $\sim 600$  pb, more than four times the maximum cross section of the theoretical prediction ( $\sim 130$  pb). The theory is generally accurate to within a factor of two in estimating the maximum cross section of cold fusion

reactions. The additional factor of two may be caused by the onset of second-chance fission in the excited compound nucleus a few hundred keV higher in energy than expected. The sticking cross section would continue to increase until this onset, resulting in a higher 1n cross section.

Lastly, a non-upper-limit cross section for the production of  $^{261}\text{Bh}$  ( $32_{-21}^{+43}$  pb) in the  $^{208}\text{Pb}(^{55}\text{Mn}, \text{n})$  reaction was established only at the highest beam energy,  $E_{\text{col}} = 268.0$  MeV. This is consistent with the expectation that the 2n excitation function should reach its maximum approximately 9-10 MeV higher in the lab-frame, have a slightly greater width, and have a lower maximum cross section than the 1n excitation function. As stated previously, it would be valuable to continue this study at higher beam energies to observe the onset of 2n product formation and determine its excitation function.

## 5.6. Comparison of $^{208}\text{Pb}(^{55}\text{Mn}, \text{n})$ and $^{209}\text{Bi}(^{54}\text{Cr}, \text{n})$ Excitation Functions

In addition to the  $^{208}\text{Pb}(^{55}\text{Mn}, \text{n})^{262}\text{Bh}$  excitation function, Fig. 5.1 also shows the  $^{209}\text{Bi}(^{54}\text{Cr}, \text{n})^{262}\text{Bh}$  excitation function reported by Münzenberg *et al.* in [Münzenberg1989]. Unexpectedly, the maximum cross section for the  $^{55}\text{Mn} + ^{208}\text{Pb}$  reaction ( $540_{-150}^{+180}$  pb) is larger than for the  $^{54}\text{Cr} + ^{209}\text{Bi}$  reaction ( $163 \pm 34$  pb). This appears to be due to the fact that Münzenberg *et al.* used higher  $^{54}\text{Cr}$  beam energies than would now seem optimal for the production of the 1n evaporation product. Their excitation function is peaked at an excitation energy of  $20 \pm 2$  MeV, much higher than the excitation energy of 14.3 MeV observed in the current work for maximum production of the 1n product. At their next lower beam energy, the excitation energy was  $17 \pm 2$  MeV, but the total dose was only  $7 \times 10^{16}$  projectiles, resulting in cross sections of  $93_{-50}^{+93}$  pb (100% upper limit error) for

production of  $^{262}\text{Bh}^m$  and an upper limit of 51 pb for production of  $^{262}\text{Bh}^g$ . These values may be an indication that only a few decay chains were observed, which may be due to a statistical anomaly. It seems likely that if the  $^{209}\text{Bi}(\text{Cr}, \text{n})^{262}\text{Bh}$  reaction were studied at lower beam energies with larger projectile doses then the maximum of the 1n excitation function would be found at a lower energy and have a larger cross section. However, “target problems” were reported for similar experiments using the same facilities [Heßberger1985]. The excitation energy of the maximum of the excitation function may not be well established in the work by Münzenberg *et al.* but their results concerning decay properties would still be valid.

## 6. Conclusions and Future Work

### 6.1. Conclusions

The cross section of the even- $Z$ -projectile  $^{208}\text{Pb}(^{64}\text{Ni}, \text{n})^{271}\text{Ds}$  reaction was measured at two new energies using the BGS at the LBNL 88-Inch Cyclotron. In total, seven decay chains attributable to  $^{271}\text{Ds}$  were observed. These data, combined with previous results, establish an excitation function for this reaction. The maximum cross section of  $20_{-11}^{+15}$  pb was observed at  $E_{\text{tot}} = 311.5$  MeV ( $E_{\text{tot}}^* = 14.1$  MeV). The decay chains showed excellent agreement with previously published data. Charge states and magnetic rigidities of the implanting EVRs were estimated.

The data from the  $^{271}\text{Ds}$  experiments were used to estimate the optimum beam energy for the new odd- $Z$ -projectile  $^{208}\text{Pb}(^{65}\text{Cu}, \text{n})^{272}\text{Bh}$  reaction using the “Fusion by Diffusion” theory proposed by Świątecki, Siwek-Wilczyńska, and Wilczyński. A cross section for this reaction was measured for the first time, at  $E_{\text{tot}} = 321.1$  MeV ( $E_{\text{tot}}^* = 13.2$  MeV). One decay chain was observed, resulting in a measured cross section of  $1.7_{-1.4}^{+3.9}$  pb. This decay chain showed good agreement with previously published data on the decay of  $^{272}\text{Bh}$ .

The excitation function for the odd- $Z$ -projectile  $^{208}\text{Pb}(^{55}\text{Mn}, \text{n})^{262}\text{Bh}$  reaction was measured for the first time at three beam energies. A total of 33  $^{262}\text{Bh}$  decay chains was

observed. The maximum cross section of  $540_{-150}^{+180}$  pb was observed at  $E_{col} = 264.0$  MeV ( $E_{col}^* = 14.3$  MeV). This cross section is much higher than that reported for the analogous  $^{209}\text{Bi}({}^{54}\text{Cr}, \text{n})^{262}\text{Bh}$  reaction. The existence of a shorter-lived isomeric state in  $^{262}\text{Bh}$  decaying by the emission of high-energy alpha-particles was confirmed. Additionally, two decay chains attributed to  $^{261}\text{Bh}$  were observed.

In summary, the BGS is a feasible apparatus for performing transactinide element experiments. Its high transmission, coupled with the relatively high beam intensity available at the 88-Inch Cyclotron, makes it especially attractive for these studies. The separation factor is sufficient to ensure that the observed correlations are not the result of random correlations of unrelated events. The BGS should continue to be an effective device as we continue our studies toward heavier transactinide elements requiring more difficult experiments.

## 6.2. Future Work

The results described in this work suggest a number of different directions for future research. Continuing with cold fusion reactions using odd-Z projectiles, one possibility is to measure the cross section for production of  $^{271}\text{111}$  in the  $^{207}\text{Pb}({}^{65}\text{Cu}, \text{n})$  reaction. The maximum cross section of the analogous  $^{270}\text{Ds}$  reaction  $^{207}\text{Pb}({}^{64}\text{Ni}, \text{n})^{270}\text{Ds}$  has been found to be  $13 \pm 5$  pb [Hofmann2001], essentially the same as the  $15_{-6}^{+9}$  pb reported by the same group [Hofmann1998] for the  $^{208}\text{Pb}({}^{64}\text{Ni}, \text{n})^{271}\text{Ds}$  reaction. It would be interesting to know if this trend continues.

The difference in cross section between the  $^{209}\text{Bi}({}^{64}\text{Ni}, \text{n})^{272}\text{111}$  and  $^{208}\text{Pb}({}^{65}\text{Cu}, \text{n})^{272}\text{111}$  reactions was studied in this work. A similar comparison could be made for the

$^{209}\text{Bi}(^{70}\text{Zn}, \text{n})^{278}\text{113}$  and  $^{208}\text{Pb}(^{71}\text{Ga}, \text{n})^{278}\text{113}$  reactions. Unfortunately, both of these reactions are extraordinarily difficult to study, as shown by Morita *et al.*, who measured a cross section of only  $55^{+150}_{-45}$  fb for the  $^{70}\text{Zn} + ^{209}\text{Bi}$  reaction [Morita2004a]. It is unlikely that either of these reactions will be studied in the near future using the BGS.

More realistically, experiments on the production of bohrium are possible. The cross section of the  $^{208}\text{Pb}(^{55}\text{Mn}, \text{n})^{262}\text{Bh}$  reaction measured in this work is much larger than that reported for the  $^{209}\text{Bi}(^{54}\text{Cr}, \text{n})^{262}\text{Bh}$  reaction [Münzenberg1989]. As noted in Sec. 5.6, it would be informative to repeat the  $^{54}\text{Cr} + ^{209}\text{Bi}$  experiments, even if only at a single beam energy. Plans are in progress to do this experiment in the first half of 2005. The large  $^{55}\text{Mn} + ^{208}\text{Pb}$  cross section also raises the possibility of using this reaction to study alpha-gamma coincidences in the decay of  $^{262}\text{Bh}$ . Using maximum beam intensity at the peak of the excitation function, the rate of production of  $^{262}\text{Bh}$  was approximately  $1.5\text{-}2 \text{ h}^{-1}$ , so a reasonable number of coincidences could be obtained in only a few days of beam time. Such data would help determine the spin, parity, and deformation of the ground state and isomer. Bohrium would be one of the heaviest elements for which alpha-gamma coincidences have been observed.

A natural extension of the current work is to study the  $^{208}\text{Pb}(^{59}\text{Co}, \text{n})^{266}\text{Mt}$  reaction. An excitation function has been measured for the similar  $^{209}\text{Bi}(^{58}\text{Fe}, \text{n})^{266}\text{Mt}$  reaction [Hofmann1997] and the maximum cross section found to be  $7.5 \pm 2.7$  pb.  $^{266}\text{Mt}$  decays by alpha-emission into the  $^{262}\text{Bh}$  decay chain, which is now well-characterized, and populates both the ground state and isomeric state of  $^{262}\text{Bh}$ . It is difficult to predict from the current work what the cross section for the  $^{59}\text{Co} + ^{208}\text{Pb}$  reaction will be; the element 111 experiment shows that it may be comparable, but the element 107 experiment is inconclusive in this respect, at least until the new  $^{54}\text{Cr} + ^{209}\text{Bi}$  experiment is complete.

Regardless, the  $^{59}\text{Co} + ^{208}\text{Pb}$  experiment should be within the current capabilities of the 88-Inch Cyclotron and BGS.

Another experiment that should be reinvestigated is the  $^{209}\text{Bi}(^{59}\text{Co}, \text{n})^{267}\text{Ds}$  reaction. This reaction was studied by Ghiorso *et al.* [Ghiorso1995a, Ghiorso1995b], but only one decay chain was observed with a cross section of approximately 1 pb. However, this one decay chain was incomplete; one alpha event was assumed to be “lost” because of malfunctioning electronics. This experiment is challenging not just because of the small cross section, but because the lifetime of the  $^{267}\text{Ds}$  nucleus was only  $\sim 4 \mu\text{s}$ . The timing system would need to be upgraded to measure such a short lifetime accurately ( $\pm 0.1 \mu\text{s}$ ). 4  $\mu\text{s}$  is also comparable to the conversion time of the BGS electronics, so detailed preliminary experiments would be required to establish whether alpha particle energies could be measured accurately when occurring so close in time to an implantation event.

Finally, once the new ECR ion source VENUS (Versatile ECR ion source for NUclear Science) [Leitner2001] is brought online for user experiments, the beam intensity available at the LBNL 88-Inch Cyclotron should be increased significantly, especially for projectiles with masses greater than 60. Increased beam intensity, along with improved target technology, will be required to extend experiments at LBNL on the chemistry and physics of nuclides with still smaller production cross sections.

## 7. References

[Abe1997] Y. Abe, Y. Aritomo, T. Wada, and M. Ohta, A New Mechanism for Synthesis of Superheavy Elements, *J. Phys. G* **23**, 1275 (1997).

[Abe2002] Y. Abe, Reaction Dynamics of Synthesis of Superheavy Elements, *Eur. Phys. J. A* **13**, 143 (2002).

[Alberi1976] J. L. Alberi and V. Radeka, Position Sensing by Charge Division, *IEEE Trans. Nucl. Sci.*, **NS-23**, 251 (1976).

[Amiel1957] S. Amiel, A. Chetham-Strode, Jr., G. R. Choppin, A. Ghiorso, B. G. Harvey, L. W. Holm, and S. G. Thompson, Production and Properties of the Nuclides Fermium-250, 251, and 252, *Phys. Rev.* **106**, 553 (1957).

[Andreyev1994] A. N. Andreyev, D. D. Bogdanov, V. I. Chepigin, A. P. Kabachenko, O. N. Malyshев, Yu. Ts. Oganessian, A. G. Popeko, J. Roháč, R. N. Sagaidak, A. V. Taranenko, G. M. Ter-Akopian, and A. V. Yeremin, Neutron-to-Total Width Ratios for Highly Excited Transcurium Compound Nuclei, in *Heavy-Ion Fusion: Exploring the Variety of Nuclear Properties*, edited by A. M. Stefanini, G. Nebbia, S. Lunardi, G. Montagnoli (World Scientific, Singapore, 1994), p. 260.

[Armbruster2003] P. Armbruster, On the Production of Superheavy Elements, *Acta Phys. Pol. B* **34**, 1825 (2003).

[Audi2003] G. Audi, A. H. Wapstra, and C. Thibault, The AME2003 Atomic Mass Evaluation: (II). Tables, Graphs and References, *Nucl. Phys.* **A729**, 337 (2003).

[Bemis1977] C. E. Bemis, Jr., P. F. Dittner, R. J. Silva, R. L. Hahn, J. R. Tarrant, L. D. Hunt, and D. C. Hensley, Production, *L* X-Ray Identification, and Decay of the Nuclide  $^{260}105$ , *Phys. Rev. C* **16**, 1146 (1977).

[Bemis1981] C. E. Bemis, Jr., P. F. Dittner, R. L. Ferguson, D. C. Hensley, F. Plasil, and F. Pleasonton, Spontaneous-Fission Branching in the Decay of  $^{259}104$ , Phys. Rev. C **23**, 555 (1981).

[Bethe1936] H. A. Bethe and R. F. Bacher, Nuclear Physics: A. Stationary States of Nuclei, Rev. Mod. Phys. **8**, 82 (1936).

[Betz1972] H. D. Betz, Charge States and Charge-Changing Cross Sections of Fast Heavy Ions Penetrating Through Gaseous and Solid Media, Rev. Mod. Phys. **44**, 465 (1972).

[Bohr1939] N. Bohr and J. A. Wheeler, The Mechanism of Nuclear Fission, Phys. Rev. **56**, 426 (1939).

[Corish2003] J. Corish and G. M. Rosenblatt, Name and Symbol of the Element with Atomic Number 110, Pure Appl. Chem. **75**, 1613 (2003).

[Ćwiok1996] S. Ćwiok, J. Dobaczewski, P.-H. Heenen, P. Magierski, and W. Nazarewicz, Shell Structure of the Superheavy Elements, Nucl. Phys. **A611**, 211 (1996).

[Düllmann2002] Ch. E. Düllmann, W. Brüchle, R. Dressler, K. Eberhardt, B. Eichler, R. Eichler, H. W. Gäggeler, T. N. Ginter, F. Glaus, K. E. Gregorich, D. C. Hoffman, E. Jäger, D. T. Jost, U. W. Kirbach, D. M. Lee, H. Nitsche, J. B. Patin, V. Pershina, D. Piguet, Z. Qin, M. Schädel, B. Schausten, E. Schimpf, H.-J. Schött, S. Soverna, R. Sudowe, P. Thörle, S. N. Timokhin, N. Trautmann, A. Türler, A. Vahle, G. Wirth, A. B. Yakushev, and P. M. Zielinski, Chemical Investigation of Hassium (Element 108), Nature (London) **418**, 859 (2002).

[Eichler2000] R. Eichler, W. Brüchle, R. Dressler, Ch. E. Düllmann, B. Eichler, H. W. Gäggeler, K. E. Gregorich, D. C. Hoffman, S. Hübener, D. T. Jost, U. W. Kirbach, C. A. Laue, V. M. Lavanchy, H. Nitsche, J. B. Patin, D. Piguet, M. Schädel, D. A. Shaughnessy, D. A. Strellis, S. Taut, L. Tobler, Y. S. Tsyganov, A. Türler, A. Vahle, P. A. Wilk, and A. B. Yakushev, Chemical Characterization of Bohrium (Element 107), Nature (London) **407**, 63 (2000).

[Eskola1971] K. Eskola, P. Eskola, M. Nurmia, and A. Ghiorso, Studies of Lawrencium Isotopes with Mass Numbers 255 Through 260, Phys. Rev. C **4**, 632 (1971).

[Eskola1973] P. Eskola, Studies of Mendelevium Isotopes with Mass Numbers 248 Through 252, Phys. Rev. C **7**, 280 (1973).

[Essel1992] H. G. Essel, J. Hoffmann, M. Richter, and D. Schall, VME Trigger Description, available at [http://www-gsi-vms.gsi.de/goodoc/GM\\_VME\\_TRIG.ps](http://www-gsi-vms.gsi.de/goodoc/GM_VME_TRIG.ps) (1992).

[Essel1996] H. G. Essel, J. Hoffmann, N. Kurz, R. S. Mayer, W. Ott, and D. Schall, The New Data Acquisition System at GSI, IEEE Trans. Nucl. Sci. **NS-43**, 132 (1996).

[Essel2000] H. G. Essel and N. Kurz, The General Purpose Data Acquisition System MBS, IEEE Trans. Nucl. Sci. **NS-47**, 337 (2000).

[Evans1955] R. D. Evans, *The Atomic Nucleus* (McGraw-Hill, New York, 1955), p. 361.

[Ewald1976] H. Ewald, K. Gütter, G. Münzenberg, P. Armbruster, W. Faust, S. Hofmann, K. H. Schmidt, W. Schneider, and K. Valli, Report on the Heavy Ion Separator SIS at the GSI, Nucl. Instrum. Methods **139**, 223 (1976).

[Firestone1996] R. B. Firestone, *Table of Isotopes*, 8th Ed., edited by V. S. Shirley (John Wiley & Sons, New York, 1996), Vol. II.

[Flerov1987] G. N. Flerov and G. M. Ter-Akopian, Synthesis and Study of Atomic Nuclei with  $Z > 100$ , Prog. Part. Nucl. Phys. **19**, 197 (1987).

[Gan2004] Z. G. Gan, J. S. Guo, X. L. Wu, Z. Qin, H. M. Fan, X. G. Lei, H. Y. Liu, B. Guo, H. G. Xu, R. F. Chen, C. F. Dong, F. M. Zhang, H. L. Wang, C. Y. Xie, Z. Q. Feng, Y. Zhen, L. T. Song, P. Luo, H. S. Xu, X. H. Zhou, G. M. Jin, and Z. Ren, New Isotope  $^{265}\text{Bh}$ , Eur. Phys. J. A **20**, 385 (2004).

[Ghiorso1955] A. Ghiorso, B. G. Harvey, G. R. Choppin, S. G. Thompson, and G. T. Seaborg, New Element Mendelevium, Atomic Number 101, Phys. Rev. **98**, 1518 (1955).

[Ghiorso1969] A. Ghiorso, M. Nurmia, J. Harris, K. Eskola, and P. Eskola, Positive Identification of Two Alpha-Particle-Emitting Isotopes of Element 104, Phys. Rev. Lett., **22**, 1317 (1969).

[Ghiorso1970] A. Ghiorso, M. Nurmia, K. Eskola, J. Harris, and P. Eskola, New Element Hahnium, Atomic Number 105, Phys. Rev. Lett., **24**, 1498 (1970).

[Ghiorso1974] A. Ghiorso, J. M. Nitschke, J. R. Alonso, C. T. Alonso, M. Nurmia, G. T. Seaborg, E. K. Hulet, and R. W. Lougheed, Element 106, Phys. Rev. Lett., **33**, 1490 (1974).

[Ghiorso1988] A. Ghiorso, S. Yashita, M. E. Leino, L. Frank, J. Kalnins, P. Armbruster, J.-P. Dufour, and P. K. Lemmertz, SASSY, a Gas-Filled Magnetic Separator for the Study of Fusion Reaction Products, Nucl. Instrum. Methods Phys. Res. **A269**, 192 (1988).

[Ghiorso1995a] A. Ghiorso, D. Lee, L. P. Somerville, W. Loveland, J. M. Nitschke, W. Ghiorso, G. T. Seaborg, P. Wilmarth, R. Leres, A. Wydler, M. Nurmia, K. Gregorich, R. Gaylord, T. Hamilton, N. J. Hannink, D. C. Hoffman, C. Jarzynski, C. Kacher, B. Kadkhodayan, S. Kreek, M. Lane, A. Lyon, M. A. McMahan, M. Neu, T. Sikkeland, W. J. Swiatecki, A. Türler, J. T. Walton, and S. Yashita, Evidence for the Synthesis of  $^{267}\text{110}$  Produced by the  $^{59}\text{Co} + ^{209}\text{Bi}$  Reaction, *Nucl. Phys.* **A583**, 861 (1995).

[Ghiorso1995b] A. Ghiorso, D. Lee, L. P. Somerville, W. Loveland, J. M. Nitschke, W. Ghiorso, G. T. Seaborg, P. Wilmarth, R. Leres, A. Wydler, M. Nurmia, K. Gregorich, K. Czerwinski, R. Gaylord, T. Hamilton, N. J. Hannink, D. C. Hoffman, C. Jarzynski, C. Kacher, B. Kadkhodayan, S. Kreek, M. Lane, A. Lyon, M. A. McMahan, M. Neu, T. Sikkeland, W. J. Swiatecki, A. Türler, J. T. Walton, and S. Yashita, Evidence for the Possible Synthesis of Element 110 by the  $^{59}\text{Co} + ^{209}\text{Bi}$  Reaction, *Phys. Rev. C* **51**, R2293 (1995).

[Ginter2003] T. N. Ginter, K. E. Gregorich, W. Loveland, D. M. Lee, U. W. Kirbach, R. Sudowe, C. M. Folden III, J. B. Patin, N. Seward, P. A. Wilk, P. M. Zielinski, K. Aleklett, R. Eichler, H. Nitsche, and D. C. Hoffman, Confirmation of Production of Element 110 by the  $^{208}\text{Pb} + ^{64}\text{Ni}, n$  Reaction, *Phys. Rev. C* **67**, 064609 (2003).

[Gregorich1991] K. E. Gregorich, Maximum Likelihood Decay Fits by the Simplex Method, *Nucl. Instrum. Methods Phys. Res.* **A302**, 135 (1991).

[Gregorich1994] K. E. Gregorich, M. R. Lane, M. F. Mohar, D. M. Lee, C. D. Kacher, E. R. Sylwester, and D. C. Hoffman, First Confirmation of the Discovery of Element 106, *Phys. Rev. Lett.* **72**, 1423 (1994).

[Gregorich2000] K. E. Gregorich and V. Ninov, Superheavy Elements with the Berkeley Gas-Filled Separator, *J. Nucl. Radiochem. Sci.* **1**, 1 (2000).

[Gregorich2004] K. E. Gregorich (private communication).

[Heßberger1985] F. P. Heßberger, G. Münzenberg, S. Hofmann, Y. K. Agarwal, K. Poppensieker, W. Reisdorf, K.-H. Schmidt, J. R. H. Schneider, W. F. W. Schneider, H. J. Schött, P. Armbruster, B. Thuma, C.-C. Sahm, and D. Vermeulen, The New Isotopes  $^{258}\text{105}$ ,  $^{257}\text{105}$ ,  $^{254}\text{Lr}$ , and  $^{253}\text{Lr}$ , *Z. Phys. A* **322**, 557 (1985).

[Hoffman1998] D. C. Hoffman, The Transuranium Elements: From Neptunium to Element 112, in *Actinides and the Environment*, edited by P. A. Sterne, A. Gonis, and A. A. Borovoi (Kluwer Academic Publishers, Norwell, Massachusetts, 1998), p. 3.

[Hoffman2000] D. C. Hoffman, A. Ghiorso, and G. T. Seaborg, *The Transuranium People: The Inside Story* (Imperial College Press, London, 2000).

[Hoffman2003] D. C. Hoffman and D. M. Lee, Superheavy Elements, in *Handbook of Nuclear Chemistry*, edited by A. Vértes, S. Nagy, and Z. Klencsár (Kluwer Academic Publishers, Dordrecht, The Netherlands, 2003), Vol. 2, p. 397.

[Hofmann1995a] S. Hofmann, V. Ninov, F. P. Heßberger, P. Armbruster, H. Folger, G. Münzenberg, H. J. Schött, A. G. Popeko, A. V. Yeremin, A. N. Andreyev, S. Saro, R. Janik, and M. Leino, Production and Decay of  $^{269}\text{110}$ , *Z. Phys. A* **350**, 277 (1995).

[Hofmann1995b] S. Hofmann, V. Ninov, F. P. Heßberger, P. Armbruster, H. Folger, G. Münzenberg, H. J. Schött, A. G. Popeko, A. V. Yeremin, A. N. Andreyev, S. Saro, R. Janik, and M. Leino, The New Element 111, *Z. Phys. A* **350**, 281 (1995).

[Hofmann1995c] S. Hofmann, V. Ninov, F. P. Heßberger, P. Armbruster, H. Folger, G. Münzenberg, H. J. Schött, A. G. Popeko, A. V. Yeremin, A. N. Andreyev, S. Saro, R. Janik, and M. Leino, Production and Decay of  $^{269}\text{110}$  and  $^{271}\text{110}$ , *GSI Scientific Report 1994*, GSI Report 95-1 (1995).

[Hofmann1996] S. Hofmann, V. Ninov, F. P. Heßberger, P. Armbruster, H. Folger, G. Münzenberg, H. J. Schött, A. G. Popeko, A. V. Yeremin, S. Saro, R. Janik, and M. Leino, The New Element 112, *Z. Phys. A* **354**, 229 (1996).

[Hofmann1997] S. Hofmann, F. P. Heßberger, V. Ninov, P. Armbruster, G. Münzenberg, C. Stodel, A. G. Popeko, A. V. Yeremin, S. Saro, and M. Leino, Excitation Function for the Production of  $^{265}\text{108}$  and  $^{266}\text{109}$ , *Z. Phys. A* **358**, 377 (1997).

[Hofmann1998] S. Hofmann, New Elements—Approaching  $Z = 114$ , *Rep. Prog. Phys.* **61**, 639 (1998).

[Hofmann2000] S. Hofmann and G. Münzenberg, The Discovery of the Heaviest Elements, *Rev. Mod. Phys.* **72**, 733 (2000).

[Hofmann2001] S. Hofmann, F. P. Heßberger, D. Ackermann, S. Antalic, P. Cagarda, S. Ćwiok, B. Kindler, J. Kojouharova, B. Lommel, R. Mann, G. Münzenberg, A. G. Popeko, S. Saro, H. J. Schött, and A.V. Yeremin, The New Isotope  $^{270}\text{110}$  and Its Decay Products  $^{266}\text{Hs}$  and  $^{262}\text{Sg}$ , *Eur. Phys. J. A* **10**, 5 (2001).

[Hofmann2002] S. Hofmann, F. P. Heßberger, D. Ackermann, G. Münzenberg, S. Antalic, P. Cagarda, B. Kindler, J. Kojouharova, M. Leino, B. Lommel, R. Mann, A. G. Popeko, S. Reshitko, S. Saro, J. Uusitalo, and A. V. Yeremin, New Results on Elements 111 and 112, *Eur. Phys. J. A* **14**, 147 (2002).

[Hofmann2003] S. Hofmann, Synthesis and Properties of Superheavy Elements, *J. Nucl. Radiochem. Sci.* **4**, R1 (2003).

[Hyde1987] E. K. Hyde, D. C. Hoffman, and O. L. Keller, A History and Analysis of the Discovery of Elements 104 and 105, *Radiochim. Acta* **42**, 57 (1987).

[Jackson1956] J. D. Jackson, A Schematic Model for  $(p, xn)$  Cross Sections in Heavy Elements, *Can. J. Phys.* **34**, 767 (1956).

[Kirbach2002] U. W. Kirbach, C. M. Folden III, T. N. Ginter, K. E. Gregorich, D. M. Lee, V. Ninov, J. P. Omtvedt, J. B. Patin, N. K. Seward, D. A. Strellis, R. Sudowe, A. Türler, P. A. Wilk, P. M. Zielinski, D. C. Hoffman, H. Nitsche, The Cryo-Thermochromatographic Separator (CTS): A New Rapid Separation and  $\alpha$ -Detection System for On-Line Chemical Studies of Highly Volatile Osmium and Hassium ( $Z = 108$ ) Tetroxides, *Nucl. Instrum. Methods Phys. Res. A* **484**, 587 (2002).

[Krane1988] K. S. Krane, *Introductory Nuclear Physics* (John Wiley & Sons, New York, 1988).

[Lazarev1994] Yu. A. Lazarev, Yu. V. Lobanov, Yu. Ts. Oganessian, V. K. Utyonkov, F. Sh. Abdullin, G. V. Buklanov, B. N. Gikal, S. Iliev, A. N. Mezentsev, A. N. Polyakov, I. M. Sedykh, I. V. Shirokovsky, V. G. Subbotin, A. M. Sukhov, Yu. S. Tsyanov, V. E. Zhuchko, R. W. Lougheed, K. J. Moody, J. F. Wild, E. K. Hulet, and J. H. McQuaid, Discovery of Enhanced Nuclear Stability Near the Deformed Shells  $N = 162$  and  $Z = 108$ , *Phys. Rev. Lett.* **73**, 624 (1994).

[Lazarev1995] Yu. A. Lazarev, Yu. V. Lobanov, Yu. Ts. Oganessian, Yu. S. Tsyanov, V. K. Utyonkov, F. Sh. Abdullin, S. Iliev, A. N. Polyakov, J. Rigol, I. V. Shirokovsky, V. G. Subbotin, A. M. Sukhov, G. V. Buklanov, B. N. Gikal, V. B. Kutner, A. N. Mezentsev, I. M. Sedykh, D. V. Vakatov, R. W. Lougheed, J. F. Wild, K. J. Moody, and E. K. Hulet, New Nuclide  $^{267}108$  Produced by the  $^{238}\text{U} + ^{34}\text{S}$  Reaction, *Phys. Rev. Lett.* **75**, 1903 (1995).

[Lazarev1996] Yu. A. Lazarev, Yu. V. Lobanov, Yu. Ts. Oganessian, V. K. Utyonkov, F. Sh. Abdullin, A. N. Polyakov, J. Rigol, I. V. Shirokovsky, Yu. S. Tsyanov, S. Iliev, V. G. Subbotin, A. M. Sukhov, G. V. Buklanov, B. N. Gikal, V. B. Kutner, A. N. Mezentsev, and K. Subotic, J. F. Wild, R. W. Lougheed, and K. J. Moody,  $\alpha$  Decay of  $^{273}110$ : Shell Closure at  $N = 162$ , *Phys. Rev. C* **54**, 620 (1996).

[Leino1999] M. Leino, H. Kankaanpää, R.-D. Herzberg, A. J. Chewter, F. P. Heßberger, Y. Le Coz, F. Becker, P. A. Butler, J. F. C. Cocks, O.

Dorvaux, K. Eskola, J. Gerl, P. T. Greenlees, K. Helariutta, M. Houry, G. D. Jones, P. Jones, R. Julin, S. Juutinen, H. Kettunen, T. L. Khoo, A. Kleinböhl, W. Korten, P. Kuusiniemi, R. Lucas, M. Muikku, P. Nieminen, R. D. Page, P. Rahkila, P. Reiter, A. Savelius, Ch. Schlegel, Ch. Theisen, W. H. Trzaska, H.-J. Wollersheim, In-Beam Study of  $^{254}\text{No}$ , *Eur. Phys. J. A* **6**, 63 (1999).

[Leitner2001] M. A. Leitner, C. M. Lyneis, D. C. Wutte, C. E. Taylor, and S. R. Abbot, Construction of the Superconducting ECR Ion Source Venus, *Physica Scripta* **T92**, 171 (2001); <http://ecrgroup.lbl.gov>.

[Lougheed1994] R. W. Lougheed, K. J. Moody, J. F. Wild, E. K. Hulet and J. H. McQuaid, Yu. A. Lazarev, Yu. V. Lobanov, Yu. Ts. Oganessian, V. K. Utyonkov, F. Sh. Abdullin, G. V. Buklanov, B. N. Gikal, S. Iliev, A. N. Mezentsev, A. N. Polyakov, I. M. Sedykh, I. V. Shirokovsky, V. G. Subbotin, A. M. Sukhov, Yu. S. Tsyganov and V. E. Zhuchko, Observation of Enhanced Nuclear Stability Near the 162 Neutron Shell, *J. Alloy Compd.* **213**, 61 (1994).

[Loveland2000] W. Loveland, Recent Advances in Understanding Nuclear Reactions, *J. Radioanal. Nucl. Chem.* **243**, 147 (2000).

[Loveland2001] W. Loveland, Nuclear Chemistry Progress Report (2001), available at <http://oregonstate.edu/dept/nchem/menu/prog01.htm>.

[Loveland2003] W. Loveland, Nuclear Chemistry Progress Report (2003), available at <http://osu.orst.edu/dept/nchem/menu/prog03.pdf>.

[Mayer1948] M. G. Mayer, On Closed Shells in Nuclei, *Phys. Rev.* **74**, 235 (1948).

[Mayer1950a] M. G. Mayer, Nuclear Configurations in the Spin-Orbit Coupling Model. I. Empirical Evidence, *Phys. Rev.* **78**, 16 (1950).

[Mayer1950b] M. G. Mayer, Nuclear Configurations in the Spin-Orbit Coupling Model. II. Theoretical Considerations, *Phys. Rev.* **78**, 22 (1950).

[Meldner1967] H. Meldner, Predictions of New Magic Regions and Masses for Super-Heavy Nuclei from Calculations with Realistic Shell Model Single Particle Hamiltonians, *Ark. Fys.* **36**, 593 (1967).

[Möller1995] P. Möller, J. R. Nix, W. D. Myers, and W. J. Świątecki, Nuclear Ground-State Masses and Deformations, *At. Data Nucl. Data Tables* **59**, 185 (1995).

[Moretto1972] L. G. Moretto, Statistical Description of Deformation in Excited Nuclei and Disappearance of Shell Effects with Excitation Energy, *Nucl. Phys.* **A182**, 641 (1972).

[Morimoto2004] K. Morimoto and RIKEN SHE Group, Recent Results of Superheavy Element Research using GARIS at RIKEN, Presentation to the 3rd Workshop on Recoil Separator for Superheavy Element Chemistry, Darmstadt, Germany, August 27, 2004.

[Morita2002] K. Morita, K. Morimoto, D. Kaji, A. Yoneda, A. Yoshida, T. Suda, E. Ideguchi, T. Ohnishi, Y.-L. Zhao, H. Xu, T. Zheng, H. Haba, H. Kudo, K. Sueki, A. Ozawa, F. Tokanai, H. Koura, A. V. Yeremin, R. Kanungo, K. Katori, and I. Tanihata, Measurement of an Excitation Function of Production Cross Section of  $^{271}\text{110}$  via  $^{208}\text{Pb} + ^{64}\text{Ni} \rightarrow ^{271}\text{110} + n$  Reaction, RIKEN Accel. Prog. Rep. **35** (2002); Confirmation of the Synthesis of Isotope  $^{271}\text{110}$  of the Element 110, RIKEN Accel. Prog. Rep. **35** (2002).

[Morita2003] K. Morita, K. Morimoto, D. Kaji, T. Chihara, H. Haba, H. Hasebe, Y. Higurashi, E. Ideguchi, N. Iwasa, T. Kamigaito, R. Kanungo, T. Kato, K. Katori, M. Kidera, H. Koura, H. Kudo, T. Ohnishi, T. Suda, K. Sueki, I. Sugai, T. Suzuki, S. Takeuchi, F. Tokanai, K. Uchiyama, Y. Wakasaya, H. Xu, T. Yamaguchi, A. Yeremin, A. Yoneda, A. Yoshida, Y. L. Zhao, T. Zheng, and I. Tanihata, Conformation of  $^{271}\text{[110]}$  and Discovery of  $^{234}\text{Bk}$  and  $^{230}\text{Am}$  at RIKEN GARIS Facility, in *Proceedings of the International Symposium on Frontiers of Collective Motions (CM2002), Aizu, Japan, 2002*, edited by H. Sagawa and H. Iwasaki (World Scientific, New Jersey, 2003), p. 140.

[Morita2004a] K. Morita, K. Morimoto, D. Kaji, T. Akiyama, S. Goto, H. Haba, E. Ideguchi, R. Kanungo, K. Katori, H. Koura, H. Kudo, T. Ohnishi, A. Ozawa, T. Suda, K. Sueki, H. Xu, T. Yamaguchi, A. Yoneda, A. Yoshida and Y. Zhao, Experiment on the Synthesis of Element 113 in the Reaction  $^{209}\text{Bi}(\text{Zn},n)^{278}\text{113}$ , J. Phys. Soc. Japan **73**, 2593 (2004).

[Morita2004b] K. Morita, K. Morimoto, D. Kaji, H. Haba, E. Ideguchi, J. C. Peter, R. Kanungo, K. Katori, H. Koura, H. Kudo, T. Ohnishi, A. Ozawa, T. Suda, K. Sueki, I. Tanihata, H. Xu, A. V. Yeremin, A. Yoneda, A. Yoshida, Y.-L. Zhao, T. Zheng, S. Goto and F. Tokanai, Production and Decay of  $^{272}\text{111}$  and Its Daughter Nuclei, J. Phys. Soc. Japan **73**, 1738 (2004).

[Morita2004c] K. Morita, K. Morimoto, D. Kaji, S. Goto, H. Haba, E. Ideguchi, R. Kanungo, K. Katori, H. Koura, H. Kudo, T. Ohnishi, A. Ozawa, J. C. Peter, T. Suda, K. Sueki, I. Tanihata, F. Tokanai, H. Xu, A. V. Yeremin, and A. Yoneda, A. Yoshida, Y.-L. Zhao, and T. Zheng, Status of Heavy Element Research Using GARIS at RIKEN, Nucl. Phys. **A734**, 101 (2004).

[Morita2004d] K. Morita, K. Morimoto, D. Kaji, H. Haba, E. Ideguchi, R. Kanungo, K. Katori, H. Koura, H. Kudo, T. Ohnishi, A. Ozawa, T. Suda, K. Sueki, I. Tanihata, H. Xu, A. V. Yeremin, A. Yoneda, A. Yoshida, Y.-L. Zhao, and T. Zheng, Production and Decay of the Isotope  $^{271}\text{Ds}$  ( $Z = 110$ ), *Eur. Phys. J. A* **21**, 257 (2004).

[Morita2004e] K. Morita *et al.*, *Nucl. Instrum. Methods* (to be published).

[Moulton1978] J. B. Moulton, J. E. Stephenson, R. P. Schmitt, and G. J. Wozniak, A New Method for Calibrating the Pulse-Height Defect in Solid State Detectors, *Nucl. Instrum. Methods* **157**, 325 (1978).

[Münzenberg1979] G Münzenberg, W. Faust, S. Hofmann, P. Armbruster, K. Güttner, and H. Ewald, The Velocity Filter SHIP, A Separator of Unslowed Heavy Ion Fusion Products, *Nucl. Instrum. Methods*. **161**, 65 (1979).

[Münzenberg1981a] G. Münzenberg, S. Hofmann, F. P. Heßberger, W. Reisdorf, K. H. Schmidt, J. H. R. Schneider, P. Armbruster, C. C. Sahm, and B. Thuma, Identification of Element 107 by  $\alpha$  Correlation Chains, *Z. Phys. A* **300**, 107 (1981).

[Münzenberg1981b] G. Münzenberg, S. Hofmann, W. Faust, F. P. Heßberger, W. Reisdorf, K.-H. Schmidt, T. Kitahara, P. Armbruster, K. Güttner, B. Thuma, and D. Vermeulen, The New Isotopes  $^{247}\text{Md}$ ,  $^{243}\text{Fm}$ ,  $^{239}\text{Cf}$ , and Investigation of the Evaporation Residues from Fusion of  $^{206}\text{Pb}$ ,  $^{208}\text{Pb}$ , and  $^{209}\text{Bi}$  with  $^{40}\text{Ar}$ , *Z. Phys. A* **302**, 7 (1981).

[Münzenberg1982] G. Münzenberg, P. Armbruster, F. P. Heßberger, S. Hofmann, K. Poppensieker, W. Reisdorf, J. H. R. Schneider, W. F. W. Schneider, K.-H. Schmidt, C.-C. Sahm, and D. Vermeulen, Observation of One Correlated  $\alpha$ -Decay in the Reaction  $^{58}\text{Fe}$  on  $^{209}\text{Bi} \rightarrow ^{267}109$ , *Z. Phys. A* **309** 89 (1982).

[Münzenberg1984a] G. Münzenberg, W. Reisdorf, S. Hofmann, Y. K. Agarwal, F. P. Heßberger, K. Poppensieker, J. R. H. Schneider, W. F. W. Schneider, K.-H. Schmidt, H.-J. Schött, P. Armbruster, C.-C. Sahm, and D. Vermeulen, Evidence for Element 109 from One Correlated Decay Sequence Following the Fusion of  $^{58}\text{Fe}$  with  $^{209}\text{Bi}$ , *Z. Phys. A* **315**, 145 (1984).

[Münzenberg1984b] G. Münzenberg, P. Armbruster, H. Folger, F. P. Heßberger, S. Hofmann, J. Keller, K. Poppensieker, W. Reisdorf, K.-H. Schmidt, H.-J. Schött, M. E. Leino, and R. Hingmann, The Identification of Element 108, *Z. Phys. A* **317**, 235 (1984).

[Münzenberg1987] G. Münzenberg, P. Armbruster, G. Berthes, H. Folger, F. P. Heßberger, S. Hofmann, J. Keller, K. Poppensieker, A. B. Quint,

W. Reisdorf, K.-H. Schmidt, H.-J. Schött, K. Sümmerer, I. Zychor, M. E. Leino, R. Hingmann, U. Gollerthan, and E. Hanelt, Observation of the Isotopes  $^{264}\text{108}$  and  $^{265}\text{108}$ , *Z. Phys. A* **328**, 49 (1987).

[Münzenberg1988] G. Münzenberg, S. Hofmann, F. P. Heßberger, H. Folger, V. Ninov, K. Poppensieker, A. B. Quint, W. Reisdorf, H.-J. Schött, K. Sümmerer, P. Armbruster, M. E. Leino, D. Ackermann, U. Gollerthan, E. Hanelt, W. Morawek, Y. Fujita, T. Schwab, and A. Türler, New Results on Element 109, *Z. Phys. A* **330**, 435 (1988).

[Münzenberg1989] G. Münzenberg, P. Armbruster, S. Hofmann, F. P. Heßberger, H. Folger, J. G. Keller, V. Ninov, K. Poppensieker, A. B. Quint, W. Reisdorf, K.-H. Schmidt, J. R. H. Schneider, H.-J. Schött, K. Sümmerer, I. Zychor, M. E. Leino, D. Ackermann, U. Gollerthan, E. Hanelt, W. Morawek, D. Vermeulen, Y. Fujita, and T. Schwab, Element 107, *Z. Phys. A* **333**, 163 (1989).

[Myers1966] W. D. Myers and W. J. Swiatecki, Nuclear Masses and Deformations, *Nucl. Phys.* **81**, 1 (1966).

[Myers1967] W. D. Myers and W. J. Swiatecki, Anomalies in Nuclear Masses, *Ark. Fys.* **36**, 343 (1967).

[Myers1994] W. D. Myers and W. J. Swiatecki, Nuclear Properties According to the Thomas-Fermi Model, *Nucl. Phys.* **A601**, 141 (1996); Table of Nuclear Masses According to the 1994 Thomas-Fermi Model, Lawrence Berkeley Laboratory Report LBL-36803, 1994 (unpublished), available at <http://ie.lbl.gov/txt/ms.txt>.

[Myers1999] W. D. Myers and W. J. Świątecki, Thomas-Fermi Fission Barriers, *Phys. Rev. C* **60**, 014606 (1999).

[Nilsson1955] S. G. Nilsson, Binding States of Individual Nucleons in Strongly Deformed Nuclei, *Dan. Vid. Selsk. Mat. Fys. Medd.* **29**, no. 16 (1955).

[Ninov1998] V. Ninov, K. E. Gregorich, and C. A. McGrath, The Berkeley Gas-Filled Separator, in *ENAM 98: Exotic Nuclei and Atomic Masses*, edited by B. M. Sherrill, D. J. Morrissey, and C. N. Davids (American Institute of Physics, Woodbury, New York, 1998), p. 704.

[Nitschke1979] J. M. Nitschke, R. E. Leber, M. J. Nurmia, and A. Ghiorso, Observations in the Reaction of Two Magic Nuclei:  $^{208}\text{Pb}$  and  $^{48}\text{Ca}$ , *Nucl. Phys.* **A313**, 236 (1979).

[Nurmia1967] M. Nurmia, T. Sikkeland, R. Silva, and A. Ghiorso, Spontaneous Fission of Light Fermium Isotopes; New Nuclides  $^{244}\text{Fm}$  and  $^{245}\text{Fm}$ , *Phys. Lett.* **26B**, 78 (1967).

[Oganessian1975] Yu. Ts. Oganessian, A. S. Iljinov, A. G. Demin, and S. P. Tretyakova, Experiments on the Production of Fermium Neutron-Deficient Isotopes and New Possibilities of Synthesizing Elements with  $Z > 100$ , *Nucl. Phys.* **A239**, 353 (1975).

[Oganessian1976] Yu. Ts. Oganessian, A. G. Demin, N. A. Danilov, G. N. Flerov, M. P. Ivanov, A. S. Iljinov, N. N. Kolesnikov, B. N. Markov, V. M. Plotko, and S. P. Tretyakova, On Spontaneous Fission of Neutron-Deficient Isotopes of Elements 103, 105, and 107, *Nucl. Phys.* **A273**, 505 (1976).

[Oganessian1984] Yu. Ts. Oganessian, M. Hussonnois, A. G. Demin, Yu. P. Kharitonov, H. Bruchertseifer, O. Constantinescu, Yu. S. Korotkin, S. P. Tretyakova, V. K. Utyonkov, I. V. Shirovsky, and J. Estevez, Experimental Studies on the Formation and Radioactive Decay of Isotopes with  $Z = 104\text{--}109$ , *Radiochim. Acta* **37**, 113 (1984).

[Oganessian1999] Yu. Ts. Oganessian, A. V. Yeremin, A. G. Popeko, S. L. Bogomolov, G. V. Buklanov, M. L. Chelnokov, V. I. Chepigin, B. N. Gikal, V. A. Gorshkov, G. G. Gulbekian, M. G. Itkis, A. P. Kabachenko, A. Yu. Lavrentev, O. N. Malyshев, J. Rohac, R. N. Sagaidak, S. Hofmann, S. Saro, G. Giardina, and K. Morita, Synthesis of Nuclei of the Superheavy Element 114 in Reactions Induced by  $^{48}\text{Ca}$ , *Nature (London)* **400**, 242 (1999).

[Oganessian2001] Yu. Ts. Oganessian, V. K. Utyonkov, Yu. V. Lobanov, F. Sh. Abdullin, A. N. Polyakov, I. V. Shirokovsky, Yu. S. Tsyanov, G. G. Gulbekian, S. L. Bogomolov, B. N. Gikal, A. N. Mezentsev, S. Iliev, V. G. Subbotin, A. M. Sukhov, O. V. Ivanov, G. V. Buklanov, K. Subotic, and M. G. Itkis, K. J. Moody, J. F. Wild, N. J. Stoyer, M. A. Stoyer, R. W. Lougheed, C. A. Laue, Ye. A. Karelina, A. N. Tatarinov, Observation of the Decay of  $^{292}\text{116}$ , *Phys. Rev. C* **63**, 011301(R) (2001).

[Oganessian2002] Yu. Ts. Oganessian, V. K. Utyonkov, Yu. V. Lobanov, F. Sh. Abdullin, A. N. Polyakov, I. V. Shirokovsky, Yu. S. Tsyanov, G. G. Gulbekian, S. L. Bogomolov, B. N. Gikal, A. N. Mezentsev, S. Iliev, V. G. Subbotin, A. M. Sukhov, O. V. Ivanov, G. V. Buklanov, K. Subotic, A. A. Voinov, M. G. Itkis, K. J. Moody, J. F. Wild, N. J. Stoyer, M. A. Stoyer, R. W. Lougheed, and C. A. Laue, Synthesis of Superheavy Nuclei in the Reactions of  $^{244}\text{Pu}$  and  $^{248}\text{Cm}$  with  $^{48}\text{Ca}$ , *Eur. Phys. J. A* **15**, 201 (2002).

[Oganessian2004a] Yu. Ts. Oganessian, V. K. Utyonkov, Yu. V. Lobanov, F. Sh. Abdullin, A. N. Polyakov, I. V. Shirokovsky, Yu. S. Tsyganov, G. G. Gulbekian, S. L. Bogomolov, A. N. Mezentsev, S. Iliev, V. G. Subbotin, A. M. Sukhov, A. A. Voinov, G. V. Buklanov, K. Subotic, V. I. Zagrebaev, M. G. Itkis, J. B. Patin, K. J. Moody, J. F. Wild, M. A. Stoyer, N. J. Stoyer, D. A. Shaughnessy, J. M. Kenneally, and R. W. Lougheed, Experiments on the Synthesis of Element 115 in the Reaction  $^{243}\text{Am}(^{48}\text{Ca},xn)^{291-x}115$ , Phys. Rev. C **69**, 021601(R) (2004).

[Oganessian2004b] Yu. Ts. Oganessian, V. K. Utyonkov, Yu. V. Lobanov, F. Sh. Abdullin, A. N. Polyakov, I. V. Shirokovsky, Yu. S. Tsyganov, G. G. Gulbekian, S. L. Bogomolov, B. N. Gikal, A. N. Mezentsev, S. Iliev, V. G. Subbotin, A. M. Sukhov, A. A. Voinov, G. V. Buklanov, K. Subotic, V. I. Zagrebaev, M. G. Itkis, J. B. Patin, K. J. Moody, J. F. Wild, M. A. Stoyer, N. J. Stoyer, D. A. Shaughnessy, J. M. Kenneally, and R. W. Lougheed, Measurements of Cross Sections for the Fusion-Evaporation Reactions  $^{244}\text{Pu}(^{48}\text{Ca},xn)^{292-x}114$  and  $^{245}\text{Cm}(^{48}\text{Ca},xn)^{293-x}116$ , Phys. Rev. C **69**, 054607 (2004).

[Oganesyan1976] Yu. Ts. Oganesyan, A. G. Demin, N. A. Danilov, M. P. Ivanov, A. S. Il'ин N. N. Kolesnikov, B. N. Markov, V. M. Plotko, S. P. Tret'yakova, and G. N. Flerov, Experiments on the Synthesis of Element 107, Pis'ma Zh. Eksp. Teor. Fiz. **23**, 306 (1976) [JETP Lett. **23**, 277 (1976)].

[Omtvedt2002] J. P. Omtvedt, J. Alstad, H. Breivik, J. E. Dyve, K. Eberhardt, C. M. Folden III, T. Ginter, K. E. Gregorich, E. A. Hult, M. Johansson, U. W. Kirbach, D. M. Lee, M. Mendel, A. Nähler, V. Ninov, L. A. Omtvedt, J. B. Patin, G. Skarnemark, L. Stavsetra, R. Sudowe, N. Wiehl, B. Wierczinski, P. A. Wilk, P. M. Zielinski, J. V. Kratz, N. Trautmann, H. Nitsche, and D. C. Hoffman, SISAK Liquid-Liquid Extraction Experiments with Preseparated  $^{257}\text{Rf}$ , J. Nucl. Radiochem. Sci. **3**, 121 (2002).

[Patin2002a] J. B. Patin, Experimental Cross Sections for Reactions of Heavy Ions and  $^{208}\text{Pb}$ ,  $^{209}\text{Bi}$ ,  $^{238}\text{U}$ , and  $^{248}\text{Cm}$  Targets, Ph.D. Thesis, University of California, Berkeley (2002); Lawrence Berkeley National Laboratory Report LBNL-49593, 2002 (unpublished).

[Patin2002b] J. B. Patin (private communication).

[Patyk1991] Z. Patyk and A. Sobiczewski, Ground-State Properties of the Heaviest Nuclei Analyzed in a Multidimensional Deformation Space, Nucl. Phys. **A533**, 132 (1991).

[Pershina2002] V. Pershina, T. Bastug, T. Jacob, B. Fricke, and S. Varga, Intermetallic Compounds of the Heaviest Elements: The Electronic

Structure and Bonding of Dimers of Element 112 and Its Homolog Hg, *Chem. Phys. Lett.* **365**, 276 (2002).

[Peterson2004] D. A. Peterson (private communication).

[Pitzer1975] K. S. Pitzer, Are Elements 112, 114, and 118 Relatively Inert Gases?, *J. Chem. Phys.* **65**, 1032 (1975).

[Pyykkö1979] P. Pyykkö and J.-P. Desclaux, Relativity and the Periodic System of Elements, *Acc. Chem. Res.* **12**, 276 (1979).

[Randrup1976] J. Randrup, S. E. Larsson, P. Möller, S. G. Nilsson, K. Pomorski, and A. Sobiczewski, Spontaneous-Fission Half-Lives for Even Nuclei with  $Z \geq 92$ , *Phys. Rev. C* **13**, 229 (1976).

[Rutz1997] K. Rutz, M. Bender, T. Bürvenich, T. Schilling, P.-G. Reinhard, J. A. Maruhn, and W. Greiner, Superheavy Nuclei in Self-Consistent Nuclear Calculations, *Phys. Rev. C* **56**, 238 (1997).

[Schädel1997] M. Schädel, W. Brüchle, R. Dressler, B. Eichler, H. W. Gäggeler, R. Günther, K. E. Gregorich, D. C. Hoffman, S. Hübener, D. T. Jost, J. V. Kratz, W. Paulus, D. Schumann, S. Timokhin, N. Trautmann, A. Türler, G. Wirth, and A. Yakushev, Chemical Properties of Element 106 (Seaborgium), *Nature (London)* **388**, 55 (1997).

[Schmidt1984] K.-H. Schmidt, C.-C. Sahm, K. Pielenz, and H.-G. Clerc, Some Remarks on the Error Analysis in the case of Poor Statistics, *Z. Physik A* **316**, 19 (1984).

[Seaborg1990] G. T. Seaborg and W. D. Loveland, *The Elements Beyond Uranium* (John Wiley & Sons, New York, 1990), p. 121.

[Segrè1977] E. Segrè, *Nuclei and Particles: An Introduction to Nuclear and Subnuclear Physics*, 2nd. Ed. (Benjamin/Cummings, Reading, Massachusetts, 1977), pp. 26-27.

[Sikkeland1967] T. Sikkeland, Synthesis of Nuclei in the Region of  $Z = 126$  and  $N = 184$ , *Ark. Fys.* **36**, 539 (1967).

[Sikkeland1968a] T. Sikkeland, J. Maly, and D. F. Lebeck, Evaporation of 3 to 8 Neutrons in Reactions Between  $^{12}\text{C}$  and Various Uranium Nuclides, *Phys. Rev.* **169**, 1000 (1968).

[Sikkeland1968b] T. Sikkeland, A. Ghiorso, and M. J. Nurmia, Analysis of Excitation Functions in  $\text{Cm}(\text{C}, xn)\text{No}$  Reactions, *Phys. Rev.* **172**, 1232 (1968).

[Smolańczuk1999] R. Smolańczuk, Production Mechanism of Superheavy Nuclei in Cold Fusion Reactions, *Phys. Rev. C* **59**, 2634 (1999).

[Sobiczewski1966] A. Sobiczewski, F. A. Gareev, and B. N. Kalinkin, Closed Shells for  $Z > 82$  and  $N > 126$  in a Diffuse Potential Well, *Phys. Lett.* **22**, 500 (1966).

[Sobiczewski1987] A. Sobiczewski, Z. Patyk, and S. Cwiok, Do the Superheavy Nuclei Really form an Island?, *Phys. Lett. B* **186**, 6 (1987).

[Sobiczewski1998] A. Sobiczewski, Stability of the Heaviest Elements, in *ENAM 98: Exotic Nuclei and Atomic Masses*, edited by B. M. Sherrill, D. J. Morrissey, and C. N. Davids (American Institute of Physics, Woodbury, New York, 1998), p. 639.

[Sobiczewski2001] A. Sobiczewski, I. Muntian, and Z. Patyk, Problem of “Deformed” Superheavy Nuclei, *Phys. Rev. C* **63**, 034306 (2001).

[Strutinski1966] V. M. Strutinski, Influence of Nuclear Shells on the Energy of a Nucleus, *Yad. Fiz.* **3**, 614 (1966) [Sov. J. Nucl. Phys. **3**, 449 (1966)].

[Strutinsky1967] V. M. Strutinsky, Shell Effects in Nuclear Masses and Deformation Energies, *Nucl. Phys.* **A95**, 420 (1967).

[Strutinsky1968] V. M. Strutinsky, “Shells” in Deformed Nuclei, *Nucl. Phys.* **A122**, 1 (1968).

[Sudowe2002] R. Sudowe, K. E. Gregorich, D. C. Hoffman, J. P. Omtvedt, L. A. Omtvedt, L. Stavsetra and H. Nitsche, Extraction Systems for SISAK-BGS Transactinide Experiments: A New Look at Selectivity and Extraction Yields, in *Nuclear Science Division Annual Report 2001*, Lawrence Berkeley National Laboratory Report LBNL-49957, 2002 (unpublished).

[Świątecki2003] W. J. Świątecki, K. Siwek-Wilczyńska, and J. Wilczyński, Fusion by Diffusion, *Acta Phys. Pol. B* **34**, 2049 (2003).

[Świątecki2004a] W. J. Świątecki, K. Siwek-Wilczyńska, and J. Wilczyński, Fusion by Diffusion II, submitted to *Phys. Rev. C* (2004).

[Świątecki2004b] W. J. Świątecki, K. Siwek-Wilczyńska, and J. Wilczyński, Calculations of Cross Sections for the Synthesis of Super-Heavy Nuclei in Cold Fusion Reactions, *Int. J. Mod. Phys. E* **13**, 261 (2004).

[Türler1998] A. Türler, R. Dressler, B. Eichler, H. W. Gäggeler, D. T. Jost, M. Schädel, W. Brückle, K. E. Gregorich, N. Trautmann, S. Taut, Decay Properties of  $^{265}\text{Sg}(Z=106)$  and  $^{266}\text{Sg}(Z=106)$ , *Phys. Rev. C* **57**, 1648 (1998).

[Türler2003] A. Türler, Ch. E. Düllmann, H. W. Gäggeler, U. W. Kirbach, A. B. Yakushev, M. Schädel, W. Brückle, R. Dressler, K. Eberhardt, B.

Eichler, R. Eichler, T. N. Ginter, F. Glaus, K. E. Gregorich, D. C. Hoffman, E. Jäger, D. T. Jost, D. M. Lee, H. Nitsche, J. B. Patin, V. Pershina, D. Piguet, Z. Qin, B. Schausten, E. Schimpf, H.-J. Schött, S. Soverna, R. Sudowe, P. Thörle, S. N. Timokhin, N. Trautmann, A. Vahle, G. Wirth, and P.M. Zielinski, On the Decay Properties of  $^{269}\text{Hs}$  and Indications for the New Nuclide  $^{270}\text{Hs}$ , *Eur. Phys. J. A* **17**, 505 (2003).

[Vandenbosch1973] R. Vandenbosch and J. R. Huizenga, *Nuclear Fission* (Academic Press, New York, 1973), pp. 227-33.

[Weizäcker1935] C. F. von Weizäcker, Zur Theorie der Kernmassen, *Z. Phys.* **96**, 29 (1935) (in German).

[Wilk2000] P. A. Wilk, K. E. Gregorich, A. Türler, C. A. Laue, R. Eichler, V. Ninov, J. L. Adams, U. W. Kirbach, M. R. Lane, D. M. Lee, J. B. Patin, D. A. Shaughnessy, D. A. Strellis, H. Nitsche, and D. C. Hoffman, Evidence for New Isotopes of Element 107:  $^{266}\text{Bh}$  and  $^{267}\text{Bh}$ , *Phys. Rev. Lett.* **85**, 2697 (2000).

[Xu2004] F. R. Xu, E. G. Zhao, R. Wyss, and P. M. Walker, Enhanced Stability of Superheavy Nuclei Due to High-Spin Isomerism, *Phys. Rev. Lett.* **92**, 252501 (2004).

[Ziegler2003] J. F. Ziegler, computer code SRIM-2003, available from <http://www.srim.org>.

[Zubov2003] A. S. Zubov, G. G. Adamian, N. V. Antonenko, S. P. Ivanova, W. Scheid, Survival Probability of Excited Heavy Nuclei, *Acta Phys. Pol. B* **34**, 2083 (2003).

## **Corrigendum**

After initial publication of this dissertation it was discovered that the multi-wire proportional counter (MWPC) was incorrectly described as a multi-wire avalanche counter (MWAC). Throughout the text, all references to “multi-wire avalanche counter” or “MWAC” have been changed to “multi-wire proportional counter” or “MWPC” as appropriate. Also, the sentence on page 55 which previously read, “Any EVR passing through the MWAC initiates a charge avalanche which is collected at electrodes on the top, bottom, left, and right sides” has been replaced with, “Any EVR passing through the MWPC initiates a process of charge multiplication, and this charge is collected at electrodes on the top, bottom, left, and right sides.” The reported results are unaffected by these changes in the text.

## **Disclaimer**

This document was prepared as an account of work sponsored by the United States Government. While this document is believed to contain correct information, neither the United States Government nor any agency thereof, nor The Regents of the University of California, nor any of their employees, makes any warranty, express or implied, or assumes any legal responsibility for the accuracy, completeness, or usefulness of any information, apparatus, product, or process disclosed, or represents that its use would not infringe privately owned rights. Reference herein to any specific commercial product, process, or service by its trade name, trademark, manufacturer, or otherwise, does not necessarily constitute or imply its endorsement, recommendation, or favoring by the United States Government or any agency thereof, or The Regents of the University of California. The views and opinions of authors expressed herein do not necessarily state or reflect those of the United States Government or any agency thereof, or The Regents of the University of California.

Ernest Orlando Lawrence Berkeley National Laboratory is an equal opportunity employer.